Faster than Nyquist transceiver design : algorithms for a global transmission-reception enhancement

Naila Lahbabi

IMT Atlantique
Bretagne-Pays de la Loire
École Mines-Télécom

UNIVERSITE BRETAGNE LOIRE

THÈSE / IMT Atlantique

sous le sceau de l'Université Bretagne Loire

pour obtenir le grade de

DOCTEUR D'IMT Atlantique

Mention : Sciences et Technologies de l'Information et de la Communication

École Doctorale Sicma

Présentée par

Naila Lahbabi

Préparée dans le département Electronique

Laboratoire Labsticc

Conception de transrécepteurs au-delà de la cadence de Nyquist: algorithmes de transmission et réception et optimisation globale

Faster than Nyquist transceiver design: algorithms for a global transmission-reception enhancement

Thèse soutenue le 22 juin 2017

devant le jury composé de :

Jean-François Hélard
Professeur des universités, INSA - Rennes / président

Michel Terré
Professeur des universités, CNAM - Paris / rapporteur

Cyrille Siclet
Maître de conférences (HDR), université Joseph Fourier / examinateur

Hao Lin
Senior research engineer, Orange Labs / examinateur

Abdel Nour Charbel
Maître de conférences (HDR), IMT Atlantique / examinateur

Catherine Douillard
Professeure, IMT Atlantique / directrice de thèse

Pierre Siohan
Chercheur indépendant / invité

Thesis N° 2017IMTA0017

IMT Atlantique
Bretagne-Pays de la Loire
École Mines-Télécom

orange™

Dissertation

In Partial Fulfillment of the Requirements
for the Degree of Doctor of Philosophy
from IMT Atlantique Bretagne-Pays de la Loire

Naila Lahbabi

Faster than Nyquist transceiver design: algorithms for transmission and reception and global enhancements

Defended on June, 22 2017 in front of a jury composed of:

President	Mr. J-F. Hélard
Reporters	Mr. M. Terré
Examiners	Mr. C. Abdel Nour
	Ms. C. Douillard
	Mr. C. Siclet
	Mr. H. Lin
Invited	Mr. P. Siohan

This thesis took place at Orange Labs (RNM/AWE/CREM), Rennes.

To my beloved parents Fatima and Saad

To my husband Taoufik

...

Acknowledgements

I wish to express my sincere feelings of gratitude to every person who crossed my path and helped make these 3 years a pleasant journey to always remember.

I am truly and forever grateful to my supervisors Dr. Hao Lin and Dr. Pierre Siohan, and to my thesis supervisors Prof. Catherine Douillard and Ass. Prof. Charbel Abdel Nour for their continuous support, help and motivation. Their guidance helped me in all the time of research and writing of this thesis. I could not have imagined having better advisors for my Ph.D study.

I would like to thank my thesis committee Prof. Jean-François Hélard, Prof. Michel Terré and Ass. Prof. Cyrille Siclet for reviewing my thesis and for their insightful comments.

I wish also to thank all those who gave me the opportunity of doing this thesis in the first place. A special gratitude goes to Mr. Jean-Christophe Rault for having welcomed me within the CREAM's team and for his continuous support. My sincere thanks goes to all my colleagues at Orange with special mention to my office mates: Marc-Antoine, Senad, Wissem, Ibrahima and Kaouthar with whom I shared many enriching discussions.

Last, but by no means least, I would like to thank my family and friends who have supported me along the way. I am and will always be grateful to my beloved parents Fatima and Saad for their love, support and expecting nothing but excellence from me. I am also grateful to my parents in law Houria and Mohammed for their continuous support. I wish also to thank my husband Taoufik for his unconditional love, patience and for always believing in me. My sincere thanks goes also to my brothers Ismail, Hamza and Awane for being always there for me. I am also grateful to all my family members whose encouragements and prayers helped me successfully complete this work, especially my grandparents Amina and Mostapha, my aunts and uncles.

August 2017
Naila Lahbabi
Rennes

Abstract

The exponential growth of wireless data traffic driven by mobile Internet and smart devices constrains the future radio systems to include advanced modulations/waveforms offering higher data rates with more efficient bandwidth usage. One possibility is to violate the well known Nyquist criterion by transmitting faster than the Nyquist rate, i.e., using a technique also known as Faster-Than-Nyquist (FTN) signaling. Nyquist-based systems have the advantage of simple transmitter and receiver architectures at the detriment of bandwidth efficiency. The idea of signaling beyond the Nyquist rate to trade the interference-free transmission for more throughput goes back to 1975. In this dissertation, we investigate the concept of FTN signaling over Additive White Gaussian Noise (AWGN) channel in the context of Orthogonal Frequency Division Multiplexing with Offset Quadrature Amplitude Modulation OFDM/OQAM modulation.

The main objective of our work is to present an OFDM/OQAM system signaling faster than the Nyquist one and explore its potential rate improvement while keeping under consideration the overall system complexity. First, we propose a new efficient FTN implementation of OFDM/OQAM systems, denoted by FTN-OQAM, that has the same complexity as OFDM/OQAM systems, while approaching very closely the FTN theoretical rate improvement. As the Nyquist condition is no longer respected, severe interference impacts the transmitted signals. To deal with the introduced interferences, we propose a turbo-like receiver based on Minimum Mean Square Error Linear Equalization and Interference Cancellation, named MMSE LE-IC. The aim of our system is to boost the transmission rate, which means that high constellation orders will be targeted. In this respect, the MMSE LE-IC, whose complexity is independent of the constellation, turns out to be a good candidate. Since OFDM/OQAM modulation can be equipped with different types of pulse shapes, we propose an algorithm to find, for different constellation orders, the minimum achieved FTN packing factor for various pulse shapes. Then, we aim at improving the iterative processing of the introduced transceiver. The proposed method involves combining a precoder with the FTN-OQAM system in order to remove FTN-induced interference at the transmitter. We also present a sparse precoding pattern as it is difficult to jointly precode all the transmitted symbols. We introduce three families of precoders along with the corresponding receivers. Furthermore, we propose several modifications of the FTN-OQAM transmitter concerning different blocks such as channel coding, bits mapping and symbols mapping to further enhance the FTN-OQAM transceiver design. Presented results reveal the significant potential of the proposed methods.

Keywords: Faster-Than-Nyquist, OFDM/OQAM, channel coding, precoding, turbo equalization, interference cancellation.

Résumé

La croissance exponentielle du trafic de données sans fils, causée par l'Internet mobile et les smartphones, contraint les futurs systèmes radio à inclure des modulations/formes d'ondes plus avancées offrant un débit plus élevé et une utilisation efficace des ressources spectrales. Les transmissions dites Faster-Than-Nyquist (FTN), introduites en 1975, sont parmi les meilleurs candidates pour répondre à ces besoins. En transmettant les symboles à une cadence plus rapide que celle définie par le critère de Nyquist, FTN peut théoriquement augmenter le débit mais en introduisant des interférences en contrepartie. Dans cette thèse, nous explorons le concept des transmissions FTN à travers un canal AWGN (Additive White Gaussian Noise) dans le contexte des modulations OFDM/OQAM (Orthogonal Frequency Division Multiplexing with Offset Quadrature Amplitude Modulation).
L'objectif principal de cette thèse est de présenter un système OFDM/OQAM qui permet de transmettre l'information au-delà de la cadence de Nyquist tout en tenant en compte la complexité globale du système. Tout d'abord, nous proposons une nouvelle implémentation efficace des systèmes OFDM/OQAM appliquant le concept FTN, désignée ici par FTN-OQAM, qui garde la même complexité que les systèmes OFDM/OQAM et qui permet un gain en débit très proche du gain théorique. Vu que la condition de Nyquist n'est plus respectée, le signal transmis est maintenant perturbé par des interférences. Pour remédier à ce problème, nous proposons un récepteur basé sur le principe de l'égalisation linéaire sous le critère minimum erreur quadratique moyenne avec annulation d'interférences appelé MMSE LE-IC. Le but de notre système est d'augmenter le débit de transmission, ce qui signifie que des constellations d'ordres élevés seront ciblées. Dans ce contexte, le MMSE LE-IC, dont la complexité est indépendante de la constellation, représente un bon compromis entre efficacité et complexité. Puisque la modulation OFDM/OQAM utilise différents types de formes d'ondes, nous proposons pour plusieurs d'entre elles un algorithme pour déterminer la valeur minimale du facteur d'accélération, en fonction de l'ordre de constellation, qui apporte un gain en efficacité spectrale tout en gardant les mêmes performances que les systèmes respectant le critère de Nyquist à un SNR fixé. Ensuite, nous étudions l'amélioration du traitement itératif de l'émetteur-récepteur. La méthode proposée consiste à combiner un précodeur avec le système FTN-OQAM afin de réduire les interférences causées par du FTN à l'émission. Nous proposons un modèle de précodage dispersé, car il est difficile de précoder conjointement tous les symboles transmis. Nous présentons trois familles de précodeurs avec les récepteurs correspondants. En outre, nous modifions différents blocs de l'émetteur FTN-OQAM tels que le codage canal, le mappage des bits et le mappage des symboles afin d'améliorer d'avantage le transmetteur FTN-OQAM. Les résultats présentés révèlent le potentiel important des systèmes proposés.

Mot clés: Faster-Than-Nyquist, OFDM/OQAM, codage canal, précodage, turbo égalisation, annulation d'interférence.

Contents

Acknowledgements iii

Abstract v

Résumé vii

Contents viii

List of Figures xii

List of Tables xviii

Abbreviations xx

Résumé Français 1

1 Introduction 38

2 State of the Art and Background 43

2.1 Introduction . . . 43
2.2 OFDM . . . 43
2.3 OFDM/OQAM . . . 45
2.3.1 Continuous OFDM/OQAM . . . 45
2.3.2 Discrete OFDM/OQAM . . . 48
2.3.3 Time-frequency localization of prototype filters . . . 49
2.3.3.1 Ambiguity function . . . 49
2.3.3.2 Time-Frequency localization . . . 49
2.3.3.3 The Square Root Raised Cosine Filter (SRRC) . . . 50
2.3.3.4 The Extended Gaussian Function (EGF) . . . 52
2.3.3.5 Time Frequency Localization (TFL) filter . . . 53
2.3.3.6 Frequency Selective (FS) filter . . . 53
2.4 Faster Than Nyquist Signaling . . . 56
2.4.1 Nyquist criterion . . . 56
2.4.2 FTN signaling . . . 58
2.4.3 Related FTN research . . . 60
2.5 Selected channel coding and precoding techniques . . . 68
2.5.1 BCJR Algorithm . . . 68
2.5.2 Turbo coding and turbo equalization . . . 72

2.5.3 Turbo equalization . . . 73
2.5.4 Convergence analysis using EXIT charts . . . 77
2.5.5 Tomlinson Harashima Precoding . . . 79
2.6 Conclusion . . . 81

3 An FTN transceiver for OFDM/OQAM systems 82
3.1 Introduction . . . 82
3.2 FTN-OQAM modem . . . 83
3.2.1 FTN-OQAM modulator . . . 83
3.2.1.1 The modulator structure for non-causal prototype filter . 83
3.2.1.2 The modulator structure for causal prototype filter . . . 84
3.2.2 FTN-OQAM demodulator . . . 85
3.3 Interference analysis for the FTN-OQAM transceiver . . . 86
3.3.1 Interference analysis for continuous-time FTN-OQAM transceiver . 86
3.3.2 Interference analysis for discrete-time FTN/OQAM transceiver . . 89
3.4 The FTN-OQAM receiver . . . 93
3.4.1 Time-domain MMSE turbo-equalization . . . 94
3.4.2 Frequency-domain MMSE turbo-equalization . . . 97
3.5 Simulation results . . . 99
3.5.1 Effective minimum lossless packing factor investigation . . . 99
3.5.2 Performance of the proposed FTN-OQAM transceiver . . . 104
3.5.3 A word about complexity . . . 108
3.6 Conclusion . . . 109

4 Precoded FTN-OQAM 111
4.1 Introduction . . . 111
4.2 Precoded FTN-OQAM transceiver: ISI and ICI cancellation . . . 113
4.2.1 SIPC along time and frequency axes . . . 113
4.2.2 The receiver structure . . . 114
4.2.3 BCJR decoder modification . . . 118
4.2.4 Simulation results . . . 119
4.2.5 A word about complexity . . . 122
4.3 Precoded FTN-OQAM transceiver: ISI cancellation . . . 124
4.3.1 SIPC along time axis . . . 124
4.3.2 The receiver structure . . . 126
4.3.3 BCJR decoder modification . . . 126
4.3.4 Simulation results . . . 126
4.3.5 A word about complexity . . . 129
4.4 Precoded FTN-OQAM transceiver: ICI cancellation . . . 132
4.4.1 SIPC along frequency axis . . . 132
4.4.2 The receiver structure . . . 132
4.4.3 BCJR decoder modification . . . 134
4.4.4 Simulation results . . . 135
4.4.5 A word about complexity . . . 138
4.5 Performance comparison between the proposed precoders . . . 138
4.6 Conclusion . . . 143

5 An enhanced design for FTN-OQAM transceiver 146
5.1 Introduction . . . 146
5.2 Channel coding rate adaptation . . . 146
5.3 Gray mapping enhancement . . . 159
5.3.1 Non-precoded FTN-OQAM transceiver . . . 159
5.3.2 Precoded FTN-OQAM transceiver . . . 162
5.4 Symbols mapping enhancement . . . 166
5.4.1 Precoded FTN-OQAM transceiver . . . 167
5.4.1.1 SIPC-t precoding . . . 168
5.4.1.2 SIPC-f precoding . . . 169
5.4.2 Non-precoded FTN-OQAM transceiver . . . 170
5.4.3 Simulation results . . . 171
5.4.3.1 SIPC-t precoding . . . 171
5.4.3.2 SIPC-f precoding . . . 174
5.4.3.3 Non-precoded FTN-OQAM transceiver . . . 176
5.5 Bits mapping Vs. Symbols mapping . . . 178
5.6 Joint enhancement of channel coding and Gray mapping . . . 179
5.7 Joint enhancement of channel coding and symbol mapping . . . 179
5.8 Conclusion . . . 184

6 Conclusion 185
6.1 Research contribution . . . 185
6.2 Directions for future work . . . 187
6.2.1 Channel coding . . . 187
6.2.2 PAPR . . . 188
6.2.3 Other equalization schemes . . . 188

Bibliography 190

List of Figures

1 *Le modulateur causal FTN-OQAM.* . . . 8
2 *Le démodulateur causal FTN-OQAM.* . . . 9
3 Puissance moyenne d'ICI et d'ISI pour différentes formes d'onde et facteurs FTN. . . . 10
4 Chaîne de transmission FTN-OQAM. . . . 11
5 Structure de l'égaliseur SISO MMSE LE-IC. . . . 12
6 Processus de recherche de la valeur minimale effective du facteur FTN. . . . 13
7 L'émetteur-récepteur FTN-OQAM proposé. Les blocs en pointillés sont liés à la méthode SIPC. . . . 16
8 Lattice temps-fréquence du FTN-OQAM avec le précodage SIPC-tf. Les triangles verts représentent les symboles précodés. Les triangles rouges et bleus représentent les symboles non précodés. . . . 17
9 Structure de l'égaliseur SISO MMSE IC-LE utilisé pour le précodage SIPC-tf. . . . 18
10 Lattice temps-fréquence du FTN-OQAM avec le précodage SIPC-t. Les triangles verts et rouges représentent les symboles précodés et non précodés, respectivement. . . . 19
11 Structure de l'égaliseur SISO MMSE IC-LE utilisé pour le précodage SIPC-t. . . . 20
12 Lattice temps-fréquence du FTN-OQAM avec le précodage SIPC-f. Les triangles verts et rouges représentent les symboles précodés et non précodés, respectivement. . . . 21
13 Evaluation BER de FTN-OQAM combiné avec le précodage SIPC-f pour la modulation QPSK et les facteurs FTN $\tau = 0.7$ et $\tau = 0.8$. . . . 22
14 Evaluation BER de FTN-OQAM combiné avec le précodage SIPC-tf pour la modulation 16-QAM et les facteurs FTN $\tau = 0.7$ et $\tau = 0.8$. . . . 23
15 Evaluation BER de FTN-OQAM combiné avec le précodage SIPC-t pour la modulation 64-QAM et le facteur FTN $\tau = 0.8$. . . . 24
16 Le codage canal et l'entrelaceur proposés. . . . 25
17 Mapping Gray: 16-QAM. . . . 27
18 Mapping Gray: 64-QAM. . . . 28
19 Le mapping des symboles proposé dans le cas de l'émetteur-récepteur FTN-OQAM précodé. . . . 31
20 Le mapping des symboles proposé pour l'émetteur-récepteur FTN-OQAM. 33

2.1 Analogue OFDM/OQAM modulator [1]. . . . 46
2.2 Time-frequency lattice representation of OFDM and OFDM/OQAM. . . . 46
2.3 Analogue OFDM/OQAM demodulator [1]. . . . 47
2.4 Discrete-time structure of OFDM/OQAM system. . . . 48

2.5 Time-frequency comparison: SRRC ($b = 4, \rho = 0.5$) vs. rectangular window. 51
2.6 Ambiguity function representation of the SRRC ($b = 4, \rho = 0.5$) filter. . . 51
2.7 Time-frequency comparison: IOTA ($b = 4$) vs. rectangular window. 52
2.8 Ambiguity function representation of the IOTA ($b = 4$) filter. 53
2.9 Time-frequency comparison: TFL ($b = 1$) vs. rectangular window. 54
2.10 Ambiguity function representation of the TFL ($b = 1$) filter. 54
2.11 Time-frequency comparison: FS ($b = 4, \rho = 1$) vs. rectangular window. . . 55
2.12 Ambiguity function representation of the FS ($b = 4$) filter. 55
2.13 Time-frequency lattice of FTN and OQAM symbols. 63
2.14 FTN-OQAM transmitter architecture, [2]. 64
2.15 FTN-OQAM receiver architecture, [3]. 64
2.16 Rate 1/2 Recursive Systematic Convolutional code. 69
2.17 One trellis stage of the RSC code (1, 5/7). The encoder input and output bits are denoted by in/out labels at each trellis edge. 69
2.18 Turbo encoder architecture. 72
2.19 Turbo decoder architecture. 73
2.20 Turbo equalizer structure. 74
2.21 Structure of the SISO MMSE equalizer. 74
2.22 Practical implementation of the MMSE linear equalizer. 76
2.23 Typical EXIT chart diagram. 78
2.24 Structure of the inverse filter. 80
2.25 Structure of the THP precoder. 80

3.1 *FTN-OQAM non-causal modulator.* 84
3.2 *FTN-OQAM causal modulator.* 85
3.3 *FTN-OQAM causal demodulator.* 86
3.4 *The rate improvement of FTN-OQAM as a function of τ.* 87
3.5 Interference mean power using the IOTA filter ($L = 4M$) and $\tau = 0.7$. . . 91
3.6 Interference mean power for different pulse shapes and FTN packing factors. 92
3.7 Interference mean power for different pulse shapes and FTN packing factors. 93
3.8 ICI and ISI mean power for different pulse shapes and FTN packing factors. 93
3.9 FTN-OQAM time-frequency lattice. Circles represent Nyquist data while triangles represent FTN data. 94
3.10 FTN-OQAM transmission chain. 94
3.11 Structure of the SISO MMSE LE-IC. 97
3.12 Time-domain ICI and ISI prediction and canceling. 97
3.13 Frequency-domain ICI and ISI prediction and canceling. 98
3.14 BER performance of the proposed FTN-OQAM transceiver using FS filtering, QPSK and different coding rates. 100
3.15 Search process for the effective minimum lossless FTN packing factor. . . 101
3.16 EXIT chart for MMSE LE-IC with QPSK using IOTA at SNR=6.2 dB. The FTN packing factor ranges from 0.4 (bottom) to 0.9 (top) in step of 0.1. 102
3.17 EXIT chart for MMSE LE-IC with 16-QAM using IOTA at SNR=12.6 dB. The FTN packing factor ranges from 0.5 (bottom) to 0.9 (top) in step of 0.1. 103
3.18 EXIT chart for MMSE LE-IC with 64-QAM using IOTA at SNR=18.2 dB. The FTN packing factor ranges from 0.8 (bottom) to 0.9 (top). 103

3.19 EXIT chart for MMSE LE-IC with 64-QAM and $\tau = 0.9$, using time-domain and frequency-domain equalization. 104
3.20 BER performance of the FTN-OQAM transceiver using different pulse shapes and modulation orders, and $\tau = 0.9$. 105
3.21 BER performance of the FTN-OQAM transceiver Vs. Nyquist system for different modulation orders 106
3.22 BER performance of the FTN-OQAM transceiver Vs. Nyquist system using QPSK modulation, PHYDYAS filtering and $\tau = 0.7$ and 0.8. 106
3.23 BER performance of the FTN-OQAM transceiver Vs. Nyquist system using 16-QAM modulation, PHYDYAS filtering and τ =0.8. 107
3.24 BER performance of the FTN-OQAM transceiver Vs. Nyquist system using 64-QAM modulation, SRRC (ρ=0.5) filtering and τ =0.8. 107

4.1 The proposed precoded FTN-OQAM transceiver. Dashed blocks are related to the SIPC method. 113
4.2 Time-frequency lattice of FTN-OQAM with SIPC-tf precoding. Green triangles represent precoded symbols while the red and blue triangles represent OQAM symbols. 114
4.3 Structure of the SISO MMSE IC-LE used for SIPC-tf precoding. 116
4.4 EXIT chart analysis of the FTN-OQAM transceiver combined with SIPC-tf precoding for QPSK, 16-QAM, 64-QAM and $\tau = 0.9$. 119
4.5 BER vs. SNR performance of the proposed FTN-OQAM transceiver combined with SIPC-tf precoding for QPSK, 16-QAM, 64-QAM and $\tau = 0.9$. . 120
4.6 Comparison of the EXIT chart analysis between the precoded and non-precoded FTN-OQAM transceiver using SRRC (ρ=0.5) filtering, $\tau = 0.9$ and different modulation orders. 121
4.7 Comparison of the BER performance between the precoded and non-precoded FTN-OQAM transceiver using SRRC (ρ=0.5) filtering, $\tau = 0.9$ and different modulation orders. 122
4.8 Time-frequency lattice of FTN-OQAM with SIPC-t precoding. The green and red triangles represent precoded and OQAM symbols, respectively. . . 125
4.9 Structure of the SISO MMSE IC-LE used for FTN-OQAM with SIPC-t precoding. 127
4.10 EXIT chart analysis of the proposed FTN-OQAM transceiver combined with SIPC-t precoding for QPSK, 16-QAM, 64-QAM and $\tau = 0.9$. 128
4.11 BER vs. SNR performance of the proposed FTN-OQAM transceiver combined with SIPC-t precoding for QPSK, 16-QAM, 64-QAM and $\tau = 0.9$. . 129
4.12 Comparison of the EXIT chart analysis between the precoded and non-precoded FTN-OQAM transceiver using SRRC (ρ=0.5, 0.3) filtering, τ = 0.9 and different modulation orders. 130
4.13 Comparison of the BER performance between the precoded and non-precoded FTN-OQAM transceiver using SRRC (ρ=0.5, 0.3) filtering, τ = 0.9 and different modulation orders. 131
4.14 Time-frequency lattice of FTN-OQAM with SIPC-f precoding. Green and red triangles contain precoded and OQAM symbols, respectively. 133
4.15 EXIT chart analysis of the proposed FTN-OQAM transceiver with SIPC-f precoding for QPSK, 16-QAM, 64-QAM and $\tau = 0.9$. 134
4.16 BER vs. SNR performance of the proposed FTN-OQAM transceiver with SIPC-f precoding for QPSK, 16-QAM, 64-QAM and $\tau = 0.9$. 135

4.17 Comparison of the EXIT chart analysis between the precoded and non-precoded FTN-OQAM transceiver using SRRC (ρ=0.5) filtering, $\tau = 0.9$ and different modulation orders. 136
4.18 Comparison of the BER performance between the precoded and non-precoded FTN-OQAM transceiver using SRRC (ρ=0.5) filtering, $\tau = 0.9$ and different modulation orders. 137
4.19 BER comparison of the three precoders using QPSK modulation. 140
4.20 BER comparison of the three precoders using 16-QAM modulation. 141
4.21 BER comparison of the three precoders using 64-QAM modulation. 141
4.22 BER evaluation of the FTN-OQAM transceiver combined with SIPC-f precoding for QPSK modulation and FTN packing factors $\tau = 0.7$ and $\tau = 0.8$. 142
4.23 BER evaluation of the FTN-OQAM transceiver combined with SIPC-tf precoding for 16-QAM modulation and FTN packing factors $\tau = 0.7$ and $\tau = 0.8$. 142
4.24 BER evaluation of the FTN-OQAM transceiver combined with SIPC-t precoding for 64-QAM modulation and FTN packing factor $\tau = 0.8$. . . . 143
4.25 BER comparison between the precoded and non-precoded FTN-OQAM transceiver using different pulse shapes, 16-QAM-modulation and $\tau = 0.9$. 145

5.1 BER evaluation of the FTN-OQAM transceiver using SIPC-t precoding, 16-QAM modulation and PHYDYAS filtering. 148
5.2 BER evaluation of the FTN-OQAM transceiver using SIPC-t precoding, 64-QAM modulation and PHYDYAS filtering. 149
5.3 The proposed channel encoder and interleaver. 149
5.4 EXIT chart analysis of the FTN-OQAM transceiver combined with SIPC-t precoding using PHYDYAS filtering, 16-QAM modulation and $\tau = 0.7$. . . 150
5.5 BER evaluation of the enhanced channel coding in case of PHYDYAS filtering, 16-QAM modulation and $\tau = 0.7$. 151
5.6 EXIT chart analysis of the FTN-OQAM transceiver combined with SIPC-t precoding using PHYDYAS filtering, 16-QAM modulation and $\tau = 0.8$. . . 153
5.7 BER evaluation of the enhanced channel coding in case of PHYDYAS filtering, 16-QAM modulation and $\tau = 0.8$. 153
5.8 EXIT chart analysis of the FTN-OQAM transceiver combined with SIPC-t precoding using SRRC (ρ=0.5) filtering, 16-QAM modulation and $\tau = 0.9$. 154
5.9 BER evaluation of the enhanced channel coding in case of SRRC (ρ=0.5) filtering, 16-QAM modulation and $\tau = 0.9$. 154
5.10 EXIT chart analysis of the FTN-OQAM transceiver combined with SIPC-t precoding using PHYDYAS filtering, 64-QAM modulation and $\tau = 0.8$. . . 155
5.11 BER evaluation of the enhanced channel coding in case of PHYDYAS filtering, 64-QAM modulation and $\tau = 0.8$. 156
5.12 EXIT chart analysis of the FTN-OQAM transceiver combined with SIPC-t precoding using PHYDYAS filtering, 64-QAM modulation and $\tau = 0.9$. . . 157
5.13 BER evaluation of the enhanced channel coding in case of PHYDYAS filtering, 64-QAM modulation and $\tau = 0.9$. 158
5.14 BER evaluation of the enhanced channel coding in case of FS and SRRC (ρ=0.5) filtering, 64-QAM modulation and $\tau = 0.9$. 158
5.15 16-QAM Gray Mapping. 159
5.16 64-QAM Gray Mapping. 160

5.17 BER evaluation of the FTN-OQAM transceiver using the proposed bit-to-symbol mapping in case of PHYDYAS filtering and 16-QAM modulation. 161
5.18 BER evaluation of the FTN-OQAM transceiver using the proposed bit-to-symbol mapping in case of PHYDYAS filtering, 64-QAM modulation and τ=0.9. 162
5.19 BER evaluation of the FTN-OQAM transceiver combined with SIPC-t precoding and the proposed bit-to-symbol mapping in case of PHYDYAS filtering and 16-QAM modulation. 163
5.20 BER evaluation of the FTN-OQAM transceiver combined with SIPC-t precoding and the proposed bit-to-symbol mapping in case of SRRC (ρ=0.5) filtering and 16-QAM modulation. 164
5.21 BER evaluation of the FTN-OQAM transceiver combined with SIPC-t precoding and the proposed bit-to-symbol mapping in case of PHYDYAS filtering, 64-QAM modulation and $\tau = 0.8$. 164
5.22 BER evaluation of the FTN-OQAM transceiver combined with SIPC-t precoding and the proposed bit-to-symbol mapping in case of SRRC (ρ=0.5) filtering, 64-QAM modulation and $\tau = 0.9$. 165
5.23 BER evaluation of the FTN-OQAM transceiver combined with SIPC-f precoding and the proposed bit-to-symbol mapping using PHYDYAS filtering, 16 and 64-QAM modulation and $\tau = 0.8$ and 0.9. 166
5.24 The proposed symbols to time-frequency positions mapping in case of the precoded FTN-OQAM transceiver. 168
5.25 The proposed symbols to time-frequency positions mapping for the FTN-OQAM transceiver. 171
5.26 Interference power as a function of the time index position n_0. 172
5.27 BER evaluation of the FTN-OQAM transceiver using the proposed symbols mapping and SIPC-t precoding in case of 16-QAM modulation and IOTA filtering. 173
5.28 BER evaluation of the FTN-OQAM transceiver using the proposed symbols mapping and SIPC-t precoding in case of 64-QAM modulation and IOTA filtering. 174
5.29 BER evaluation of the FTN-OQAM transceiver using the proposed symbols mapping and SIPC-t precoding in case of 16-QAM modulation for $\tau = 0.7$ and the PHYDYAS and FS pulse shapes. 174
5.30 BER evaluation of the FTN-OQAM transceiver using the proposed symbols mapping and SIPC-f precoding in case of 16-QAM modulation for $\tau = 0.7$ and the IOTA, TFL, PHYDYAS and FS pulse shapes. 175
5.31 BER evaluation of the FTN-OQAM transceiver using the proposed symbols mapping and SIPC-f precoding in case of 64-QAM modulation for $\tau = 0.8$ and the PHYDYAS and FS pulse shapes. 175
5.32 BER evaluation of the FTN-OQAM transceiver using the proposed symbols mapping, 16-QAM modulation and IOTA filtering. 177
5.33 BER evaluation of the FTN-OQAM transceiver using SIPC-t precoding and PHYDYAS filtering. 177
5.34 Joint enhancement of channel encoding and symbols mapping of the precoded FTN-OQAM transceiver. 181
5.35 BER evaluation of the FTN-OQAM transceiver using SIPC-t precoding, PHYDYAS filtering and 16-QAM modulation. 182

5.36 BER evaluation of the FTN-OQAM transceiver using SIPC-t precoding, PHYDYAS filtering, 64-QAM modulation and $\tau = 0.8$. 183
5.37 BER evaluation of the FTN-OQAM transceiver using SIPC-t precoding, SRRC (ρ=0.5) filtering, 64-QAM modulation and $\tau = 0.9$. 183

List of Tables

2 Valeurs minimales numériques des facteurs FTN et domaines d'égalisation recommandés pour chaque filtre et ordre de constellation. 13
3 Nombres d'itérations nécessaires pour chaque ordre de constellation et pour un facteur FTN de 0.9. 13
4 Formes d'ondes recommandées et nombre d'itérations pour chaque ordre de constellation et facteur FTN. 14
5 Formes d'ondes recommandées et nombre d'itérations pour différents facteurs FTN et ordres de modulation et le précodage SIPC-tf. 22
6 Formes d'ondes recommandées et nombre d'itérations pour différents facteurs FTN et ordres de modulation et le précodage SIPC-t. 22
7 Formes d'ondes recommandées et nombre d'itérations pour différents facteurs FTN et ordres de modulation et le précodage SIPC-f. 22
8 Précodeurs recommandés pour différents facteurs FTN et ordres de constellation. 23
9 Schéma de transmission des symboles de la modulation OFDM/OQAM. . 29
10 Stratégies de mapping recommandées pour l'émetteur-récepteur FTN-OQAM. 34
11 Stratégies de mapping recommandées pour l'émetteur-récepteur FTN-OQAM avec le précodage SIPC-t. 34

3.1 The global period N_0^G for different FTN packing factors (M=64). 90
3.2 Numerical values of the effective minimum lossless FTN packing factors and recommended equalization domain for different pulse shapes and modulation orders. 104
3.3 Recommended pulse shapes for different modulation orders and τ=0.9. . . 105
3.4 Number of iterations needed for each modulation order to reach an effective minimum lossless FTN packing factor equal to 0.9. 107
3.5 Recommended pulse shapes and number of necessary iterations for each modulation order to reach different FTN packing factors. 108
3.6 Number of performed additions and multiplications performed by each block of the receiver. 108
3.7 Complexity of one performed iteration at the receiver side considering different modulation orders. 109

4.1 Number of necessary iterations for each pulse shape in case of SIPC-tf precoding and $\tau = 0.9$. 121
4.2 Recommended pulse shapes and number of necessary iterations for each modulation order in case of SIPC-tf precoding and τ=0.9. 122
4.3 Number of performed additions and multiplications by SIPC-tf precoder. . 123

4.4 Number of necessary iterations for each pulse shape in case of SIPC-t precoding and $\tau = 0.9$. 128
4.5 Recommended pulse shapes and number of necessary iterations for each modulation order in case of SIPC-t precoding. 130
4.6 Number of performed additions and multiplications by SIPC-t precoder. . 131
4.7 Number of necessary iterations for each pulse shape in case of SIPC-f precoding and $\tau = 0.9$. 136
4.8 Recommended pulse shapes and number of necessary iterations for different modulation orders in case of SIPC-f precoding and for $\tau = 0.9$. 138
4.9 Number of performed additions and multiplications by SIPC-f precoding. . 138
4.10 Recommended pulse shapes and number of necessary iterations for different modulation orders in case of SIPC-tf precoding. 139
4.11 Recommended pulse shapes and number of necessary iterations for different modulation orders in case of SIPC-t precoding. 139
4.12 Recommended pulse shapes and number of necessary iterations for different modulation orders in case of SIPC-f precoding. 139
4.13 Recommended precoders for different modulation orders and packing factors. 140

5.1 Symbols transmission scheme of OFDM/OQAM modulation. 166
5.2 Sorted time indices n_0 in ascending order of their interference power. . . . 172
5.3 Recommended mapping strategy for the FTN-OQAM transceiver. 178
5.4 Recommended mapping strategy for the FTN-OQAM transceiver combined with SIPC-t precoding. 179
5.5 Recommended mapping strategy for the FTN-OQAM transceiver combined with SIPC-f precoding. 179

Abbreviations

ADSL	**A**symmetric **D**igital **S**ubscriber **L**ine
APP	**A** **p**osteriori **P**robability
APSK	**A**mplitude and **P**hase **S**hift **K**eying
AWGN	**A**dditive **W**hite **G**aussian **N**oise
BCJR	**B**ahl **C**ocke **J**elinek **R**aviv
BER	**B**it **E**rror **R**ate
BICM	**B**it **I**nterleaved **C**oded **M**odulation
BPSK	**B**inary **P**hase **S**hift **K**eying
CCDF	**C**omplementary **C**umulative **D**istribution **F**unction
CFO	**C**arrier **F**requency **O**ffset
CP	**C**yclic **P**refix
CSI	**C**hannel **S**tate **I**nformation
DAB	**D**igital **A**udio **B**roadcasting
DAC	**D**igital to **A**nalog **C**onversion
DFE	**D**ecision **F**eedback **E**qualizer
DPSWF	**D**iscrete **P**rolate **S**pheroidal **W**ave **F**unctions
DVB	**D**igital **V**ideo **B**roadcasting
EGF	**E**xtended **G**aussian **F**unction
EXIT	**EX**trinsic **I**nformation **T**ransfer
FBMC	**F**ilter **B**ank **M**ulti **C**arrier
FFT	**F**ast **F**ourier **T**ransform
FPGA	**F**ield **P**rogrammable **G**ate **A**rrays
FS	**F**requency **S**elective
FTN	**F**aster **T**han **N**yquist
GMD	**G**eometric to **M**ean **D**ecomposition
HPA	**H**igh **P**ower **A**mplifier
HSPA	**H**igh **S**peed **P**acket **A**ccess
IC	**I**nterference **C**anceller
ICI	**I**nter **C**arrier **I**nterference
i.i.d	**i**ndependent and **i**dentically **d**istributed
IMT	**I**nternational **M**obile **T**elecommunications
IFFT	**I**nverse **F**ast **F**ourier **T**ransform
IOTA	**I**sotropic **O**rthogonal **T**ransform **A**lgorithm
ISI	**I**nter **S**ymbol **I**nterference
LDPC	**L**ow **D**ensity **P**arity **C**heck
LE	**L**inear **E**qualizer
LLR	**L**og **L**ikelihood **R**atio
LTE	**L**ong **T**erm **E**volution
LUT	**L**ook **U**p **T**able

MAP	**M**aximum ***A*** ***P****osteriori*
MCM	**M**ulti **C**arrier **M**odulation
MLSD	**M**aximum **L**ikelihood **S**equence **D**etection
MMSE	**M**inimum **M**ean **S**quare **E**rror
NEF	**N**yquist **E**rror **F**ree
OBE	**O**ut-of-**B**and **E**nergy
OFDM	**O**rthogonal **F**requency **D**ivision **M**ultiplexing
OQAM	**O**ffset **Q**uadrature **A**mplitude **M**odulation
PAM	**P**ulse **A**mplitude **M**odulation
PAPR	**P**eak-to-**A**verage **P**ower **R**atio
PHYDYAS	**PHY**sical layer for **DY**n**A**mic **S**pectrum access and cognitive radio
PSD	**P**ower **S**pectral **D**ensity
PSK	**P**hase **S**hift **K**eying
P/S	**P**arallel to **S**erial
QAM	**Q**uadrature **A**mplitude **M**odulation
QPSK	**Q**uadrature **P**hase **S**hift **K**eying
RSC	**R**ecursive **S**ystematic **C**onvolutional
SIC	**S**oft **I**nterference **C**ancellation
SIPC	**S**parse **I**nterference **P**re-**C**ancellation
SISO	**S**oft **I**n **S**oft **O**ut
SNR	**S**ignal to **N**oise **R**atio
SOTA	**S**tate **O**f **T**he **A**rt
SRRC	**S**quare **R**oot **R**aised **C**osine
SVD	**S**ingular **V**alue **D**ecomposition
THP	**T**omlinson **H**arashima **P**recoding
TFL	**T**ime **F**requency **L**ocalization
TMUX	**T**ransmultiplexer
UMTS	**U**niversal **M**obile **T**elecommunications **S**ystem
WLAN	**W**ireless **L**ocal **A**rea **N**etworks

Résumé Français

Chapitre 1

Le premier chapitre fait l'objet d'une présentation au contexte général de la thèse. La croissance récente des réseaux cellulaires et des communications haut débit est principalement motivée par l'invention des ordinateurs portables et des tablettes mobiles. L'information à la demande et le divertissement en temps réel seront progressivement fournis par les systèmes de communication mobiles et sans fil. Ces applications conduiront à une avalanche du volume de données mobiles. La plupart des smartphones peuvent déjà recevoir des débits qui dépassent les capacités du réseau [4]. Selon "Cisco Visual Networking Index" [5], le trafic mondial de données mobiles a augmenté de 63% en 2016 et représentera 20% du trafic IP total d'ici 2021 et atteindra 49 ExaBytes par mois d'ici 2021. À l'avenir, les réseaux sans fil rencontreront plus de problèmes d'encombrement qu'aujourd'hui [6]. En outre, il est prévu que l'Internet des objets connectera un nombre énorme d'appareils. Selon [5], il y aura 11,6 milliards d'appareils connectées d'ici 2021, dépassant la population du monde prévue à ce moment-là. Par conséquent, les futurs systèmes sans fil sont contraints de fournir des solutions avancées offrant des débits de données plus élevés avec une utilisation efficace de la bande passante.

Actuellement, les réseaux d'évolution à long terme (LTE) promettent des débits de données de téléchargement de 100Mb/s, ce qui est 10 fois plus rapide que les réseaux de troisième génération (3G) tout en permettant une utilisation plus efficace du spectre radioélectrique. LTE s'appuie sur des technologies de pointe pour atteindre ces objectifs, tels que la modulation OFDM (Orthogonal Frequency Division Multiplexing), les systèmes MIMO (Multiple Input Multiple Output) et le codage canal avancé. Toutefois, en raison de l'augmentation exponentielle des périphériques sans fil, les débits de données offerts peuvent ne pas répondre à la demande croissante des consommateurs. Depuis le début de 2010, des projets collaboratifs tels que METIS [7] et 5GNOW [8] étudient des technologies avancées pour la cinquième génération (5G). Et plus récemment, les organismes de normalisation, par exemple 3GPP, ont également commencé à étudier des solutions orientées 5G. La 5G devrait être déployée vers 2020 et devra supporter des applications multimédia aux exigences diverses, y compris des débits et un nombre d'utilisateurs plus élevés, une latence réduite et une efficacité énergétique améliorée [9].

Dans ce premier chapitre, nous rappelons brièvement le critère de Nyquist. En effet, les systèmes de communication numérique modernes s'appuient généralement sur les travaux pionniers de Nyquist datant de 1924 [10] et 1928 [11]. Nyquist a formulé le modèle de bande de base pour la transmission des données à travers des canaux à bande limitée et continus en temps. Le signal en temps continu transmis en bande de base peut être exprimé comme suit:

$$S(t) = \sum_n x[n]g(t - nT),$$

où $x[n]$ sont les symboles transmis, g la fonction de modulation supposée être limitée à W Hertz et T la durée d'un symbole. Les fonctions de modulation peuvent se chevaucher dans le temps aussi longtemps qu'elles restent orthogonales les unes aux autres. Nyquist a déclaré que, pour obtenir une transmission sans interférences entre les symboles (ISI),

la cadence de signalisation maximale $\frac{1}{T}$ est donnée par $2W$ impulsions par seconde. Cette cadence, appelée cadence de Nyquist, assure une architecture simple du récepteur basée sur un filtre adapté à la fonction de modulation et un échantillonneur à la cadence de Nyquist [12], [13]. Ce récepteur maximise le rapport signal à bruit pour les transmissions à travers un canal Gaussian.

Bien que le critère de Nyquist assure l'orthogonalité des fonctions de modulation afin d'éviter les interférences entre symboles, l'efficacité de la bande passante est sacrifiée pour garantir une telle orthogonalité. Les systèmes dits Faster-Than-Nyquist (FTN) permettent la transmission des données au-delà de la cadence de Nyquist, pourvu que les ISI soient tolérés. En fait, la transmission de l'information à une cadence plus rapide que celle de Nyquist a attiré de nombreux chercheurs au cours des dernières années: [14], [15], [16]. Cependant, le concept n'a pas été considéré comme un moyen attractif jusqu'à ce que l'explosion des exigences en termes du débit devienne inévitable. Ceci est principalement attribué au traitement complexe nécessaire pour traiter les interférences introduites par la signalisation FTN.

Cette dissertation est motivée par la combinaison de la signalisation FTN avec les modulations multi-porteuses. Les systèmes FTN utilisant la modulation OFDM ont été discutés dans [17]. Bien que cette modulation soit largement utilisée dans les systèmes modernes de communication numérique, notre travail s'est concentré sur une alternative à l'OFDM connue sous le nom d'OFDM avec Modulation d'amplitude en quadrature décalée (QAM) et désignée ici par OFDM/OQAM [18]. Ceci est principalement dû au fait que la modulation OFDM/OQAM ne nécessite pas l'insertion d'un préfixe cyclique. En outre, la modulation OFDM/OQAM, souvent appelée maintenant FBMC/OQAM, peut être équipée de différentes formes d'onde ayant différentes propriétés de localisation temps-fréquence. Cependant, les résultats de ce rapport ne sont pas exclusifs à la forme d'onde OFDM/OQAM et peuvent être étendus à d'autres formes d'onde, y compris l'OFDM. Le concept FTN a été introduit à l'origine pour rapprocher les signaux transmis dans le domaine temporel, par rapport au critère de Nyquist [19]. L'extension du concept FTN aux modulations multiporteuses a été discutée dans [20], où les auteurs ont montré que les signaux transmis peuvent être rapprochés dans le domaine temporel et fréquentiel. Dans cette dissertation, nous considérons la transmission de signaux indépendants et identiques (i.i.d) à travers un canal AWGN et supposons que le concept FTN n'est appliqué que dans le domaine temporel.

L'objectif de cette dissertation est d'étudier d'abord une nouvelle implémentation du concept FTN dans le cadre des système OFDM/OQAM qui permet de passer d'une manière flexible du mode Nyquist au mode FTN avec une augmentation limitée de la complexité par rapport aux systèmes OFDM/OQAM tout en offrant un débit proche du débit théorique promis par le concept FTN. Bien que les signaux ne soient rapprochés que dans le domaine temporel, les interférences ISI et les interférences entre porteuses (ICI) sont intentionnellement ajoutées aux signaux transmis, ce qui nécessite des algorithmes plus complexes au niveau du récepteur. L'émetteur-récepteur FTN était à l'origine basé sur un algorithme non linéaire de détection de séquence "Maximum *A Posteriori*" (MAP) [21], [3] qui offre de bonnes performances. Cependant, la complexité est exponentiellement proportionnelle aux ordres de la constellation. Dans l'état de l'art,

seules les constellations faibles, essentiellement BPSK ou QPSK sont présumées. Par conséquent, l'utilisation des constellations élevées dans les systèmes FTN est un problème ouvert. Une façon intuitive de réduire la complexité dans le cas des constellations d'ordre élevé est de considérer une égalisation linéaire qui devrait être indépendante de l'ordre de la constellation. Par conséquent, nous avons proposé un récepteur turbo basé sur le concept de l'égalisation linéaire (LMMSE) et sur l'annulation des interférences pour traiter les interférences induites par le FTN. En réduisant la complexité de l'égalisation, nous avons découvert rapidement que la performance est dégradée, surtout lors de la première itération. En conséquence, la réduction de la complexité d'égalisation vient au coût de plus d'itérations pour annuler l'interférence intrinsèque. Nous avons identifié que la dégradation était principalement due à la détection inefficace des symboles lors de la première itération. Pour améliorer cela, il pourrait y avoir deux directions: 1) appliquer l'égalisation MAP pour seulement la première itération. Cependant, la complexité de l'algorithme MAP reste un problème comme indiqué précédemment et cette solution ne répond pas entièrement à notre objectif. 2) Déséquilibrez le niveau d'interférence pour que certains symboles subissent moins d'interférence que les autres. Ainsi, pour les symboles moins affectés, l'égaliseur LMMSE peut fournir une meilleure estimation, avec laquelle la turbo-égalisation globale peut fonctionner plus efficacement. Comme les interférences FTN sont introduites intentionnellement, elles sont parfaitement connues à la fois par l'émetteur et le récepteur. La première contribution de cette thèse est la proposition de nouveaux schémas de précodage visant à réduire cette interférence afin d'améliorer les performances de l'émetteur-récepteur FTN-OQAM. Nous avons également identifié que le codage canal pourrait être optimisé conjointement avec le modèle de déséquilibre d'interférence que nous avons intentionnellement crée, ce qui constitue la deuxième contribution de cette thèse. Enfin, nous avons trouvé que l'interférence induite par le FTN n'est pas uniformément répartie entre les symboles transmis. La troisième contribution de cette thèse est la proposition d'un nouvel mapping des symboles aux positions en temps et en fréquence pour équilibrer la distribution de l'interférence.

Chapitre 2

Notre objectif principal dans le deuxième chapitre est de fournir des éléments préliminaires pour l'étude de la signalisation FTN et son association avec la modulation OFDM/OQAM et les techniques avancées de codage canal et de précodage. Tout d'abord, nous présentons brièvement deux technologies de modulation multiporteuses largement utilisées: les modulations OFDM et OFDM/OQAM. Deuxièmement, nous présentons une étude chronologique des solutions FTN présentées dans la littérature. Dans la dernière section, nous examinons certains concepts du codage canal et de la turbo égalisation. Enfin, le célèbre précodage Tomlinson-Harashima est revu.

La modulation OFDM est utilisée dans divers standards tels que DVB, DAB, WLAN et LTE. Cette technique de modulation transforme un canal de large bande sélectif en fréquence en un groupe de sous-canaux à bande étroite, tout en préservant l'orthogonalité dans le domaine fréquentiel, ce qui rend l'OFDM robuste contre les grands délais de propagation. Pour éviter l'impact de l'ISI, la modulation OFDM insère un intervalle de garde au début de chaque symbole OFDM. Un préfixe cyclique (CP) est généré en insérant les derniers G échantillons de la sortie de l'IFFT et en les ajoutant au début de chaque symbole OFDM [22]. Une autre alternative à la modulation OFDM est OFDM/OQAM.

Contrairement à OFDM, qui utilise la forme d'onde rectangulaire dans le domaine temporel, OFDM/OQAM a la flexibilité d'utiliser différentes formes d'onde avec différentes propriétés de localisation temps-fréquence. Cela rend l'OFDM/OQAM moins sensible au décalage de fréquence provoqué par le canal de transmission et le récepteur. En outre, OFDM/OQAM n'utilise aucun CP, et est donc plus efficace spectrallement qu'OFDM. Les premières études liées à OFDM/OQAM ont été présentées dans [23] et [24]. Dans [23], [24], les auteurs ont introduit un décalage temporel sur chaque sous-porteuse pour transmettre des constellations PAM et QAM, respectivement. Pour cette dernière, un décalage temporel entre les parties réelles et imaginaires est introduit. Dans [25], les auteurs ont souligné l'importance des propriétés de localisation temps-fréquence des filtres prototypes pour des transmissions à travers des canaux dispersifs en temps et en fréquence. Certaines fonctions prototypes optimisées autres que la fonction rectangulaire ont également été présentées.
La modulation OFDM consiste à transmettre un symbole complexe $c_{m,n} = c_{m,n}^{\Re} + jc_{m,n}^{\Im}$ de durée T_0 à l'instant n, c'est-à-dire nT_0 et sur la porteuse m, c'est-à-dire mF_0, avec $F_0 = \frac{1}{T_0}$ l'espacement entre sous-porteuses et $j^2 = -1$. L'OFDM/OQAM transmet la partie réelle ou la partie imaginaire du symbole complexe $c_{m,n}$ avec un décalage en temps égal à $\frac{T_0}{2}$. En outre, un décalage de phase de $\frac{\pi}{2}$ est introduit entre deux symboles adjacents en temps ou en fréquence. Dans le chapitre 2, nous présentons les expressions du signal transmis en temps continu et discret. La structure du modulateur/démodulateur est également présentée dans le cas continu et discret. Nous discutons ensuite les propriétés de localisation en temps-fréquences des différents filtres prototypes: SRRC, FS, IOTA, EGF et TFL.

Dans la section suivante, nous rappelons le théorème de signalisation de Nyquist. Le modèle général en bande de base pour la transmission de données à travers un canal à bande limitée et continu en temps a été formulé par Nyquist dans ses travaux pionniers en 1924 et 1928 [10], [11]. Dans ces travaux, Nyquist a étudié la cadence de signalisation maximale sans introduire d'interférences entre symboles. Il a montré que la cadence maximale est directement liée à la bande passante du canal. Cette cadence est souvent appelée la cadence de signalisation de Nyquist. Le signal PAM en bande de base transmis à travers un canal continu en temps est exprimé comme suit:

$$s(t) = \sum_n x[n]g(t - nT),$$

où $x[n]$ sont les symboles transmis, $g(t)$ est la forme d'onde utilisée supposée limitée à W Hertz et T est la durée du symbole. La cadence de signalisation de ce schéma de transmission est $\frac{1}{T}$ symboles par seconde. Le signal reçu est exprimé comme suit:

$$y(t) = \sum_n x[n]h(t - nT) + z(t)$$

où $z(t)$ est le signal de bruit et $h(t)$ est la convolution du filtre d'émission $g(t)$, le filtre de canal $c(t)$ et le filtre de réception $r(t)$. Pour assurer une transmission sans ISI, Nyquist a formulé une condition suffisante et nécessaire pour $H(f)$, la transformée de Fourier de $h(t)$:

Théorème de Nyquist pour zéro ISI: Une condition nécessaire et suffisante pour assurer une transmission sans ISI est [11]:

$$\sum_{k=-\infty}^{+\infty} H(f + \frac{k}{T}) = T$$

En conséquence, une condition suffisante pour récupérer les données transmises sans interférence est $1/T = 2W$, également appelé la cadence de signalisation de Nyquist. Par conséquent, le critère de Nyquist garantit une architecture simple du récepteur basée sur un filtre adapté à la forme de l'onde de l'émission et un échantillonneur à la cadence de Nyquist [12], [13]. Lors de la transmission sur un canal AWGN, cette structure est connue maximiser le rapport signal à bruit à la réception.

En 1975, Mazo a souligné que la cadence de transmission n'est pas nécessairement limitée par le critère de Nyquist, ce qui signifie qu'une cadence plus rapide peut être envisagée pour échanger la transmission sans interférences pour plus de débit. Le concept est connu sous le nom de Faster-Than-Nyquist (FTN). En fait, les avantages de la signalisation FTN ont été examinés par de nombreux chercheurs: [14], [15], [16]. Cependant, le concept n'a pas été considéré comme un moyen attractif jusqu'à ce que l'explosion du débit devienne inévitable. Ceci est principalement attribué au traitement complexe nécessaire pour traiter les interférences introduites par FTN. En fait, étant donné que l'orthogonalité des formes d'onde n'est plus respectée, la signalisation FTN induit une interférence importante au signal utile qui nécessite un traitement plus sophistiqué et plus complexe du côté du récepteur.
En raison de la baisse du coût des unités de traitement, l'importance des ressources spectrales a surmonté la complexité du traitement requise. En outre, les progrès dans le traitement du signal ont permis la mise en oeuvre de techniques avancées de codage et d'égalisation pour traiter les interférences causées par la signalisation FTN. Par conséquent, le concept de transmissions FTN a récemment été étudié et est maintenant considéré comme un bon candidat offrant des débits plus élevés avec une utilisation plus efficace de la bande passante.
Comme indiqué précédemment, le concept de signalisation FTN a été introduit par Mazo dans [19]. Il a montré que des formes d'onde T-orthogonales peuvent être envoyées plus rapidement que la cadence de Nyquist ($1\ /T$), tout en maintenant la distance Euclidienne minimale inchangée. Bien que l'ISI soit introduit car les formes d'onde ne sont plus orthogonales, le taux d'erreur asymptotique d'un décodeur optimal reste le même.
Plus précisément, Mazo a étudié les signaux modulés en bande de base PAM de la forme:

$$s(t) = \sum_n a_n g(t - nT),$$

où $a_n \in \{-1, +1\}$, $g(t)$ est la fonction Sinc et T la durée du symbole. Pour FTN, les fonctions Sinc sont rapprochées dans le temps, par rapport au critère de Nyquist, et $s(t)$ est réécrit comme suit:

$$s(t) = \sum_n a_n g(t - n\tau T),$$

avec $0 \leq \tau < 1$. Mazo a montré que τ peut être réduit à un certain seuil sans changer la distance minimale Euclidienne. En fait, il a montré que τ peut être réduit jusqu'à 0,802, ce qui signifie qu'une augmentation de débit de 25% peut être obtenue dans la même

bande passante sans affecter la distance Euclidienne. La valeur $0.802T$ est appelée la limite de Mazo.

En désignant par $D(\mathbf{a_1}, \mathbf{a_2})$ la distance entre deux signaux $S_{\mathbf{A1}}(t)$ et $S_{\mathbf{a_2}}(t)$, nous avons:

$$D(\mathbf{a_1}, \mathbf{a_2})^2 = \int_{-\infty}^{+\infty} |S_{\mathbf{a_1}}(t) - S_{\mathbf{a_2}}(t)|^2 dt.$$

Si $\{g(t-nT)\}$ constitue une base orthogonale, la distance mesurée entre $S_{\mathbf{a_1}}(t)$ et $S_{\mathbf{A_2}}(t)$ est proportionnelle à la différence entre les séquences de symboles correspondantes $a_1[n]$ et $a_2[n]$. Cependant, pour les fonctions non orthogonales $\{g(t-nT)\}$, comme dans le cas FTN, la distance entre les séquences de symboles n'est plus représentative de la distance du signal.

On définit la distance normalisée $d(\mathbf{a_1}, \mathbf{a_2})$ comme suit:

$$d(\mathbf{a_1}, \mathbf{a_2})^2 = \frac{D(\mathbf{a_1}, \mathbf{a_2})^2}{2E_b},$$

où E_b est l'énergie par bit. La distance minimale est définie par:

$$d_{min} = \min_{\mathbf{a_1} \neq \mathbf{a_2}} d(\mathbf{a_1}, \mathbf{a_2})$$

La limite de Mazo est définie comme le facteur minimum qui permet de rapprocher les formes d'onde entre elles, par rapport au critère de Nyquist, tout en maintenant la distance minimale inchangée:

$$\tau^+ = \min\{\tau; d_{min} = d_0\},$$

où d_0 est la distance minimale quand $\tau = 1$.

L'idée de transmettre à une cadence plus rapide que celle de Nyquist remonte au milieu des années 1960. Cependant, elle a été récemment étudiée par plusieurs chercheurs. Dans la section suivante de ce chapitre, nous présentons un état de l'art lié au concept FTN.

Bien que le concept FTN ait été abordé par de nombreux chercheurs au cours des dernières années comme un moyen prometteur d'augmenter le débit de transmission, il s'agit encore d'un domaine de recherche en cours. La combinaison de la signalisation FTN avec des modulations multi-porteuses largement utilisées telles que OFDM et OFDM/OQAM a attiré de nombreux chercheurs pour étudier des systèmes FTN offrant une efficacité spectrale plus élevée que les systèmes Nyquist. En outre, les avantages de la modulation OFDM/OQAM en font un bon candidat à combiner avec la signalisation FTN. En fait, une architecture d'un modem OFDM/OQAM combiné avec FTN a été proposée dans [2]. Malgré les avantages du schéma proposé, l'implémentation proposée augmente considérablement la complexité de l'émetteur-récepteur par rapport aux systèmes OFDM/OQAM. Par conséquent, des implémentations FTN plus efficaces offrant une commutation flexible entre les modes FTN et Nyquist avec une augmentation limitée de la complexité de l'émetteur-récepteur devraient être étudiées. En outre, les interférences dues à la signalisation FTN sont également une question cruciale puisque

l'orthogonalité des impulsions n'est plus respectée, ce qui nécessite des récepteurs plus complexes. Dans [3], le récepteur proposé est basé sur l'algorithme MAP, dont la complexité augmente avec l'ordre de la modulation. D'autre part, la complexité des égaliseurs linéaires est indépendante de l'ordre de la modulation ce qui les rend des bons candidats lorsque des ordres de modulation élevés sont ciblés. Comme les interférences introduites sont parfaitement connues par l'émetteur et le récepteur, les techniques d'annulation des interférences devraient également être examinées.

Dans ce chapitre, nous examinons brièvement certains concepts de codage canal, de précodage et d'égalisation. En particulier, l'algorithme BCJR et sa version simplifiée, l'égalisation turbo basée sur des égaliseurs linéaires ainsi que le précodage Tomlinson-Harashima sont décrits. Ces concepts seront utilisés dans les chapitres suivants pour la transmission FTN.

Chapitre 3

Dans ce chapitre, nous considérons le concept des transmissions FTN dans le cas de la modulation OFDM/OQAM, noté par FTN-OQAM, à travers un canal AWGN. Tout d'abord, nous présentons une nouvelle réalisation de FTN-OQAM qui garde les avantages de la solution de l'état de l'art et résout en même temps les problèmes restants. Ensuite, nous proposons un récepteur turbo basé sur le filtrage linéaire MMSE et sur l'annulation des interférences SIC dont la complexité est indépendante de l'ordre de la constellation. Cela en fait un bon candidat lorsque des constellations d'ordre élevé sont envisagées.

Nous présentons une nouvelle implémentation FTN pour les systèmes OFDM/OQAM en supposant que les signaux sont rapprochés uniquement dans le domaine temporel par rapport au critère de Nyquist. L'implémentation proposée n'augmente pas la complexité par rapport aux systèmes classiques OFDM/OQAM et a la flexibilité de commuter entre les modes Nyquist et FTN. En plus, le débit effectif approche le débit théorique promis par le concept FTN. Ensuite, nous présentons le modem FTN-OQAM dans le cas d'un filtre prototype causal et non-causal.

En fait, le signal FTN-OQAM continu en temps et transmis en bande de base est exprimé comme suit:

$$s(t) = \sum_{m=0}^{M-1} \sum_{n=-\infty}^{+\infty} a_{m,n} g(t - \frac{n\tau T_0}{2}) e^{j2\pi m\zeta F_0 t} e^{j\Phi_{m,n}},$$

où $0 < \tau \leq 1$ et $0 < \zeta \leq 1$ sont les facteurs d'emballage FTN en temps et en fréquence, respectivement. Nous supposons que $\zeta = 1$ et considérons que les symboles ne sont rapprochés que dans le domaine temporel, c'est-à-dire $\tau < 1$. La version discrète est obtenue en échantillonnant le signal à $T_s = \frac{T_0}{M}$:

$$s[k] = \underbrace{\sum_{m=0}^{M-1} a_{m,n} e^{j\Phi_{m,n}} e^{\frac{j2\pi mk}{M}}}_{Fourier\ Transform} \sum_{n=-\infty}^{+\infty} g[k - nN_f].$$

La transformée de Fourier est implémentée à l'aide de l'algorithme IFFT, selon la causalité du prototype de filtre g. Quand le filtre prototype g est causal, $k \in [0, L-1]$ où L est la longueur du filtre. Le signal transmis peut être reformulé comme suit:

$$s[k] = \underbrace{\sum_{n=0}^{+\infty} g[k-nN_f] \underbrace{\sum_{m=0}^{M-1} \underbrace{a_{m,n} e^{j\Phi_{m,n}} e^{\frac{j2\pi m(nN_f - \frac{D}{2})}{M}}}_{Pre-processing} e^{\frac{j2\pi m(k-nN_f)}{M}}}_{IFFT+CYCEXD}}_{filtering}$$

La structure du modulateur est présentée dans la Figure. 1. Grâce à la périodicité de l'IFFT, le filtrage est réalisé par une extension cyclique par bloc, suivi par une opération de multiplication par un coefficient et enfin par une conversion parallèle en série. **CYCEXD** est une matrice $L \times M$:

$$\mathbf{CYCEXD}_{L\times M} = \begin{bmatrix} \mathbf{I}_{M\times M} \\ ... \\ \mathbf{I}_{M\times M} \end{bmatrix}_{L\times M} :.$$

où $\mathbf{I}_{M\times M}$ est la matrice identité.

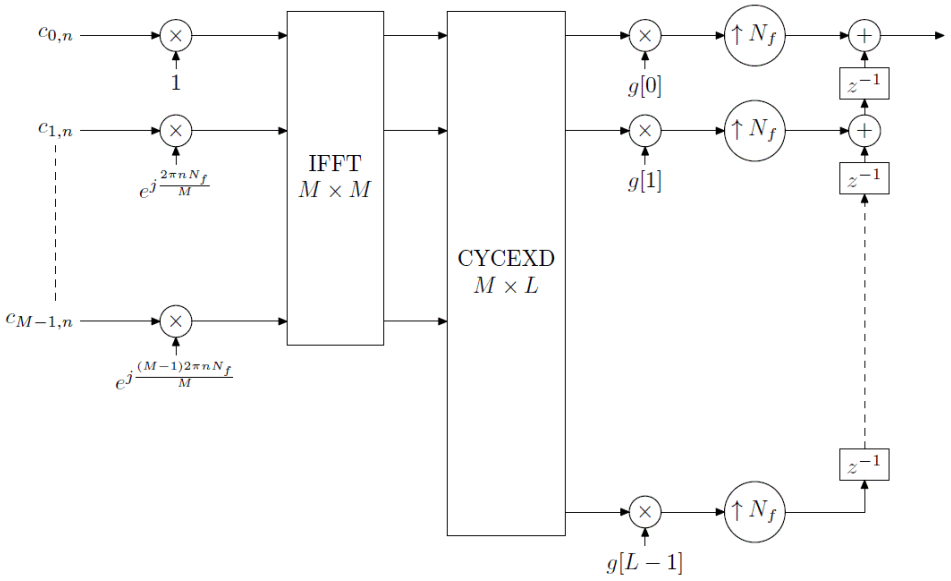

FIGURE 1: *Le modulateur causal FTN-OQAM.*

Au côté du récepteur, le démodulateur effectue les opérations inverses du modulateur. La structure du démodulateur dans le cas d'un filtre prototype causale est représentée dans la Figure. 2. Étant donné que la démodulation OFDM/OQAM extrait uniquement la partie réelle du signal reçu, le signal démodulé à l'instant n_0 et sur la sous-porteuse m_0 est:

$$y_{m_0,n_0} = \Re\{\sum_k s[k]g[k-n_0N_f]e^{-j\Phi_{m_0,n_0}} e^{-\frac{j2\pi m_0(k-\frac{D}{2})}{M}}\}.$$

Comme $g[k]$ est causal, $k \in [n_0 N_f, n_0 N_f + L - 1]$. Afin d'effectuer la FFT, le signal reçu est reformulé comme suit:

$$y_{m_0,n_0} = \Re\{ \underbrace{\sum_{k=n_0N_f}^{n_0N_f+M-1} \underbrace{\sum_{l=0}^{L/M} s[k+lM]g[k+lM-n_0N_f]\, e^{-\frac{j2\pi m_0(k-n_0N_f)}{M}}}_{filtering+CYCCOMB} \underbrace{e^{-j\Phi_{m_0,n_0}} e^{-\frac{j2\pi m_0(n_0N_f-\frac{D}{2})}{M}}}_{post-processing}}_{FFT} \}$$

où L est supposé être un multiple de M. L'opération inverse de **CYCEXD** est effectuée à la réception par un bloc nommé **CYCCOMB**:

$\mathbf{CYCCOMB}_{M\times L} = \mathbf{CYCEXD}^T_{L\times M}$, où $(.)^T$ est l'opération de transposé.

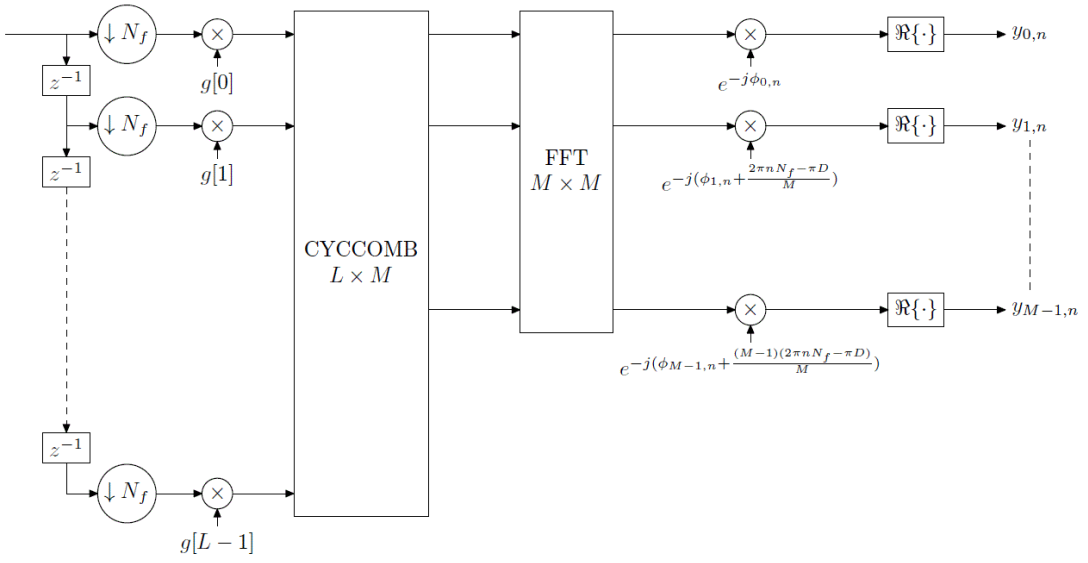

FIGURE 2: *Le démodulateur causal FTN-OQAM.*

Le modem proposé peut produire des symboles OQAM à la cadence Nyquist et FTN, simplement en ajustant le facteur FTN N_f. En plus la complexité est similaire au modem OFDM/OQAM classique [18], bien que la manière d'implémentation soit différente.

Dans la section suivante, nous analysons l'interférence induite par FTN. Les fonctions prototypes sont définies en temps continu, ayant donc un support infini, ou en temps discret avec une longueur finie. L'analyse des interférences est présentée dans le cas d'un émetteur-récepteur FTN-OQAM continu et discret. Nous supposons un canal de transmission idéal, c'est-à-dire sans bruit, sans distorsion et avec un traitement analogique parfait, et $\Phi_{m,n} = \frac{pi}{2}(m+n)$.

Dans le chapitre précédent, nous avons mentionné que, contrairement à OFDM, la modulation OFDM/OQAM utilise différentes formes d'onde avec différentes propriétés de localisation temps-fréquence. Selon ces caractéristiques, l'utilisation d'une forme d'onde donnée g entraînera soit un ISI ou ICI élevé. Ainsi, la puissance d'interférence dans le

cas discret peut être formulée comme suit:

$$P_I(n_0) = \underbrace{\sigma_a^2 L^2 \sum_{q^0} \cos(\pi \frac{q}{2})^2 A_g[qN_f, 0]^2}_{ISI} + \underbrace{\sigma_a^2 L^2 \sum_{p \neq 0, q} \cos(\pi(\frac{p+q}{2} + \frac{2p(n_0 N_f - \frac{D}{2})}{M}))^2 A_g[qN_f, pb]^2}_{ICI_{n_0}} .$$

A partir de cette équation, on constate que contrairement à ISI, ICI dépend de l'indice n_0. Nous illustrons dans la Figure. 3 la puissance moyenne ICI et ISI pour différentes formes d'onde. Comme prévu, une forme d'onde bien localisée en fréquence est plus impactée par ISI que par ICI, et vice versa. Comme mentionné précédemment, lors

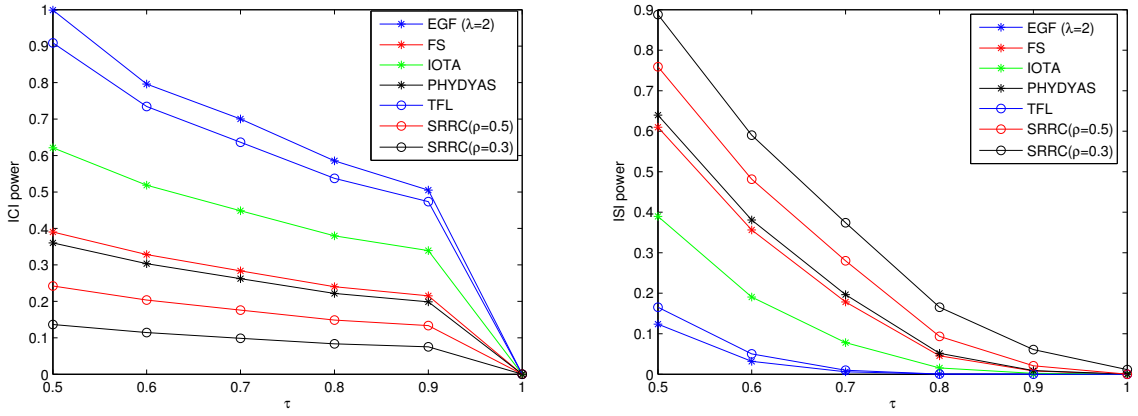

FIGURE 3: Puissance moyenne d'ICI et d'ISI pour différentes formes d'onde et facteurs FTN.

de la signalisation au-delà de la cadence de Nyquist, la condition d'orthogonalité n'est plus valide. Cela signifie que, même pour un canal idéal, des interférences sont ajoutées au signal utile. Même si nous considérions que les signaux OQAM sont rapprochés uniquement dans le domaine temporel, le signal utile est également perturbé par ICI. La chaîne de transmission du FTN-OQAM codé est rapportée dans la Figure. 4, où les bits d'information sont d'abord codés, entrelacés, mappés aux symboles OQAM, puis modulés. Afin de traiter les interférences induites par le FTN, nous proposons un récepteur turbo basé sur MMSE LE-IC. Contrairement à l'égaliseur basé sur MAP, la complexité de l'égalisation MMSE LE-IC est indépendante de l'ordre de la constellation et dépend uniquement de la longueur de la réponse impulsionnelle du canal d'interférence. Par conséquent, ce récepteur est un bon candidat lorsque des ordres de constellation élevés sont ciblés. Dans ce chapitre, nous présentons l'égalisation MMSE LE-IC dans le domaine temporel, et fréquentiel.

Sur le côté récepteur, en supposant un canal idéal, le signal est d'abord démodulé par le bloc *FTN-OQAM demodulator*. Nous assumons un filtre prototype d'énergie unitaire g. Ainsi, $\sum_k g[k]^2 = 1$ et $LA_g[0,0] = 1$. À l'instant n_0 et sur la sous-porteuse m_0, le signal

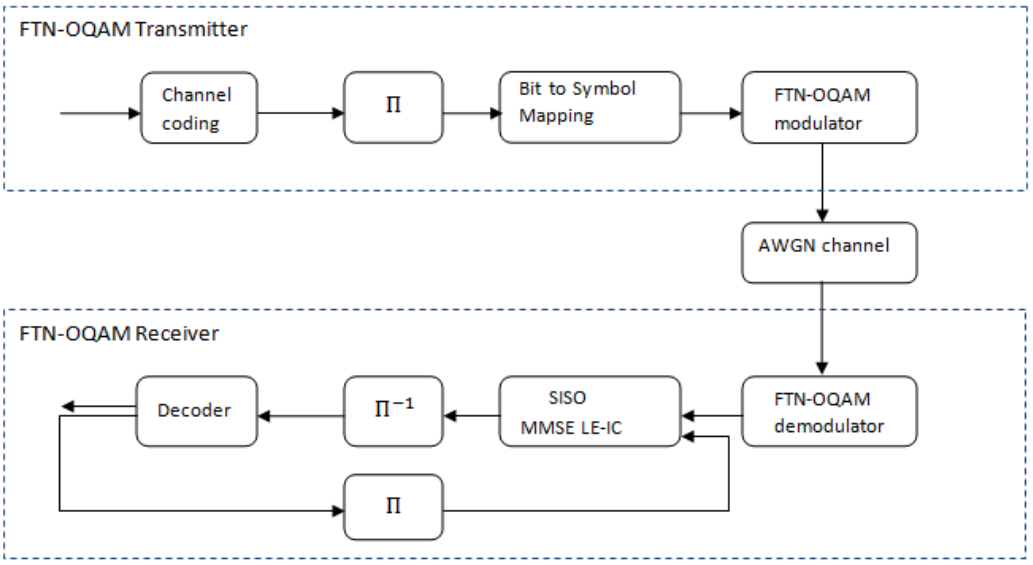

FIGURE 4: Chaîne de transmission FTN-OQAM.

reçu est exprimé comme suit:

$$y_{m_0,n_0} = \underbrace{a_{m_0,n_0}}_{useful\ signal} + \underbrace{\Re\{\sum_{p^0,q^0} a_{m_0+p,n_0+q} e^{j\pi(\frac{p+q}{2}+\frac{2p(n_0N_f-\frac{D}{2})}{M})} \times LA_g[-qN_f,-pb]\}}_{ISI+ICI}, \quad (1)$$

où $a_{m,n}$ sont les symboles OQAM transmis à l'instant n et sur la sous-porteuse m, et $(p,q) \in [-l^{'},l^{'}]\times[-l,l], (l,l^{'}) \in \mathbb{Z}^2$. Bien que l'interférence s'étende à toutes les fréquences et les instants en temps, nous considérons qu'elle est essentiellement due aux symboles voisins les plus proches dans une zone $[-l^{'},l^{'}] \times [-l,l]$. Les facteurs $(l^{'},l)$ représentent la zone des symboles contribuant à ICI et ISI, respectivement. Ils dépendent du filtre prototype et du facteur FTN τ.
Les symboles démodulés $\mathbf{y}$ sont ensuite transmis au SISO MMSE IC-LE pour supprimer de manière itérative les interférences causées par FTN. L'annulation d'interférence est un processus en deux étapes, ce qui signifie qu'il annule premièrement ICI ensuite ISI. La structure SISO MMSE LE-IC est rapportée à la Figure. 5, où ICI et ISI sont prédits en utilisant l'information soft du décodeur puis annulés. Les fonctions *SISO mapping* et *SISO demapping* sont utilisées pour traduire l'information du niveau bit au niveau symbole et vice versa et ainsi échanger l'information soft entre l'égaliseur et le décodeur.

Dans la section suivante, nous évaluons la performance de l'émetteur-récepteur FTN-OQAM proposé en termes de BER vs SNR. Tout d'abord, nous présentons un algorithme pour étudier le facteur d'emballage que notre émetteur-récepteur peut atteindre tout en gardant sa performance proche de celle des systèmes OFDM/OQAM classiques. Ensuite, nous comparons les performances de l'émetteur-récepteur FTN-OQAM en utilisant différentes formes d'onde.

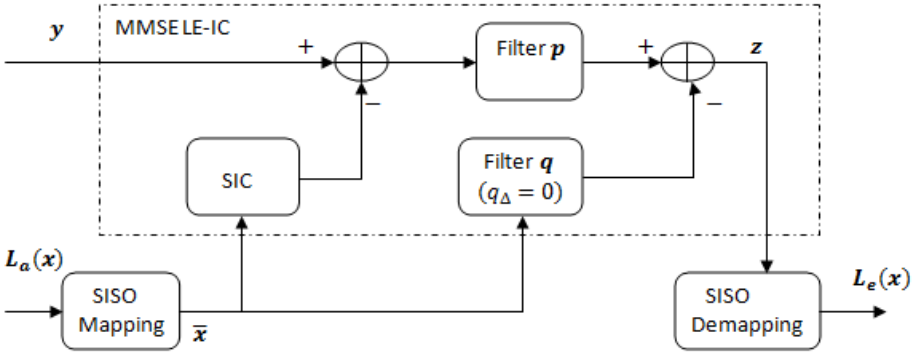

FIGURE 5: Structure de l'égaliseur SISO MMSE LE-IC.

Nous étudions la valeur minimale du facteur d'emballage que l'émetteur-récepteur FTN-OQAM peut atteindre, tout en offrant des performances proches de Nyquist sous la même condition SNR. La valeur numérique minimale de ce facteur d'emballage est étudiée pour chaque forme d'onde et ordre de constellation. L'algorithme proposé est basé sur l'analyse EXIT du turbo égaliseur MMSE LE-IC [26]. Notre objectif est de trouver le facteur d'emballage le plus petit que l'émetteur-récepteur FTN-OQAM peut atteindre sans dégrader les performances, et ceci en fonction du rendement de codage, de la forme d'onde, de l'ordre de modulation et du SNR. L'algorithme est résumé dans la Figure. 6. Le critère de convergence cible avec la signalisation de Nyquist est fixé à un BER de 10^{-5}, que nous appelons la performance de "Nyquist Error-Free" (NEF) dans la suite. Le processus de recherche commence par générer la valeur SNR correspondant au point NEF et initialiser le facteur d'emballage FTN à 0.1. En utilisant ces valeurs, le diagramme EXIT est généré. Si le tunnel EXIT est fermé ou si le diagramme EXIT n'atteint pas les performances NEF, le facteur d'emballage est incrémenté d'une valeur fixe et l'opération précédente est répétée. Le processus itératif se poursuit jusqu'à ce que le tunnel EXIT soit ouvert et le point NEF soit atteint. Le facteur d'emballage FTN estimé à l'aide de cette méthode est une valeur numérique, dont la précision dépend de la valeur du pas. Notez que l'algorithme proposé ne fournit qu'une valeur numérique du plus petit facteur d'emballage et non le nombre d'itérations nécessaires à la convergence.

Le processus de recherche est effectué pour différents filtres: SRRC ($L = 4M$) avec différents facteurs (ρ); PHYDYAS ($L = 4M$); TFL ($L = M$), FS ($L = 4M$); EGF ($L = 4M, \lambda = 2$) et IOTA ($L = 4M$). Le tableau 1 résume les valeurs numériques minimales des facteurs FTN pour chaque forme d'onde et ordre de constellation ainsi que le domaine d'égalisation recommandé.

Ensuite, nous comparons les performances BER de l'émetteur-récepteur FTN-OQAM à un système classique OFDM/OQAM. Nous résumons dans le tableau 2 le nombre d'itérations nécessaires à la réception, ainsi que l'augmentation du débit obtenue. Dans la suite, nous évaluons la performance de l'émetteur-récepteur FTN-OQAM pour d'autres facteurs FTN. Lorsque $\tau = 0,7$, le débit est augmenté par 42% au coût d'une perte de performance BER par rapport au cas Nyquist (perte de 1,5 dB à un BER autour de 10^{-4}). Le nombre d'itérations nécessaires à la convergence est égal à 3. Pour $\tau = 0,8$, le débit est augmenté par 25 % avec moins de 1 dB de perte à un BER de 10^{-5}, alors que le nombre d'itérations nécessaires n'est que de 2. Nous résumons dans le tableau

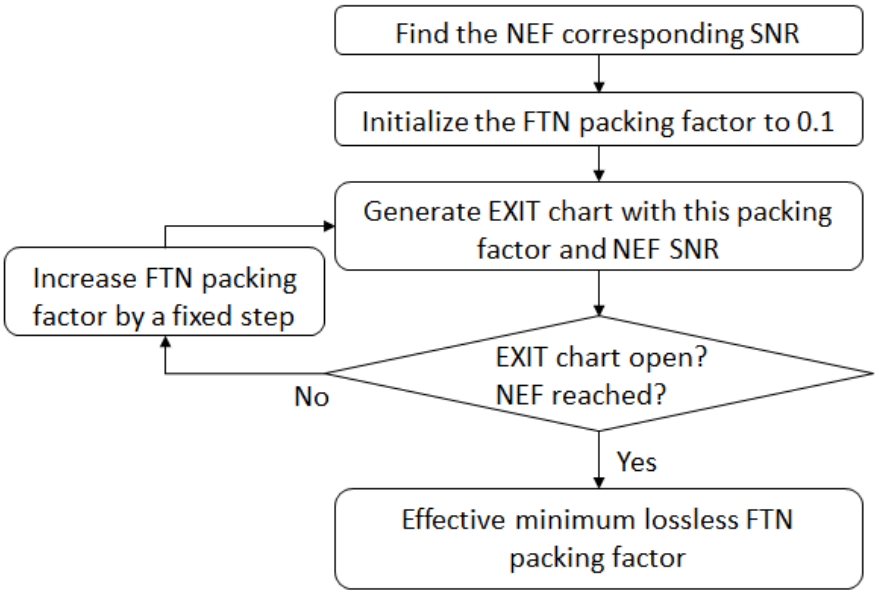

FIGURE 6: Processus de recherche de la valeur minimale effective du facteur FTN.

Formes d'ondes	Domaine d'égalisation	QPSK	16-QAM-	64-QAM
SRRC ($\rho = 0.5$)	fréquentiel	0.9	0.9	0.9
SRRC ($\rho = 0.3$)	fréquentiel	0.9	0.9	0.9
PHYDYAS	fréquentiel	0.9	0.9	0.9
FS	fréquentiel	0.9	0.9	0.9
IOTA	temporel	0.9	0.9	0.9
TFL	temporel	0.9	0.9	> 0.9
EGF ($\lambda = 2$)	temporel	0.9	0.9	> 0.9

TABLE 2: Valeurs minimales numériques des facteurs FTN et domaines d'égalisation recommandés pour chaque filtre et ordre de constellation.

Ordre de constellation	Nombre d'itérations	Amélioration du débit
QPSK	2	1.11
16-QAM	3	1.11
64-QAM	5	1.11

TABLE 3: Nombres d'itérations nécessaires pour chaque ordre de constellation et pour un facteur FTN de 0.9.

3 les formes d'onde recommandées, trouvées à travers des simulations, et le nombre d'itérations nécessaires pour chaque τ.

Chapitre 4

Dans ce chapitre, nous visons à améliorer l'émetteur-récepteur FTN-OQAM présenté

Ordre de constellation	Facteur FTN	Formes d'ondes recommandées	# d'itérations
QPSK	$\tau = 0.7$	PHYDYAS	3
	$\tau = 0.8$	PHYDYAS, SRRC (ρ =0.3, 0.5)	2
16-QAM	$\tau = 0.8$	FS, PHYDYAS, SRRC (ρ=0.5)	4
64-QAM	$\tau = 0.8$	SRRC (ρ=0.5)	9

TABLE 4: Formes d'ondes recommandées et nombre d'itérations pour chaque ordre de constellation et facteur FTN.

dans le chapitre 3. Bien que les signaux ne soient rapprochés que dans le domaine temporel, comparé au critère de Nyquist, le signal utile est également influencé par ICI en plus d'ISI. Comme les interférences induites par du FTN sont parfaitement connues par l'émetteur, des techniques visant à annuler les interférences à l'émission peuvent être considérées. Notre objectif dans ce chapitre est d'étudier une nouvelle technique de précodage afin de réduire les interférences dues à FTN. À cette fin, nous présentons trois familles de précodeurs à l'émission afin de supprimer ICI et/ou ISI et détaillons les récepteurs correspondants.

Supposant que le canal de transmission est idéal et sans distorsion, le signal reçu à l'instant n_0 et sur la sous-porteuse m_0 peut être exprimé par:

$$y_{m_0,n_0} = a_{m_0,n_0} + \underbrace{\sum_{\substack{q=-l \\ q\neq 0}}^{l} h_q a_{m_0,n_0+q}}_{ISI} + \underbrace{\sum_{\substack{p=-l' \\ p\neq 0}}^{l'} \sum_{q=-l}^{l} l_{p,q,n_0} a_{m_0+p,n_0+q}}_{ICI_{n_0}},$$

où $a_{m,n}$ sont les symboles OQAM transmis et les facteurs (l, l') représentent la zone des symboles contribuant au ISI et ICI, respectivement.

$$h_q = L\cos(\frac{\pi}{2}q)A_g[-qN_f, 0],$$

et

$$l_{p,q,n_0} = L\cos(\pi(\frac{p+q}{2} + \frac{2p(n_0N_f - \frac{D}{2})}{M}))A_g[-qN_f, -pb]$$

sont les coefficients du canal équivalent d'ISI et d'ICI, respectivement. L est la longueur du filtre g et A_g est sa fonction d'ambiguïté discrète. M est le nombre de sous-porteuses, $D = L - 1$ et $N_f = \lfloor \tau.\frac{M}{2} \rfloor$ est le facteur FTN d'expansion/décimation.
Le signal reçu est la somme du signal utile et des interférences connues par l'émetteur. Par conséquent, ce terme supplémentaire peut être calculé et annulé. Une méthode de précodage basée sur la pré-annulation des interférences est Tomlinson-Harashima Precoding (THP) présentée au chapitre 2.
Selon cette technique, l'émetteur connait parfaitement les coefficients du canal et précode successivement chaque symbole $a_{m,n}$ en supprimant les interférences causées par les symboles précédents $a_{m,nq}$, avec $1 \leq q \leq l$ et l la longueur de la réponse impulsionnelle du canal. Pour FTN, chaque symbole $a_{m,n}$ interfère avec les symboles $a_{m+p,n+q}$ avec $(p, q) \in [-l', l'] \times [-l, l]$, c'est-à-dire que les interférences induites par FTN sont causées par les symboles passés et futurs. Pour notre émetteur-récepteur FTN-OQAM,

les symboles précodés à l'instant temps n et sur la sous-porteuse m peuvent être exprimés comme suit:

$$c_{m,n} = a_{m,n} \underbrace{- \sum_{q=-l}^{-1} h_q c_{m,n+q} - \sum_{p=-l'}^{-1} \sum_{q=-l}^{l} l_{p,q,n} c_{m+p,n+q}}_{Past\ precoded\ symbols} \underbrace{- \sum_{q=1}^{l} h_q a_{m,n+q} - \sum_{p=1}^{l'} \sum_{q=-l}^{l} l_{p,q,n} a_{m+p,n+q}}_{Future\ symbols}$$

où, $c_{m+p,n+q}, (p,q) \in [-l', -1] \times [-l, -1]$ sont les symboles précédemment précodés selon la méthode THP, et $a_{m+p,n+q}, (p,q) \in [1, l'] \times [1, l]$ sont les symboles interférant futurs. Lorsque ces derniers sont également précodés, ils provoquent une nouvelle interférence différente de celle supprimée de $a_{m,n}$. Par conséquent, la nature de l'interférence causée par FTN rend difficile le précodage conjoint de tous les symboles transmis.

Dans ce qui suit, nous détaillons notre solution de précodage proposée pour l'émetteur-récepteur FTN-OQAM appelée "Sparse Interference Pre-Cancellation" (SIPC). Tout d'abord, nous proposons de précoder uniquement un sous-groupe de symboles transmis, ce qui signifie que les symboles utilisés pour précoder le symbole $a_{m,n}$ ne seront pas modifiés. Deuxièmement, l'opération de modulo utilisée dans la méthode THP est supprimée. Cette opération a été initialement introduite pour contrôler l'amplitude des symboles précodés. Bien que cette opération soit supprimée, la puissance du signal transmis n'augmente pas. Par rapport au cas de Nyquist, la puissance du signal FTN augmente en raison des interférences supplémentaires. Comme ces dernières sont réduites par le précodage, la puissance du signal diminue comparé à l'émetteur-récepteur non précodé. La structure proposée de l'émetteur-récepteur FTN-OQAM précodé est représentée dans la Figure. 7, où les blocs en pointillés sont liés à la méthode SIPC. Nous considérons trois familles de précodeurs selon qu'ICI et/ou ISI sont pré-annulés. Pour chaque précodeur, nous détaillons la structure de l'émetteur et de son récepteur correspondant. Ensuite, nous évaluons la performance BER compte tenu des valeurs numériques des facteurs FTN trouvées dans le chapitre précédent, c'est-à-dire $\tau = 0,9$ et différents ordres de constellation. Nous présentons les filtres prototypes recommandés pour chaque précodeur ainsi que le nombre d'itérations nécessaires au côté du récepteur. Dans la dernière section, nous évaluons la performance de l'émetteur-récepteur FTN-OQAM précodé lorsque τ est inférieur à 0,9 (τ = 0,7, 0,8). Pour chaque ordre de constellation et facteur FTN, les précodeurs recommandés sont présentés puis comparés à l'émetteur-récepteur FTN-OQAM décrit au chapitre 3 pour mettre en évidence les avantages du précodage.

SIPC en temps et en fréquence

Dans cette section, nous présentons le précodage SIPC en temps et en fréquence (SIPC-tf). Notre objectif est d'annuler ICI et ISI à partir d'un sous-groupe de symboles transmis. Les symboles précodés à l'instant temps n et sur la sous-porteuse m sont formulés comme suit:

$$c_{m,n} = a_{m,n} - \alpha\{ \sum_{\substack{q=-k \\ q\neq 0}}^{k} h_q a_{m,n+q} \} - \beta\{ \sum_{\substack{p=-k' \\ p\neq 0}}^{k'} \sum_{q=-l}^{l} l_{p,q,n} a_{m+p,n+q} \},$$

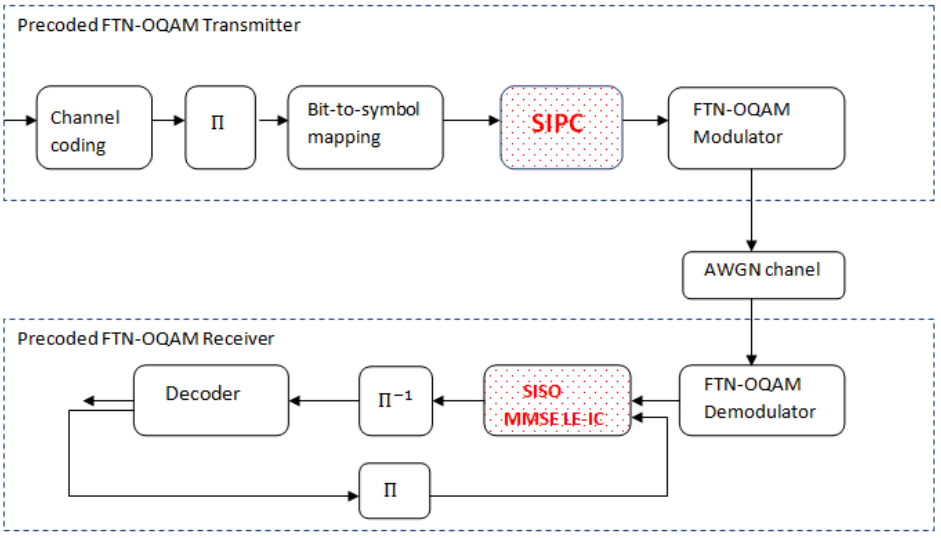

FIGURE 7: L'émetteur-récepteur FTN-OQAM proposé. Les blocs en pointillés sont liés à la méthode SIPC.

où $a_{m,n}$ sont des symboles OQAM. La paire $(k, k') \in \mathbb{Z}^2$ représente l'intervalle des symboles considérés pour pré-annuler les ISI et ICI, respectivement. En outre, nous introduisons deux facteurs α et β pour contrôler la quantité d'interférences supprimée. Considérant la lattice temps-fréquence, les symboles précodés sont positionnés sur les porteuses m et aux instants temps n tels que:

$$\begin{cases} m = b \bmod(k'+1), \ (b \in \mathbb{N}, \ b \leq k') \\ n = a \bmod(k+2), \text{ et } n = (a+1) \bmod(k+2), \ (a \in \mathbb{N}, \ a \leq (k+1)) \end{cases}$$

La Figure. 8 illustre un exemple de modèle de précodage. Les triangles verts représentent les symboles précodés, tandis que les triangles bleus et rouges représentent les symboles non précodés. Dans cet exemple, nous considérons que les deux symboles les plus proches, représentés ici par les triangles bleus, contribuent principalement à ISI, c'est-à-dire que nous considérons que $k = 2$. Sur une sous-porteuse m, nous alternons entre deux symboles précodés et non précodés. En fait, pour chaque symbole à l'instant temps n, il est démontré que les symboles aux positions impaires ne contribuent pas à ISI. De même, nous considérons que les symboles des sous-porteuses les plus proches, représentés ici par les triangles rouges, contribuent principalement à ICI, c'est-à-dire que nous considérons que $k' = 1$.

L'émetteur-récepteur FTN-OQAM proposé est illustré par la Figure. 7. D'abord, les bits d'information sont encodés. En définissant les facteurs (k, k'), nous déterminons le nombre de symboles précodés et non précodés. Considérant que B symboles sont transmis et que $(k = 2, \ k' = 1)$, le nombre de symboles précodés et non précodés est $B_1 = \frac{B}{4}$ Et $B_2 = \frac{3B}{4}$, respectivement. Ensuite, les bits codés constituant les différents groupes de symboles sont entrelacés séparément. Enfin, le module *SIPC* précode les symboles aux positions temps-fréquence choisies.

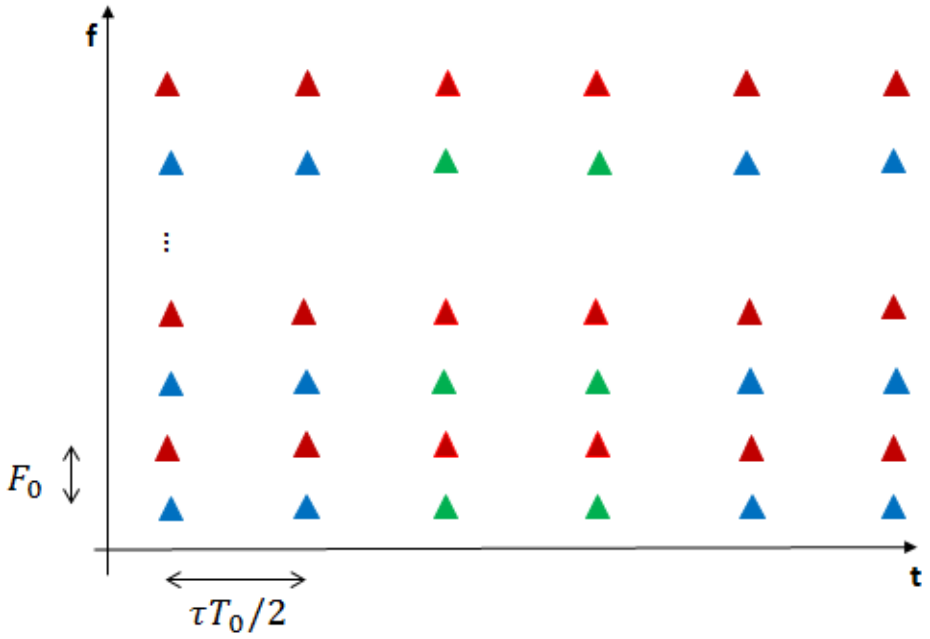

FIGURE 8: Lattice temps-fréquence du FTN-OQAM avec le précodage SIPC-tf. Les triangles verts représentent les symboles précodés. Les triangles rouges et bleus représentent les symboles non précodés.

A la réception, l'égaliseur MMSE LE-IC détaillé dans le chapitre précédent est modifié pour prendre en compte le module SIPC introduit. Nous proposons un égaliseur MMSE LE-IC en 3 étapes pour traiter séparément les symboles précodés et non précodés. En gardant la même configuration que dans la section précédente ($k = 2$, $k' = 1$), les symboles aux positions vertes sont décodés en premier, suivis par ceux aux positions bleues et enfin par ceux représentés par les triangles rouges. Les symboles précodés représentés par les triangles verts sont décodés en premier puisqu'ils sont moins affectés par les interférences. Ainsi, leur contribution à l'ISI impactant les symboles non précodés sur les mêmes sous-porteuses, représentées ici par les triangles bleus, peut être supprimée. Ces derniers sont ensuite décodés dans la deuxième étape. Enfin, la contribution des symboles représentés par les triangles verts et bleus à l'ICI impactant ceux représentés par les triangles rouges peut être annulée et ceux-ci sont ensuite détectés. Par exemple, nous considérons que:

$$\begin{aligned} \text{triangles verts} &= \{(m,n),(m \text{ pair}, n = 3 \text{ et } 0 \bmod(4))\} \\ \text{triangles bleus} &= \{(m,n),(m \text{ pair}, n = 1 \text{ et } 2 \bmod(4))\} \\ \text{triangles rouges} &= \{(m,n), m \text{ impair }\} \end{aligned}$$

L'égaliseur MMSE LE-IC est détaillé dans la Figure. 9. Pour décoder le signal reçu, le bloc *SIC1* supprime en premier l'ICI utilisant les symboles estimés et délivrés par le décodeur et le *SISO mapping*. Selon le domaine d'égalisation considéré, les coefficients des filtres $\mathbf{p}_1$ et $\mathbf{q}_1$ sont calculés et le signal est ensuite égalisé. Comme dans le chapitre précédent, les modules *SISO Mapping* et *SISO Demapping* sont utilisés pour échanger d'information soft au niveau bit et symbole entre l'égaliseur et le décodeur.
Dans une deuxième étape, nous décodons les symboles non précodés reçus sur les mêmes

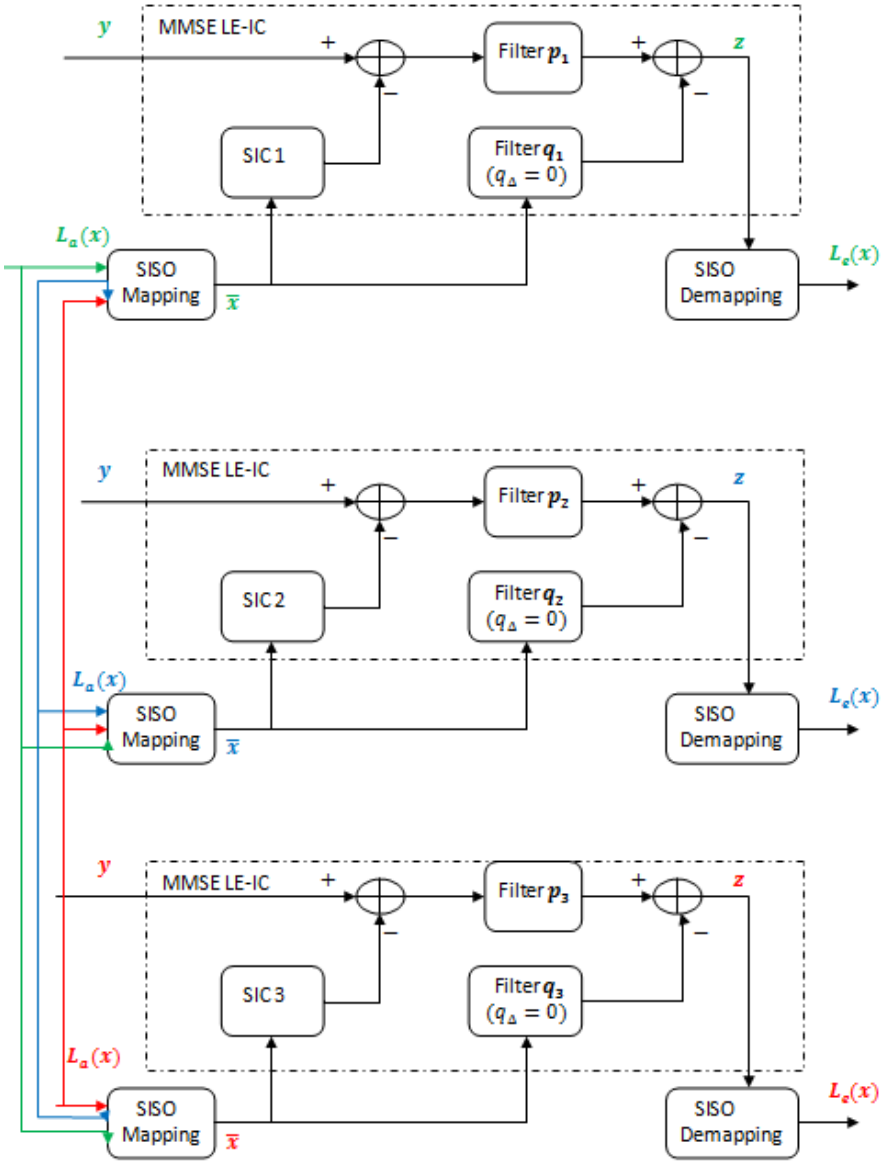

FIGURE 9: Structure de l'égaliseur SISO MMSE IC-LE utilisé pour le précodage SIPC-tf.

sous-porteuses m. Tout d'abord, en utilisant les LLRs délivrés par le décodeur à l'étape 1, le bloc *SISO Mapping* calcule les symboles estimés correspondants. Par conséquent, le module *SIC2* annule ICI venant des sous-porteuses voisines ainsi que l'ISI causé par les symboles précodés. Ensuite, les coefficients des filtres $\mathbf{p}_2$ et $\mathbf{q}_2$ sont calculés. Enfin, le signal est égalisé et décodé. À la troisième étape, nous décodons les symboles non précodés reçus sur les sous-porteuses impairs m.

SIPC en temps

Le deuxième précodeur proposé est le SIPC selon l'axe temporel (SIPC-t). Nous envisageons de supprimer ISI d'un sous-groupe des symboles transmis. À cette fin, ces

symboles sont précodés en annulant les ISI causés par leurs voisins tandis que ceux-ci ne sont pas modifiés. Dans ce scénario, le facteur $\beta = 0$ et les symboles précodés sont exprimés comme suit:

$$c_{m,n} = a_{m,n} - \alpha\{\sum_{\substack{q=-k \\ q\neq 0}}^{k} h_q a_{m,n+q}\},$$

où k définit l'intervalle des symboles considérés pour la pré-annulation de l'ISI. Comme la solution de précodage est disperse, seuls les symboles aux positions (m, n) sont modifiés. Considérons la lattice temps-fréquence, m et n sont les sous-porteuses et les indices temps, respectivement. Sur chaque sous-porteuse m, les symboles précodés sont situés aux positions n tels que:

$$\{n = a \bmod(k+2) \quad \text{et } n = a+1 \bmod(k+2),\ a \in \mathbb{N},\ a \leq k+1\}.$$

Nous illustrons un exemple de précodage dans la Figure. 10, où les triangles verts et rouges représentent respectivement les symboles précodé et non précodé. Dans cet exemple, nous considérons que ISI est principalement causé par les deux symboles les plus proches et que $k = 2$. Sur une sous-porteuse m,nous proposons d'alterner deux symboles précodés et non précodés:

$$\begin{aligned} \text{triangles verts} &= \{(m,n), (m \ \text{ pair}, n = 3 \text{ et } 0 \bmod(4))\} \\ \text{triangles rouges} &= \{(m,n), (m \ \text{ impair}, n = 1 \text{ et } 2 \bmod(4))\} \end{aligned}$$

Du côté du récepteur, nous proposons une égalisation en deux étapes comme représenté

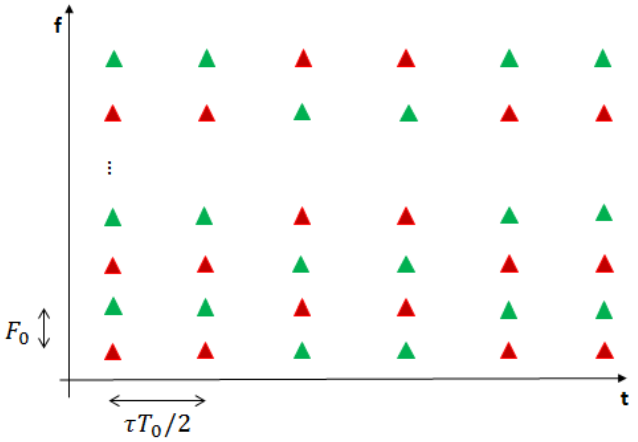

FIGURE 10: Lattice temps-fréquence du FTN-OQAM avec le précodage SIPC-t. Les triangles verts et rouges représentent les symboles précodés et non précodés, respectivement.

dans la Figure. 11. La première étape consiste à décoder les symboles précodés tandis que les symboles non précodés sont détectés dans la deuxième étape.
Tout d'abord, nous déterminons les coefficients des filtres $\mathbf{p}_1$ et $\mathbf{q}_1$ selon le principe de l'égalisation turbo. Le bloc *SIC 1* supprime l'ICI causé par les sous-porteuses voisines. Le signal résultant est ensuite égalisé et utilisé par le bloc *Decoder*. À la deuxième étape, les coefficients des filtres $\mathbf{p}_2$ et $\mathbf{q}_2$ sont d'abord déduits. Le bloc *SIC 2* supprime l'ICI ainsi que de l'ISI causé par les symboles précodés. Le signal résultant est ensuite égalisé

et décodé par le bloc *Decoder*.

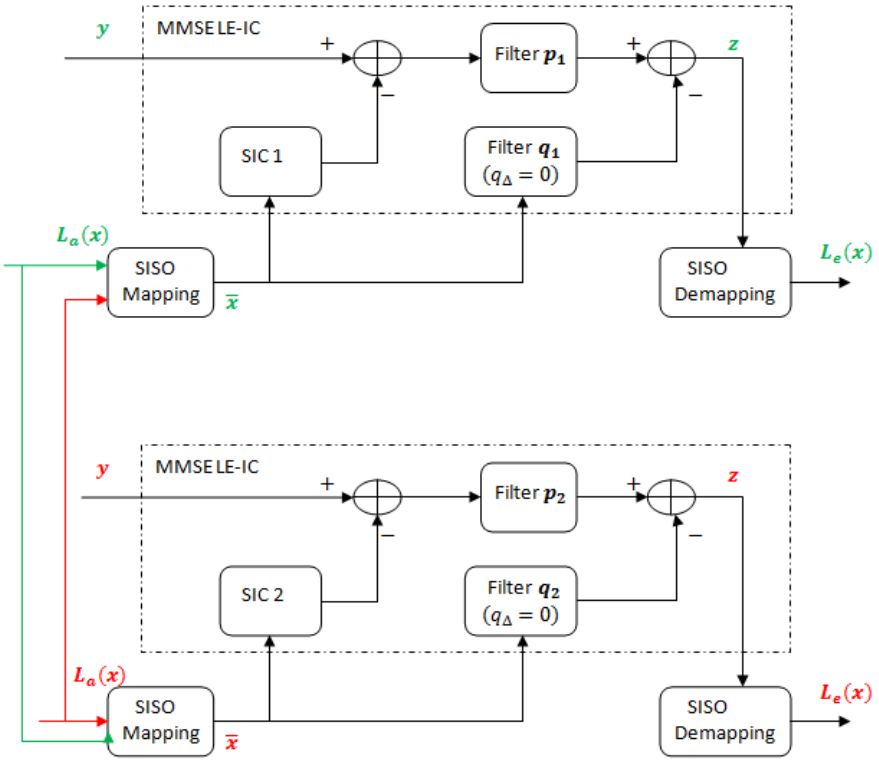

FIGURE 11: Structure de l'égaliseur SISO MMSE IC-LE utilisé pour le précodage SIPC-t.

SIPC en fréquence

Le troisième précodeur proposé, visant la pré-annulation d'ICI, est le SIPC sur l'axe fréquentiel (SIPC-f). Dans ce scénario, $\alpha = 0$ et un sous-groupe des symboles transmis sont précodés:

$$c_{m,n} = a_{m,n} - \beta\{\sum_{\substack{p=-k' \\ p\neq 0}}^{k'} \sum_{q=-l}^{l} l_{p,q,n} a_{m+p,n+q}\}$$

Où k' définit l'intervalle des symboles considérés pour l'annulation d'ICI. Étant donné que la méthode de précodage proposée est disperse, seuls les symboles sur les sous-porteuses m tels que:

$$\{m = b \bmod(k'+1),\ b \in \mathbb{N},\ b \leq k'\}$$

sont précodés alors que le reste des symboles ne sont pas modifiés. Un exemple de modèle de précodage est illustré à la Figure. 12, où les triangles verts et rouges représentent respectivement des sous-porteuses précodées et non précodées. Dans cette configuration, nous avons considéré que ICI est principalement causé par les sous-porteuses les plus proches, c'est-à-dire que $k' = 1$.

Le récepteur proposé utilise un traitement en deux étapes pour décoder séparément

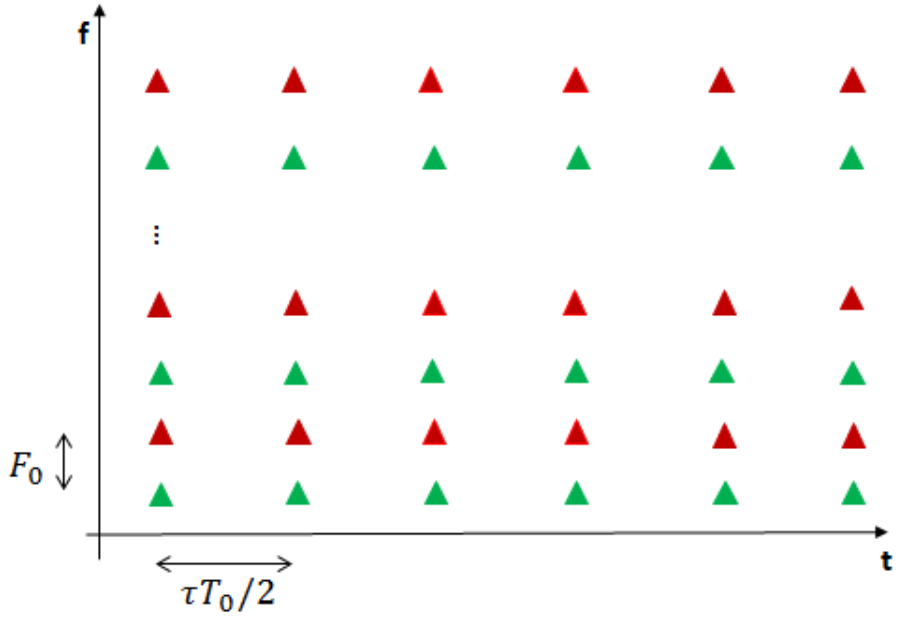

FIGURE 12: Lattice temps-fréquence du FTN-OQAM avec le précodage SIPC-f. Les triangles verts et rouges représentent les symboles précodés et non précodés, respectivement.

les différents groupes de symboles. La structure du récepteur est similaire à celle du précodeur SIPC-t. Les coefficients des filtres $\mathbf{p}_1$ et $\mathbf{q}_1$ sont calculés selon le principe de la turbo égalisation. En utilisant les symboles estimés fournis par le module *SISO Mapping*, le bloc *SIC 1* supprime ICI du signal reçu. Le signal résultant est ensuite égalisé et envoyé au bloc *Decoder*. Au deuxième stade, les symboles non précodés sont détectés.

Nous comparons ensuite les performances BER des trois précodeurs. Sur la base de nos résultats de simulation, nous présentons les formes d'onde recommandées pour chaque précodeur en fonction de l'ordre de la constellation et du facteur FTN. Ensuite, nous donnons le précodeur recommandé pour chaque ordre de constellation et τ. Enfin, nous comparons l'émetteur-récepteur FTN-OQAM précodé et non précodé pour souligner les avantages du précodage proposé.

Sur la base des résultats BER de l'émetteur-récepteur FTN-OQAM précodé, nous avons résumé dans les tableaux 4, 5 et 6 les formes d'onde recommandées ainsi que le nombre d'itérations nécessaires pour chaque précodeur. Ensuite, nous avons comparé les performances de l'émetteur-récepteur FTN-OQAM en utilisant les différents précodeurs et les filtres recommandés. Les précodeurs recommandés pour chaque ordre de constellation et facteur FTN sont résumés dans le tableau 7. Enfin, la performance de l'émetteur-récepteur FTN-OQAM utilisant ces précodeurs est évaluée et comparée à l'émetteur-récepteur non précodé dans les Figures. 13, 14 et 15.

Ordre de constellation	τ	Formes d'ondes recommandées	# d'itérations
QPSK	0.7	IOTA	3
	0.8	FS, SRRC (ρ=0.5, 0.3), PHYDYAS	2
16-QAM	0.7	FS, IOTA	6
	0.8	FS, PHYDYAS	3
64-QAM	0.8	PHYDYAS, FS	6

TABLE 5: Formes d'ondes recommandées et nombre d'itérations pour différents facteurs FTN et ordres de modulation et le précodage SIPC-tf.

Ordre de constellation	τ	Formes d'ondes recommandées	# d'itérations
QPSK	0.7	IOTA TFL, EGF (λ=2)	3
	0.8	FS, PHYDYAS	2
16-QAM	0.7	FS, PHYDYAS	7
	0.8	FS, PHYDYAS, IOTA	4
64-QAM	0.8	PHYDYAS, FS	8

TABLE 6: Formes d'ondes recommandées et nombre d'itérations pour différents facteurs FTN et ordres de modulation et le précodage SIPC-t.

Ordre de constellation	τ	Formes d'ondes recommandées	# d'itérations
QPSK	0.7	IOTA, TFL, FS, PHYDYAS	3
	0.8	PHYDYAS, SRRC (ρ=0.5, 0.3), IOTA	2
16-QAM	0.7	FS, PHYDYAS, IOTA, TFL	8
	0.8	FS, PHYDYAS	3
64-QAM	0.8	PHYDYAS, FS	7

TABLE 7: Formes d'ondes recommandées et nombre d'itérations pour différents facteurs FTN et ordres de modulation et le précodage SIPC-f.

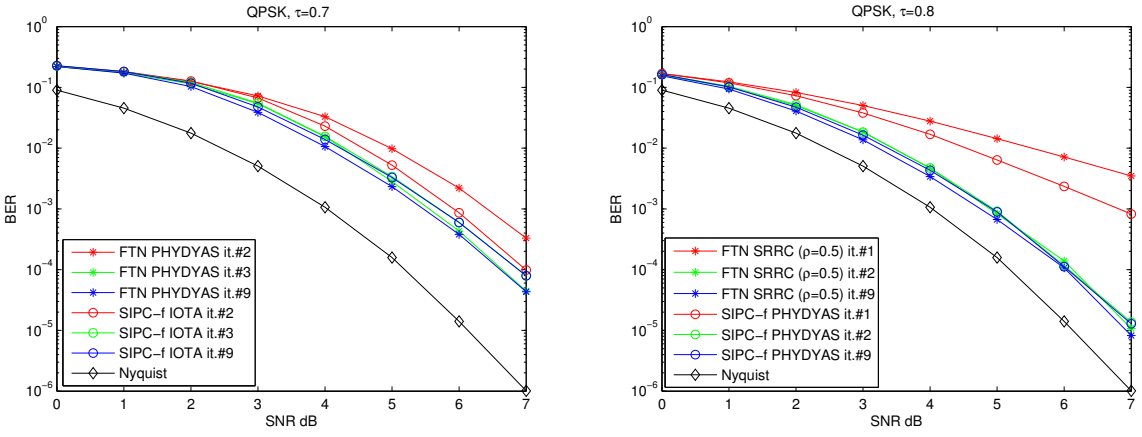

FIGURE 13: Evaluation BER de FTN-OQAM combiné avec le précodage SIPC-f pour la modulation QPSK et les facteurs FTN $\tau = 0.7$ et $\tau = 0.8$.

La Figure. 13 montre les résultats BER pour la modulation QPSK. Dans le cas de

Ordre de constellation	Facteur FTN	Précodeurs recommandés
QPSK	$\tau = 0.7$	SIPC-f, SIPC-tf, SIPC-t
	$\tau = 0.8$	SIPC-f, SIPC-tf, SIPC-t
	$\tau = 0.9$	SIPC-f, SIPC-t, SIPC-tf
16-QAM	$\tau = 0.7$	SIPC-tf, SIPC-t
	$\tau = 0.8$	SIPC-tf
	$\tau = 0.9$	SIPC-f, SIPC-tf
64-QAM	$\tau = 0.8$	SIPC-tf, SIPC-t
	$\tau = 0.9$	SIPC-tf, SIPC-t

TABLE 8: Précodeurs recommandés pour différents facteurs FTN et ordres de constellation.

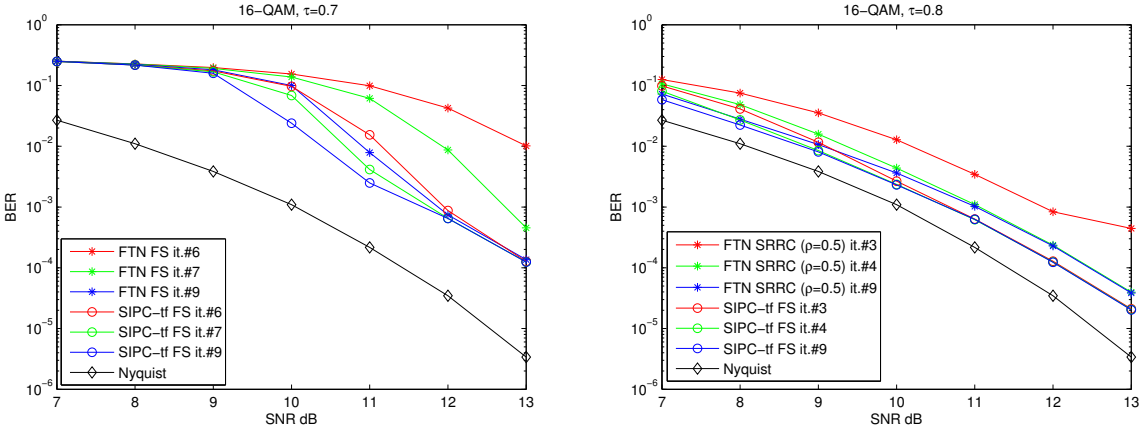

FIGURE 14: Evaluation BER de FTN-OQAM combiné avec le précodage SIPC-tf pour la modulation 16-QAM et les facteurs FTN $\tau = 0.7$ et $\tau = 0.8$.

$\tau = 0,7$, la technique de précodage proposée SIPC-f permet à l'émetteur-récepteur FTN-OQAM d'effectuer seulement 2 itérations au lieu de 3 à la réception. À un BER autour de 10^{-4}, l'émetteur-récepteur FTN-OQAM précodé a moins de 2 dB de perte par rapport aux systèmes basés sur Nyquist. Cependant, une augmentation de 42 % du débit est obtenue. Pour un facteur FTN $\tau = 0,8$, les deux systèmes convergent après avoir effectué 2 itérations à la réception. Cependant, la première itération est améliorée par le précodage SIPC-f. Une augmentation du débit de 25 % est obtenue pour une perte de 1 dB à un BER autour de 10^{-5}.

Les résultats pour la modulation 16-QAM sont illustrés à la Figure. 14. Dans le cas $\tau = 0,7$, le précodage SIPC-tf permet au récepteur FTN-OQAM de converger après avoir effectué 6 itérations au lieu de 9. Le débit est augmenté dans ce cas par 42 % au détriment d'une perte de 2 dB à un BER autour de 10^{-4}. Dans le cas $\tau = 0.8$, le précodage SIPC-tf permet au récepteur d'effectuer seulement 3 itérations au lieu de 4. Un gain de 25 % est atteint pour moins de 1 dB de perte à un BER autour 10^{-5}.

La Figure. 15 illustre les performances BER des deux systèmes en cas d'une modulation 64-QAM et $\tau = 0.8$. Le précodage SIPC-t proposé permet au récepteur de converger après avoir effectué 8 itérations au lieu de 9. Comme on le remarque, les courbes BER

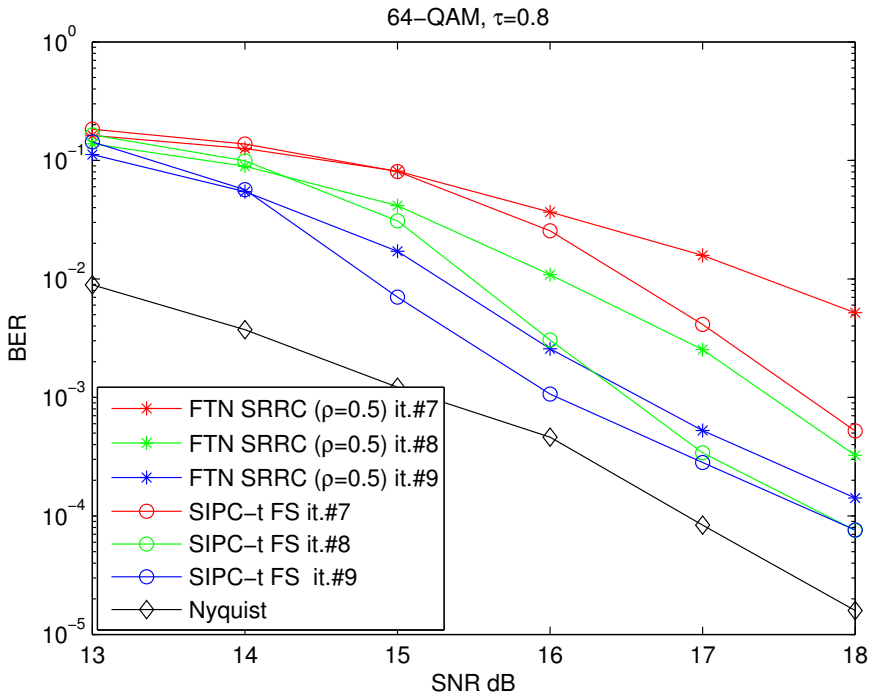

FIGURE 15: Evaluation BER de FTN-OQAM combiné avec le précodage SIPC-t pour la modulation 64-QAM et le facteur FTN $\tau = 0.8$.

des différentes itérations sont améliorées par la solution de précodage. Dans ce scénario, un gain de 25 % de débit est obtenu pour une perte de 1 dB à un BER autour de 10^{-4}. En outre, la technique de précodage proposée améliore la performance de l'émetteur-récepteur FTN-OQAM indépendamment de la forme d'onde utilisée.

Chapitre 5

Dans le chapitre précédent, nous avons décrit une nouvelle technique de précodage pour la signalisation FTN combinée avec la modulation OFDM/OQAM. Nous avons proposé de supprimer les interférences FTN uniquement d'un sous-groupe des symboles transmis sans modifier le reste des symboles. Par conséquent, les symboles précodés et non précodés sont affectés différemment par l'interférence induite par la signalisation FTN. Dans le chapitre 5, nous visons à améliorer l'émetteur-récepteur FTN-OQAM pour approcher la performance des systèmes basés sur Nyquist avec une meilleure efficacité spectrale. Tout d'abord, nous proposons de modifier le codage canal en utilisant différents rendements de codage pour les bits composant les symboles précodés et non précodés. Ensuite, nous modifions le mapping des bits aux symboles pour tenir compte des différents niveaux de protection du mapping Gray. Enfin, nous proposons également un nouveau mapping des symboles aux positions temps-fréquence différent de celui classiquement utilisé par la modulation OFDM/OQAM.

Adaptation du rendement de code

Nous considérons l'émetteur-récepteur FTN-OQAM précodé représenté sur la Figure. 7, où le bloc *Channel coding* code N_i bits d'informations et fournit N_c bits codés. Nous considérons également que les bits codés N_c sont convertis en B OQAM symboles. Nous avons:

$$\begin{aligned} B &= B_1 + B_2 \\ N_c &= N_{c1} + N_{c2} \\ N_i &= N_{i1} + N_{i2} \end{aligned}$$

Où l'indice 1 en N_{i1} et N_{c1} fait référence aux symboles précodés, tandis que l'indice 2 en N_{i2} et N_{c2} se réfère aux symboles non-précodés. Les bits codés N_{c1}, correspondants aux bits d'information N_{i1}, sont entrelacés puis convertis en B_1 OQAM symboles. De même, les bits codés N_{c2} correspondants aux bits d'information N_{i2} sont entrelacés et convertis en B_2 OQAM symboles. Le nombre de symboles précodés et non précodés est déterminé par les paramètres de précodage k et k'. Ensuite, le module *SIPC* annule, à partir des symboles B_1, l'interférence provoquée par les symboles B_2. Contrairement au schéma de codage de la Figure. 7, où les N_{i1} et N_{i2} bits sont codés avec le même rendement de codage, nous proposons d'utiliser différents rendements de code locaux r_1 et r_2 pour coder les bits d'information N_{i1} et N_{i2}, respectivement. Le nombre de bits codés N_c est maintenu inchangé et N_{i1} et N_{i2} sont choisis comme multiples de r_1 et r_2, respectivement. Ainsi, différents niveaux de protection en termes de codage canal sont assurés pour les symboles précodés et non précodés. Selon que $r_1 \leq r_2$ ou $r_2 \leq r_1$, les symboles précodés sont plus protégés que les non précodés et vice versa.

Nous supposons que $r_1 \leq r_2$ et nous remplaçons les modules *Channel coding* et Π par le schéma représenté sur la Figure. 16. Le premier groupe de N_{i1} bits est encodé et ensuite poinçonné par le bloc $Punct_1$, résultant en un groupe de $N_{c1} = \frac{N_{i1}}{R_1}$ bits. Ces bits sont ensuite entrelacés. De même, le deuxième groupe de N_{i2} bits est encodé et poinçonné, ce qui entraîne un groupe de $N_{c2} = \frac{N_{i2}}{r_2}$ bits, qui sont ensuite entrelacés . Ces deux groupes de bits sont concaténés pour obtenir les bits codés N_c et sont ensuite convertis en symboles OQAM. Selon le précodage choisi, les symboles B_1 sont ensuite précodés. Bien que plusieurs rendements de codage locaux soient utilisés, le rendement de code global initial reste inchangé. Des modifications similaires sont introduites lorsque les rendements de codage locaux sont choisis de telle sorte que $r_2 \leq r_1$.

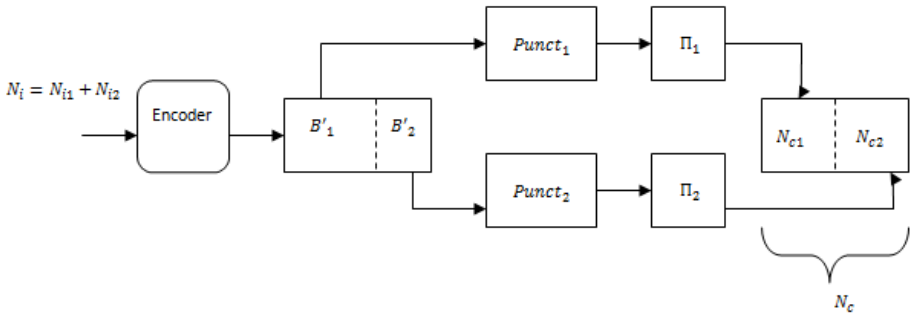

FIGURE 16: Le codage canal et l'entrelaceur proposés.

Dans la section suivante, nous évaluons l'impact de l'adaptation du rendement de code sur la performance BER du schéma de transmission, en fonction de l'ordre de constellation et du facteur FTN. Les résultats de simulation sont fournis en termes de BER vs SNR. Nous utilisons différents rendements pour coder les bits d'information N_{i1} et N_{i2}, tout en conservant le même rendement initial, c'est-à-dire $r = \frac{1}{2}$. Nous considérons un codeur RSC avec un rendement $\frac{1}{4}$ et des polynômes générateurs en notation octale (1, 15/13, 15/13, 17/13):

$$\begin{aligned} g_1(x) &= 1 \\ g_2(x) &= \frac{1+x^2+x^3}{1+x+x^3} \\ g_3(x) &= \frac{1+x^2+x^3}{1+x+x^3} \\ g_4(x) &= \frac{1+x+x^2+x^3}{1+x+x^3} \end{aligned}$$

Nous considérons également un mapping Gray et un entrelacement aléatoire. La méthode de précodage est SIPC-t, visant à l'annulation ISI, avec $k = 2$. Nous gardons la même configuration du récepteur que dans la section précédente: le récepteur est basé sur l'égalisation MMSE LE-IC, le filtre MMSE est de longueur 30 avec un délai 15, et le décodeur est basé sur l'algorithme Max-Log-MAP. Tout d'abord, nous traçons le diagramme EXIT représentant l'échange d'information mutuelle entre l'égaliseur et le décodeur en tenant compte de plusieurs rendements de codage:

$$\{\frac{8}{13}, \frac{5}{13}, \frac{8}{14}, \frac{6}{14}, \frac{8}{15}, \frac{7}{15}, \frac{8}{16}, \frac{8}{17}, \frac{9}{17}, \frac{8}{18}, \frac{10}{18}, \frac{8}{19}, \frac{11}{19}\}$$

Ensuite, nous sélectionnons les paires de rendements de codage (r_1, r_2) qui assurent un tunnel ouvert entre l'égaliseur et le décodeur. Enfin, nous évaluons les performances BER de l'émetteur-récepteur FTN-OQAM en utilisant les rendements de codage sélectionnés r_1 et r_2 en cas de la modulation 16-QAM et 64-QAM.

A partir des résultats de simulations, nous pouvons déduire que le codage canal proposé est recommandé lorsque le diagramme EXIT montre que la courbe de l'égaliseur est très proche du décodeur, ce qui signifie qu'il améliore l'échange d'information soft entre l'égaliseur et le décodeur. Compte tenu de l'émetteur-récepteur FTN-OQAM précodé, nous avons montré que le codage canal introduit est recommandé pour les facteurs FTN faibles: $\tau = 0,7$ pour la modulation 16-QAM et $\tau = 0,8$ pour la modulation 64-QAM. Dans ces scénarios, l'émetteur-récepteur FTN-OQAM précodé présente de meilleurs résultats BER lors de l'utilisation de différents rendements de codage locaux r_1 et r_2 pour coder les N_{i1} et N_{i2} bits d'information, respectivement avec $r_1 \leq r_2$. Nous devons mentionner que la complexité de l'émetteur-récepteur, en termes de nombre d'opérations d'addition et de multiplication, n'augmente pas lorsque le codage proposé est utilisé.

Amélioration du mapping Gray

Considérant une modulation d'ordre élevé telle que 16-QAM et 64-QAM, le niveau de protection de chaque bit dépend de sa position dans le mapping Gray. Nous considérons le mapping Gray, 16 et 64-QAM représenté dans les Figures. 17 et 18. En cas de la

modulation 16-QAM, deux niveaux de protection sont disponibles pour chaque symbole de 4 bits. Le premier niveau est représenté par les bits b_0 et b_2, tandis que le deuxième niveau est représenté par les bits b_1 et b_3. D'autre part, la modulation 64-QAM présente trois niveaux de protection pour chaque symbole de 6 bits. Les bits b_0 et b_3 constituent le premier niveau, tandis que les bits b_1 et b_4 constituent le deuxième niveau et les bits b_2 et b_5 le troisième niveau. Dans la Figure. 4, le codeur canal RSC a un rendement effectif $r = \frac{1}{2}$ et délivre des bits codés qui sont d'abord entrelacés puis mappés sur des symboles complexes. Dans cette section, nous proposons un nouvel mapping pour placer les bits systématiques dans les positions hautement protégées par le mapping Gray. En effet, le codeur RSC délivre des bits systématiques représentant les bits d'information à son entrée et des bits de redondance, c'est-à-dire des bits de parité. Le mapping des bits proposé vise à améliorer le décodage des bits d'information transmis. À cette fin, les bits systématiques et de parité délivrés par l'encodeur canal sont entrelacés individuellement puis réorganisés avant d'être convertis en symboles complexes. Dans ce qui suit, nous détaillons les modifications du mapping des bits pour les émetteurs-récepteurs FTN-OQAM non précodé et précodé.

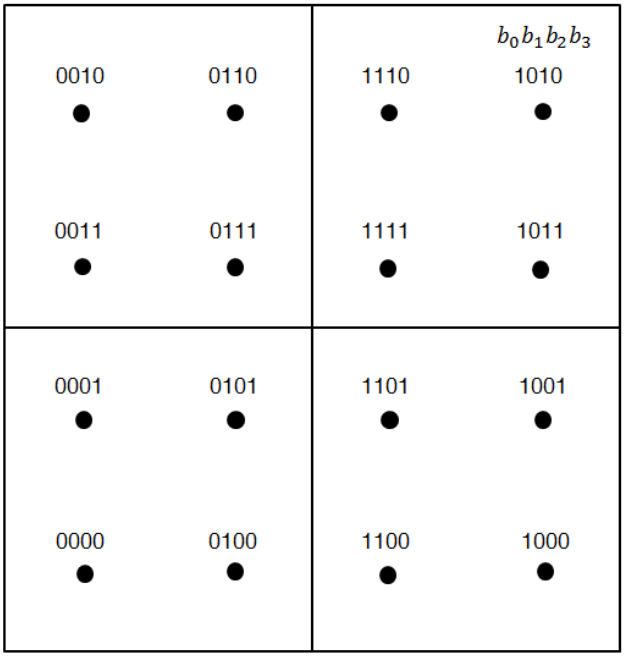

FIGURE 17: Mapping Gray: 16-QAM.

Emetteur-récepteur FTN-OQAM non précodé

Nous considérons l'émetteur-récepteur FTN-OQAM détaillé à la Figure. 4. Le codeur canal RSC délivre des bits systématiques, c'est-à-dire des bits d'information et des bits de parité, c'est-à-dire une redondance. Les bits systématiques et de parité sont ensuite entrelacés séparément. Lorsque la modulation 16-QAM est envisagée, les bits systématiques entrelacés sont placés aux positions b_0 et b_2. Les positions restantes b_1 et b_3 sont occupées par les bits de parité correspondants. Ensuite, chaque 4 bits sont convertis en symboles complexes et délivrés au bloc *FTN-OQAM modulator*. Ainsi, le réordonnancement de bits garantit que les bits utiles, c'est-à-dire les bits d'information transmis,

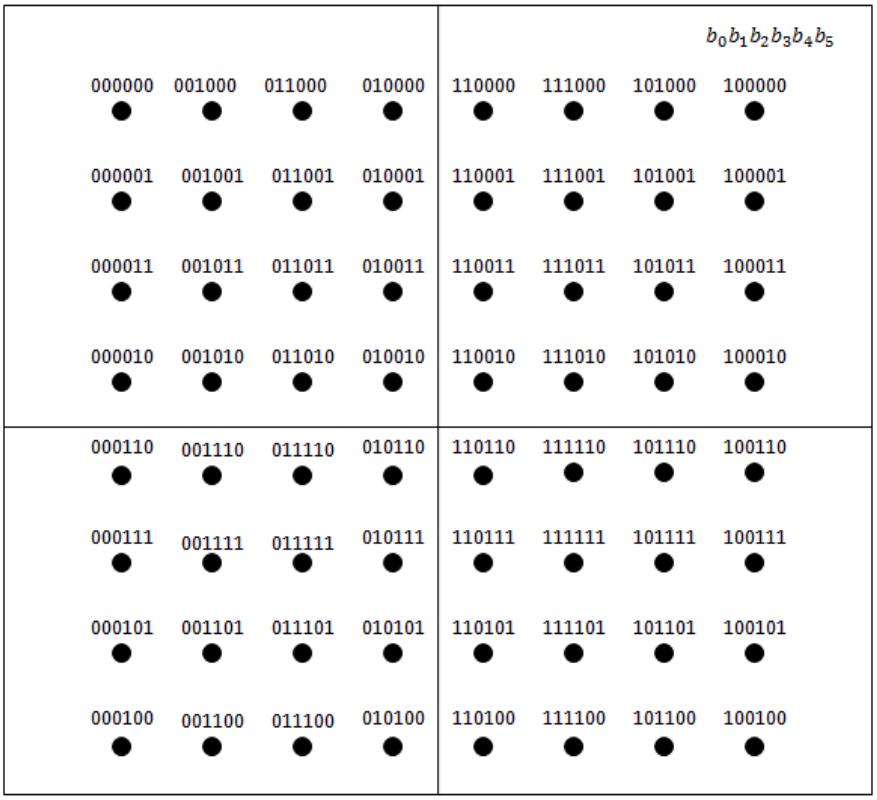

FIGURE 18: Mapping Gray: 64-QAM.

occupent les positions hautement protégées du mapping Gray. La même idée s'applique en cas de la modulation 64-QAM où chaque symbole complexe est composé de 6 bits. De même, les bits systématiques et de parité sont entrelacés séparément. Dans ce scénario, trois niveaux de protection sont disponibles. Les bits systématiques entrelacés sont placés aux positions b_0, b_3 et b_1, tandis que leurs bits de parité entrelacés sont placés aux positions b_4, b_2 et b_5, respectivement. Notez que les bits de parité correspondant aux bits systématiques placés aux positions b_1 sont mappés aux positions b_4, car ils constituent le deuxième niveau de protection. Les bits réorganisés sont ensuite convertis en symboles complexes et délivrés au bloc *FTN-OQAM modulator*.
Du côté du récepteur, nous conservons le même égaliseur turbo présenté au chapitre 3. Cependant, les LLRs calculés par le module *SISO mapping* doivent être réorganisés avant l'étape de décodage. En fonction de l'ordre de constellation et de l'ordre des bits utilisés, nous récupérons les LLRs des bits systématiques et de parité. Ensuite, ils sont désentrelacés séparément et alimentés au décodeur canal. Après l'étape de décodage, les nouveaux LLRs calculés sont entrelacés individuellement, réordonnés et alimentés au MMSE SISO pour la prochaine itération.

Emetteur-récepteur FTN-OQAM précodé

Considérant, l'émetteur-récepteur FTN-OQAM précodé, deux sous-groupes de symboles sont transmis. Nous désignons par S_1 et P_1 l'ensemble des bits systématiques et de parité composant les symboles précodés. Nous utilisons le mapping des bits détaillé dans le

paragraphe précédent. Selon l'ordre de constellation envisagé, les bits entrelacés S_1 sont mappés aux positions hautement protégées du mapping Gray. Les positions restantes sont occupées par les P_1 bits entrelacés correspondants. De même, les ensembles S_2 et P_2 représentent les bits systématiques et de parité composant les symboles non précodés. Selon l'ordre de constellation utilisé, les bits entrelacés S_2 sont mappés aux positions avec le meilleur niveau de protection, tandis que les positions restantes contiennent les P_2 bits entrelacés. Enfin, les bits entrelacés sont convertis en symboles complexes et l'opération de précodage est effectuée par le module SIPC.
A la réception, il faut tenir compte de la réorganisation des LLRs à l'entrée et à la sortie du décodeur canal. Comme dans la section précédente, les LLRs des bits systématiques et de parité doivent être désentrelacés individuellement. Après l'étape de décodage, les nouveaux LLRs calculés des bits systématiques et de parité sont entrelacés séparément, réorganisés puis alimentés au module *SISO mapping*.

À partir des résultats de simulations, nous concluons que le mapping des bits proposé est recommandé pour des valeurs τ élevées pour les émetteurs-récepteurs précodés et non précodés. Les résultats ont montré une amélioration considérable de BER au détriment d'une augmentation du nombre d'itérations. Dans le chapitre précédent, nous avons montré que le précodage SIPC permet de diminuer le nombre d'itérations nécessaires. Compte tenu du mapping des bits proposé, le précodage permet toujours d'effectuer moins d'itérations au niveau du récepteur que l'émetteur-récepteur non précodé. Notez que le mapping Gray amélioré n'augmente pas la complexité, en termes de nombre d'opérations d'addition et de multiplication, des différents blocs de la chaîne de transmission. En fait, les modifications proposées n'impliquent que la réorganisation des bits et ne causent aucune complexité supplémentaire. L'augmentation de la complexité est uniquement due à l'augmentation du nombre d'itérations nécessaires.

Amélioration du mapping Symbols

Notre objectif dans cette section est de prendre en compte les interférences FTN lors du mapping des symboles OQAM aux positions en temps-fréquence. Classiquement, dans la modulation OFDM/OQAM, les parties réelles et imaginaires d'un symbole complexe $c_{m,n}$ sont transmises séparément avec un décalage temporel égal à $\frac{T_0}{2}$, tout en exigeant que deux symboles adjacents en temps et en fréquence ont une différence de phase égale à $\frac{\pi}{2}$. Le tableau 8 détaille la structure de transmission. Lorsque la modulation OFDM/OQAM

	$nT_0 - \frac{T_0}{2}$	nT_0	$nT_0 + \frac{T_0}{2}$
$(2m+1)F_0$	$c^{\Re}_{2m+1,n-1}$	$jc^{\Im}_{2m+1,n}$	$c^{\Re}_{2m+1,n+1}$
$2mF_0$	$jc^{\Im}_{2m,n-1}$	$c^{\Re}_{2m,n}$	$jc^{\Im}_{2m,n+1}$
$(2m-1)F_0$	$c^{\Re}_{2m-1,n-1}$	$jc^{\Im}_{2m-1,n}$	$c^{\Re}_{2m-1,n+1}$

TABLE 9: Schéma de transmission des symboles de la modulation OFDM/OQAM.

est combinée avec du FTN, des interférences sont introduites au signal transmis. Dans les chapitres précédents, nous avons montré que l'interférence due à FTN dépend de l'indice en temps des symboles transmis. Compte tenu de l'émetteur-récepteur FTN-OQAM représenté sur la Figure. 4, le symbole reçu à l'indice n_0 et sur la sous-porteuse

m_0 est:

$$y_{m_0,n_0} = a_{m_0,n_0} + \underbrace{\sum_{\substack{q=-l \\ q\neq 0}}^{l} h_q a_{m_0,n_0+q}}_{ISI} + \underbrace{\sum_{\substack{p=-l' \\ p\neq 0}}^{l'} \sum_{q=-l}^{l} l_{p,q,n_0} a_{m_0+p,n_0+q}}_{ICI_{n_0}},$$

où: $a_{m,n}$ sont les symboles OQAM transmis, les facteurs (l, l') définissent l'intervalle des symboles contribuant aux ISI et ICI, respectivement,

$$h_q = L\cos(\frac{\pi}{2}q)A_g[-qN_f, 0],$$

et

$$l_{p,q,n_0} = L\cos(\pi(\frac{p+q}{2} + \frac{2p(n_0N_f - \frac{D}{2})}{M}))A_g[-qN_f, -pb]$$

sont les canaux équivalents d'ISI et ICI, respectivement. L est la longueur de la forme d'onde g et A_g est sa fonction d'ambiguïté discrète. $D = L - 1$, M le nombre de sous-porteuses et N_f est le facteur FTN de décimation/expansion. Dans le chapitre 3, nous avons formulé la puissance d'interférence et nous avons montré qu'elle dépend du temps et est périodique. Sa période N_0 est exprimée par:

$$N_0(p, N_f) = \begin{cases} 1, & \text{si} \quad p = 0 \\ \frac{M}{2pN_f}, & \text{si} \quad p \neq 0 \quad \text{et} \quad \text{mod}(M, 2pN_f) = 0 \\ \frac{M}{\text{gcd}(M,2pN_f)} & \text{si} \quad p \neq 0 \quad \text{et} \quad \text{mod}(M, 2pN_f) \neq 0, \end{cases}$$

où p est l'indice des sous-porteuses. Indépendamment de p, nous définissons la période globale comme suit:

$$N_0^G = N_0(1, N_f)$$

Dans la Figure. 4, l'émetteur emploie un codage canal RSC et entrelace aléatoirement les bits codés. Ces bits sont ensuite convertis en symboles OQAM puis mappés en positions temps-fréquence. Par conséquent, les bits systématiques et de parité du même mot de code peuvent être tous les deux convertis en symboles et mappés sur des positions fortement influencées par les interférences. Pour remédier à ce problème, nous proposons d'abord d'entrelacer séparément les bits systématiques et de parité. Les bits entrelacés sont ensuite convertis en symboles OQAM. Enfin, nous plaçons les symboles composés de bits systématiques aux positions les moins affectées par les interférences et les symboles composés de bits de parité aux autres positions. Dans ce qui suit, nous présentons un nouveau mapping des symboles aux positions temps-fréquence pour l'émetteur-récepteur FTN-OQAM précodé et non précodé.

Emetteur-récepteur FTN-OQAM précodé

Nous considérons l'émetteur-récepteur FTN-OQAM précodé, représenté à la Figure. 7, et nous modifions les blocs Π et *bit-to-symbol mapping* comme illustré dans la Figure. 19. Nous gardons le même codeur RSC $(1, \frac{5}{7})$ avec le rendement de codage $r = \frac{1}{2}$. Le bloc *Channel coding* fournit $N_c = N_{c1} + N_{c2}$ bits codés, avec N_{c1} et N_{c2} le nombre de bits composant les symboles précodés et non précodés, respectivement. Nous désignons

par S_1 et S_2 les ensembles de bits systématiques des bits codés N_{c1} et N_{c2}, respectivement. De même, les ensembles P_1 et P_2 contiennent les bits de parité des N_{c1} et N_{c2} bits, respectivement. Tout d'abord, comme l'interférence est connue à l'émission, nous calculons sa puissance aux positions des symboles précodées. Ces positions sont ensuite triées en ordre croissant de leur puissance d'interférence et divisées en deux ensembles I_1 et I_2 de longueur égale. L'ensemble I_1 contient la première moitié de ces positions, tandis que l'ensemble I_2 contient l'autre moitié. Notez que les positions dans I_1 sont moins affectées par les interférences que les positions en I_2. Enfin, les S_1 bits sont entrelacés et convertis en symboles OQAM puis mappés successivement aux positions de I_1. De même, les symboles obtenus à partir des bits entrelacés en P_1 sont mappés aux positions dans I_2. D'autre part, nous calculons la puissance d'interférence aux positions des symboles non précodés. Ces positions sont triées en ordre croissant et divisées en deux ensembles J_1 et J_2 de longueur égale. De même, les symboles obtenus à partir de bits systématiques entrelacés S_2 sont mappés aux positions dans J_1, tandis que les symboles obtenus à partir de bits entrelacés P_2 sont mappés aux positions dans J_2. Enfin, le module SIPC annule les interférences causées par les symboles localisés aux positions en I_1 et I_2.

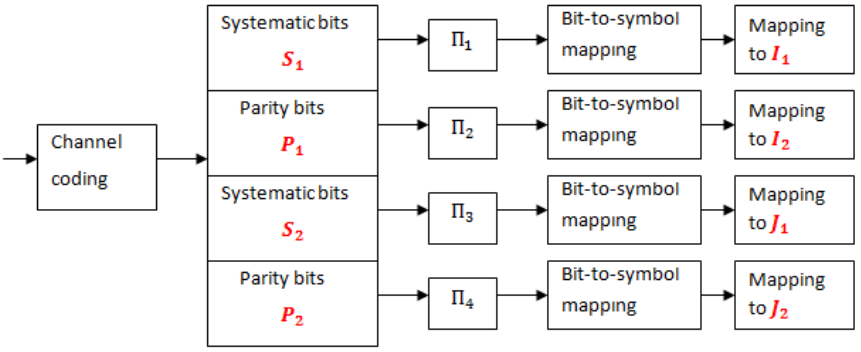

FIGURE 19: Le mapping des symboles proposé dans le cas de l'émetteur-récepteur FTN-OQAM précodé.

Précodage SIPC-t

Dans ce paragraphe, nous détaillons le mapping de symboles proposé dans le cas de l'émetteur-récepteur FTN-OQAM combiné avec la méthode de précodage SIPC-t. Les symboles précodés sont exprimés par:

$$c_{m,n} = a_{m,n} - \alpha\{\sum_{\substack{q=-k \\ q\neq 0}}^{k} h_q a_{m,n+q}\}.$$

Chaque sous-porteuse est composée de N_s symboles, avec N_s étant un multiple de la période N_0^G:

$$N_s = dN_0^G,\ d \in \mathbb{N}.$$

Nous considérons une sous-porteuse d'indice m et calculons la puissance d'interférence aux premiers indices temps de N_0^G. Ces N_0^G positions sont ensuite triées par ordre

croissant de leur puissance d'interférence. Considérons I l'ensemble des indices temps-fréquence (m,n) des symboles précodés, nous avons:

$$I = \{(m,n) :\ n = a \bmod(k+2) \quad et \quad n = a+1 \bmod(k+2),\ \ a \in \mathbb{N},\ a \leq k+1\},$$

avec $0 \leq n \leq N_0^G - 1$,$0 \leq m \leq M-1$, et:

$$I^G = \{(m,n) :\ n = n' + bN_0^G\ (m,n') \in I,\ b \in \mathbb{N},\ 1 \leq b \leq d-1\}$$

L'ensemble des indices triés de tous les symboles précodés. Comme le rendement de codage considéré est $r = \frac{1}{2}$, le bloc de bits systématiques et de parité est de longueur égale. Tout d'abord, les bits systématiques entrelacés S_1 sont convertis en symboles OQAM. Ces symboles sont ensuite mappés aux positions temps-fréquence dans l'ensemble I_1 défini par:

$$I_1 = \{(m,n) \in I^G,\ 0 \leq n \leq \frac{N_0^G}{2} - 1\}.$$

De même, les bits de parité entrelacés P_1 sont d'abord convertis en symboles OQAM puis mappés en positions temps-fréquence dans l'ensemble I_2 défini par:

$$I_2 = \{(m,n) \in I^G,\ \frac{N_0^G}{2} \leq n \leq N_0^G - 1\}.$$

Nous procédons de manière similaire pour les symboles non précodés. Considérons J l'ensemble des indices triés (m,n) des symboles non précodés avec:

$$0 \leq m \leq M-1, \quad \text{et} \quad 0 \leq n \leq N_0^G - 1,$$

et

$$J^G = \{(m,n) :\ n = n' + bN_0^G\ (m,n') \in J,\ b \in \mathbb{N},\ 1 \leq b \leq d-1\}$$

Les indices triés de tous les symboles non précodés. Les bits systématiques entrelacés S_2 sont convertis en symboles OQAM et ensuite mappés aux positions (m,n) dans l'ensemble J_1 défini comme suit:

$$J_1 = \{(m,n) \in J^G,\ 0 \leq n \leq \frac{N_0^G}{2} - 1\}.$$

Les bits de parité entrelacés P_2 sont convertis en symboles OQAM puis mappés aux positions temps-fréquence dans l'ensemble J_2 défini par:

$$J_2 = \{(m,n) \in J^G,\ \frac{N_0^G}{2} \leq n \leq N_0^G - 1\}.$$

Emetteur-récepteur FTN-OQAM non précodé

Le mapping des symboles proposé dans le cas de l'émetteur-récepteur FTN-OQAM est représenté sur la Figure. 20. Dans ce scénario, la puissance des interférences aux indices temps $0 \leq n \leq N_0^G - 1$ d'une sous-porteuse m est d'abord calculée. Ces positions sont ensuite classées par ordre croissant de leur puissance d'interférence. Nous définissons J comme:

$$J = \{(m,n) :\ 0 \leq m \leq M-1,\ 0 \leq n \leq N_0^G - 1\}$$

et

$$J^G = \{(m,n) : \ n = n' + bN_0^G, \ (m,n') \in J, \ b \in \mathbb{N}, \ 1 \leq b \leq d-1\}.$$

L'encodeur canal délivre des bits systématiques S et des bits de parité P qui sont entrelacés séparément. Ensuite, les bits entrelacés S sont convertis en symboles OQAM et mappés aux positions temps-fréquence dans l'ensemble J_1 défini par:

$$J_1 = \{(m,n) \in J^G, \ 0 \leq n \leq \frac{N_0^G}{2} - 1\}. \tag{2}$$

De même, les bits de parité entrelacés P sont d'abord convertis en symboles OQAM puis mappés aux positions temps-fréquence dans l'ensemble J_2 défini par:

$$J_2 = \{(m,n) \in J^G, \ \frac{N_0^G}{2} \leq n \leq N_0^G - 1\}.$$

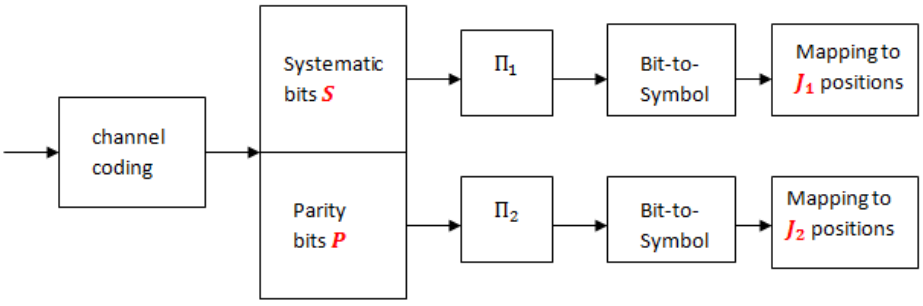

FIGURE 20: Le mapping des symboles proposé pour l'émetteur-récepteur FTN-OQAM.

Pour les deux émetteurs-récepteurs FTN-OQAM précodés et non précodés, certaines modifications doivent être prises en compte à la réception. Nous conservons le même récepteur turbo, où les LLRs sont échangés entre l'égaliseur et le décodeur. Après le *SISO demapping*, les LLRs des bits systématiques et de parité sont désentrelacés individuellement. Après le décodage, les nouveaux LLRs des bits systématiques et de parité sont entrelacés séparément, puis convertis en symboles par le module *SISO mapping*. Ces symboles sont ensuite mappés aux positions définies avant l'étape de l'égalisation.

À la lumière des résultats de simulation, nous concluons que le mapping des symboles proposé est recommandé dans le cas des modulations d'ordre élevé et des facteurs FTN faibles ce qui correspond au cas où les interférences induites par FTN sont plus sévères. En fait, le nouveau mapping de symboles donne de meilleurs résultats pour 16-QAM et avec $\tau = 0.7$ et 64-QAM avec $\tau = 0.8$ et ceci dans le cas précodé et non précodé.

L'évaluation BER du mapping des bits et des symboles proposés montre que les résultats dépendent du facteur FTN τ. Dans ce paragraphe, nous présentons la technique recommandée pour chaque émetteur-récepteur FTN-OQAM. Le tableau 9 résume les modifications recommandées pour l'émetteur-récepteur FTN-OQAM, ainsi que le nombre d'itérations nécessaires pour la convergence du récepteur. Comme mentionné précédemment, le mapping de symboles proposé améliore la performance de l'émetteur-récepteur pour des valeurs faibles de τ, alors que le mapping des bits proposé conduit à de meilleurs

résultats en cas de valeurs τ élevées.

Nous obtenons les mêmes conclusions en cas de l'émetteur-récepteur FTN-OQAM pré-

Ordre de constellation	τ	Formes d'ondes	Mapping recommandé	# d'itérations
16-QAM	0.7	FS	Symbols mapping	9
		PHYDYAS	Symbols mapping	9
		SRRC (ρ=0.5)	Symbols mapping	9
	0.8	FS	Bits mapping	6
		PHYDYAS	Bits mapping	6
		SRRC (ρ=0.5)	Bits mapping	6
	0.9	FS	Bits mapping	5
		PHYDYAS	Bits mapping	5
		SRRC (ρ=0.5)	Bits mapping	4
64-QAM	0.8	FS	Symbols mapping	9
		PHYDYAS	Symbols mapping	9
		SRRC (ρ=0.5)	Symbols mapping	9
	0.9	FS	Bits mapping	8
		PHYDYAS	Bits mapping	8
		SRRC (ρ=0.5)	Bits mapping	7

TABLE 10: Stratégies de mapping recommandées pour l'émetteur-récepteur FTN-OQAM.

codé, voir tableau 10. Le mapping des symboles proposé est recommandé pour les valeurs τ faibles, alors que le mapping des bits est recommandé en cas de valeurs τ élevées.

Ordre de constellation	τ	Formes d'ondes	Mapping recommandé	# d'itérations
16-QAM	0.7	PHYDYAS	Symbols mapping	8
	0.8	PHYDYAS	Bits mapping	6
	0.9	SRRC (ρ=0.5)	Bits mapping	3
64-QAM	0.8	PHYDYAS	Symbols mapping	8
	0.9	PHYDYAS	Bits mapping	7
		SRRC (ρ=0.5)	Bits mapping	5

TABLE 11: Stratégies de mapping recommandées pour l'émetteur-récepteur FTN-OQAM avec le précodage SIPC-t.

Chapitre 6

Notre travail a été motivé par l'augmentation constante du volume de données mobiles ce qui contraint les futurs systèmes radio à inclure des modulations avancées/formes d'onde offrant des débits de données plus élevés avec une utilisation plus efficace de la bande passante. Une possibilité est d'améliorer les systèmes de transmission numérique classiques Nyquist en signalant plus rapidement que la cadence de Nyquist. Les transmissions FTN ont été initialement introduites par Mazo comme un moyen d'améliorer l'efficacité spectrale. Il a déclaré que le taux de transmission n'est pas nécessairement limité par le critère de Nyquist, ce qui signifie qu'une cadence de transmission plus rapide peut être

envisagée à condition que les interférences soient acceptées. L'objectif principal de ma thèse était de définir et d'évaluer un nouveau mode de transmission impliquant la signalisation FTN avec la modulation OFDM/OQAM pour augmenter le débit de transmission.

Dans cette dissertation, nous nous sommes surtout concentrés sur les systèmes OFDM/OQAM signalant à une cadence plus rapide que Nyquist. Les principales contributions de notre travail ont impliqué une nouvelle implémentation efficace d'un émetteur-récepteur FTN à l'aide de la modulation OFDM/OQAM (chapitre 3), une nouvelle technique de précodage visant à réduire les interférences FTN du côté de l'émetteur (chapitre 4) et la proposition d'une amélioration de l'émetteur-récepteur FTN-OQAM (chapitre 5).

Le premier travail concernant les émetteurs-récepteurs FTN-OQAM a été présenté dans [2]. Cependant, la complexité de leur solution augmente par rapport aux systèmes OFDM/OQAM traditionnels en raison des blocs liés au FTN introduits. En outre, leur récepteur s'appuie sur l'algorithme MAP, ce qui signifie que sa complexité augmente avec l'ordre de modulation. Dans le chapitre 3, nous avons étudié le concept de signalisation FTN combiné avec la modulation OFDM/OQAM à travers un canal AWGN. Notre objectif est de proposer une nouvelle implémentation du FTN approchant le débit de transmission théorique promis par FTN sans augmentation de la complexité comparé aux systèmes classiques. Contrairement à la solution de l'état de l'art, nous avons proposé un récepteur turbo basé sur l'égalisation MMSE linéaire. La complexité de ces égaliseurs dépend uniquement de la réponse impulsionnelle du canal et est indépendante de l'ordre de modulation ce qui les rend bon candidats si des ordres de constellation élevés sont envisagés. Étant donné que la modulation OFDM/OQAM emploie différentes formes d'onde ayant différentes propriétés de localisation temps-fréquence, nous avons montré que l'égaliseur MMSE devrait mieux fonctionner selon l'axe temporel lorsque le filtre prototype est bien localisé en temps et vice-versa. En outre, nous avons proposé un algorithme basé sur l'analyse EXIT pour étudier le plus petit facteur FTN que l'émetteur-récepteur FTN-OQAM peut atteindre tout en offrant une performance BER proche de Nyquist. Contrairement à la solution de l'état de l'art, nous avons ciblé des ordres de modulation élevés et nous avons montré qu'une amélioration du débit de 11 % est réalisable, en cas de la modulation 64-QAM, avec une performance très proche de Nyquist et après avoir effectué seulement 5 itérations à la réception. Nous avons également montré que l'amélioration du débit peut aller jusqu'à 25 % avec la modulation 16-QAM au coût d'une perte de 1 dB autour d'un BER de 10^{-4} par rapport à la performance de Nyquist alors que seulement 4 itérations sont nécessaires à la réception.

Lors d'une signalisation plus rapide que Nyquist, l'orthogonalité des filtres n'est plus valide et des interférences sont intentionnellement ajoutées au signal transmis même lors de la transmission sur un canal AWGN. Au chapitre 3, nous avons fourni une expression analytique de cette interférence et avons montré qu'elle peut être modélisée par un canal d'interférence équivalent. Cependant, cette interférence est parfaitement connue à la fois par l'émetteur et par le récepteur qui est similaire aux transmissions à travers des canaux multi-trajets avec une parfaite CSI à l'émission. Au chapitre 4, nous avons étudié un nouveau système de précodage, pour éliminer les interférences induites par le FTN à l'émission. Compte tenu de la nature de cette interférence, il est difficile de précoder conjointement tous les symboles transmis. Par conséquent, nous avons proposé de supprimer les interférences uniquement d'un sous-groupe des symboles transmis, d'où

la nature disperse de notre méthode. À cette fin, nous avons introduit trois familles de précodeurs en fonction de l'annulation de l'ISI et/ou de l'ICI. Les récepteurs correspondants décodent d'abord les symboles précodés, puis les symboles non précodés. Notre objectif principal était d'améliorer le décodage des symboles précodés et de supprimer leur contribution aux interférences avec les symboles non précodées avant de décoder ces derniers. Un gain significatif peut être obtenu grâce au précodage proposé, en particulier dans le cas des modulations d'ordres élevés et de faibles facteurs FTN. Étant donné que moins d'interférence est introduite aux symboles transmis, l'analyse EXIT a montré que le tunnel entre l'égaliseur et le décodeur est maintenant plus large par rapport au scénario FTN-OQAM non précodé, ce qui signifie que l'échange d'information mutuelle entre l'égaliseur et Le décodeur est amélioré. Ceci est confirmé par le fait que moins d'itérations sont nécessaires à la réception. En outre, un gain important en termes de BER est obtenu pour des modulations d'ordre élevé et des facteurs FTN faibles (les résultats ont été donnés pour 16-QAM avec $\tau = 0.7$ et 64-QAM avec $\tau = 0.8$).

Notre objectif dans le chapitre 5 était d'améliorer les différents blocs de l'émetteur-récepteur FTN-OQAM pour tenir compte de l'interférence introduite par FTN. Les modifications proposées concernent le codeur canal, le mapping bits en symbols et le mapping des symboles aux positions temps-fréquence. Pour l'émetteur-récepteur FTN-OQAM précodé, les symboles précodés et non précodés présentent différents BER car ils sont affectés différemment par les interférences. Ainsi, nous avons proposé d'adapter le codeur canal en utilisant différents rendements de codage locaux, pour coder les symboles précodés et non précodés, tout en maintenant le rendement de codage initial inchangé. Nous avons montré qu'un gain important est obtenu en cas d'ordres de modulation élevés et de faibles facteurs FTN (16-QAM avec $\tau = 0.7$ et 64-QAM avec $\tau = 0.8$) lorsqu'on utilise un code fort pour coder les symboles précodés. Deuxièmement, nous avons proposé de profiter des différents niveaux de protection des bits dans le mapping Gray en cas des modulations d'ordre élevé. Comme le codage canal est basé sur des codes convolutifs, nous avons proposé de réorganiser les bits codés pour placer les bits d'information aux positions hautement protégées et les bits de redondance aux positions les moins protégées. Le nouveau mapping des bits a permis une amélioration significative du BER pour les facteurs FTN élevés: $0.8 \leq \tau$ pour la modulation 16-QAM et $\tau = 0.9$ pour la modulation 64-QAM. Enfin, nous avons proposé un nouveau mapping des symboles aux positions temps-fréquence différent de celui du mapping classique utilisé par la modulation OFDM/OQAM. Nous avons proposé un mapping des symboles composés de bits d'information aux positions temps-fréquence qui sont moins affectées par les interférences et de placer les symboles composés des bits de redondance aux positions restantes. Notre méthode a permis d'améliorer le BER pour des modulations d'ordres élevés (16 et 64-QAM) et des facteurs FTN faibles (τ = 0,7 et 0,8, respectivement).

Publications et brevets

Au cours de ma thèse, j'ai publié trois articles de conférence et déposé deux brevets comme indiqué ci-dessous. Je rédige également un article de journal décrivant la nouvelle implémentation proposée du FTN avec les systèmes OFDM/OQAM et le précodage SIPC.

Articles de conférences

H. Lin, N. Lahbabi, P. Siohan and X. Jiang, “An efficient FTN implementation of the OFDM/OQAM system ", ICC’15, London, UK, June 2015, pp.4787-4792.

N. Lahbabi, H. Lin, C. Abdel Nour, C. Douillard and P. Siohan, “Sparse Interference Pre-Cancellation for FTN-OQAM systems ", EW’16, Oulu, Finland, May 2016, pp. 1-6.

N. Lahbabi, H. Lin, C. Abdel Nour, C. Douillard and P. Siohan, “An enhanced coding strategy for FTN-OFDM/OQAM transceiver design ", ICC’17, Paris, France, May 2017.

Brevets

N. Lahbabi, H. Lin and P. Siohan, “ Pré-annulation dispersée des interférences pour les transmissions FTN. " 2015. Reference N° R27445FR.

N. Lahbabi, H. Lin, C. Abdel Nour, C. Douillard and P. Siohan, “ Optimisation de la pré-annulation dispersée des interférences pour les transmissions FTN" 2016. Reference N° R28751FR.

Chapter 1

Introduction

The recent growth of mobile cellular and broadband subscriptions is mainly driven by the invention of mobile smartphones and tablets computers. The consumed mobile media shows an increasing usage of data-intensive applications such as live video streaming or TV, social networking and web browsing. On-demand information and real-time entertainment will be progressively provided over mobile and wireless communication systems. These heavy-data applications will lead to an avalanche of mobile data volume. Most smartphones can already accommodate data rates that exceed the networks' capabilities [4]. According to the Cisco Visual Networking Index [5], global mobile data traffic grew 63 percent in 2016 and will represent 20 percent of the total IP traffic by 2021 reaching 49 ExaBytes per month by 2021. In the future, wireless networks will face more congestion problems than today [6]. Further, it is predicted that the so-called Internet of Things will complement the human-centric communications by connecting a tremendous number of devices. According to [5], there will be 11.6 billion mobile-connected devices by 2021, including Machine-to-Machine (M2M) modules, exceeding the world's projected population at that time. Therefore, future wireless systems are constrained to provide advanced solutions offering higher data rates with efficient bandwidth usage.

Today's Long Term Evolution (LTE) networks promise peak download data rates of 100 Mb/s, which is more than 10 times faster than the rates of third generation (3G) standards, while making more efficient usage of the radio spectrum. LTE relies on advanced technologies to achieve these targets, such as Orthogonal Frequency Division Multiplexing (OFDM), Multiple Input Multiple Output (MIMO) systems and advanced channel coding. However, due to the exponential increase of wireless devices, the offered data rates may not keep up with the increasing consumers demands of multimedia contents. Since the beginning of 2010, the research community has been looking beyond fourth generation (4G) and into fifth generation (5G) technologies through collaborative projects such as METIS [7] and 5GNOW [8]. And more recently, standardization body, e.g. 3GPP, has also started to study 5G-oriented solutions. 5G is expected to be deployed around 2020 and will have to support multimedia applications with a wide variety of requirements including higher peak and user data rates, reduced latency and improved energy efficiency [9].

Nyquist signaling rate

The modern digital communication systems generally rely on Nyquist pioneering works dating back to 1924 [10] and 1928 [11]. Nyquist has formulated the baseband model for data transmission over continuous-time bandlimited channels. The transmitted continuous-time baseband signal can be expressed as:

$$s(t) = \sum_{n} x[n]g(t - nT), \tag{1.1}$$

where $x[n]$ are modulating symbols, g the modulating pulses which are assumed to be bandlimited to W Hertz and T the symbol duration. The modulating pulses can overlap in time as long as they remain orthogonal to one another. Nyquist stated that, in order to achieve interference-free transmission, the maximal signaling rate $\frac{1}{T}$ is given by $2W$ pulses per second. This rate, referred to as the Nyquist rate, ensures a simple receiver architecture based on a matched filter to the modulating pulse and a sampler at Nyquist rate [12], [13]. This receiver is known to maximize the Signal to Noise Ratio (SNR) when transmitting over Additive White Gaussian Noise (AWGN) channel. Most current digital communication systems are based on the Nyquist criterion.

Faster than Nyquist signaling

Although the Nyquist criterion ensures pulses orthogonality to avoid Inter-Symbol Interference (ISI), bandwidth efficiency is sacrificed to guarantee such orthogonality. Faster-Than-Nyquist (FTN) systems allow the transmission of data beyond the Nyquist rate, provided that ISI is tolerated. Even if interference is intentionally introduced to the transmitted signal, sophisticated algorithms should be envisaged at the receiver to deal with it. Actually, the question of whether signaling faster than the Nyquist rate is of any merit has attracted many researchers in the past years: [14], [15], [16]. However, the concept was not deemed as an attractive means until the trend of the explosion of throughput requirements becomes unavoidable. This is mainly attributed to the complex processing necessary to deal with the interference introduced by FTN signaling.

Because of the declining cost of processing units, the importance of bandwidth resources and spectrally efficient solutions overcame the amount of processing required. In fact, advances in semiconductor technology allow the number of transistors in integrated circuits to double every 18 months (a phenomenon referred to as the Moore's law [27]). Additionally, the density of the memory storage has been observed to increase at even a faster rate (known by the Kryder's law [28]). Moreover, important advancement in signal processing and coding have been achieved in the past years. Consequently, the available data and signal processing ability enables to practically implement advanced channel coding and equalization techniques to deal with the interference caused by FTN signaling. Hence, the concept of FTN transmissions has been recently re-investigated and is now deemed being worthy for further investigation.

Thesis contributions and structure

This dissertation is motivated by the combination of FTN signaling with Multi Carrier Modulations (MCM). FTN systems using OFDM modulation were discussed in [17].

Although this modulation is widely used in modern digital communication systems, our work focused on an attractive alternative to OFDM known as OFDM with Offset Quadrature Amplitude Modulation (QAM) and denoted here by OFDM/OQAM [18]. This is mainly because OFDM/OQAM modulation does not necessitate the insertion of a Cyclic Prefix (CP), reaching therefore a full Nyquist rate. Further, OFDM/OQAM modulation, also often now named Filter Bank MultiCarrier (FBMC)/OQAM, can be equipped by different modulating pulses having different time-frequency localization properties. However, the findings from this report are not exclusive to OFDM/OQAM waveform. Instead, they can be well extended to other waveforms including OFDM. The FTN concept was originally introduced to pack the transmitted signals closer in time domain, with respect to the Nyquist rate [19]. The extension of the FTN concept to MCM was discussed in [20], where the authors showed that the signals can be packed closer both in time and frequency domains. The concept is referred to as the two-dimensional Mazo limit. In this dissertation, we consider the transmission of independent and identically distributed (i.i.d) signals over AWGN channel and assume that the FTN concept is only applied in time domain.

The goal of this dissertation is to first study a new efficient FTN implementation of the OFDM/OQAM system which allows to switch flexibly from Nyquist to FTN mode with limited complexity increase compared to OFDM/OQAM systems, while approaching very closely the theoretical rate growth promised by the FTN concept. Although the signals are only packed closer in time domain, both ISI and Inter Carrier interference (ICI) are intentionally added to the transmitted signals, which calls for more complex algorithms at the receiver end. The FTN transceiver was originally based on non-linear Maximum *A Posteriori* (MAP) sequence detection algorithm [21], [3] which achieves good performance. However the complexity is exponentially proportional to the constellation orders. Supporting higher constellations is an important request for high throughput transmission. But in the state of the art, only low constellations, basically Binary Phase Shift Keying (BPSK) or Quadrature Phase Shift Keying (QPSK), are assumed. Therefore, supporting high constellations in FTN systems is an open issue. An intuitive way of reducing the complexity for high constellation transmission is to consider linear equalization which should be independent of the constellation. Consequently, we proposed a turbo-like receiver based on Linear Minimum Mean Square Error (LMMSE) equalization and interference cancellation to deal with FTN-induced interference. By reducing the equalization complexity, we quickly found out that the performance is degraded accordingly, especially at the first iteration. In consequence, reducing the equalization complexity comes at the cost of more iterations to cancel the intrinsic interference, which leaves the previous open issue still open. We identified that the degradation was mainly due to the inefficient symbol detection from the LMMSE at the first iteration. To improve this, there could be two directions: 1) apply MAP equalization for only the 1^{st} iteration, however, the complexity for conducting MAP algorithm remains an issue as stated previously and this solution does not fully address our design target. 2) Imbalance the interference level to make some of the symbols experience less interference than the others. Thus for those less affected symbols, LMMSE equalizer can provide a better estimation, with which the overall turbo-equalization may run more efficiently. As FTN-self interferences are intentionally introduced, they are perfectly known by both the transmitter and the receiver. The first contribution of this thesis is the proposal of new precoding schemes to reduce this interference in order to improve the performance of the FTN-OQAM transceiver. We further identified that the

channel coding could be jointly optimized with the interference imbalance pattern that we intentionally created. This is the second contribution of this thesis. Finally, we found out that FTN-induced interference is not equivalently distributed among the transmitted symbols. The third contribution of this thesis is the proposal of a new mapping of symbols to time and frequency positions to balance the distribution of interference.

The rest of this dissertation is organized as follows. Chapter 2 provides a brief introduction to OFDM and OFDM/OQAM modulations followed by the basic knowledge related to FTN signaling. In addition, we provide a chronological literature survey of the FTN concept presenting the related FTN research followed by an overview of important concepts regarding channel coding, turbo equalization and precoding. In chapter 3, we introduce a new implementation of FTN signaling for OFDM/OQAM systems. The structure of the modulator and the demodulator is first detailed. Then, we provide the analytical expression of FTN-self interference and deduce the expression of the discrete equivalent channel. Further, we present a turbo-like receiver which is based on a soft linear equalizer and a soft channel decoder. In addition, we present an algorithm to investigate the minimum achieved packing factor without performance loss compared to Nyquist-based systems. The algorithm is based on the EXtrinsic Information Transfer (EXIT) chart analysis of the turbo-receiver. Finally, we evaluate the performance of our FTN-OQAM transceiver in terms of Bit Error Rate (BER) vs. SNR and deduce the recommended pulse shapes for each modulation order and FTN packing factor. In chapter 4, we present a new precoding scheme, called Sparse Interference Pre-Cancellation (SIPC), to combine with the FTN-OQAM transceiver. Our objective is to take into account the transmitter knowledge about FTN-induced interference in order to reduce it and to improve the transceiver performance. To this end, we introduce three families of precoders aiming at reducing ISI and/or ICI at the transmitter side along with the corresponding receivers. Due to the nature of FTN interferences, it is difficult to jointly remove ISI and/or ICI from all the transmitted symbols. Therefore the proposed precoders remove the interference from only a sub-group of the transmitted symbols, while keeping the rest of the OQAM symbols unchanged. Finally, we evaluate the BER performance of the proposed precoders and highlight the benefits of the SIPC precoding. In chapter 5, we introduce several modifications to the FTN-OQAM transceiver. First, we propose a channel coding rate adaptation to improve the precoded FTN-OQAM transceiver by employing different local coding rates to encode the precoded and non-precoded symbols. This is motivated by the fact that the precoded and non-precoded symbols exhibit different BER. Secondly, we modify the Gray bit mapping to take into account the different bit level protections of the Gray mapping. Finally, we propose a new mapping of OQAM symbols to time and frequency positions different from the classical mapping used by OFDM/OQAM modulation. Chapter 6 provides a summary of our work achievements and directions for future work.

Publications and patents

During my Ph. D program, I have published three conference papers an filed two patents as listed below. I am also writing a journal paper describing the proposed FTN implementation of OFDM/OQAM systems and SIPC precoding.

Conference papers

H. Lin, N. Lahbabi, P. Siohan and X. Jiang, “An efficient FTN implementation of the OFDM/OQAM system ", ICC’15, London, UK, June 2015, pp.4787-4792.

N. Lahbabi, H. Lin, C. Abdel Nour, C. Douillard and P. Siohan, “Sparse Interference Pre-Cancellation for FTN-OQAM systems ", EW’16, Oulu, Finland, May 2016, pp. 1-6.

N. Lahbabi, H. Lin, C. Abdel Nour, C. Douillard and P. Siohan, “An enhanced coding strategy for FTN-OFDM/OQAM transceiver design ", ICC’17, Paris, France, May 2017.

Patents

N. Lahbabi, H. Lin and P. Siohan, “ Pré-annulation dispersée des interférences pour les transmissions FTN. " 2015. Reference N° R27445FR.

N. Lahbabi, H. Lin, C. Abdel Nour, C. Douillard and P. Siohan, “ Optimisation de la pré-annulation dispersée des interférences pour les transmissions FTN" 2016. Reference N° R28751FR.

Chapter 2

State of the Art and Background

2.1 Introduction

Our main objective in this chapter is to provide preliminary requirements for the study of Faster-Than-Nyquist (FTN) signaling and its association with OFDM/OQAM modulation and advanced channel coding and precoding techniques. First, we briefly introduce two widely used multi-carrier modulation technologies: OFDM and OFDM/OQAM modulations. Secondly, we present a chronological survey of FTN solutions presented in the literature. In the last section, we review some concepts of channel coding and turbo codes. Moreover, the concept of turbo equalization applied to Inter Symbol Interference (ISI) channels is also presented. Finally, the well known Tomlinson-Harashima precoding is reviewed.

2.2 OFDM

Orthogonal Frequency Division Multiplexing (OFDM) is a Multi-Carrier Modulation (MCM) technology widely used in both wired systems (such as Asymmetric Digital Subscriber Line ADSL) and wireless systems [29], [30]. It has been adopted by many wireless applications such as Digital Video Broadcasting (DVB), Digital Audio Broadcasting (DAB), Wireless Local Area Networks (WLANs) and Long Term Evolution standard (LTE). OFDM modulation, which is a particular case of multi-carrier transmission, is considered as an attractive means in case of frequency selective channels and high data rates. This modulation technique transforms a frequency selective wide-band channel into a group of flat narrowband subchannels, while preserving orthogonality in the frequency domain, which makes OFDM robust against large delay spreads.

When transmitting high-rate information serially, inter-symbol interferences occur when the symbol duration is smaller than the channel delay spread. The mitigation of ISI necessitates a complex equalization procedure. The equalization complexity grows with the channel memory. In OFDM, the high rate information stream is split into M-rate subcarriers. Therefore, data is transmitted by blocks of size M: $s_k = [s_k(0), ..., s_k(i), ...s_k(M-1)]^T$, where subscript k is the index of the OFDM symbol block, i is the subcarrier index and $[.]^T$ denotes the vector (matrix) transpose. The M parallel data streams are

first modulated and then processed by an Inverse Fast Fourier Transform (IFFT), which yields to the time domain vector $x_k = [x_k(0), ..., x_k(i), ...x_k(M-1)]^T$ of size M.

To avoid the impact of ISI, OFDM modulation inserts a guard interval at the beginning of each OFDM symbol. A Cyclic Prefix (CP) is generated by duplicating the last G samples of the IFFT output and appending them at the beginning of each OFDM symbol [22]. This version of OFDM is named CP-OFDM modulation. Therefore, the time domain vector x_k is transformed into: $[x_k(M-G), ...x_k(M-1), x_k(0), ..., x_k(i), ...x_k(M-1)]^T$. To eliminate ISI, the CP length must be longer than the longest channel impulse response. After Parallel to Serial (P/S) and Digital to Analog Conversion (DAC), the signal is sent through the frequency selective channel.

At the receiver side, the CP-OFDM signal is demodulated using the reverse operations. The first G samples are discarded to suppress the inter-block interference. Adding the CP at the transmitter transforms the multipath linear convolution into a circular one, which is converted by a Fast Fourier Transform (FFT) to a multiplicative operation in the frequency domain. Consequently, OFDM reduces the complexity to only one FFT and one-tap scalar equalization at the receiver.

Although OFDM has been widely used in radio-communications, it suffers from several drawbacks. In fact, the CP insertion reduces the bandwidth efficiency of the system, since it carries redundant information. In addition, the use of the Sinc pulse shape in the frequency domain leads to poor power spectrum localization which causes large Inter Carrier Interference (ICI) and makes OFDM modulation vulnerable to Carrier Frequency Offset (CFO). Moreover, the transmitted signals in an OFDM system can have high peak values in the time domain since many subcarrier components are added via the IFFT. As a result, OFDM systems are known to have high Peak-to-Average Power Ratio (PAPR) when compared to single-carrier systems. The high PAPR represents one of the most disadvantages of OFDM systems as it requires complex High Power Amplifier (HPA) operating on a very large linear range at the transmitter. Otherwise, the nonlinearity of the HPA leads to in-band distortion, which increases the Bit Error Rate (BER) of the system, and out-of-band distortion, which introduces high adjacent channel interference [31].
Let us consider the discrete-time baseband OFDM signal:

$$x_n = \frac{1}{\sqrt{M}} \sum_{k=0}^{M-1} s_k e^{\frac{j2\pi kn}{M}}, \qquad 0 \leq n \leq M-1 \tag{2.1}$$

where M is the number of subcarriers and n is the discrete time index. The PAPR of an OFDM signal is defined as the ratio between its maximum and its average power as [31]:

$$PAPR(x) = 10\log_{10} \frac{\max\{|x_n|^2\}}{E\{|x|^2\}}, \qquad 0 \leq n \leq M-1 \tag{2.2}$$

where $E\{.\}$ denotes the expected value operation, $x = [x_0, ..., x_{M-1}]^T$ and $|.|$ is the signal magnitude.

2.3 OFDM/OQAM

Another alternative to OFDM modulation is OFDM with Offset Quadrature Amplitude Modulation (QAM), or OFDM/OQAM in short. Unlike OFDM, which uses rectangular pulse shape in time domain, OFDM/OQAM has the flexibility of using various pulse shapes with different time-frequency localization properties. This makes OFDM/OQAM less sensitive to the frequency offset caused by the transmission channel and the receiver. Moreover, OFDM/OQAM does not use any CP, hence being more spectrally efficient than OFDM. The first studies related to OFDM/OQAM were presented in [23] and [24]. In [23], [24], their authors introduced a time-offset on each sub-carrier to transmit Pulse Amplitude Modulation (PAM) and QAM constellations, respectively. For the latter, a time shift between the real and imaginary parts is introduced. In [25], the authors highlighted the importance of time-frequency localization features of the prototype filters when transmitting over time-frequency dispersive channels. Some optimized prototype functions other than the rectangular function were also presented. From the signal processing perspective, the link to digital filter banks was first initiated in [32] and then carried out in [33],[18], [1] where the authors presented an implementation design in case of discrete-time prototypes. Hence, OFDM/OQAM is usually referred to as Filter Bank MultiCarrier (FBMC)/OQAM modulation.

2.3.1 Continuous OFDM/OQAM

OFDM modulation consists in transmitting a complex symbol $c_{m,n} = c^{\Re}_{m,n} + jc^{\Im}_{m,n}$ of duration T_0 at time instance n, i.e., nT_0 and frequency m, i.e., mF_0, with $F_0 = \frac{1}{T_0}$ the subcarrier spacing and $j^2 = -1$. The particularity of OFDM/OQAM is to transmit either the real or the imaginary part of the complex symbol $c_{m,n}$ with a time offset equal to $\frac{T_0}{2}$. Moreover, a phase shift of $\frac{\pi}{2}$ is introduced between two adjacent symbols in time and frequency. Assuming an even number of subcarriers M, the baseband continuous OFDM/OQAM signal is [34], [1]:

$$\begin{aligned} s(t) &= \sum_{n=-\infty}^{+\infty}\sum_{m=0}^{N-1}(c^{\Re}_{2m,n}g(t-nT_0) + jc^{\Im}_{2m,n}g(t-\frac{T_0}{2}-nT_0)e^{j2\pi(2m)F_0t} \\ &\quad +(jc^{\Im}_{2m+1,n}g(t-nT_0) + c^{\Re}_{2m+1,n}g(t-\frac{T_0}{2}-nT_0))e^{j2\pi(2m+1)F_0t} \end{aligned} \tag{2.3}$$

where $N = M/2$ and g is a symmetrical real-valued pulse shape. By setting:

$$a_{2m,2n} = c^{\Re}_{2m,n}, \qquad g_{2m,2n}(t) = g(t-nT_0)e^{j2\pi(2m)F_0t} \tag{2.4}$$

$$a_{2m,2n+1} = c^{\Im}_{2m,n}, \qquad g_{2m,2n+1}(t) = jg(t-nT_0-\frac{T_0}{2})e^{j2\pi(2m)F_0t} \tag{2.5}$$

$$a_{2m+1,2n} = c^{\Im}_{2m+1,n}, \qquad g_{2m+1,2n}(t) = jg(t-nT_0)e^{j2\pi(2m+1)F_0t} \tag{2.6}$$

$$a_{2m+1,2n+1} = c^{\Re}_{2m+1,n}, \qquad g_{2m+1,2n+1}(t) = g(t-nT_0-\frac{T_0}{2})e^{j2\pi(2m+1)F_0t} \tag{2.7}$$

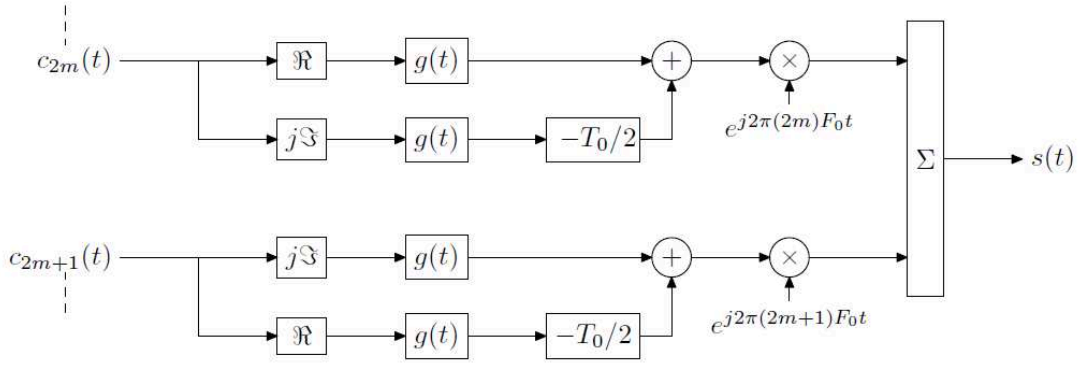

FIGURE 2.1: Analogue OFDM/OQAM modulator [1].

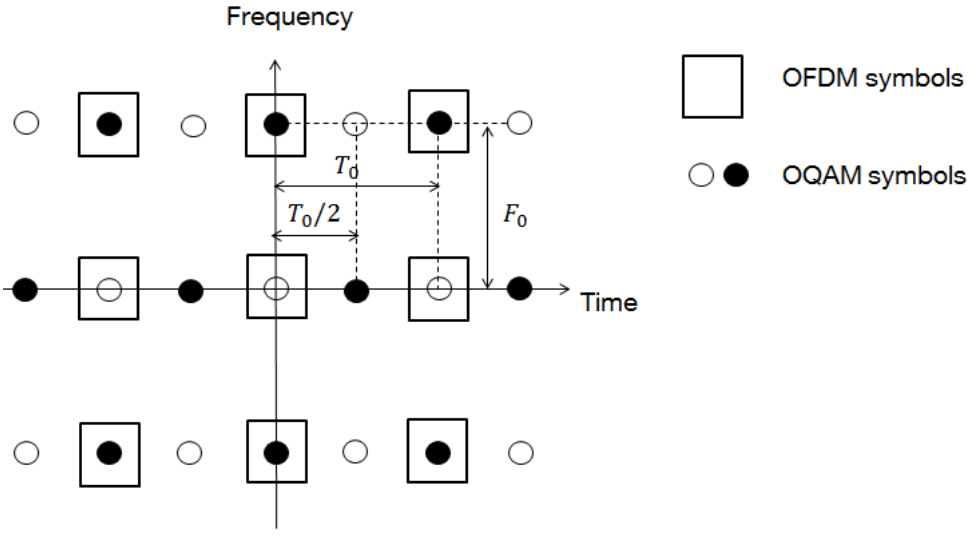

FIGURE 2.2: Time-frequency lattice representation of OFDM and OFDM/OQAM.

and considering a phase term $\Phi_{m,n}$ such as:

$$\Phi_{m,n} = \begin{cases} 0, \text{if } m \text{ and } n \text{ have the same parity,} \\ \frac{\pi}{2}, \text{if } m \text{ and } n \text{ are of different parities,} \end{cases}$$

the signal $s(t)$ in (2.3) can be reformulated as:

$$s(t) = \sum_{n=-\infty}^{+\infty} \sum_{m=0}^{M-1} a_{m,n} g_{m,n}(t), \tag{2.8}$$

where,

$$g_{m,n}(t) = g(t - n\frac{T_0}{2}) e^{j2\pi m F_0 t} e^{j\Phi_{m,n}}. \tag{2.9}$$

The structure corresponding to (2.3) is represented in Fig. 2.1. The real-valued symbols $a_{m,n}$, obtained by taking the real and imaginary parts of the complex valued $c_{m,n}$, have staggered positions.

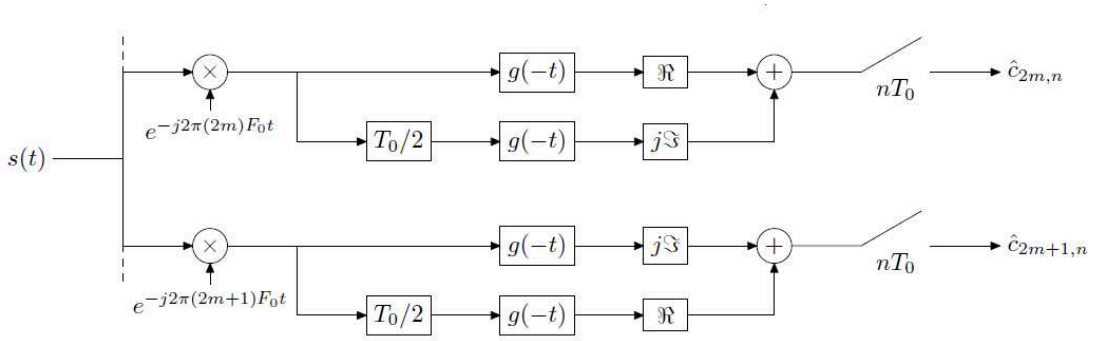

FIGURE 2.3: Analogue OFDM/OQAM demodulator [1].

Fig. 2.2 represents the time-frequency lattice for both OFDM and OFDM/OQAM transmission schemes. In case of OFDM, complex QAM symbols are placed at positions (nT_0, mF_0), having therefore a density $\rho = \frac{1}{F_0T_0} = 1$. In case of OFDM/OQAM transmission, each real-valued symbol is placed at $(n\frac{T_0}{2}, mF_0)$. In fact, the solid circles represent the symbols having $\frac{\pi}{2}$ phase offset with regard to the in-phase ones represented by hollow circles. Although OFDM/OQAM seems to increase the density to 2, it actually has the same density as OFDM transmission without the CP. On the other hand, since OFDM/OQAM separately transmits the real and imaginary parts of QAM symbols, the orthogonality constraint is relaxed to only the real-domain. This provides more degrees of freedom for designing orthogonal prototype filters with good time-frequency localization properties.

At the demodulator's output of Fig. 2.3, symbols are estimated as:

$$\hat{c}^{\Re}_{2m,n} = \Re \int_{-\infty}^{+\infty} s(t) g^*_{2m,2n}(t) dt \tag{2.10}$$

$$\hat{c}^{\Im}_{2m,n} = \Im \int_{-\infty}^{+\infty} s(t) g^*_{2m,2n+1}(t) dt \tag{2.11}$$

$$\hat{c}^{\Im}_{2m+1,n} = \Im \int_{-\infty}^{+\infty} s(t) g^*_{2m+1,2n}(t) dt \tag{2.12}$$

$$\hat{c}^{\Re}_{2m+1,n} = \Re \int_{-\infty}^{+\infty} s(t) g^*_{2m+1,2n+1}(t) dt \tag{2.13}$$

Indeed, equations (2.10) to (2.13) show that the orthogonality constraint in the complex domain is no longer needed.

2.3.2 Discrete OFDM/OQAM

In this section, we briefly introduce the discrete-time version of OFDM/OQAM and its implementation. According to [1], [18], the baseband discrete-time modulated signal is:

$$s[k] = \sum_{m=0}^{M-1} \sum_{n \in Z} a_{m,n} g[k - nN] e^{\frac{j2\pi m(k-\frac{D}{2})}{M}} e^{j\Phi_{m,n}}, \tag{2.14}$$

with

$$\Phi_{m,n} = \Phi_0 + \frac{\pi}{2}(m+n) \mod(\pi), \tag{2.15}$$

and mod stands for the modulo operation. $D = L - 1$, with L the length of the pulse shape g. As shown in [1], L can be either an odd or an even integer. $N = \frac{M}{2}$ is the discrete-time offset. $\Phi_{m,n}$ is the additional phase term and Φ_0 is arbitrarily chosen. The transmitted symbols $a_{m,n}$ are real-valued and obtained from a 2^{2K}-QAM constellation by taking the real and the imaginary parts of the complex symbols.

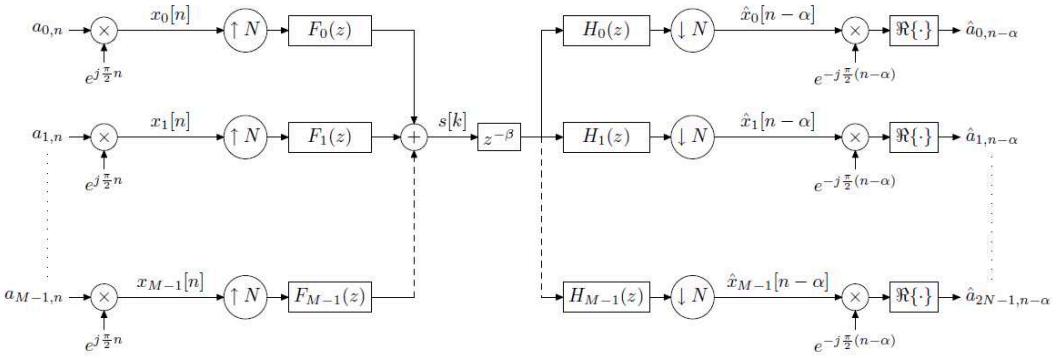

FIGURE 2.4: Discrete-time structure of OFDM/OQAM system.

Assuming that g has unit energy, the derivation of the transmultiplexer (TMUX) in [18] leads to the following expressions of the synthesis and analysis filter banks:

$$f_m[k] = g[k] e^{j\frac{2\pi}{M} m(k - \frac{D-N}{2})}, \tag{2.16}$$

$$h_m[k] = g[k] e^{j\frac{2\pi}{M} m(k - \frac{D+N}{2})}, \tag{2.17}$$

with $m = 0, ..., M-1$ and $k = 0, ..., D$.

In [18], L is expressed as $L - 1 = \alpha N - \beta$, with α and β two integers such that $\alpha > 0$ and $0 \leq \beta \leq N - 1$. Hence, the TMUX reported in Fig. 2.4 is causal with a delay of α symbols. Assuming that g is a symmetrical real-valued prototype filter, we have:

$$h_m[k] = f_m[k], \qquad \text{for all } m \text{ and } k. \tag{2.18}$$

The perfect orthogonality of the OFDM/OQAM is provided if [18]:

$$P_l(z)P_l(z^{-1}) + P_{l+N}(z)P_{l+N}(z^{-1}) = \frac{1}{N}, \qquad \forall z, 0 \leq l \leq N-1. \tag{2.19}$$

where $P_l(z)$ represents the polyphase components of order $2N$, of the prototype filter $G(z)$ in z domain:

$$G(z) = \sum_{l=0}^{2N-1} z^{-l} P_l(z^{2N}) \quad \text{with} \quad P_l(z) = \sum_n g[l+2N]z^{-n}. \tag{2.20}$$

2.3.3 Time-frequency localization of prototype filters

As presented previously, the OFDM/OQAM modulation scheme relies on the principle of offsetting complex QAM while maintaining the perfect reconstruction constraint, i.e., meaning that for an OFDM/OQAM system as in Fig. 2.4, $\hat{a}_{m,n-\alpha} = a_{m,n-\alpha}, \bigvee m, n$. Moreover, a good pulse shape with good time-frequency localization properties can be obtained. In this section, we discuss some well designed prototype filters for OFDM/OQAM modulation. First, we give the following definitions:

2.3.3.1 Ambiguity function

The orthogonality property of a pulse shape $g(t)$ over a phase space can be analyzed by its ambiguity function $A_g(\tau, \nu)$ defined as:

$$A_g(\tau, \nu) = \int_{-\infty}^{+\infty} g(t + \frac{\tau}{2}) g^*(t - \frac{\tau}{2}) e^{-j2\pi\nu t} dt. \tag{2.21}$$

The ambiguity function of a given pulse shape also gives an insight of its energy leakage over time and frequency axes. The sampled version of the ambiguity function is defined as:

$$A_g[l, k] = A_g(lT_0, kF_0), \tag{2.22}$$

and the orthogonality property (i.e. the perfect reconstruction) is satisfied if $A_g[0, 0] = 1$ and $A_g[nT_0, mF_0] = 0$ for $(m, n) \neq (0, 0)$.

2.3.3.2 Time-Frequency localization

Let g be a function of $L_2(R)$ with G_ν its Fourier transform. We denote by $||.||$ the norm associated with $L_2(R)$. The moments of order 1 and 2 in time and frequency are expressed as follows:

- moment of order 1 in time:

$$m^{(1)}(g) = \frac{1}{||g||^2} \int_{-\infty}^{+\infty} t|g(t)|^2 dt; \tag{2.23}$$

- moment of order 2 in time:

$$m^{(2)}(g) = \frac{1}{||g||^2} \int_{-\infty}^{+\infty} (t - m^{(1)}(g))^2 |g(t)|^2 dt; \tag{2.24}$$

- moment of order 1 in frequency:

$$M^{(1)}(g) = \frac{1}{||g||^2} \int_{-\infty}^{+\infty} \nu |G(\nu)|^2 d\nu; \tag{2.25}$$

- moment of order 2 in frequency:

$$M^{(2)}(g) = \frac{1}{||g||^2} \int_{-\infty}^{+\infty} (\nu - M^{(1)}(g))^2 |g(\nu)|^2 d\nu; \tag{2.26}$$

Similarly to [25], the time frequency localization of a function g of $L_2(R)$ is the quantity $\zeta(g)$ defined by:

$$\zeta(g) = \frac{1}{4\pi\sqrt{m^{(2)}(g)M^{(2)}(g)}}, \tag{2.27}$$

Note that $0 \leq \zeta(g) \leq 1$ and the equality $\zeta(g) = 1$ is reached if and only if g is the Gaussian function.

2.3.3.3 The Square Root Raised Cosine Filter (SRRC)

It is well known, in digital communication systems, that the combination of the transmit and receiver SRRC filters satisfies the Nyquist criterion, although this requires the SRRC filter to be continuous-time with infinite length. The truncated discrete-time SRRC is still widely used in digital communications. In frequency domain, the SRRC filter is expressed as:

$$R_C(\nu) = \begin{cases} \frac{1}{\sqrt{F_0}} & |\nu| \leq (1-\rho)\frac{F_0}{2}, \\ \frac{1}{\sqrt{F_0}} \cos(\frac{\pi}{2\rho}(\frac{|\nu|}{F_0} - \frac{1-\rho}{2})) & (1-\rho)\frac{F_0}{2} < |\nu| \leq (1+\rho)\frac{F_0}{2}, \\ 0, & (1+\rho)\frac{F_0}{2} < |\nu|, \end{cases}$$

where $0 \leq \rho \leq 1$ is the roll-off factor. The continuous-time version of the temporal response of SRRC filter is:

$$r_c(t) = \sqrt{F_0} \frac{4\rho F_0 t \cos(\pi(1+\rho)F_0 t) + \sin(\pi(1-\rho)F_0 t)}{(1-(4\rho F_0 t)^2)\pi F_0 t} \tag{2.28}$$

The filter length can be set to $L = bM, \quad b \in \mathbb{N}$, with M the number of carriers. Compared with the rectangular filter, SRRC (ρ=0.5) has better frequency localization feature at the cost of time localization loss. Fig. 2.5 shows a comparison between the SRRC filter vs. the rectangular one in time and frequency domains, with SRRC filter length $4M$ and $\rho = 0.5$.
The ambiguity function representation in Fig. 2.6, shows the energy leakage of the SRRC filter. At the receiver, the energy of SRRC is highly concentrated in frequency but a little leakage appears in time domain. Hence, using SRRC filters, the system suffers more from the interference in the time domain (ISI) than in the frequency domain (ICI).

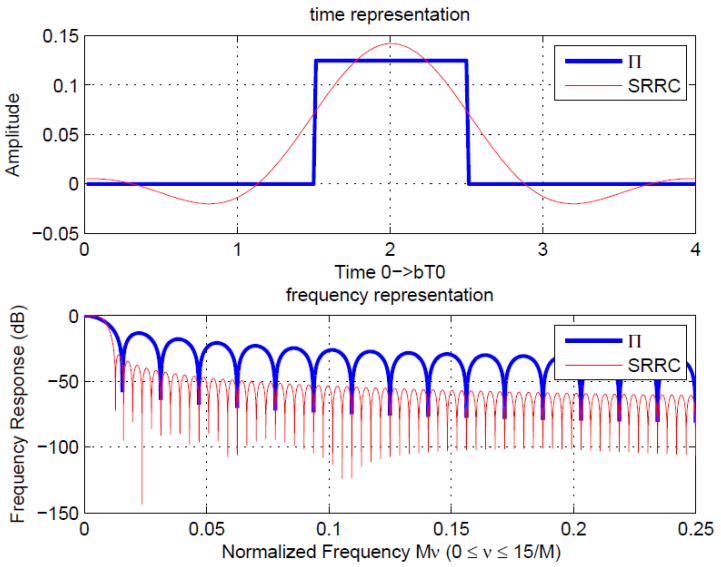

FIGURE 2.5: Time-frequency comparison: SRRC ($b = 4, \rho = 0.5$) vs. rectangular window.

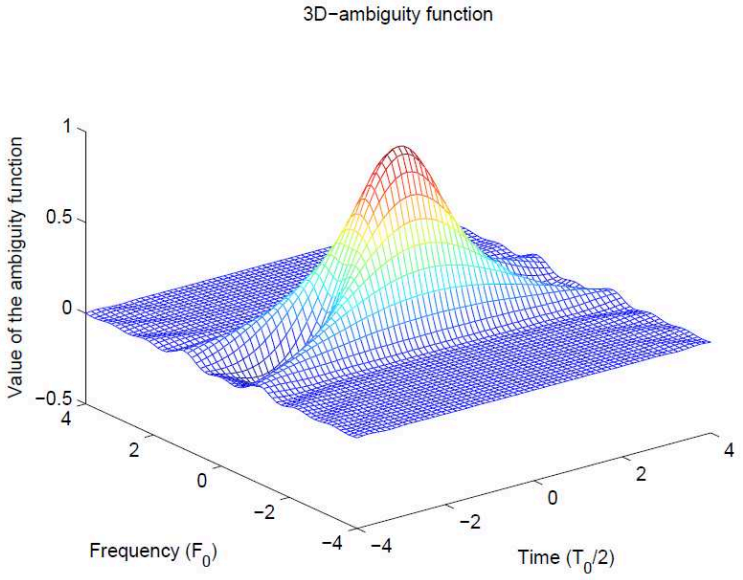

FIGURE 2.6: Ambiguity function representation of the SRRC ($b = 4, \rho = 0.5$) filter.

2.3.3.4 The Extended Gaussian Function (EGF)

This class of prototype function results from an orthogonalization procedure of the Gaussian function [25]. Since the Gaussian function is a well-localized non-orthogonal function, it has been proposed to orthogonalize it and to truncate it to a desired length. The orthogonalization method leads to a prototype function named Isotropic Orthogonal Transform Algorithm (IOTA). The EGF function is deduced from the same algorithm and defined by [35]:

$$z_{\lambda,\nu_0,\tau_0}(t) = \frac{1}{2}\sum_{k=0}^{+\infty} d_{k,\lambda,\nu_0}[g_\lambda(t+\frac{k}{\nu_0}) + g_\lambda(t-\frac{k}{\nu_0})]\sum_{l=0}^{+\infty} d_{l,\frac{1}{\lambda},\tau_0}\cos(2\pi l\frac{t}{\tau_0}), \tag{2.29}$$

where d_{k,λ,ν_0} are real coefficients and g_λ is the Gaussian function:

$$g_\lambda(t) = (2\lambda)^{1/4}\exp(-\pi\lambda t^2),$$

with $\lambda > 0$ the spreading parameter. $\tau_0 = \frac{T_0}{2}$ and $\nu_0 = F_0$ are the time and frequency real parameters of the modulation system, $\tau_0\nu_0 = 1/2$. Setting $\lambda = 1$ leads to the IOTA prototype filter. An overview of the main properties of IOTA filters was introduced in [25].
The comparison between IOTA and rectangular filters in time and frequency domains is reported in Fig. 2.7. It shows that the IOTA filter, with a length of $4M$, has better frequency localization than the rectangular one. The ambiguity function presented in Fig. 2.8 shows that the energy of the IOTA filter has a nearly isotropic spreading over time and frequency axes.

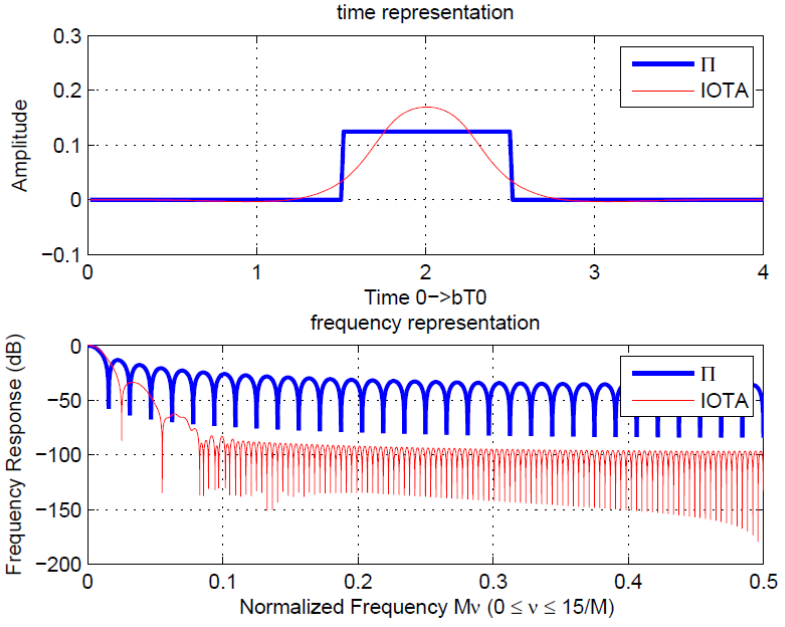

FIGURE 2.7: Time-frequency comparison: IOTA ($b = 4$) vs. rectangular window.

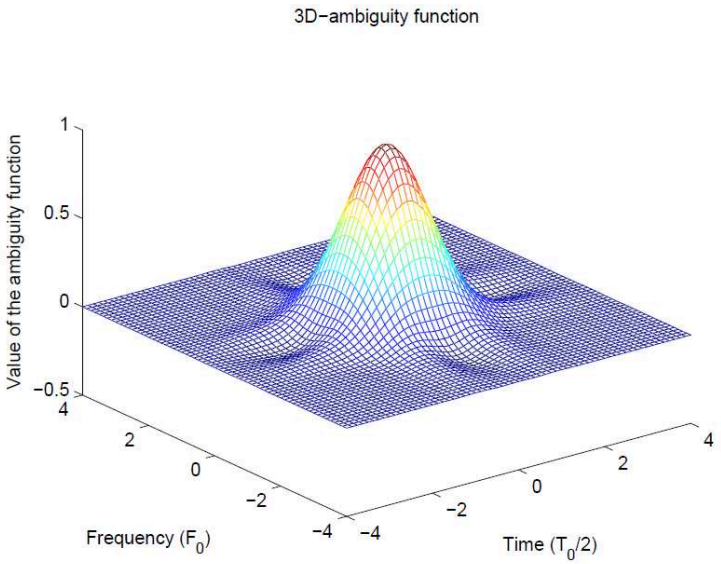

FIGURE 2.8: Ambiguity function representation of the IOTA ($b = 4$) filter.

2.3.3.5 Time Frequency Localization (TFL) filter

The SRRC and IOTA pulse shapes are both orthogonal in the sense of continuous-time. A digitized-truncated version of these filters is normally used in digital communications systems, which leads to orthogonality loss. It is stated in [18] that by using the same truncation length, the orthogonality loss is worse in case of an SRRC filter than it is for a IOTA filter. To avoid this loss, the filter design should be carried out directly in the discrete-time domain taking into account the orthogonality conditions.
Based on the discrete orthogonality condition (2.19), the design of a perfectly orthogonal discrete filter is feasible. Two design criteria are proposed by Pinchon *et al.* in [36] and [37]. The first presented criterion aims at maximizing the time-frequency localization factor under the constraint of (2.19). The filter length can be defined as a multiple of M, i.e., bM with b a positive integer. The comparison between the TFL ($b = 1$) filter and the rectangular one is given in Fig. 2.9. The ambiguity function of the TFL filter represented in Fig. 2.10 shows that it has better localization in time than in frequency domain.

2.3.3.6 Frequency Selective (FS) filter

The second criterion presented in [36] and [37] is the minimization of the out-of-band energy. Under the assumption of a normalized frequency, meaning that the sampling frequency equals 1, the minimization function is:

$$\min_{\{parameters\}} \frac{E(f_c)}{E(0)} \quad \text{with} \quad E(f_c) = \int_{f_c}^{1/2} |P(e^{j2\pi n\nu})|^2 d\nu, \tag{2.30}$$

f_c is the cutoff frequency expressed as: $f_c = (1+\rho)\frac{1}{2M}$. The factor $0 \leq \rho \leq 1$ can be seen as a roll-off factor and “parameters" represent the prototype filter coefficients or a set of variables related to them.
The Frequency Selective (FS) filter is obtained by minimizing the above function under

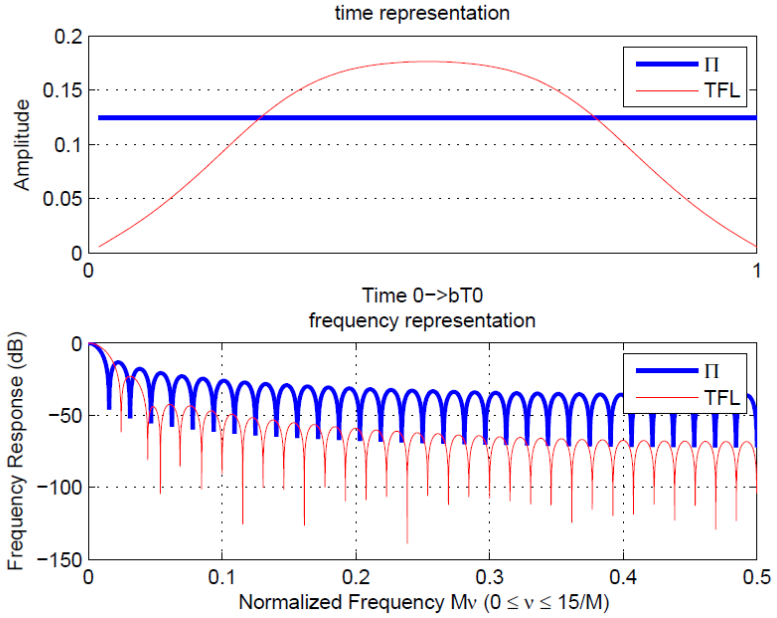

FIGURE 2.9: Time-frequency comparison: TFL ($b = 1$) vs. rectangular window.

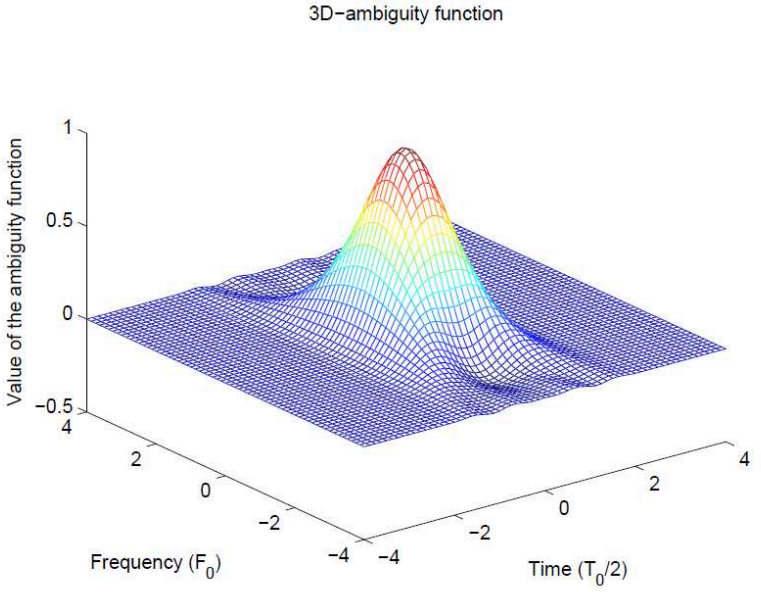

FIGURE 2.10: Ambiguity function representation of the TFL ($b = 1$) filter.

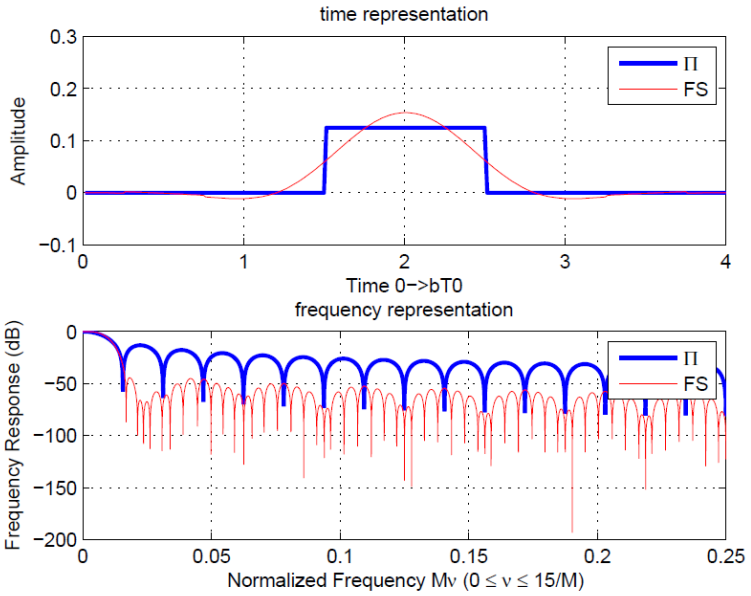

FIGURE 2.11: Time-frequency comparison: FS ($b = 4, \rho = 1$) vs. rectangular window.

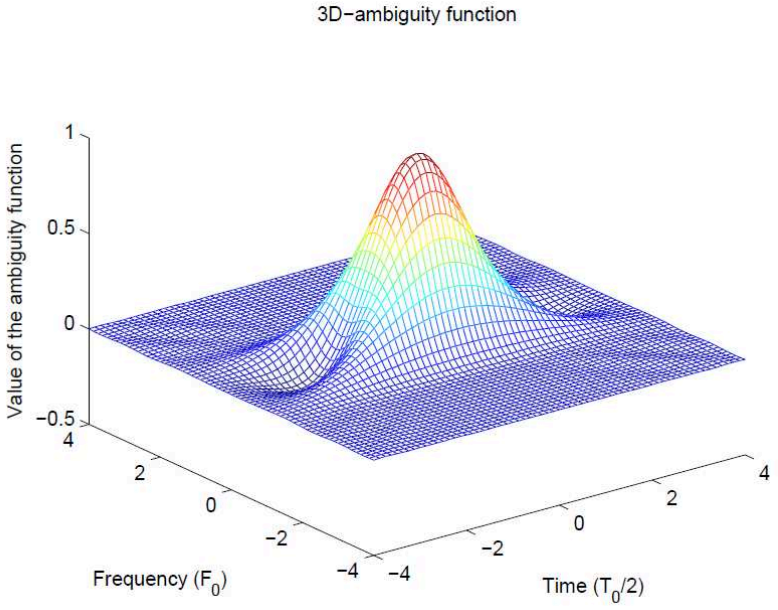

FIGURE 2.12: Ambiguity function representation of the FS ($b = 4$) filter.

the assumption of the orthogonality constraint (2.19). Similar to TFL filter, the filter length can be equal to bM. The comparison between the FS filter ($b = 4$) and the rectangular one is shown in Fig. 2.11. The ambiguity function, illustrated by Fig. 2.12, shows that the FS filter is better localized in frequency than in time domain.

2.4 Faster Than Nyquist Signaling

2.4.1 Nyquist criterion

The general baseband model for transmitting data over continuous-time bandlimited channel was formulated by Nyquist in his pioneering works in 1924 and 1928 [10], [11]. In these works, Dr. Nyquist investigated the maximum signaling rate over such channels without causing inter symbol interferences. He showed that the maximum rate is directly linked to the channel bandwidth. This maximum rate is referred to as Nyquist signaling rate. Let us consider a standard Pulse Amplitude Modulation (PAM) baseband continuous-time signal expressed as:

$$s(t) = \sum_{n} x[n]g(t - nT), \tag{2.31}$$

where $x[n]$ are binary or multilevel symbols, $g(t)$ is the used pulse shape assumed to be bandlimited to W Hertz and T is the symbol duration. The signaling rate of this transmission scheme is $\frac{1}{T}$ symbols per second. The received signal is expressed as:

$$y(t) = \sum_{n} x[n]h(t - nT) + z(t) \tag{2.32}$$

where $z(t)$ is a noise signal and $h(t)$ is the convolution of the transmit filter $g(t)$, the channel filter $c(t)$ and the receiver filter $r(t)$. By sampling the received signal at $t = nT$, we obtain:

$$y(nT) = x[n]h(0) + \sum_{m \neq n} h((n - m)T) + z(nT) \tag{2.33}$$

where the useful signal $x[n]$ is affected by ISI represented by the summation term. To ensure ISI-free transmission, a necessary and sufficient condition is: $h((n-m)T) = 0$ for all $m \neq n$ and $h(0) \neq 0$. Assuming that $h(0) = 1$, by normalizing the received signal, the ISI-free condition is:

$$h(nT) = \begin{cases} 1, & n = 0 \\ 0, & n \neq 0 \end{cases} \tag{2.34}$$

To ensure ISI-free transmission, Nyquist derived a sufficient and necessary condition for $H(f)$, the Fourier transform of $h(t)$, such as (2.34) is satisfied.

Theorem: Nyquist criterion for zero ISI: A necessary and sufficient condition for $H(f)$ to satisfy (2.34) is [11]:

$$\sum_{k=-\infty}^{+\infty} H(f + \frac{k}{T}) = T \tag{2.35}$$

Proof: the following proof is reproduced from [29]. Firstly, $h(t)$ can be expressed using the inverse Fourier transform of $H(f)$:

$$h(t) = \int_{-\infty}^{+\infty} H(f)e^{j2\pi ft}df \tag{2.36}$$

By sampling at the rate $t = nT$, we obtain:

$$h(nT) = \int_{-\infty}^{+\infty} H(f)e^{j2\pi fnT}df \tag{2.37}$$

Equation (2.37) can be further expressed as:

$$\begin{aligned} h(nT) &= \sum_{m=-\infty}^{+\infty} \int_{(2m-1)/2T}^{(2m+1)/2T} H(f)e^{j2\pi fnT}df \\ &= \sum_{m=-\infty}^{+\infty} \int_{-1/2T}^{1/2T} H(f+\frac{m}{T})e^{j2\pi fnT}df \\ &= \int_{-1/2T}^{1/2T} [\sum_{m=-\infty}^{+\infty} H(f+\frac{m}{T})]e^{j2\pi fnT}df \\ &= \int_{-1/2T}^{1/2T} B(f)e^{j2\pi fnT}df \end{aligned} \tag{2.38}$$

where $B(f)$ is defined as:

$$B(f) = \sum_{m=-\infty}^{+\infty} H(f+\frac{m}{T}). \tag{2.39}$$

Since $B(f)$ is a periodic function with period $\frac{1}{T}$, it can be expanded in terms of its Fourier series coefficients b_n as:

$$B(f) = \sum_{n=-\infty}^{+\infty} b_n e^{j2\pi fnT}, \tag{2.40}$$

where coefficients b_n are given by:

$$b_n = T\int_{-1/2T}^{1/2T} B(f)e^{-j2\pi fnT}df. \tag{2.41}$$

From (2.38) and (2.41), we obtain:

$$b_n = Th(-nT). \tag{2.42}$$

Then, the necessary and sufficient condition to satisfy (2.34) is:

$$b_n = \begin{cases} T, & n = 0 \\ 0, & n \neq 0 \end{cases}$$

Substituting (2.42) in (2.40), we obtain:

$$B(f) = T, \tag{2.43}$$

which leads to:

$$\sum_{m=-\infty}^{+\infty} H(f+\frac{m}{T}) = T, \tag{2.44}$$

and concludes the proof. As a result, when $\frac{1}{T} > 2W$, ISI is unavoidable.

Theorem: Nyquist criterion in strictly bandlimited channel. Considering a modulating pulse $g(t)$ strictly bandlimited to $[-W, W]$ where W is the frequency in Hz, the smallest symbol period T ensuring ISI-free transmission is called the Nyquist symbol rate and defined as: $T = \frac{1}{2W}$.

Proof: Let us consider $p(t) = \sum_n x[n]\delta(t-nT)$. Therefore:

$$\begin{aligned} p(t) * g(t) &= \int_{-\infty}^{+\infty} p(u)g(t-u)du = \sum_n x[n] \int_{-\infty}^{+\infty} \delta(u-nT)g(t-u)du \\ &= \sum_n x[n]g(t-nT), \end{aligned} \tag{2.45}$$

where $a(t) * b(t) = \int a(u)b(t-u)du$ is the convolution operation and $\delta(.)$ is the Dirac delta function. The Fourier transform gives us the frequency response as:

$$F\{p(t) * g(t)\} = P(f)G(f) = (\sum_n x[n]e^{-j2\pi fnT})G(f), \tag{2.46}$$

where $P(f)$ and $G(f)$ are the Fourier transforms of $p(t)$ and $g(t)$, respectively. As can be noticed, $P(f) = \sum_n x[n]e^{-j2\pi fnT}$ is periodic with period $1/T$. Since $G(f)$ is bandlimited to $[-W, W]$, the frequency components of $P(f)$ that are outside the interval $[-W, W]$ will be clipped off due to the multiplication in (2.46). Additionally, the periodicity of $P(f)$ makes it possible to deduce the data symbols from only one period of $P(f)$. As a result, a sufficient condition to recover the transmitted data without interference is $1/T = 2W$, otherwise known as the Nyquist signaling rate.
Consequently, the Nyquist criterion ensures a simple receiver architecture based on a matched filter to the modulation pulse shape and a sampler at Nyquist rate [12], [13]. When transmitting over an AWGN channel, this receiver structure is known to maximize the received Signal-to-Noise-Ratio (SNR).

2.4.2 FTN signaling

In 1975, Mazo pointed out that the transmission rate is not necessarily limited by the Nyquist criterion, meaning that faster transmission rate can be envisaged to trade the interference-free transmission for more throughput. The concept is known as Faster-Than-Nyquist signaling. Actually, the question of whether signaling faster than the Nyquist rate is of any merit has been examined by many researchers: [14], [15], [16]. However, the concept was not deemed as an attractive means until the trend of the explosion of throughput requirements becomes unavoidable. This is mainly attributed to the complex processing necessary to deal with the interference introduced by FTN. In fact, since the pulses orthogonality condition no longer holds, FTN signaling induces significant interference to the useful signal which calls for more sophisticated and complex processing at the receiver side.

Because of the declining cost of processing units, the importance of bandwidth resources and spectrally efficient solutions overcame the amount of processing required. Moreover, advances in signal processing enabled the implementation of advanced coding and equalization techniques to deal with the interference caused by FTN signaling. Hence, the concept of FTN transmissions has been recently re-investigated and is now considered as a good candidate offering higher data rates with more efficient bandwidth usage.

FTN background

As stated earlier, the concept of FTN signaling was introduced by Mazo in [19]. He showed that T-orthogonal pulses can be sent faster than the Nyquist rate $1/T$, while keeping the minimum Euclidean distance unchanged. Although ISI is introduced since the pulses are no longer orthogonal, the asymptotic error rate behavior of an optimal decoder remains the same. The performance of FTN is guaranteed by an error probability lower bound, called Forney Bound [38]:

$$P_e \geq p_m Q(\frac{d_{min}}{\sqrt{2N_0}}), \tag{2.47}$$

where p_m is the probability of having signals with minimum distance d_{min} and N_0 is the unilateral noise Power Spectral Density (PSD).

Specifically, Mazo studied PAM baseband modulated signals of the form:

$$s(t) = \sum_n a_n g(t - nT), \tag{2.48}$$

where $a_n \in \{-1, +1\}$, $g(t)$ being the Sinc pulse and T the symbol duration. In the FTN case, Sinc pulses are packed closer in time, with respect to Nyquist rate, and $s(t)$ is rewritten as follows:

$$s(t) = \sum_n a_n g(t - n\tau T), \tag{2.49}$$

with $0 \leq \tau < 1$. Mazo showed that τ can be decreased to a certain threshold without changing the minimum Euclidean distance. In fact, he showed that τ can be decreased to 0.802, which means up to 25% more bits can be carried in the same bandwidth without affecting the Euclidean distance. The value $0.802T$ is called the Mazo limit according to the definitions given just afterwards.

Minimum distance

If we denote by $D(\mathbf{a_1}, \mathbf{a_2})$ the distance between two signals $S_{\mathbf{a_1}}(t)$ and $S_{\mathbf{a_2}}(t)$, then:

$$D(\mathbf{a_1}, \mathbf{a_2})^2 = \int_{-\infty}^{+\infty} |S_{\mathbf{a_1}}(t) - S_{\mathbf{a_2}}(t)|^2 dt. \tag{2.50}$$

If $\{g(t - nT)\}$ constitutes an orthogonal basis, the distance measured between $S_{\mathbf{a_1}}(t)$ and $S_{\mathbf{a_2}}(t)$ is proportional to the difference between the corresponding symbol sequences $a_1[n]$ and $a_2[n]$. However, for non-orthogonal pulses $\{g(t - nT)\}$, as in the FTN case,

the symbol sequence distance is no longer representative of the signal distance.
We define the normalized distance $d(\mathbf{a_1}, \mathbf{a_2})$ as:

$$d(\mathbf{a_1}, \mathbf{a_2})^2 = \frac{D(\mathbf{a_1}, \mathbf{a_2})^2}{2E_b}, \tag{2.51}$$

where E_b is the bit energy. The minimum distance is then defined as:

$$d_{min} = \min_{\mathbf{a_1} \neq \mathbf{a_2}} d(\mathbf{a_1}, \mathbf{a_2}) \tag{2.52}$$

Mazo limit

The Mazo limit is defined as the minimum factor that allows the pulses to be packed closer, with respect to Nyquist criterion, while keeping the minimum distance unchanged:

$$\tau^+ = \min\{\tau; d_{min} = d_0\}, \tag{2.53}$$

where d_0 is the minimum distance when $\tau = 1$.

2.4.3 Related FTN research

The idea of transmitting faster than the Nyquist rate dates back to mid 1960s. However, it was significantly investigated only recently by several researches. In this section, we present a state of the art related to FTN research in a chronological order.

In 1968, Saltzberg attempted to reduce the channel bandwidth below the Nyquist rate [15]. He computed an upper bound of the error probability using Sinc pulses. Saltzberg showed that the bandwidth can be slightly reduced below the Nyquist band without catastrophic results: " 97% of the Nyquist band must be preserved in order to ensure an error probability less than 10^{-7}". In 1973, Salz [16] studied the possible advantages of signaling faster than the Nyquist rate as a special case of his optimization of the equalizer and of the transmitting filter for PAM communication over a linear noisy channel. However, he concluded that FTN transmission increases the mean-square error after the equalization, thus worsening the overall communication performance.

Later in 1975, Mazo published a significant paper on FTN transmission showing that an improvement up to 25% of the transmitted rate, compared to the Nyquist rate, can be obtained while keeping the minimum Euclidean distance unchanged [19]. However, the paper considered PAM Sinc pulses without providing any details on practical FTN implementation neither the receiver architecture. Nevertheless, Mazo's work opened the door for research in the direction of improving the Nyquist rate.

In 1984, Foschini compared the performance of FTN with standard QAM transmissions over a bandlimited noisy channel [39]. He considered FTN signaling using binary symbols and Maximum Likelihood Sequence Detection (MLSD) to overcome ISI. He concluded that FTN offers minor gains over QAM transmissions, mainly due to the significant spectral sidelobes caused by FTN signaling and the high implementation complexity

of the MLSD. The comparisons were made using Nyquist pulses and Discrete Prolate Spheroidal Wave Functions (DPSWF). He also considered optimizing the pulse design by maximizing the minimum Euclidean distance under constraints of complexity, transmitted power and Out-of-Band Energy (OBE). Moreover, Foschini mentioned at the end of his paper that the competitiveness of FTN signaling using multi-level symbols with QAM systems cannot be dismissed and may have some value.

In 1988, Hajela [40] considered the problem of determining the minimum distance between received signals when data is transmitted faster than the Nyquist rate over an ideal bandlimited channel (noiseless and distortion-free channel). He showed that there is no degradation in the minimum distance for rate improvement up to 25% beyond the Nyquist rate, despite the presence of ISI. Motivated by Hajela's work, Mazo has continued his work with a joint paper with Landau [41] in 1988 to determine the minimum distance between uncoded binary sequences transmitted over an ideal bandlimited channel with a rate exceeding the Nyquist rate.
The result published by Mazo on keeping the minimum Euclidean distance unchanged up to 25% above the Nyquist rate, was first expressed mathematically by Hajela in a series of papers published between 1987 and 1992. Hajela formulated mathematically the problem of finding the minimum Euclidean distance of FTN signaling using Sinc pulses. Then, he showed that signaling at a rate up to 25% above the Nyquist rate is indeed possible. Mazo's work on the minimum Euclidean distance of FTN signaling was extended by Liveris and Georghiades in 2003 [42] to more practical Raised Cosine (RC) pulses. He verified numerically that a similar rate increase is also possible.

In 1995 Wang and Lee proposed a realizable digital signaling scheme that requires a bandwidth less than the Nyquist limit and at the same time provides the same asymptotic performance as PAM [43]. They proposed a 5-step iterative algorithm to modify realizable FTN transmit pulses in order to increase the minimum Euclidean distance of the multi-level FTN scheme. At the receiver side, they proposed to use approximate whitened matched filter and adaptive Viterbi algorithm to deal with ISI caused by FTN. On the other hand, Liveris and Georghiades [42] examined more in detail the error patterns that decrease the minimum Euclidean distance for FTN signaling using raised cosine pulses. They proposed to avoid the occurrence of such patterns through constrained coding, at the expense of small rate loss, together with low-complexity receivers in order to keep the minimum Euclidean distance constant for higher rates. An iterative receiver based on turbo-equalization and soft interference cancellation to combat ISI was also considered. They showed via simulations that ISI caused by FTN can be removed by using advanced coding and turbo-equalizers.

Recently, the FTN concept has been re-investigated as a good candidate of trading processing complexity for more throughput and improving spectral efficiency. This is mainly due to the escalating cost of bandwidth resource and the declining cost of memory and processing units. Moreover, advances in signal processing and coding techniques permit practical reduction of the interference induced by FTN signaling. The concept of FTN signaling has been extended to multicarrier systems based on OFDM technology, mainly with applications to long-haul fiber optic communication links, and underwater acoustic channels. Nowadays, the FTN concept is an interesting on-going research area with still open problems and potentials for improvements.

Rusek and Anderson from Lund University published a series of articles tackling the FTN concept, initially as a part of Rusek's Ph. D. thesis work [44]. They have studied FTN signaling under several aspects: extension of FTN to multicarrier modulation such as OFDM as well as extension of the FTN concept to frequency domain, analysis of the constrained channel capacity, design of practical coding systems and equalizers, and more recently, implementation on Field Programmable Gate Arrays (FPGA) hardware. In 2005, Rusek and Anderson generalized Mazo's FTN concept to the frequency dimension by packing signals closer both in time and frequency. The concept is called two-dimensional Mazo signaling [20]. They showed that the invariance of the minimum Euclidean distance in Mazo's work stands also when signals are packed closer in frequency or in both time and frequency. An algorithm to compute the minimum Euclidean distance was also proposed together with a simple decoder in case of SRRC pulses. Their results showed that it is possible to reduce the frequency separation of data transmissions to less than twice the bandwidth. Unfortunately, the proposed decoder works only for a small number of frequency carriers (M =2 or 4).

In 2006, Anderson and Rusek also extended Mazo's concept of FTN to OFDM transmissions and examined the minimum Euclidean distance in case of a large number of frequency carriers [17]. Their results showed that the two-dimensional Mazo limit is less than the time-only Mazo limit allowing spectral saving of at least 50%. At the receiver side, they proposed a one-dimensional Bahl-Cocke-Jelinek-Raviv (BCJR) algorithm [45] (cf. also section 2.5.1) and Soft Interference Cancellation (SIC). In their simulations, they only considered Binary Phase Shift Keying (BPSK) modulation with $((f_\Delta, T_\Delta) = (1, 0.7))$ and 20 subcarriers. (f_Δ, T_Δ) are compression factors in frequency and time domains, respectively. The results showed that their proposed system can approach the error performance of the orthogonal system at high SNR but with some performance loss in terms of BER (0.5 dB loss at a BER of 10^{-5}). The proposed receiver was improved in [46] and extended to a two-stage decoder based on M-BCJR algorithms, i.e., with a calculation reduced to a limited number of terms, and soft interference cancellation. Their results showed that the proposed scheme approached the performance of the orthogonal system for some (f_Δ, T_Δ) values but complexity is rather high. Rusek and Anderson designed also practical coding schemes for FTN signaling. In [47], the authors investigated the performance of serial and parallel concatenated coding schemes based on FTN signaling and iterative decoding. They considered an FTN transmitter using the SRRC pulse and a rate $R = \frac{b}{c}$ convolutional code for the serial concatenation scheme and a rate-1 precoder for the parallel concatenation scheme. In addition they used EXtrinsic Information Transfer (EXIT) charts to analyze the behavior of iterative decoding, [48]. Through simulations, they showed that the convolutional code can maintain its performance at roughly one third of its bandwidth thanks to FTN and iterative decoding. Simulations also showed that the parallel concatenation scheme with precoding gives stronger performance which is out of reach for standard methods based on orthogonal SRRC pulses. The minimum Euclidean distance for non-binary FTN signaling was investigated in [49], where the authors also proposed optimal precoding for binary and quaternary FTN transmission using again SRRC pulses together with an M-Algorithm based receiver.

In 2009, Rusek and Anderson analyzed the capacity of FTN signaling and compared it to the capacity of orthogonal linear modulation [50]. They showed that, when signals have excess bandwidth, the capacity of the FTN signaling exceeds that of orthogonal

signaling and that FTN signaling can achieve the ultimate capacity for a given PSD. When the modulating pulse is strictly bandlimited, the FTN capacity reduces back to the Shannon capacity of continuous-time bandlimited channel. At the same time, the concept of FTN signaling extended to OFDM was also re-examined by Rusek and Anderson [51]. They considered compressing signals both in time and frequency and studied the minimum Euclidean distance for multicarrier systems using Gaussian and SRRC pulses and binary modulation symbols over an AWGN channel. In addition, they concatenated convolutional codes with FTN and evaluated the performance of an iterative receiver based on a simplified multidimensional BCJR algorithms and SIC. Their results showed that the multistream FTN can achieve the same error performance as the ISI-free OFDM at high SNR, while using only half of the time-bandwidth product of OFDM.

Additionally, Prlja, as part of his Ph. D thesis, addressed the FTN concept in a series of papers published between 2008 and 2013, [52]-[53]. In [21], he, together with Rusek and Anderson, considered different receivers based on whitened matched filter for FTN signaling using SRRC pulses, and binary data over an AWGN channel. They analyzed the minimum Euclidean distance in case of a truncated Viterbi Algorithm. In addition, they concatenated FTN signaling with a convolutional code and considered an iterative receiver based on turbo-equalization whose performance was analyzed through EXIT charts. In 2012, Prlja and Anderson re-examined the receiver for FTN signaling and proposed new M-BCJR algorithms for uncoded and coded FTN transmissions, as a turbo-like system [53]. Their receivers were compared to the reduced-search Viterbi algorithm and BCJR benchmarks and, in case of coded FTN, were capable of removing ISI caused by FTN leading to an energy saving of 4 dB and a bandwidth reduction of 35% compared to binary orthogonal signaling.

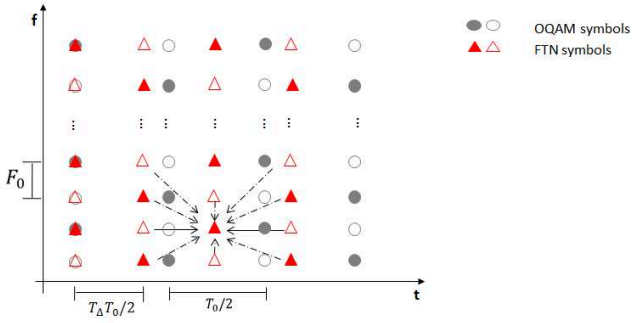

FIGURE 2.13: Time-frequency lattice of FTN and OQAM symbols.

Though the FTN concept was introduced in 1975, the implementation of FTN systems was not tackled at that time because of the high complexity of such schemes. However, advances in signal processing and silicon technology has now made FTN implementation possible. Dasalukunte, as part of his Ph. D research at Lund university, published a series of articles on the FTN concept combined with OFDM/OQAM modulation [54]-[55]. In 2009, he proposed an FTN transmitter architecture which retains the processing blocks of conventional multicarrier systems and has good flexibility when varying the time and frequency packing factors [2]. Fig. 2.13 shows a time-frequency lattice of OQAM and FTN symbols. The black solid circles represent OQAM symbols having $\frac{\pi}{2}$ phase offset

with regard to the in-phase OQAM symbols represented by hollow circles. On the other hand, the red solid triangles represent FTN symbols having $\frac{\pi}{2}$ phase offset with regard to in-phase FTN symbols represented by hollow triangles. Moreover, FTN symbols seem to appear more frequently in time. The transmitted continuous-time baseband signal $s(t)$ is expressed as:

$$s(t) = \sum_{l=-\infty}^{\infty} \sum_{k=0}^{M-1} j^{k+l} x_{k,l} p(t - lT_\Delta \frac{T_0}{2}) e^{j2\pi \frac{F_\Delta}{T} kt}, \tag{2.54}$$

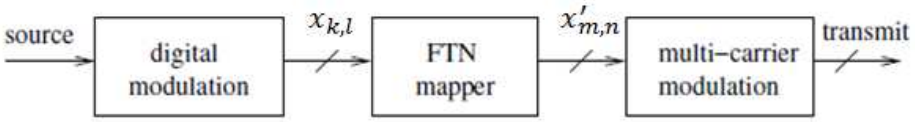

FIGURE 2.14: FTN-OQAM transmitter architecture, [2].

where M is the subcarriers number, $x_{k,l}$ are OQAM symbols, p is the Gaussian pulse shape, T_0 is the symbol duration and $(T_\Delta, F_\Delta), T_\Delta F_\Delta < 1$ are time and frequency packing factors, respectively. Dasalukunte proposed to project first the signal $s(t)$ onto a set of orthonormal basis functions $\phi(t)$, spanning both time and frequency (N_t and N_f points in time and frequency, respectively), and then transmit the projection coefficients via a standard MCM. The transmitted signal is reformulated:

$$s(t) = \sum_{l=-\infty}^{\infty} \sum_{k=0}^{M-1} j^{k+l} x'_{k,l} \phi(t - l\frac{T_0}{2}) e^{\frac{j2\pi}{T} kt}, \tag{2.55}$$

where $x'_{k,l}$ represents the projection of $s(t)$ onto $\phi(t)$. A block named *FTN mapper* in inserted between the OQAM modulation and the IFFT to carry out these projections, see Fig. 2.14. This block is based on a Look Up Table (LUT), where the projection coefficients are stored. Results showed that the IOTA function is the preferred choice as a projection basis that reduces the storage as well as the arithmetic units required for computation. This means that less (N_t and N_f) points are needed to represent the signal compared to the rectangular basis.

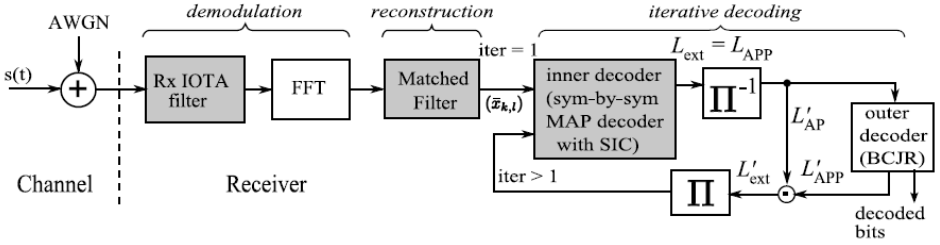

FIGURE 2.15: FTN-OQAM receiver architecture, [3].

The signal processing at the receiver side is based on iterative decoding with SIC [3]. The proposed FTN receiver is depicted in Fig. 2.15. First, the signal is processed by the Rx IOTA filter and then demodulated. Then, FTN symbols, $\bar{x}_{k,l}$, are approximated by the matched filter using the received symbols and the already known projection coefficients. An inner decoder based on Maximum *A Posteriori* (MAP) algorithm and SIC processes

the FTN symbols to deal with FTN-induced ISI and ICI. The iterative decoding is performed via soft LLR, denoted by L_{ext}, L', etc, exchange between the inner decoder and a BCJR outer decoder. Results were given for FTN signaling using binary data over an AWGN channel for different time spacings ($T_\Delta < 1, F_\Delta = 1$). They showed that FTN signaling permits transmitting twice the amount of information using the same bandwidth and an efficient hardware implementation. Furthermore, the transceiver architecture was synthesized in both 65 nm complementary metal-oxide-semiconductor (CMOS) and FPGA (130 nm), thus demonstrating that FTN systems can be efficiently implemented in practice, [56]-[55].

The FTN concept was also independently addressed by Y. J. D. Kim as part of his thesis research [57]. In 2010, he analyzed the PSD of FTN signaling with and without precoding over linear-time-invariant channels [58]. He considered convolutional precoding and showed that the PSD is a function of the signaling rate, of the channel frequency response as well as of the precoding coefficients. In addition, to avoid spectrum broadening, he showed that the precoding should be designed in conjunction with the transmission power spectrum of the FTN system. The capacity of cyclostationary FTN signaling over continuous-time ISI channels was studied in [59] and it was proved that higher capacity could be achieved compared to traditional Nyquist signaling. In 2012, Kim proposed an architecture for FTN signaling over continuous-time Gaussian broadcast channel in case of two users and showed that FTN signaling is optimal in Gaussian broadcast channel [60]. In the proposed scheme, the information sent to the different users is coded separately. Then the two users' data symbols are transmitted explicitly over the broadcast channel, while maintaining the Nyquist signaling rate for each data stream. In [61], the proposed FTN signaling is combined with turbo codes and successive interference cancellation at the receiver side. The results showed that the proposed scheme achieved spectral efficiencies, at the target performance BER, close to the capacity boundaries of the Gaussian broadcast channel. On the other hand, Kim proposed an FTN signaling scheme based on non-uniform power allocation in case of optical transmissions to achieve very low complexity decoding and high FTN rates [62]. He showed that non-uniform power allocation does not sacrifice the channel capacity and described a power allocation method when binary data is used. Simulations were given for an FTN scheme using turbo encoded binary data, the SRRC pulse shape and different FTN rates. Results showed that the proposed system performance is equivalent to high-order modulation orthogonal systems, while using only binary alphabets.

In the last decade, the topic of FTN signaling has been considered by many other researchers as well. The FTN concept has been proposed for long-haul fiber-optic communication links as a means to increase the spectral efficiency without increasing the modulation order [63],[64],[65],[66]. In [64], the concept of FTN, or what they called time-frequency packing, was applied to optical transmissions with low order modulation alphabets and compared to the traditional Nyquist system using high-order modulation symbols. They showed that FTN signaling can achieve higher spectral efficiencies even with low-order modulation, which is interesting since the system is more robust to nonlinear effects. The idea of time-frequency packing was addressed by the authors of [67] in case of linear modulations over AWGN channels. They evaluated the spectral efficiency of such schemes using a low-complexity symbol-by-symbol detector and a low-complexity equalization scheme with SIC. More advanced processing for low-order linear modulation with FTN signaling was proposed in [68] using a low-complexity trellis detector. Other

possible applications of the FTN concept, such as satellite communications and large scale antenna systems, were discussed in [69]. Non-orthogonal multicarrier modulation techniques, which are similar to the two-dimensional FTN signaling, have been also considered by other researchers (see e.g., Spectrally efficient FDM [70], [71], [72], High compaction Multicarrier-Communication [73], Overlapped FDM [74] and Weyl-Heisenberg frame transmission [75], [76]). These techniques aim at increasing the spectral efficiency of multicarrier systems by reducing the spacing between the modulating pulses in time and/or in frequency.
In 2010, Yoo and Cho [77] examined the asymptotic information rate for FTN signaling using binary symbols and showed that the system can achieve the capacity of Gaussian FTN as the signaling rates tend to infinity. They proved the asymptotic optimality of binary FTN in the capacity sense compared to Nyquist rate systems. On the other hand, McGuire and Sima investigated a discrete version of FTN signaling by transmitting data in blocks of samples [78]. The proposed scheme enables a low-complexity receiver that detects each block separately. Their results indicate that the FTN receiver can achieve the ISI-free performance for coded and uncoded transmissions at certain FTN rates. This is consistent with Mazo's result on the minimum Euclidean distance for FTN signaling.

In the last few years, the FTN concept continued to attract more and more attention as a potential candidate for the future communication systems. In 2014, the FTN concept using high-order modulation was investigated in [79] in order to further increase the data rate improvement of binary FTN signaling. The proposed receiver is based on iterative equalization and decoding using a BCJR-type algorithm for inner detection and a Low Density Parity Check (LDPC) outer decoder. Results were given for QPSK and 16-QAM transmissions over an AWGN channel using SRRC pulse shapes, and showed an FTN signaling gain about 0.7 dB for 16-QAM. The signal constellation for FTN transmissions was also addressed in [80] in case of satellite systems. In [81], the performance of single carrier FTN signaling in terms of BER and PAPR is investigated and compared to Nyquist signaling using different pulse shapes: SRRC, PHYDYAS (PHYsical layer for DYnAmic Spectrum access and cognitive radio [82]), EGF and the Hermite pulse. Results showed that uncoded and coded FTN signaling approaches the Nyquist signaling when using the same modulation order, while it outperforms the Nyquist signaling at the same spectral efficiency (EGF ($\lambda = 1, 2, 3$) 4-QAM FTN with $\tau = 0.5$ has better BER performance than 16-QAM Nyquist, with τ being the FTN packing factor). In addition, at the same spectral efficiency as well as data rate and pulse shaping, FTN signaling has lower PAPR. The FTN gains in terms of BER and PAPR increase using a pulse shape with a large excess bandwidth. In 2014, Siclet et al. investigated the multicarrier FTN signaling based on frame theory, [76]. Their work focused on the formulation and the minimization of the Mean Square Error (MSE) of such transceivers based on Weyl-Heisenberg frames. They showed that canonical dual frames minimize FTN-induced interference in case of an ideal channel, while tight frames are optimal when AWGN channels are considered. Theoretical results were validated via simulations using different pulse shapes and QPSK symbols.

In 2015, the authors of [83] considered an FTN system composed of LDPC channel coding, BPSK and 8-PSK modulation and SRRC filtering. Even when transmitting over an AWGN channel, signaling faster than the Nyquist rate introduces additional interference to the transmitted data that can be modeled as a discrete linear ISI channel perfectly known by the receiver. Therefore, the authors investigated the design of sparse graph

based codes for FTN signaling. They studied the improvement of the overall system spectral efficiency when the codes are optimized to match the FTN signaling in comparison with the use of the classical codes optimized for the AWGN channel case. They considered a Forney-type receiver, i.e., a matched filter followed by a whitening filter. To deal with FTN-induced interference, the authors proposed an iterative detection and decoding considering a turbo-equalizer based on the equivalent ISI channel. Based on this model, they performed an asymptotic analysis for turbo-equalized Bit Interleaved Coded Modulation (BICM) FTN-based systems using EXIT charts analysis and proposed an asymptotic optimization of LDPC codes to match FTN signaling. In their simulations, they considered MAP detection and linear MMSE equalization for BPSK and 8-PSK, respectively. The channel decoding is based on Belief Propagation decoding. First of all, their results showed that the achievable spectral efficiency for the FTN scheme (estimated using the area theorem, i.e., considering BICM with iterative decoding and perfectly matched inner code) is less than the one of Nyquist signaling with a roll-off $\rho = 0$ and a total bandwidth B. However, a significant improvement can be achieved when $\rho = 0.35$ with the same bandwidth. Nevertheless, FTN promises involve high decoding complexity due to the use of iterative decoding. Finally, BER results showed that significant improvement can be obtained compared to the AWGN optimized code performance in case of 8-PSK, while both methods give close performance in case of BPSK.

Later in 2016, Tajan et al. presented a transceiver design based on circular shaping signaling faster than the Nyquist rate [84]. They proposed an efficient implementation design in the frequency domain using the FFT and IFFT operations. The proposed transceiver does not require any cyclic prefix and is extendable to frequency selective channels. The receiver relies on the turbo-equalization algorithm meaning that soft information are exchanged between a linear MMSE equalizer and a soft channel decoder based on the BCJR algorithm. The transceiver performance was evaluated in case of 4-QAM modulation, SRRC filtering ($\rho = 0.35$) and AWGN channel. The EXIT charts showed that iterative decoding should converge as long as $\tau \geq 0.35$. Additionally, BER curves confirmed that BER below 10^{-5} is achievable for $\tau = 0.35$ with less than 0.5 dB loss.

The impact on PAPR when signaling faster than the Nyquist rate for satellite communications taking into account the on-board non linearities was investigated later by Lucciardi et al. in [85]. By comparing the FTN system to the Nyquist-based one at the same spectral efficiency, the authors showed an improvement in terms of BER and PAPR leading to more robust efficient waveforms in the non-linear context. The proposed system is based on convolutional codes for channel coding, M-ary PSK modulation and SRRC filtering with different roll-off factors ρ and is compared to a Nyquist-based system using an M-ary APSK modulation. The receiver is based on the turbo-equalization principle, i.e., soft information exchange between a MAP equalizer and a soft channel decoder. In satellite communications, the non-linearities represent a crucial issue and their impact increases with the modulation order as well as with the compression factor. Hence the trade-off between the spectral efficiency achieved by FTN signaling and the introduced signal envelope fluctuations and the PAPR. The authors investigated FTN systems operating at the same spectral efficiency as Nyquist-based systems, but offering better signal envelope robustness. They showed via simulations the relation between the time compression factor, the roll-off factor and the signal PAPR. For each roll-off factor, a reduced PAPR can be obtained by an optimal compression rate. At the same spectral efficiency, they proposed three FTN scenarios (scenario 1: $(\rho = 0.10, \tau = 0.75)$, scenario 2: $(\rho = 0.20, \tau = 0.6875)$, scenario 3: $(\rho = 0.35, \tau = 0.611)$) with 8-PSK modulation.

The best PAPR reduction was achieved with the highest roll-off factor of 0.35 and time compression factor of 0.61 offering a gain of 1.10 dB compared to a DVB-S2X system with 16-APSK modulation. In terms of BER, the FTN system still offers better BER performance than the DVB-S2X system at the same spectral efficiency. Their results showed a trade-off between the spectral efficiency increase and the PAPR reduction due to FTN signaling which calls for a careful selection of the modulation order, the roll-off factor and the compression factor when designing FTN systems. In the non-linear context and at the same spectral efficiency as DVB-S2X with 16-APSK, the second scenario of FTN signaling offers a 4 dB gain in terms of BER. The spectral efficiency can be increased up to 20% offering more BER gains than in the linear case.

Although the FTN concept was addressed by many researchers in the last years as a promising means to increase the transmission rate, it is still an on going research field. The combination of FTN signaling with widely used multi-carrier modulations such as OFDM and OFDM/OQAM has attracted many researchers to investigate efficient FTN schemes offering higher spectral efficiency than Nyquist-based systems without performance loss. Additionally, the advantages of OFDM/OQAM modulation (no need for cyclic-prefix and larger choice of pulse shapes having different time-frequency localization properties) make it a good candidate modulation to combine with FTN signaling. In fact, an implementation architecture of a transmitter signaling faster than the Nyquist rate in case of OFDM/OQAM modulation was proposed in [2]. Despite the advantages of the proposed scheme, it significantly increases the transceiver complexity compared to OFDM/OQAM systems. Therefore, more efficient FTN implementations offering the flexibility of switching between FTN and Nyquist modes with a limited increase of the transceiver complexity should be investigated. Moreover, interferences due to FTN signaling are also a crucial issue since pulses orthogonality is no longer respected, which calls for more complex receivers. In [3], the proposed receiver is based on MAP algorithm, the complexity of which increases with the modulation order. On the other hand, the complexity of linear equalizers is independent of the modulation order which makes them good candidates when high modulation orders are targeted. Additionally, as the introduced interference model is perfectly known by both the transmitter and the receiver, interference cancellation techniques should also be examined.

2.5 Selected channel coding and precoding techniques

In this section, we briefly review some channel coding, precoding and equalization concepts. In particular, the BCJR algorithm and its simplified version, the turbo equalization as well as Tomlinson-Harashima Precoding are described. These concepts will be used in next chapters for FTN signaling design.

2.5.1 BCJR Algorithm

For reliable data transmissions over noisy channels, error-correcting codes permit error detection and correction by adding redundancies to the transmitted data. Among the error-correcting codes, convolutional codes encode a message by continually feeding the message bits into a finite-state machine, as shown in Fig. 2.16, representing a rate-1/2 Recursive Systematic Convolutional (RSC) code. The finite-state machine is composed

of registers, denoted by D, initialized to 0, and modulo 2 adders, denoted by $\bigoplus$.

Convolutional codes can also be represented by their polynomial representation or by a trellis diagram, which describes the encoded bits in a layered direct graph. The RSC code depicted in Fig. 2.16 has two octal generator polynomials (1, 5/7) expressed as:

$$\begin{aligned} g^{(1)}(D) &= 1, \\ g^{(2)}(D) &= \frac{1+D^2}{1+D+D^2} \end{aligned} \tag{2.56}$$

The trellis representation is reported in Fig. 2.17. The set of vertices on the left-side of the diagram represents all the possible states of the convolutional encoder at the k-th stage, whereas the set of vertices on the right-side represents the possible states at the $(k+1)$-th stage. A transition between two stages is only possible if there is an edge connecting them, and is triggered by incoming bits at the encoder input. The edges labels represent the inputs/outputs of the convolutional encoder.

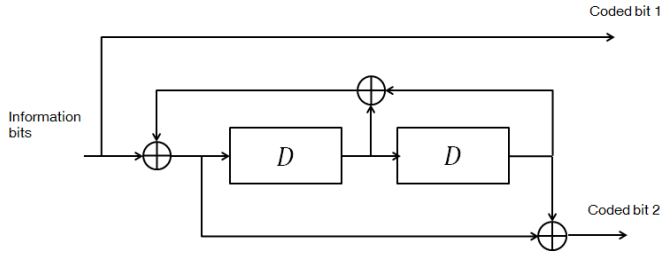

FIGURE 2.16: Rate 1/2 Recursive Systematic Convolutional code.

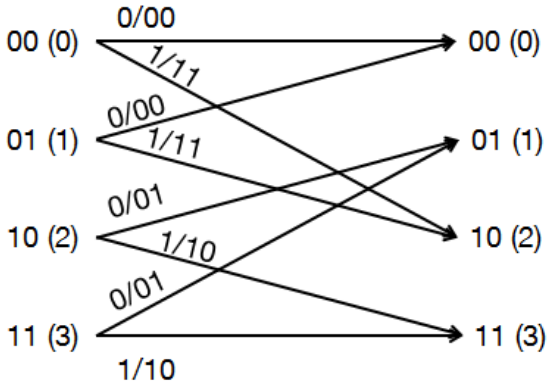

FIGURE 2.17: One trellis stage of the RSC code (1, 5/7). The encoder input and output bits are denoted by in/out labels at each trellis edge.

The trellis representation enables efficient probabilistic (Soft-In-Soft-Out (SISO)) decoding of convolutional codes. Probabilistic decoding aims at providing the probability of the k-th message bit, u_k, given a received noisy version of the corresponding codeword, $\mathbf{y}$, i.e., the *a posteriori* probabilities $p(u_k|\mathbf{y})$. These can be efficiently computed through the BCJR algorithm [45] (known also as MAP or forward-backward algorithm) applied

on the trellis representation of the convolutional encoder.

Let us consider the transmission of a vector of N_s symbols composed of n-bit codewords, $\mathbf{x} = [x_1, ..., x_{N_s}]$, where x_k is the symbol generated by the encoder at time k, while $x_{k,l}$ denotes its binary representation with $1 \leq l \leq n$. The corresponding information bit $u_k \in \{0, 1\}$ has an *a priori* probability $P(u_k)$, from which we define the log-likelihood ratio (LLR) as:

$$L(u_k) = \ln \frac{P(u_k = 1)}{P(u_k = 0)} \tag{2.57}$$

The received sequence $\mathbf{y}$ is delivered to the BCJR decoder in order to estimate the original bit sequence u_k, for which the algorithm computes the *a posteriori* LLR $L(u_k|\mathbf{y})$ defined as:

$$L(u_k|\mathbf{y}) = \ln \frac{P(u_k = 1|\mathbf{y})}{P(u_k = 0|\mathbf{y})}. \tag{2.58}$$

The LLR sign indicates which bit, 1 or 0, was coded at time k. Its magnitude is a measure of the confidence we have on the decision. Let $\mathbf{S}$ be the set of all possible states in the trellis, $s_k = s$ the state at time k and $s_{k-1} = s'$ the previous state. The received sequence $\mathbf{y}$ can be divided into three subsequences representing the past, the present and the future:

$$\mathbf{y} = \underbrace{y_1 y_2 ... y_{k-1}}_{\mathbf{y}_{<k}} y_k \underbrace{y_{k+1}, ..., y_{N_s}}_{\mathbf{y}_{>k}}.$$

The LLR can be expressed as:

$$\begin{aligned} L(u_k|\mathbf{y}) &= \ln \frac{\sum_{R_1} P(s', s, \mathbf{y})}{\sum_{R_0} P(s', s, \mathbf{y})} \\ &= \ln \frac{\sum_{R_1} \alpha_{k-1}(s')\gamma_k(s', s)\beta_k(s)}{\sum_{R_0} \alpha_{k-1}(s')\gamma_k(s', s)\beta_k(s)}, \end{aligned} \tag{2.59}$$

where, $P(s', s, \mathbf{y})$ represents the joint probability of receiving $\mathbf{y}$ and being at state s' at time $(k-1)$ and at state s at time k. R_1 and R_0 mean that the summation is computed over all the state transitions from s' to s that are due to message bit $u_k = 1$ and $u_k = 0$, respectively.
The joint probability $P(s', s, \mathbf{y})$ can be computed as the product of three probabilities:

$$P(s', s, \mathbf{y}) = \alpha_{k-1}(s')\gamma_k(s', s)\beta_k(s) \tag{2.60}$$

defined as:

$$\alpha_{k-1}(s') = P(s', \mathbf{y}_{<k}), \tag{2.61}$$

$$\gamma_k(s', s) = P(\mathbf{y}_k, s|s'), \tag{2.62}$$

$$\beta_k(s) = P(\mathbf{y}_{>k}|s). \tag{2.63}$$

The probability $\gamma_k(s', s)$ is the conditional probability that the received symbol is $\mathbf{y}_k$ at time k and the current state is s knowing that the state from which the connecting branch came from is s', and is given by:

$$\gamma_k(s', s) = P(\mathbf{y}_k|x_k)P(u_k). \tag{2.64}$$

In case of an AWGN channel, this expression becomes:

$$\gamma_k(s', s) = C_k e^{u_k L(u_k)/2} \exp(\frac{L_c}{2} \sum_{l=1}^{n} x_{k,l} y_{k,l}). \tag{2.65}$$

C_k is a quantity that will be canceled when computing the LLR, and L_c is the channel reliability measure:

$$L_c = 4\frac{E_c}{N_0} = 4R_c\frac{E_b}{N_0},$$

with, $N_0/2$ the noise bilateral power density, R_c the code rate, E_c and E_b the transmitted energy per coded bit and message bit, respectively.

On the other hand, α and β are called the forward and backward metrics associated with the past and the future of the sequence $\mathbf{y}$ and are defined as:

$$\alpha_k(s) = \sum_{s'} \alpha_{k-1}(s')\gamma_k(s', s), \tag{2.66}$$

$$\beta_{k-1}(s') = \sum_{s} \beta_k(s)\gamma_k(s', s). \tag{2.67}$$

If the beginning and ending states of the trellis are known, $\alpha_0(s)$ and $\beta_{N_s}(s)$ are initialized to 1, (while $\alpha_{k-1}(s')$ and $\beta_k(s)$ of all the remaining states are initialized to 0 by default). Finally the *a posteriori* probabilities $P(u_k = 1)$ and $P(u_k = 0)$ are computed.

Simplified BCJR

The BCJR algorithm can be simplified by considering the log-MAP and Max-Log-MAP algorithms that process the probabilities in the logarithm domain and that allow the multiplications to be replaced by additions. Three new variables are defined:

$$\begin{aligned} \Gamma_k(s', s) &= \ln \gamma_k(s', s) && (2.68)\\ &= \ln C_k + \frac{u_k L(u_k)}{2} + \frac{L_c}{2} \sum_{l=1}^{n} x_{k,l} y_{k,l} && (2.69) \end{aligned}$$

$$\begin{aligned} A_k(s) &= \ln \alpha_k(s) && (2.70)\\ &= \overset{*}{\max_{s'}}[A_{k-1}(s') + \Gamma_k(s', s)] && (2.71) \end{aligned}$$

$$\begin{aligned} B_{k-1}(s') &= \ln \beta_{k-1}(s') && (2.72)\\ &= \overset{*}{\max_{s}}[B_k(s) + \Gamma_k(s', s)] && (2.73) \end{aligned}$$

where:

$$\overset{*}{\max}(a, b) = \begin{cases} \max(a, b) + \ln(1 + e^{-|a-b|}) & \text{Log-MAP algorithm} \\ \max(a, b) & \text{Max-Log-MAP algorithm} \end{cases} \tag{2.74}$$

If the beginning and ending states of the trellis are known, $A_0(s)$ and $B_{N_s}(s)$ are initialized to 0 (while $A_{k-1}(s')$ and $B_k(s)$ of all the remaining states are initialized to $-\infty$ by default). The LLR is then approximated by:

$$L(u_k|\mathbf{y}) = \max^{*}_{R_1}[A_{k-1}(s') + \Gamma_k(s', s) + B_k(s)] - \max^{*}_{R_0}[A_{k-1}(s') + \Gamma_k(s', s) + B_k(s)] \quad (2.75)$$

2.5.2 Turbo coding and turbo equalization

Turbo codes were introduced in 1993 as practical codes to closely approach the capacity of AWGN channel within a fraction of a decibel [86]. Turbo codes have been adopted by many communications standards such as the International Mobile Telecommunications IMT-2000, Universal Mobile Telecommunications System (UMTS), High Speed Packed Access (HSPA), LTE [87], and satellite communication systems such as DVB-Return Channel via Satellite (DVB-RCS) [88], [89].

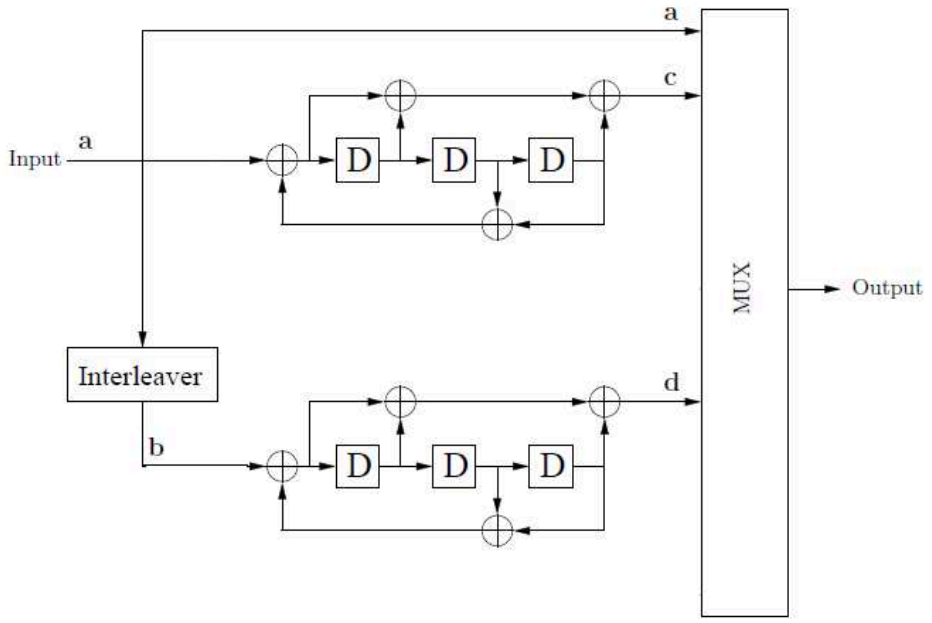

FIGURE 2.18: Turbo encoder architecture.

Turbo encoders can be composed of either parallel or serial concatenation of RSC encoders separated by an interleaver. Fig. 2.18 depicts a turbo encoder, where the input information sequence a is encoded twice by two parallel RSC encoders. The first RSC encodes a in its original order while the second RSC encodes its interleaved version, b. The decoding process uses two SISO *a posteriori* probability (APP) decoders to compute the *a posteriori* probabilities of the systematic and parity bits based on the BCJR algorithm. The turbo decoder is shown in Fig. 2.19, where sequences $\tilde{a^c}$, $\tilde{c^c}$ and $\tilde{d^c}$ are soft inputs computed by the demodulator and correspond to sequences a, c and d. To keep the correct order of the input sequences, the same interleaver (Π) and the corresponding deinterleaver (Π^{-1}) are used in the decoding process. Modules *Decoder 1* and *Decoder 2* exchange the extrinsic information, as formally defined in the following subsection, instead of *a posteriori* information. The purpose is to extract only information that is

newly learnt from the BCJR decoding. This can be obtained by a simple subtraction between the *a posteriori* information computed by each decoder and the *a priori* information at their input. The *Decoder 1* module takes as inputs the *a priori* information of parity bits $\tilde{c}^c$ as well as the sum of the *a priori* information of systematic bits delivered by the demodulator and the extrinsic information computed by the *Decoder 2* block, $\tilde{a}^a$. The whole decoding process stops when the maximum number of iterations or the required reliability are reached.

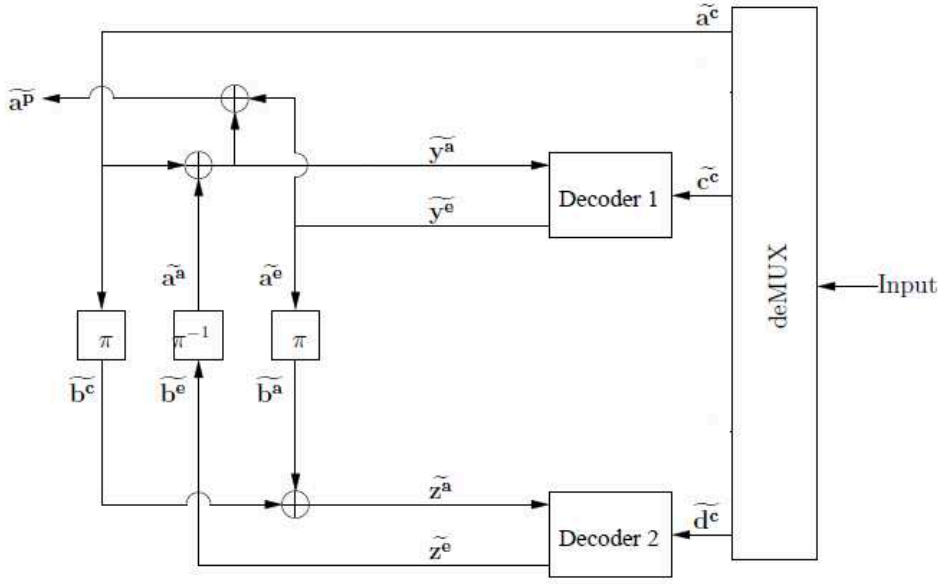

FIGURE 2.19: Turbo decoder architecture.

2.5.3 Turbo equalization

Originally, turbo codes have been introduced in case of memoryless AWGN channels and were shown to perform near the capacity limit. The turbo code principle was extended to ISI channels, as turbo equalization, and proven to be able to iteratively remove ISI. The ISI channel is considered as a constituent code for the turbo encoder and modeled as a tapped delay line with coefficients $h_{-L}, ..., h_L$. Fig. 2.20 shows a turbo equalizer where $\mathbf{y}$ is the data sequence at the channel output, $\mathbf{L}_e(\mathbf{x})$ and $\mathbf{L}_e(\mathbf{c})$ are the bit-level extrinsic information at the output of the SISO equalizer and the decoder, respectively. On the other hand, $\mathbf{L}_a(\mathbf{x})$ and $\mathbf{L}_a(\mathbf{c})$ are the input *a priori* information of the SISO equalizer and the decoder, respectively. The same interleaver (Π) and the corresponding de-interleaver (Π^{-1}) allows detecting the sequence in the correct order.

Generally, there are two families of turbo equalization. The MAP equalization is based on the BCJR algorithm and can totally remove the interference under certain conditions. However, its complexity is of order K^L, where K is the number of the modulation states and L the number of discrete channel coefficients. On the other hand, the MMSE equalization follows the MMSE criterion [90], [91]. It is realized by linear filtering leading

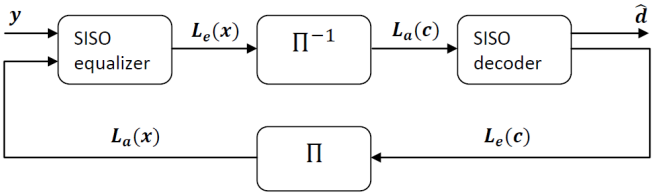

FIGURE 2.20: Turbo equalizer structure.

to a lower complexity. In fact, the complexity is independent of the modulation order and increases linearly with the ISI channel length, although the performance is sub-optimal. In 1997, Glavieux et al. put forward the first MMSE turbo equalization scheme [92], [93], [94], laying down the foundation for filter-based SISO equalizers. In their scheme, the equalizer coefficients were computed according to the Least-Mean-Square (LMS) algorithm. Later on and based on the work in [95], [96], [97], [98], Laot et al. proposed an MMSE interference canceller in infinite-length form, named MMSE Interference Canceller-Linear Equalizer (MMSE-IC-LE) [99]. The equalizer is detailed in the next section.

MMSE IC-LE structure

The SISO MMSE equalizer reported in Fig. 2.20 exchanges soft information with the SISO decoder. This requires a translation of soft information from the symbol-level to the bit-level. Hence, two functions are introduced to address this challenge: the SISO mapping and demapping. The SISO MMSE equalizer is detailed in Fig. 2.21, where $\mathbf{z}$ is the equalized sequence and $\bar{\mathbf{x}}$ is the estimated symbol sequence with variance σ_x^2.

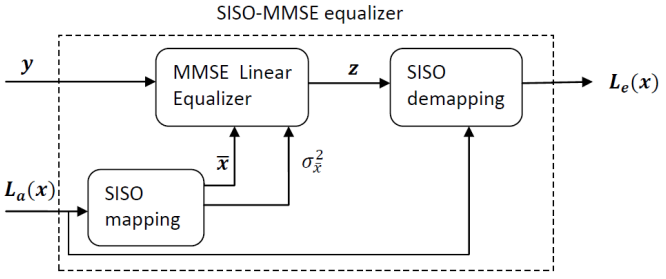

FIGURE 2.21: Structure of the SISO MMSE equalizer.

SISO Mapping

This block uses *a priori* information, delivered by the decoder, to compute the soft estimated symbols. Consider $\bar{x}_i$ the estimated symbol at time instance i, then:

$$\bar{x}_i = E_a\{x_i\} = \sum_{l=1}^{K} X_l \times P_a(X_l), \tag{2.76}$$

where $E\{.\}$ is the expectation operation and $P_a(X_l)$ represents the *a priori* probability of choosing the symbol X_l. We have put index a at the level of the expectation term

to highlight the fact that these probabilities are deduced from *a priori* information at the equalizer input. Provided the n bits making up the symbol x_i are statistically independent, $P_a(X_l)$ is calculated as follows:

$$P_a(X_l) = \prod_{j=1}^{n} P_a(X_{l,j}). \tag{2.77}$$

Considering binary elements $X_{l,j}$, the *a priori* probability $P_a(X_{l,j})$ is expressed as:

$$P_a(X_{l,j}) = \frac{1}{2}(1 + (2X_{l,j} - 1)\tanh(\frac{L_a(x_{l,j})}{2}). \tag{2.78}$$

The binary element $X_{l,j}$ takes the value 0 or 1 according to the considered symbol X_l and the mapping rule. In the particular case of BPSK modulation, the above equation can be further simplified providing the following soft estimate for $\bar{x}_i$:

$$\bar{x}_i = \tanh(\frac{L_a(x_i)}{2}). \tag{2.79}$$

The value of the estimated symbols $\bar{x}_i$ evolves as a function of the reliability of the *a priori* information provided by the decoder. They constitute random variables with zero mean and a variance $\sigma_{\bar{x}}^2$ expressed as:

$$\sigma_{\bar{x}}^2 = \frac{1}{N_c} \sum_{i=0}^{N_c-1} |\bar{x}_i|^2, \tag{2.80}$$

where N_c is the length of the symbols frame.

MMSE equalizer

The equalization is composed of an interference cancellation step, followed by a filtering operation. The equalizer coefficients are computed according to the MMSE algorithm between the equalized symbols z_i, at time instance i, and symbols $x_{i-\Delta}$. To take into account the anti-causality of the solution, a delay Δ is introduced. We consider a filter $\mathbf{f} = (\mathbf{f}_0, ..., \mathbf{f}_{F-1})$ with F coefficients and a matrix formulation for the received signal. We also suppose that the ISI channel response and the noise variance are already known by the equalizer. The F received samples up until instant i are expressed as:

$$\mathbf{y}_i = \mathbf{H}\mathbf{x}_i + \mathbf{w}_i, \tag{2.81}$$

with $\mathbf{y}_i = (y_i, .., y_{i-F+1})$, $\mathbf{x}_i = (x_i, .., x_{i-F-L+2})$ and $\mathbf{w}_i = (w_i, .., w_{i-F+1})$. $\mathbf{H}$ is a Toeplitz matrix of dimensions $F \times (F + L - 1)$ describing the channel convolution as:

$$\mathbf{H} = \begin{pmatrix} h_0 & ... & h_{L-1} & 0 & ... & 0 \\ 0 & h_{-1} & ... & h_{L-1} & & \vdots \\ \vdots & & \ddots & & \ddots & 0 \\ 0 & ... & 0 & h_{-(L-1)} & ... & h_0 \end{pmatrix} \tag{2.82}$$

The interference cancellation step is performed as :

$$\tilde{\mathbf{y}}_i = \mathbf{y}_i - \mathbf{H}\tilde{\mathbf{x}}_i, \tag{2.83}$$

where the vector $\tilde{\mathbf{x}}_i = (\bar{x}_i, ..., \bar{x}_{i-\Delta+1}, 0, \bar{x}_{i-\Delta-1}, ..., \bar{x}_{i-F-L+2})$ is a sequence of $F+L-1$ estimated symbols, and $\bar{x}_{i-\Delta}$ is set to zero in order to cancel only the ISI and not the useful symbol. The equalized sample z_i is then obtained:

$$z_i = \mathbf{f}^T \tilde{\mathbf{y}}_i. \tag{2.84}$$

Considering that the equalizer coefficients are unchanged for the same block of symbols, they are calculated using the projection theorem:

$$E\{(z_i - x_{i-\Delta})\tilde{\mathbf{y}}_i^H\} = 0, \tag{2.85}$$

where $\mathbf{A}^H$ denotes the Hermitian transpose of matrix $\mathbf{A}$. The equalizer coefficients can then be expressed as (see [90], Chap. 11] for more details):

$$\mathbf{f}^* = \frac{\sigma_x^2}{1 + \beta\sigma_{\tilde{x}}^2}\tilde{\mathbf{f}}^*, \tag{2.86}$$

with:

$$\tilde{\mathbf{f}}^* = [(\sigma_x^2 - \sigma_{\tilde{x}}^2)\mathbf{H}\mathbf{H}^H + \sigma_w^2\mathbf{I}]^{-1}\mathbf{h}_\Delta, \tag{2.87}$$

$$\beta = \tilde{\mathbf{f}}^T \mathbf{h}_\Delta. \tag{2.88}$$

$\mathbf{h}_\Delta$ is the Δ-th column of the matrix $\mathbf{H}$, $\mathbf{I}$ the identity matrix and σ_w^2 the noise variance.

The SISO MMSE equalizer adapts the equalization according to the reliability of the estimated symbols, measured by $\sigma_{\tilde{x}}^2$. On the other hand, it is worthwhile noting that the interference cancellation cannot be directly performed according to (2.84). A practical equalizer is presented in Fig. 2.22, where $\mathbf{g} = \mathbf{f}^T\mathbf{H}$ is a filter having the central coefficient g_Δ forced to zero.

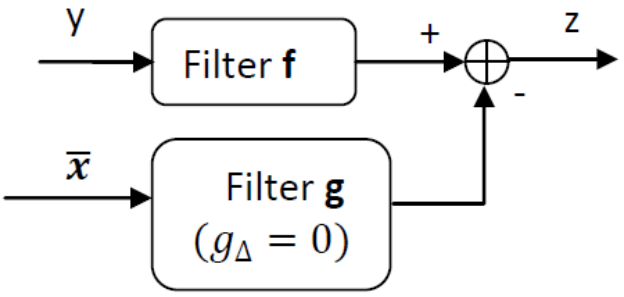

FIGURE 2.22: Practical implementation of the MMSE linear equalizer.

SISO Demapping

This function permits exchanging soft information between the equalizer and the decoder by converting the equalized symbols to LLRs on the interleaved coded bits. At the equalizer output, a sample z_i at instant i can be expressed as:

$$z_i = g_\Delta x_{i-\Delta} + v_i \tag{2.89}$$

The first term represents the useful signal multiplied with a constant factor g_Δ, while the second term represents both the noise and the residual interference. In order to perform the SISO demapping, we suppose that v_i follows a complex Gaussian distribution with zero mean and total variance σ_v^2. These parameters are computed according to:

$$g_\Delta = \mathbf{f}^T \mathbf{h}_\Delta \qquad \text{and} \quad \sigma_v^2 = E\{|z_i - g_\Delta x_{i-\Delta}|^2\} = \sigma_x^2 g_\Delta (1 - g_\Delta) \tag{2.90}$$

The demapping function computes the *a posteriori* LLRs on the coded interleaved bits, denoted $L(x_{i,j})$:

$$L(x_{i,j}) = \ln\left(\frac{Pr(x_{i,j}=1|z_i)}{Pr(x_{i,j}=0|z_i)}\right) \tag{2.91}$$

The numerator and denominator values can be expressed by summing the *a posteriori* probabilities of transmitting a symbol X_l whose $j-th$ bit is 1 or 0, respectively. Equation (2.91) is then reformulated:

$$L(x_{i,j}) = \ln\left(\frac{\sum\limits_{X_l/X_{l,j}=1} P(z_i|x_i=X_l)P_a(X_l)}{\sum\limits_{X_l/X_{l,j}=0}, P(z_i|x_i=X_l)P_a(X_l)}\right) \tag{2.92}$$

with

$$P(z_i|x_i=X_l) = \frac{1}{\pi\sigma_v^2}\exp(-\frac{|z_i - g_\Delta X_l|^2}{\sigma_v^2}). \tag{2.93}$$

The *a posteriori* LLR then becomes:

$$L(x_{i,j}) = \ln\left(\frac{\sum\limits_{X_l/X_{l,j}=1} \exp(-\frac{|z_i - g_\Delta X_l|^2}{\sigma_v^2} + \sum_{k=1}^{n} X_{l,k}L_a(x_{i,k}))}{\sum\limits_{X_l/X_{l,j}=0} \exp(-\frac{|z_i - g_\Delta X_l|^2}{\sigma_v^2} + \sum_{k=1}^{n} X_{l,k}L_a(x_{i,k}))}\right) \tag{2.94}$$

Finally, the extrinsic information is obtained as:

$$L_e(x_{i,j}) = L(x_{i,j}) - L_a(x_{i,j}) \tag{2.95}$$

2.5.4 Convergence analysis using EXIT charts

The performance of turbo equalization, in terms of BER vs. SNR, is characterized by several convergence properties such as: the convergence speed which is the number of iterations required until no further error rate decrease is observed, and the convergence SNR threshold from which the decoder can begin to correct most of the errors. These properties depend on different factors like the channel coding and decoding algorithm, the channel model and the equalizer's structure. In order to design an appropriate equalization scheme, it is important to analyze the influence of these parameters.

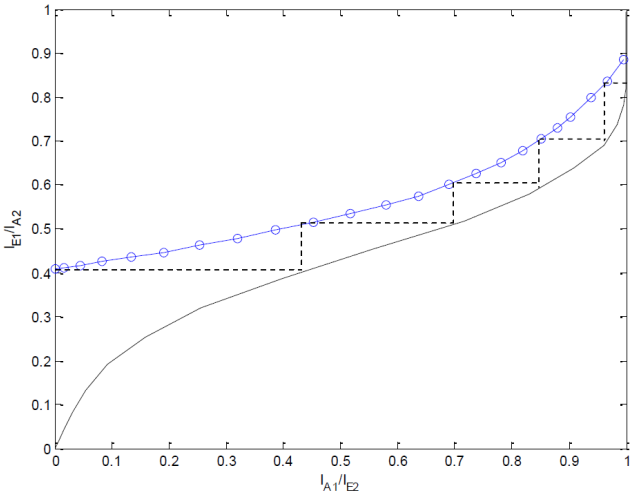

FIGURE 2.23: Typical EXIT chart diagram.

A powerful graphic tool to address this analysis is the EXIT chart introduced in 1999 by ten Brink [26]. The EXIT chart describes the evolution of mutual information between the transmitted bit and the soft information during the iterative process. Although it was originally introduced to evaluate the convergence properties of turbo codes, it can also be used in the case of turbo equalization. In this section, we briefly discuss the EXIT chart analysis for the MMSE-IC LE equalization.
The SISO equalizer in Fig. 2.20 is considered as an inner decoder which takes *a priori* LLRs and the observed data as inputs, and delivers extrinsic LLRs about the coded bits. We denote by I_{A1} the mutual information between the *a priori* LLRs and the transmitted data, and by I_{E1} the mutual information associated with the extrinsic LLRs at the equalizer's output. The SISO equalizer action can be represented as:

$$I_{E1} = T_1(I_{A1}, \text{channel}). \tag{2.96}$$

Similarly, the BCJR decoder action can be viewed as:

$$I_{E2} = T_2(I_{A2}), \tag{2.97}$$

where I_{A2} is the mutual information between the *a priori* LLRs at the decoder's input and the transmitted data. Here, the channel information is not present in the decoder's transfer function, since it only takes the *a priori* information, delivered by the equalizer, as input.
The mutual information between the transmitted data and the LLRs is measured as:

$$I(L,x) = \frac{1}{2}\sum_{x=-1,+1}\int_{-\infty}^{+\infty} f(L|x) \times \log_2[\frac{2f(L|x)}{f(L|-1)+f(L|+1)}]dz, \tag{2.98}$$

where L is the *a priori* or the output extrinsic LLR, x is the coded bit taking values $\{-1,+1\}$ according to the mapping rule: $0 \rightarrow -1, 1 \rightarrow +1$.
For the *a priori* information, the function $f(L|x)$ can be approximated as a Gaussian distribution, provided that a large interleaver is used. However, this approximation is not valid for the output extrinsic information, which calls for numerical methods to estimate its distribution (histogram measurements).
Due to the iterative decoding process, the extrinsic LLRs at the equalizer's output are

considered as *a priori* LLRs by the decoder, and vice-versa. Therefore, we have $I_{A1} = I_{E2}$ and $I_{A2} = I_{E1}$. By swapping the abscissas of the outer decoder, we can combine the transfer function of the equalizer and the decoder in the same diagram, see Fig. 2.23. This diagram is referred to as EXIT chart since the exchange of intrinsic information between the inner and outer decoder can be visualized as a decoding trajectory. In fact, the trajectory between the two transfer function curves represents the iterative process of convergence. Note that, due to the approximations, the decoding trajectory given by the EXIT chart only provides a rough indication on the minimum number of iterations required for decoding convergence.

2.5.5 Tomlinson Harashima Precoding

The concatenation of FTN signaling with precoding has been addressed by many authors. In [47], the authors investigated the performance of a rate-1 precoder combined with a parallel concatenation of FTN signaling and coding. They also studied an optimal precoder for FTN signaling in [49]. The PSD and the spectrum broadening of FTN signaling with convolutional precoding has been investigated in [58]. In [100], a precoding technique based on matrix decomposition has been proposed for FTN signaling together with receivers based on MMSE and Decision Feedback Equalizers (DFE). The authors proposed to decompose the matrix representing FTN-induced ISI using Singular Value Decomposition (SVD) and Geometric Mean Decomposition (GMD). Precoding techniques based on these decompositions were used at the receiver side. Simulation results showed the benefit of GMD precoding compared to DFE.

As mentioned earlier, FTN signaling introduces interference to the useful signal, since orthogonality conditions no longer hold. In order to reduce these interference, a precoder can be inserted at the transmitter side. An interesting means to combat interference via precoding is Tomlinson-Harashima Precoding (THP) introduced independently and almost simultaneously by Tomlinson [101] and Harashima and Miyakawa [102], [103]. In [104] and [105], the authors propose an FTN scheme for coherent optical systems enabled by THP. The ISI caused by FTN is handled by THP at the transmitter. The coefficients of the corresponding optimal DFE are calculated. Then, the FeedBack Filter (THP-FBF) is placed at the transmitter, while the FeedForward Equalizer (THP-FFE) is placed at the receiver side.

Tomlinson-Harashima precoding was originally proposed for transmissions of one-dimensional PAM signals in a set $A = \{\pm 1, \pm 3, ..., \pm(M-1)\}$, with M an even integer. The channel impulse response $h[k]$ of some order p is supposed canonical, i.e, causal, monic ($h[0] = 1$), and minimum phase. Here, we denote the corresponding transfer function by: $H(z) = 1 + \sum_{k=1}^{p} h[k]z^{-k}$. Supposing that $H(z)$ is known by the transmitter, we can pre-equalize the signal at the transmitter side using the inverse transfer function $1/H(z)$, which can be realized by the feedback structure shown in Fig. 2.24, with negative feedback $H(z) - 1$. However, the transmitted power is boosted, due to the filter $1/H(z)$. The idea of THP is to replace the linear pre-equalization by a non-linear precoder in order to avoid power increase. This makes THP similar to DFE, except that DFE error propagation is avoided, since equalization is done at the transmitter. To this end, THP replaces the adder in Fig. 2.24, by an arithmetic *modulo*-$2M$. The modulo adder assures that precoded symbols are kept in the interval $[-M, M]$: if the result of the summation

exceeds M, $2M$ is repeatedly subtracted until the result is less than M. Similarly, if the summation is less than $-M$, $2M$ is repeatedly added until the result is greater than $-M$. The structure of THP is depicted in Fig. 2.25.

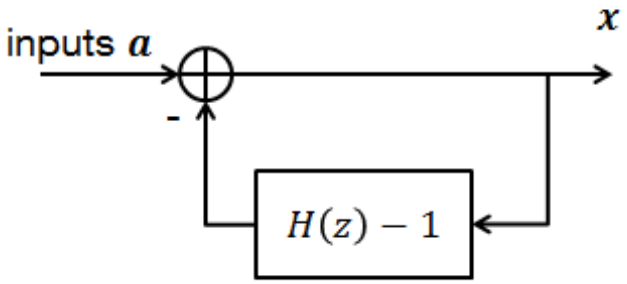

FIGURE 2.24: Structure of the inverse filter.

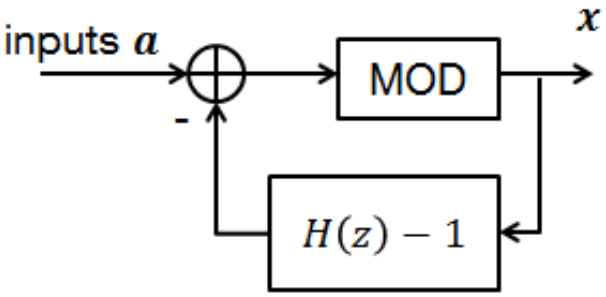

FIGURE 2.25: Structure of the THP precoder.

The effect of the modulo operation can be seen as follows: a unique precoding sequence $d[k] \in 2M\mathbb{Z}$ is added to the input sequence $a[k]$. The result sequence, named the effective sequence, is then filtered by the filter $1/H(z)$. Hence the resulted sequence:

$$x[k] = a[k] + d[k] - \sum_{l=1}^{p} h[l]x[k-l] \tag{2.99}$$

$$= v[k] - \sum_{l=1}^{p} h[l]x[k-l] \tag{2.100}$$

falls into $[-M, M]$. The modulo operation is also represented as an extension of the original signal set A, which means that each symbol has different representations based on congruent signal levels. The new signal set is expressed as follows:

$$V = A + 2M\mathbb{Z} = \{a + d, \quad a \in A, \quad d \in 2M\mathbb{Z}\} \tag{2.101}$$

The modulo operation of THP ensures selecting an effective sequence from the set V that it is congruent to the input sequence $a[k]$, and at the same time minimizes the amplitude

of the precoded symbol $x[k]$. Hence, THP is matched to the channel impulse response and to the original signal set A.
The received signal can be written as:

$$y[k] = x[k] + \sum_{l=1}^{p} h[l]x[k-l] + n[k] \quad (2.102)$$

$$= v[k] + n[k] \quad (2.103)$$

where $n[k]$ is the white Gaussian noise sequence. Thus in the absence of noise, the same modulo operation is performed by the receiver to reduce the sequence $v[k]$ to the original interval $[-M, M]$, enabling a symbol-by-symbol threshold decision. This way, THP transforms the ISI channel into a memoryless one. However, due to the modulo operation, the noise sequence is signal dependent and no longer exactly Gaussian. This effect can be neglected for moderate to high SNRs.

In the remainder of this dissertation, we will detail our studies on Faster-Than-Nyquist signaling in the framework of multi-carrier modulations. In order to push the transmitted rate to its limit, we will consider the OFDM/OQAM modulation since no cyclic-prefix is needed. Moreover, more degrees of freedom designing the modulating pulse shape with good time-frequency localization properties are possible. Our objective is to investigate low complexity transceivers signaling faster than Nyquist-based OFDM/OQAM systems. Additionally, our work is focused on linear receivers to deal with FTN-induced interferences since their complexity is independent of the modulation order and increases linearly with the length of the channel impulse response. To this end, the iterative receiver is based on the aforementioned turbo equalization principle combining a linear MMSE equalizer and a BCJR decoder. As the introduced interferences are completely known at the transmitter side, interference pre-cancellation techniques proposed in the case of perfectly known Channel State Information (CSI) by the transmitter can be envisaged. Consequently, we will propose an interference pre-cancellation technique inspired from the Tomlinson Harashima Precoding to reduce FTN-self interferences.

2.6 Conclusion

In this chapter, we provided some relevant studies concerning faster-than Nyquist transmission. We listed several FTN solutions that were presented in the literature. We also introduced two well known MCMs: OFDM and OFDM/OQAM transmissions. In the following chapters, the OFDM/OQAM scenario is considered for our work regarding FTN transmissions. Moreover, we reviewed some concepts on channel coding and turbo equalization as well as precoding. These concepts will be elaborated more in details in next chapters.

Chapter 3

An FTN transceiver for OFDM/OQAM systems

3.1 Introduction

In the previous chapter we presented the concept of FTN signaling, introduced originally by Mazo, to boost the transmission rate beyond the Nyquist limit. Indeed, Mazo showed for BPSK that as long as the boosted rate i.e., the ratio between the Nyquist and the FTN rate, does not go further $1.25x$, the resulting minimum sequence distance always keeps constant. However, this concept was not deemed as an attractive means until the trend of the explosion of throughput becomes unavoidable. Recently, FTN was re-investigated for different case scenarios, including the well known OFDM and OFDM/OQAM modulations. In fact, OFDM/OQAM has been presented as a more advanced multicarrier modulation than OFDM, since it can use waveforms having different time-frequency localization features and since no cyclic prefix is required any longer, reaching therefore full Nyquist rate.

The first work on FTN combined with OFDM/OQAM modulation, denoted here by FTN-OQAM, was presented in [2]. The authors introduced a block called *FTN mapper* to the classical OFDM/OQAM modulator. Due to this additional block, the complexity of their solution is higher than that of the classical OFDM/OQAM systems and depends on the block size. At the receiver side, they proposed a MAP-based receiver, the complexity of which increases with the modulation order [3].

In this chapter, we consider the concept of FTN signaling over an AWGN channel in the case of OFDM/OQAM modulation. First, we present a different FTN-OQAM realization that retains the advantages of the State of The Art (SoTA) solution and at the same time solves the remaining problems. Then, we propose a turbo-like receiver based on linear MMSE filtering and SIC whose complexity is independent of the modulation order. This makes it a good candidate when high modulation orders are envisaged.

3.2 FTN-OQAM modem

In this section, we present a new implementation of FTN signaling for OFDM/OQAM systems assuming that signals are only packed closer, with respect to Nyquist rate, in time domain. The proposed implementation does not increase the complexity compared to the classical Nyquist-based OFDM/OQAM systems and has the flexibility of switching between Nyquist and FTN modes. In addition, the effective rate approaches the FTN theoretical rate very closely.

3.2.1 FTN-OQAM modulator

Considering FTN signaling combined with OFDM/OQAM modulation, the transmitted continuous-time baseband signal is expressed as follows:

$$s(t) = \sum_{m=0}^{M-1} \sum_{n=-\infty}^{+\infty} a_{m,n} g(t - \frac{n\tau T_0}{2}) e^{j2\pi m\zeta F_0 t} e^{j\Phi_{m,n}}, \tag{3.1}$$

where $0 < \tau \leq 1$ and $0 < \zeta \leq 1$ are the FTN time and frequency packing factors, respectively. We assume $\zeta = 1$ and consider only packing the pulses closer in time domain, i.e., $\tau < 1$. The discrete version of (3.1) is obtained by sampling the signal at $T_s = \frac{T_0}{M}$:

$$s[k] = \sum_{m=0}^{M-1} \sum_{n=-\infty}^{+\infty} a_{m,n} g[k - nN_f] e^{\frac{j2\pi mk}{M}} e^{j\Phi_{m,n}}. \tag{3.2}$$

This expression can be reformulated as:

$$s[k] = \underbrace{\sum_{m=0}^{M-1} a_{m,n} e^{j\Phi_{m,n}} e^{\frac{j2\pi mk}{M}}}_{Fourier\ Transform} \sum_{n=-\infty}^{+\infty} g[k - nN_f]. \tag{3.3}$$

The Fourier Transform is implemented using the IFFT algorithm, and according to the causality of the prototype filter g, two implementation structures are presented.

3.2.1.1 The modulator structure for non-causal prototype filter

In this case, the prototype filter $g[k]$, with $k \in [-\frac{L-1}{2}, \frac{L-1}{2}]$ is non-causal and centered at $k = 0$. A delay $\frac{D}{2} = \frac{L-1}{2}$ is introduced to the Fourier transform, i.e., $k \in [0, L-1]$. This process can be implemented by replacing the index k by $k - nN_f + \frac{D}{2}$. The discrete-time signal is then expressed as:

$$s[k] = \underbrace{\sum_{n=0}^{+\infty} g[k - nN_f] \underbrace{\sum_{m=0}^{M-1} \underbrace{a_{m,n} e^{j\Phi_{m,n}} e^{\frac{j2\pi m(nN_f - \frac{D}{2})}{M}}}_{Pre-processing} e^{\frac{j2\pi m(k - nN_f + \frac{D}{2})}{M}}}_{IFFT+CYCEXD}}_{filtering}, \tag{3.4}$$

where the FTN expansion/decimation factor is denoted by $N_f = \lfloor \tau . \frac{M}{2} \rfloor$, with $\lfloor . \rfloor$ the floor function.
Thanks to the periodicity property of the IFFT, the filtering is realized using a cyclic extension per block, followed by a multiplication with a single coefficient and finally by a Parallel-to-Serial (P/S) conversion as shown in Fig. 3.1. Mathematically, the cyclic extension block, named **CYCEXD**, is expressed in the following $L \times M$ matrix form:

$$\mathbf{CYCEXD}_{L\times M} = \begin{bmatrix} \mathbf{I}_{M\times M} \\ ... \\ \mathbf{I}_{M\times M} \end{bmatrix}_{L\times M}$$

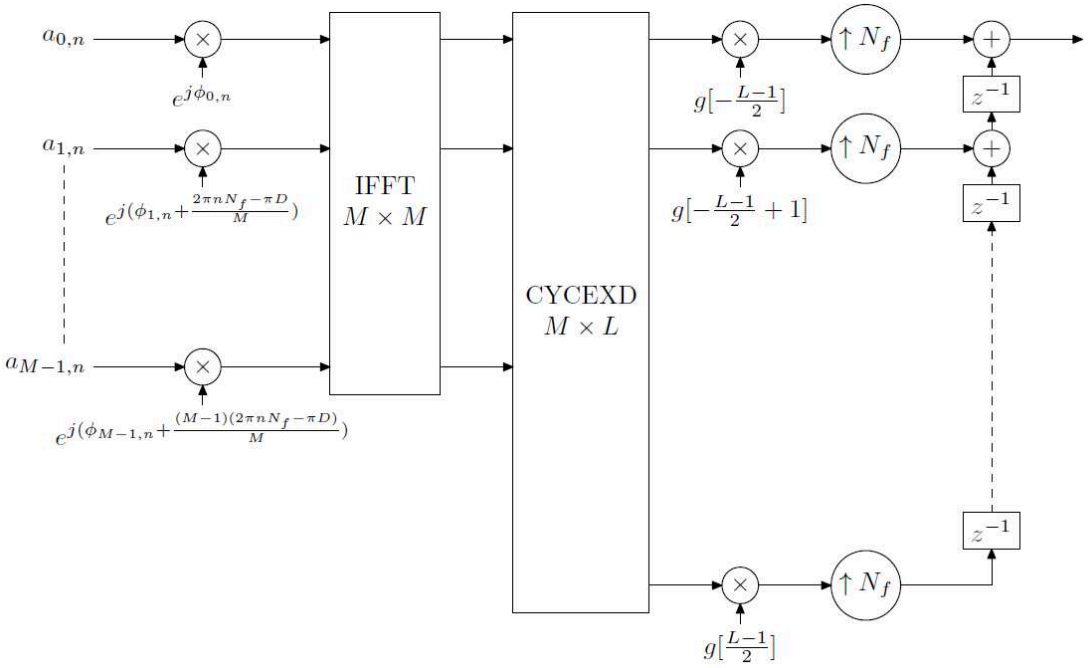

FIGURE 3.1: *FTN-OQAM non-causal modulator.*

where $\mathbf{I}_{M\times M}$ is the M-size identity matrix.

3.2.1.2 The modulator structure for causal prototype filter

The prototype filter g is supposed to be causal, i.e. $k \in [0, L-1]$. Then, (3.3) is expressed as:

$$s[k] = \underbrace{\sum_{n=0}^{+\infty} g[k-nN_f] \underbrace{\sum_{m=0}^{M-1} \underbrace{a_{m,n} e^{j\Phi_{m,n}} e^{\frac{j2\pi m(nN_f - \frac{D}{2})}{M}}}_{Pre-processing} e^{\frac{j2\pi m(k-nN_f)}{M}}}_{IFFT+CYCEXD}}_{filtering} \tag{3.5}$$

Similarly to the non-causal case, the Fourier transform is implemented using IFFT. The modulator structure is reported in Fig. 3.2, where the **CYCEXD** is the same as in the previous case.

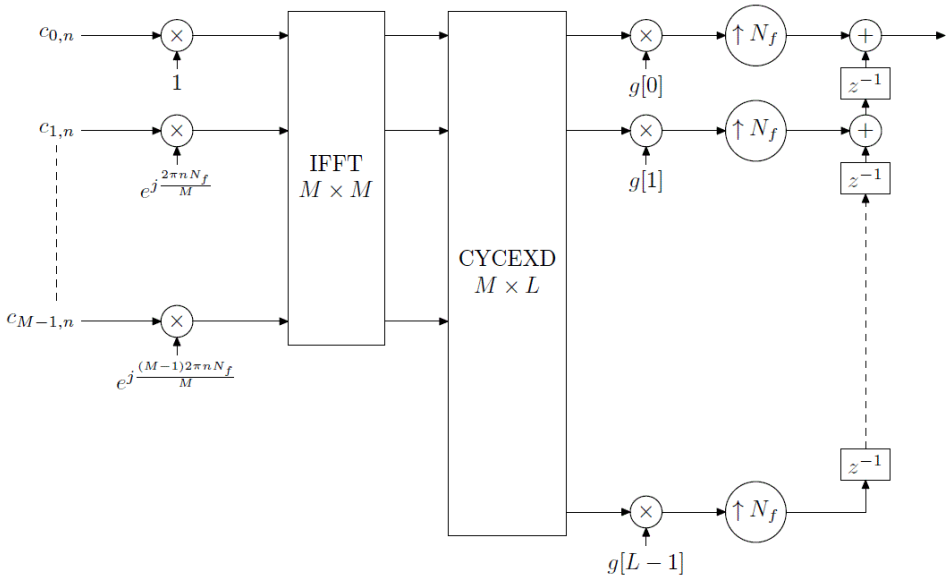

FIGURE 3.2: *FTN-OQAM causal modulator.*

3.2.2 FTN-OQAM demodulator

At the receiver side, the demodulator performs the dual operations of the modulator. The structure of the demodulator in case of a causal prototype filter is depicted in Fig. 3.3. Considering that OFDM/OQAM demodulation extracts only the real part of the received signal, the demodulated signal at time instant n_0 and at subcarrier m_0 is:

$$y_{m_0,n_0} = \Re\{\sum_k s[k]g[k-n_0N_f]e^{-j\Phi_{m_0,n_0}}e^{-\frac{j2\pi m_0(k-\frac{D}{2})}{M}}\}. \tag{3.6}$$

Since $g[k]$ of length L is causal, $k \in [n_0N_f, n_0N_f + L - 1]$. In order to perform an $M \times M$ FFT, (3.6) is modified as follows:

$$y_{m_0,n_0} = \Re\{\underbrace{\sum_{k=n_0N_f}^{n_0N_f+M-1}\underbrace{\sum_{l=0}^{L/M} s[k+lM]g[k+lM-n_0N_f]\,e^{-\frac{j2\pi m_0(k-n_0N_f)}{M}}}_{filtering+CYCCOMB}}_{FFT}\underbrace{e^{-j\Phi_{m_0,n_0}}e^{-\frac{j2\pi m_0(n_0N_f-\frac{D}{2})}{M}}}_{post-processing}\} \tag{3.7}$$

where L is now supposed to be a multiple of M. The inverse operation of the **CYCEXD** is performed at the receiver side by a block named **CYCCOMB**:

$\mathbf{CYCCOMB}_{M\times L} = \mathbf{CYCEXD}^T_{L\times M}$, where $(.)^T$ denotes transposition.

The proposed modem can produce OQAM symbols at both Nyquist and FTN rates, simply by adjusting the FTN factor N_f. As to the arithmetic complexity of our modem, it does not increase when switching from Nyquist to FTN mode. Therefore, the complexity is similar to the classical OFDM/OQAM modem [18], although the way of implementation is different. Further complexity reduction algorithms, such as in [106], can be readily applied in our modem.

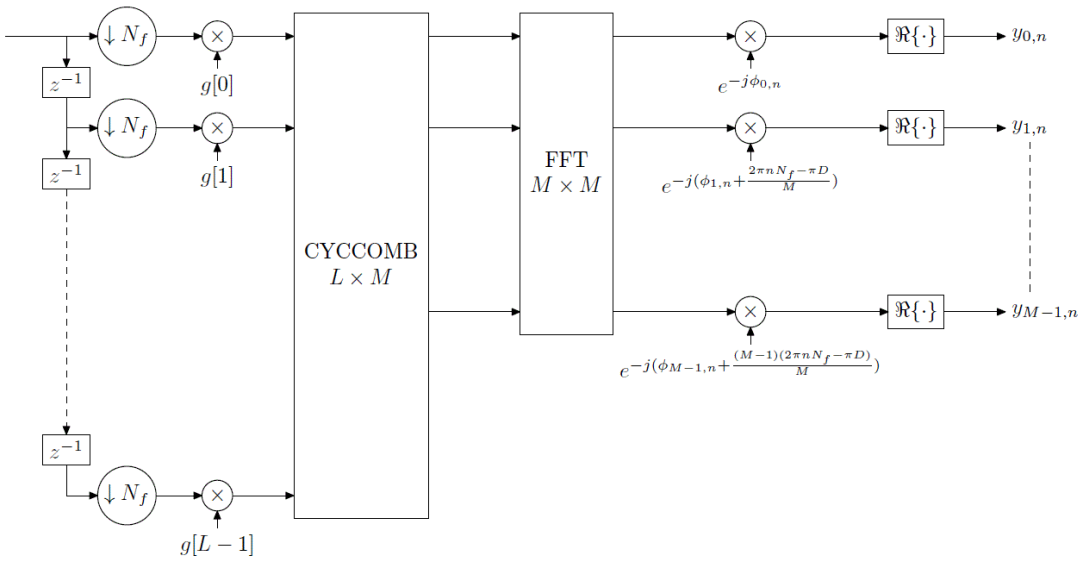

FIGURE 3.3: *FTN-OQAM causal demodulator.*

Theoretically, for a compression factor $0 < \tau \leq 1$, the transmission rate for an FTN transceiver is expected to be multiplied by $\frac{1}{\tau}$. Thus the rate growth is a hyperbolic function of τ. We compared the effective rate improvement of our proposed modem to the one of [2] assuming that one frame contains 16 symbols, $M = 128$, $F_\Delta = 1$, $(T_\Delta, \tau) \in [0.4, 0.9]$, and $\Omega_t = \Omega_f = 3$.

Fig. 3.4 shows that, unlike the SoTA solution, the effective rate improvement of our modem approaches very closely the theoretical curve. Note that using the same construction principle, we can also build an FTN-OFDM/QAM modem for the direct transmission of complex QAM symbols. In this case, the FTN factor is defined as: $N_f = \lfloor \tau.M \rfloor$.

3.3 Interference analysis for the FTN-OQAM transceiver

In this section, we provide an analysis of the FTN-induced interference. The prototype pulses are either defined in continuous-time, having therefore an infinite support, or in discrete-time with finite length. In the following, the interference analysis is given in the case of the continuous and discrete time FTN-OQAM transceiver. We suppose an ideal transmission channel, i.e., noiseless, distortion-free and with perfect analog processing, i.e., the digital modulator and demodulator blocks are back to back, and take $\Phi_{m,n} = \frac{\pi}{2}(m+n)$.

3.3.1 Interference analysis for continuous-time FTN-OQAM transceiver

The complex received signal at time instant n_0 and at subcarrier m_0 is written as:

$$y^c_{m_0,n_0} = \int_{-\infty}^{+\infty} s(t) g^*_{m_0,n_0}(t,\tau) dt. \tag{3.8}$$

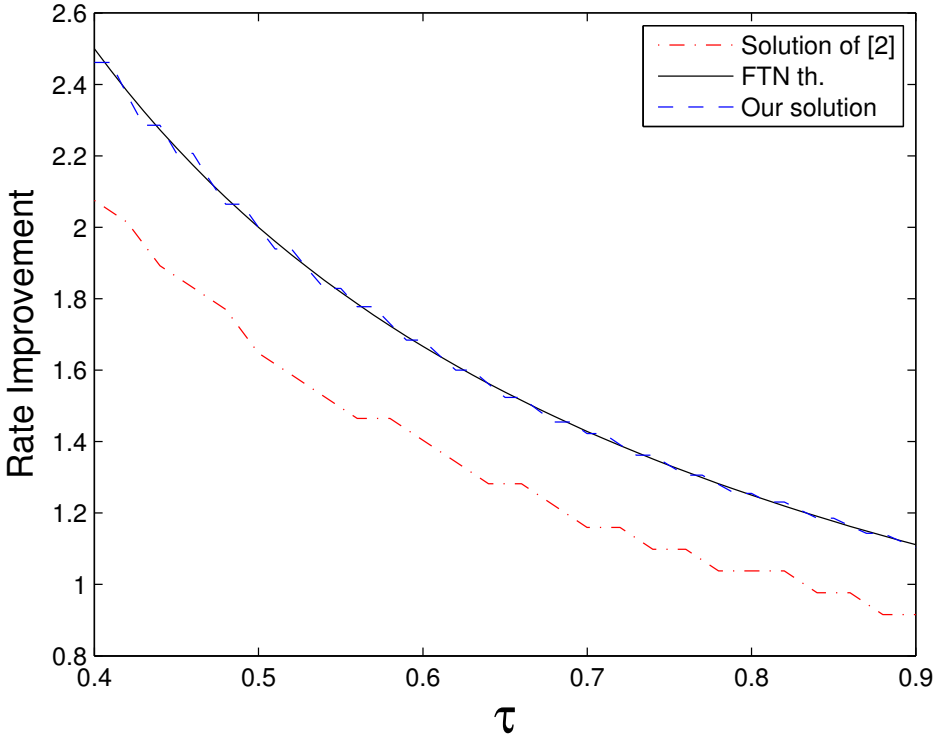

FIGURE 3.4: *The rate improvement of FTN-OQAM as a function of* τ.

Setting $\Delta\Phi = \Phi_{m,n} - \Phi_{m_0,n_0}$, we get:

$$y^c_{m_0,n_0} = \sum_{m,n} a_{m,n} e^{\Delta\Phi} \int_{-\infty}^{+\infty} g(t - n\tau\frac{T_0}{2}) g(t - n_0\tau\frac{T_0}{2}) e^{j2\pi(m-m_0)F_0 t} dt. \tag{3.9}$$

Setting $t - n\tau\frac{T_0}{2} = u - \frac{\tau'}{2}$ and $t - n_0\tau\frac{T_0}{2} = u + \frac{\tau'}{2}$, we refer to the new variables of (3.9) as:

$$\tau' = -(n_0 - n)\tau\frac{T_0}{2}; t = u + (n_0 + n)\tau\frac{T_0}{4} \tag{3.10}$$

The received signal is then reformulated as:

$$y^c_{m_0,n_0} = \sum_{m,n} a_{m,n} e^{\Delta\Phi} \int_{-\infty}^{+\infty} g(u+(n_0-n)\frac{T_0}{4}) g(u-(n_0-n)\frac{T_0}{4}) e^{j2\pi(m-m_0)F_0(u+(n+n_0)\tau\frac{T_0}{4})} du. \tag{3.11}$$

Recalling the continuous-time ambiguity function expression:

$$A_g(u,v) = \int_{-\infty}^{+\infty} g(t + \frac{u}{2}) g(t - \frac{u}{2}) e^{-j2\pi vt} dt, \tag{3.12}$$

and noting that $T_0 F_0 = 1$, we have:

$$y^c_{m_0,n_0} = \sum_{m,n} a_{m,n} e^{\Delta\Phi} e^{-j\frac{\pi}{2}(m_0-m)(n_0+n)\tau} A_g((n_0 - n)\tau\frac{T_0}{2}, (m_0 - m)F_0), \tag{3.13}$$

or equivalently,

$$y^c_{m_0,n_0} = \sum_{m,n} a_{m,n} e^{j\frac{\pi}{2}((m-m_0)+(n-n_0)+(m-m_0)(n_0+n)\tau)} A_g((n_0-n)\tau\frac{T_0}{2}, (m_0-m)F_0). \tag{3.14}$$

Then, applying substitutions $m = m_0 + p$ and $n = n_0 + q$, with $(p, q) \in \mathbb{Z}$, we obtain:

$$y^c_{m_0,n_0} = \sum_{p,q} a_{m_0+p,n_0+q} e^{j\frac{\pi}{2}(p+q+(2n_0+q)p\tau)} A_g(-q\tau\frac{T_0}{2}, -pF_0). \tag{3.15}$$

The demodulated signal hence corresponds to the superposition of a useful component and of an interference term denoted by $I(p, q, g, \tau)$:

$$y^c_{m_0,n_0} = A_g(0, 0)a_{m_0,n_0} + I(p, q, g, \tau), \tag{3.16}$$

with

$$I(p, q, g, \tau) = \sum_{p^0,q^0} a_{m_0+p,n_0+q} e^{j\frac{\pi}{2}(p+q+(2n_0+q)p\tau)} A_g(-q\tau\frac{T_0}{2}, -pF_0), \tag{3.17}$$

where p^0, q^0 denotes the set of (p, q) integer pairs excluding the case where $(p, q) = (0, 0)$.

We assume that the prototype filter g is a real-valued even function, which means that its ambiguity function A_g is real valued and symmetrical: $A_g(-q\tau\frac{T_0}{2}, -pF_0) = A_g(q\tau\frac{T_0}{2}, pF_0)$. The interference power can be written as:

$$\begin{aligned} P_I^C &= E\{|I(p, q, g, \tau)|^2\} \qquad (3.18)\\ &= \sum_{p^0,q^0}\sum_{p'^0,q'^0} E\{a_{m_0+p,n_0+q}a_{m_0+p',n_0+q'}\} e^{j\frac{\pi}{2}(p+q+(2n_0+q)p\tau)} e^{-j\frac{\pi}{2}(p'+q'+(2n_0+q')p'\tau)} \\ &\quad \times A_g(-q\tau\frac{T_0}{2}, -pF_0)A_g(-q'\tau\frac{T_0}{2}, -p'F_0). \end{aligned}$$

As the a_{m_0+p,n_0+q} symbols correspond to i.i.d random variables, only the terms such that $p = p'; q = q'$ will remain, i.e.

$$P_I^C = \sigma_a^2 \sum_{p^0,q^0} A_g^2(q\tau\frac{T_0}{2}, pF_0), \tag{3.19}$$

where σ_a^2 represents the symbols variance. Since in FTN-OQAM, only the real part of the received signal is taken into account, the actual interference power is expressed as:

$$P_I(n_0) = \sigma_a^2 \sum_{p^0,q^0} |\Re\{e^{j\frac{\pi}{2}(p+q+(2n_0+q)p\tau)}\} A_g(q\tau\frac{T_0}{2}, pF_0)|^2. \tag{3.20}$$

From this expression, we can note that the phase term is periodical in n_0 with a period denoted by N_0, i.e., the interference power is also periodic: $P_I(n_0) = P_I(n_0 + N_0)$. Assuming that τ is a rational number, denoted by $\tau = \frac{u}{v}$, this period can be expressed as:

$$N_0(p, u, v) = \begin{cases} 1, & \text{if} \quad p = 0 \\ \frac{v}{up}, & \text{if} \quad p \neq 0 \quad \text{and} \quad \text{mod}(v, up) = 0 \\ \frac{v}{\text{gcd}(v,up)}, & \text{if} \quad p \neq 0 \quad \text{and} \quad \text{mod}(v, up) \neq 0, \end{cases} \tag{3.21}$$

where, mod and gcd stand for the modulo function and the greatest common divisor function, respectively. The period N_0 depends on τ as well as on the subcarrier index p. Knowing that $N_0(1,u,v)$ is a multiple of $N_0(p,u,v)$ for $|p| \geq 2$, we define a global period for any p as:

$$N_0^G = N_0(1,u,v). \tag{3.22}$$

Finally, the interference power is:

$$P_I(n_0) = \sigma_a^2 \sum_{p^0,q^0} \cos(\frac{\pi}{2}(p+q+(2n_0+q)p\tau))^2 A_g(q\tau\frac{T_0}{2}, pF_0)^2, \tag{3.23}$$

while the mean power is given by:

$$P_I^{N_0}(n_0) = \frac{1}{N_0(1,u,v)} \sum_{n_0=0}^{N_0(1,u,v)-1} P_I(n_0). \tag{3.24}$$

3.3.2 Interference analysis for discrete-time FTN/OQAM transceiver

In this scenario, the received signal at time instant n_0 and at subcarrier m_0 is expressed as:

$$\begin{aligned} y^c_{m_0 n_0} &= \sum_{k=n_0N_f}^{n_0N_f+L-1} s[k]g[k-n_0N_f]e^{-j\Phi m_0 n_0} e^{-\frac{j2\pi m_0(k-\frac{D}{2})}{M}} \\ &= \sum_{m,n} a_{m,n} e^{j\Delta\Phi} \sum_{k=n_0N_f}^{n_0N_f+L-1} g[k-nN_f]g[k-n_0N_f] e^{\frac{j2\pi(m-m_0)(k-\frac{D}{2})}{M}}. \end{aligned} \tag{3.25}$$

Setting $m = m_0 + p$; $n = n_0 + q$, with $(p,q) \in \mathbb{Z}$ and $k' = k - n_0N_f$, the received signal is:

$$y^c_{m_0 n_0} = \sum_{p,q} a_{m_0+p,n_0+q} e^{j\frac{\pi}{2}(p+q)} \sum_{k=0}^{L-1} g[k]g[k-qN_f] e^{\frac{j2\pi p(k+n_0N_f-\frac{D}{2})}{M}}. \tag{3.26}$$

The discrete version of an aperiodic ambiguity function is written as:

$$A_g[m,n] = \frac{1}{N} \sum_{k=0}^{N-1} g[m+k]g[k]e^{-\frac{j2\pi kn}{N}}. \tag{3.27}$$

Recalling that the prototype filter length L is a multiple of M, $L = bM, b \in \mathbb{N}$, the signal $y^c_{m_0 n_0}$ is formulated as:

$$\begin{aligned} y^c_{m_0 n_0} &= \sum_{p,q} a_{m_0+p,n_0+q} e^{j\pi(\frac{p+q}{2} + \frac{2p(n_0N_f-\frac{D}{2})}{M})} \times LA_g[-qN_f, -pb] \\ &= LA_g[0,0]a_{m_0,n_0} + I[p,q,g,N_f], \end{aligned} \tag{3.28}$$

where,

$$I[p,q,g,N_f] = L\sum_{p^0q^0} a_{m_0+p,n_0+q} e^{j\pi(\frac{p+q}{2} + \frac{2p(n_0N_f-\frac{D}{2})}{M})} A_g[-qN_f, -pb] \tag{3.29}$$

is the interference term. Its power is then written as:

$$\begin{aligned} P_I^C &= E\{|I(p,q,g,N_f)|^2\} \\ &= \sum_{p^0q^0}\sum_{p'^0q'^0} L^2 E\{a_{m_0+p,n_0+q}a_{m_0+p',n_0+q'}\}e^{j\pi(\frac{p+q}{2}+\frac{2p(n_0N_f-\frac{D}{2})}{M})}A_g[-qN_f,-pb] \\ &\quad \times e^{j\pi(\frac{p'+q'}{2}+\frac{2p'(n_0N_f-\frac{D}{2})}{M})}A_g[-q'N_f,-p'b]. \end{aligned} \tag{3.30}$$

Similarly, only the terms such that $p=p'$; $q=q'$ will remain, i.e.,

$$P_I^C = \sigma_a^2 L^2 \sum_{p^0q^0} A_g[-qN_f,-pb]^2. \tag{3.31}$$

In the case of FTN-OQAM, we should take into account the real-part extraction which, in the meantime, introduces a time dependency via parameter n_0. The interference power is then:

$$P_I(n_0) = \sigma_a^2 L^2 \sum_{p^0q^0} |\Re\{e^{j\pi(\frac{p+q}{2}+\frac{2p(n_0N_f-\frac{D}{2})}{M})}\}A_g[-qN_f,-pb]|^2. \tag{3.32}$$

Similarly to the continuous-time version, the phase term is periodic in n_0 with a period denoted here by N_0 and expressed by:

$$N_0(p,N_f) = \begin{cases} 1, \text{if} \quad p=0 \\ \frac{M}{2pN_f}, \text{if} \quad p\neq 0 \quad \text{and} \quad \text{mod}(M,2pN_f)=0 \\ \frac{M}{\text{gcd}(M,2pN_f)} \text{if} \quad p\neq 0 \quad \text{and} \quad \text{mod}(M,2pN_f)\neq 0. \end{cases} \tag{3.33}$$

As in the previous case, we define a global period for any p as:

$$N_0^G = N_0(1,N_f). \tag{3.34}$$

Finally, the interference power for the discrete-time signal is expressed as:

$$P_I(n_0) = \sigma_a^2 L^2 \sum_{p^0q^0} \cos(\pi(\frac{p+q}{2}+\frac{2p(n_0N_f-\frac{D}{2})}{M}))^2 A_g[qN_f,pb]^2, \tag{3.35}$$

while the mean power is:

$$P_I^{N_0}(n_0) = \frac{1}{N_0(1,N_f)} \sum_{n_0=0}^{N_0(1,N_f)-1} P_I(n_0). \tag{3.36}$$

τ	N_f	N_0^G
0.5	16	2
0.6	19	32
0.7	22	16
0.8	26	16
0.9	29	32

TABLE 3.1: The global period N_0^G for different FTN packing factors (M=64).

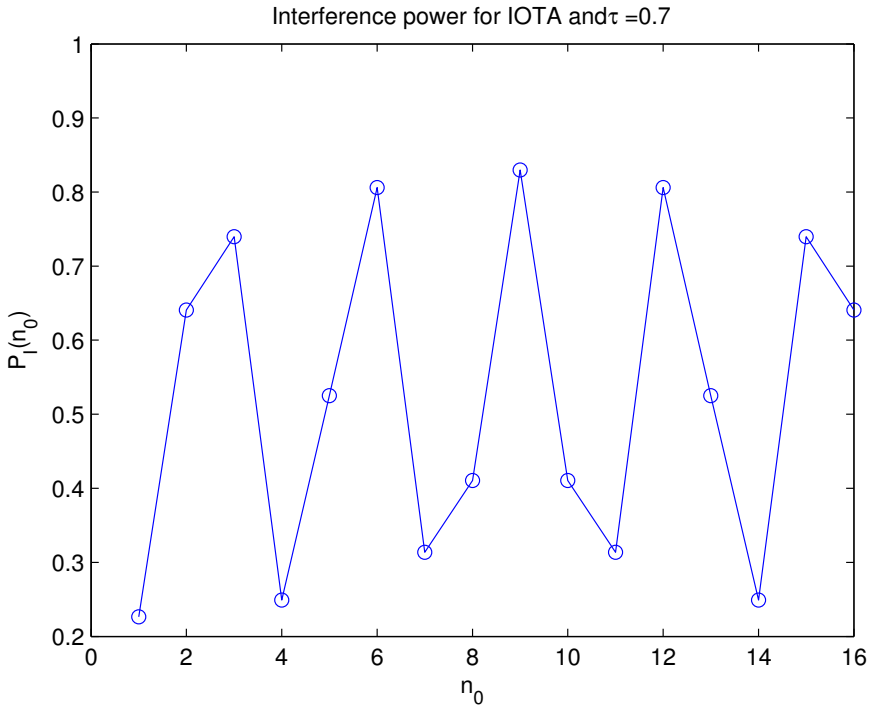

FIGURE 3.5: Interference mean power using the IOTA filter ($L = 4M$) and $\tau = 0.7$.

Fig. 3.5 illustrates the variation of the interference mean power as a function of n_0 using the IOTA filter ($L = 4M$) and $\tau = 0.7$. In accordance with the analytical study, the interference power depends on time instant n_0. For this packing factor, the global period N_0^G is equal to 16. In Table 3.1, we present numerical values of the global period N_0^G. As mentioned earlier, the period depends on the FTN packing factor N_f. The theoretical interference mean power and the simulated one, in the case of a discrete-time FTN-OQAM transceiver, are plotted in Fig. 3.6 for different pulse shapes: EGF ($L = 4M$, λ=2), TFL ($L = M$), IOTA ($L = 4M$), PHYDYAS ($L = 4M$), SRRC ($L = 4M$, ρ=0.5), SRRC ($L = 4M$, ρ=0.3) and FS ($L = 4M$). We observe that the theoretical interference mean power is identical to the simulated one, for all the different pulse shapes. The comparison between the different pulse shapes is given in Fig. 3.7. It shows that the FTN-self interference also depends on the pulse shape and increases when the TFL, EGF ($\lambda = 2$) and IOTA filters are employed.

In the previous chapter, we mentioned that unlike OFDM, OFDM/OQAM modulation has the flexibility of using various pulse shapes with different time-frequency localization features. According to these features, using a given pulse shape g will result in either high ISI or ICI. Thus, we reformulate the interference power as:

$$P_I(n_0) = \underbrace{\sigma_a^2 L^2 \sum_{q^0} \cos(\pi \frac{q}{2})^2 A_g[qN_f, 0]^2}_{ISI} + \underbrace{\sigma_a^2 L^2 \sum_{p\neq 0, q} \cos(\pi(\frac{p+q}{2} + \frac{2p(n_0 N_f - \frac{D}{2})}{M}))^2 A_g[qN_f, pb]^2}_{ICI_{n_0}} . \quad (3.37)$$

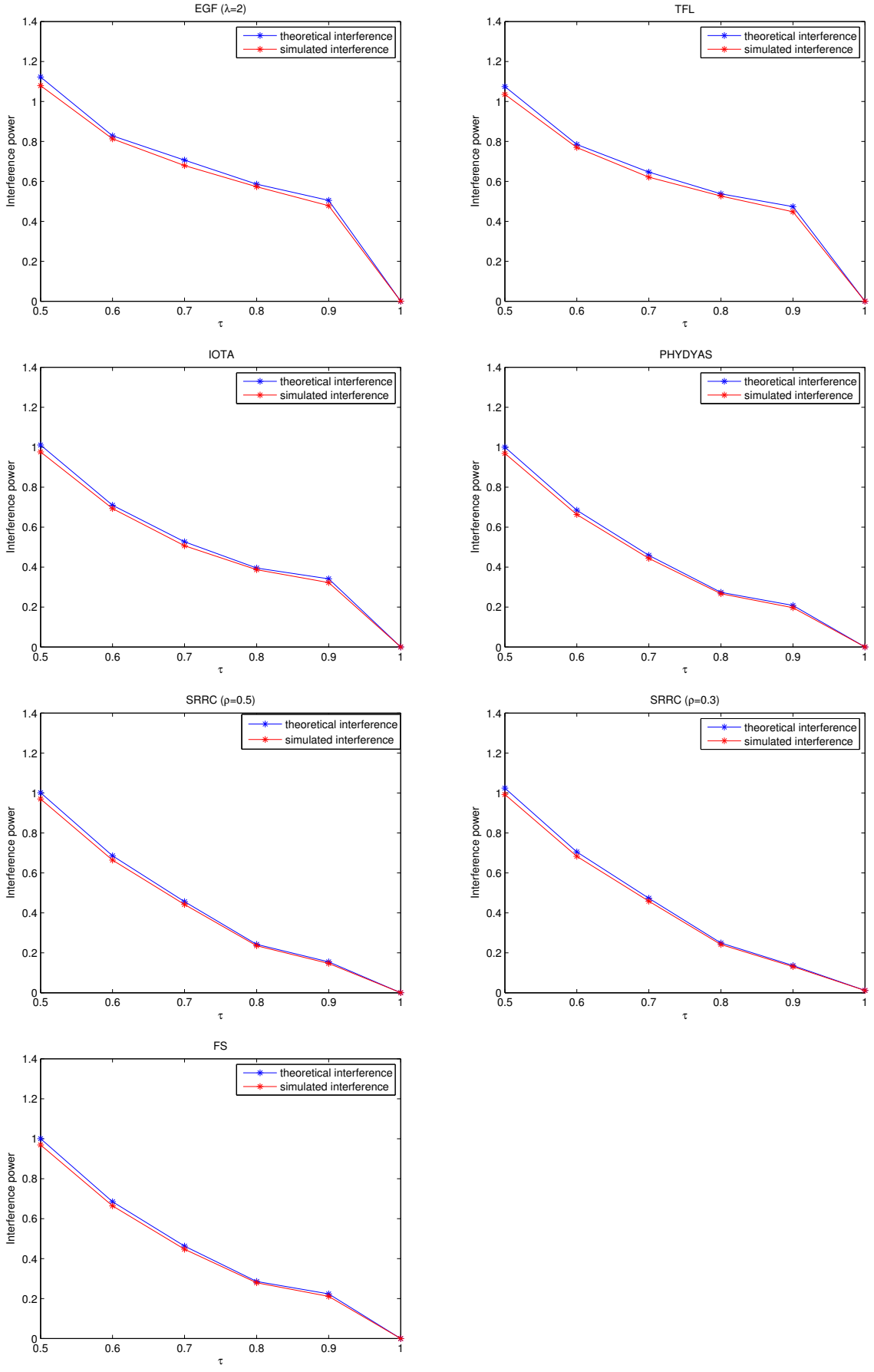

FIGURE 3.6: Interference mean power for different pulse shapes and FTN packing factors.

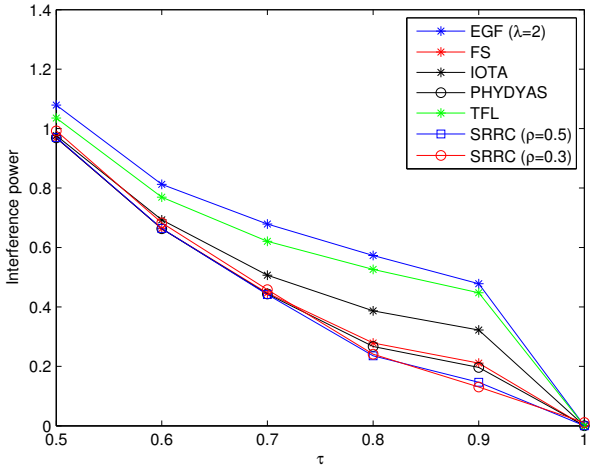

FIGURE 3.7: Interference mean power for different pulse shapes and FTN packing factors.

We can see from this equation that, unlike ISI, ICI depends on n_0. For further illustration, we give in Fig. 3.8 the mean ICI and ISI power for different pulse shapes. As predicted, a pulse shape well localized in frequency-domain suffers more from ISI than from ICI, and vice-versa.

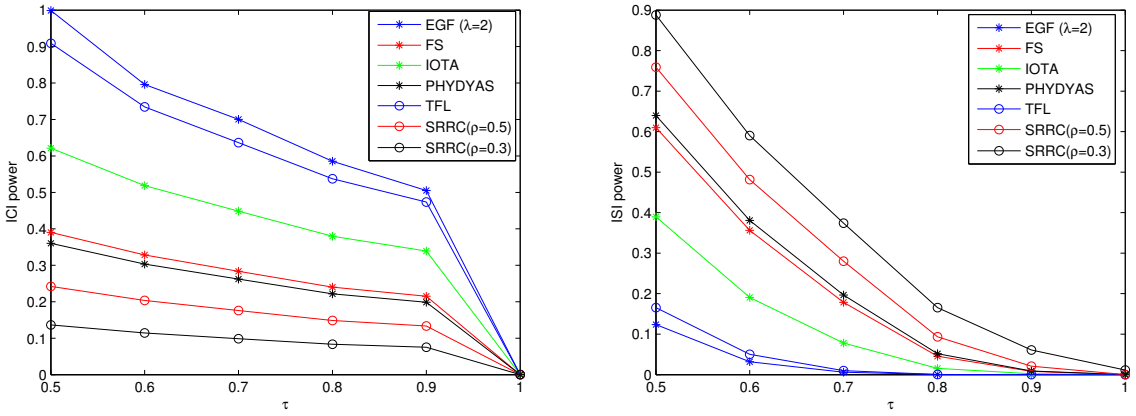

FIGURE 3.8: ICI and ISI mean power for different pulse shapes and FTN packing factors.

3.4 The FTN-OQAM receiver

As mentioned earlier, when signaling beyond the Nyquist rate, the orthogonality condition is no longer valid. This means that, even for an ideal channel, interferences are added to the useful signal. Although we considered only packing OQAM signals closer in time-domain, ICI also exists in the transmitted signal as illustrated in Fig. 3.9. Here, the FTN data on different subcarriers and time instants are represented by triangles, while the classical OQAM data are represented by circles as reference. The transmission chain of coded FTN-OQAM is reported in Fig. 3.10, where information bits are

first encoded, interleaved, mapped to OQAM symbols, and then modulated. In order to deal with FTN-induced interferences, we propose a turbo-like receiver based on MMSE LE-IC. Unlike the MAP-based equalizer, the complexity of MMSE LE-IC equalization is independent of the modulation order, and depends only on the length of the interference channel impulse response. Hence, this receiver is a good candidate when high modulation orders are targeted. In what follows, we first present the MMSE LE-IC equalization in time-domain and then in frequency-domain.

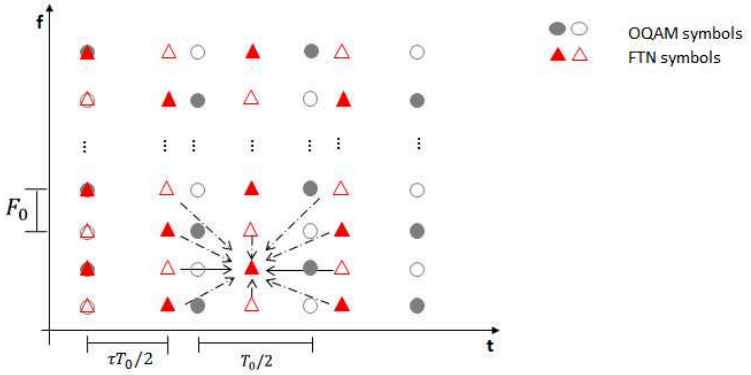

FIGURE 3.9: FTN-OQAM time-frequency lattice. Circles represent Nyquist data while triangles represent FTN data.

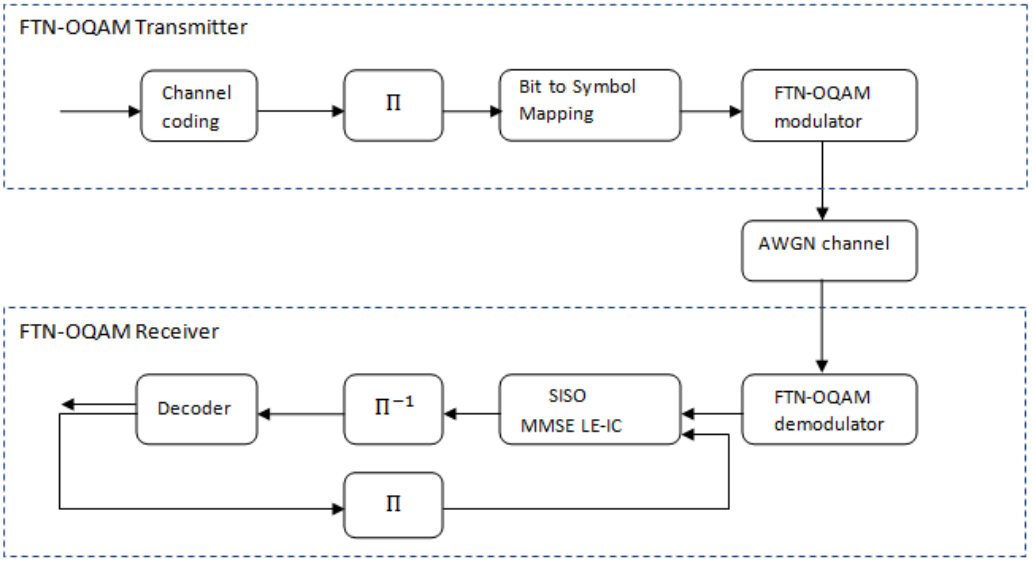

FIGURE 3.10: FTN-OQAM transmission chain.

3.4.1 Time-domain MMSE turbo-equalization

At the receiver side, assuming an ideal channel, the signal is first demodulated by the *FTN-OQAM demodulator*. We assume a unit energy prototype filter g. Thus, $\sum_k g[k]^2 = 1$ and $LA_g[0,0] = 1$. At time instant n_0 and for subcarrier m_0, the received signal is

expressed as:

$$y_{m_0,n_0} = \underbrace{a_{m_0,n_0}}_{useful\ signal} + \underbrace{\Re\{\sum_{p^0,q^0} a_{m_0+p,n_0+q} e^{j\pi(\frac{p+q}{2}+\frac{2p(n_0N_f-\frac{D}{2})}{M})} \times LA_g[-qN_f,-pb]\}}_{ISI+ICI}, \tag{3.38}$$

where, $a_{m,n}$ are the transmitted OQAM symbols at time instant n and at subcarrier m, and $(p,q) \in [-l^{'},l^{'}] \times [-l,l], (l,l^{'}) \in \mathbb{Z}^2$. Although interference extends to all frequencies and time instants, we consider that it is essentially due to the closest neighbors in a zone $[-l^{'},l^{'}] \times [-l,l]$. Factors $(l^{'},l)$ represent the zone of symbols contributing to ICI and ISI, respectively. They depend on the prototype filter and on the packing factor τ. Equation (3.38) can be reformulated as:

$$\begin{aligned} y_{m_0,n_0} = & \underbrace{a_{m_0,n_0}}_{useful\ signal} \\ & + \underbrace{\Re\{L\sum_{q\neq 0} a_{m_0,n_0+q} e^{jq\frac{\pi}{2}} A_g[-qN_f,0]\}}_{ISI} \\ & + \underbrace{\Re\{\sum_{p\neq 0,q} a_{m_0+p,n_0+q} e^{j\pi(\frac{p+q}{2}+\frac{2p(n_0N_f-\frac{D}{2})}{M})} \times LA_g[-qN_f,-pb]\}}_{ICI_{n_0}}. \end{aligned} \tag{3.39}$$

The demodulated symbols $\mathbf{y}$ are then fed to the SISO MMSE IC-LE to iteratively suppress the interferences caused by FTN. The interference cancellation is a two-stage process, meaning that it cancels ICI in the first stage and then addresses ISI. The SISO MMSE LE-IC structure is reported in Fig. 3.11, where ICI and ISI are predicted using the feedback from the decoder and then canceled. The SISO MMSE LE-IC structure is detailed in the previous chapter, section 2.5.3. The soft mapping and demapping functions are used to translate the information from bit level to symbol level and vice-versa and thus exchange information between the symbol level filter and the bit level decoder. In this section, we consider MMSE LE-IC equalization in time axis, as reported in Fig. 3.12. The red triangle is the targeted element to be equalized. The Soft Interference Canceler *(SIC)* block calculates ICI affecting the desired signal using the blue elements on side subcarriers as:

$$ICI_{n_0} = \Re\{\sum_{p\neq 0,q} \bar{x}_{m_0+p,n_0+q} e^{j\pi(\frac{p+q}{2}+\frac{2p(n_0N_f-\frac{D}{2})}{M})} \times LA_g[-qN_f,-pb]\}, \tag{3.40}$$

where $\bar{x}_{m_0+p,n_0+q}$ are estimated by the *SISO mapping* block. Let $\bar{y}_{m_0,n_0}$ be the output of *SIC* block, we have:

$$\tilde{y}_{m_0,n_0} = y_{m_0,n_0} - \bar{y}_{m_0,n_0} \tag{3.41}$$

$$
\begin{aligned}
&= a_{m_0,n_0} + \underbrace{\Re\{L\sum_{q\neq 0} a_{m_0,n_0+q} e^{jq\frac{\pi}{2}} A_g[-qN_f,0]\}}_{ISI} \\
&+ \underbrace{\Re\{\sum_{q,p\neq 0}(a_{m_0+p,n_0+q} - \bar{x}_{m_0+p,n_0+q}) e^{j\pi(\frac{p+q}{2}+\frac{2p(n_0N_f-\frac{D}{2})}{M})} \times LA_g[-qN_f,-pb]\}}_{residual\ ICI}.
\end{aligned}
$$

We can see from (3.41) that, assuming a perfect estimation $a_{m_0+p,n_0+q} = \bar{x}_{m_0+p,n_0+q}$, residual ICI is equal to zero and the signal at the MMSE equalizer is composed only of the desired signal and ISI. When, $a_{m_0+p,n_0+q} \neq \bar{x}_{m_0+p,n_0+q}$, ICI still exists in the signal to be equalized. Considering a transmission over an AWGN channel, equation (3.41) can be written as:

$$
\begin{aligned}
\tilde{y}_{m_0,n_0} &= a_{m_0,n_0} + \Re\{L\sum_{q\neq 0} a_{m_0,n_0+q} e^{jq\frac{\pi}{2}} A_g[-qN_f,0]\} + \eta_{n_0} \qquad (3.42)\\
&+ \Re\{\sum_{q,p\neq 0}(a_{m_0+p,n_0+q} - \bar{x}_{m_0+p,n_0+q}) e^{j\pi(\frac{p+q}{2}+\frac{2p(n_0N_f-\frac{D}{2})}{M})} \times LA_g[-qN_f,-pb]\},
\end{aligned}
$$

where η is the filtered noise.

Recalling that the pulse g has a real ambiguity function, (3.42) can be reformulated as:

$$
\begin{aligned}
\tilde{y}_{m_0,n_0} &= a_{m_0,n_0} + \sum_{q\neq 0} La_{m_0,n_0+q}\cos(\frac{\pi}{2}q)A_g[-qN_f,0] + \eta_{n_0} \qquad (3.43)\\
&+ \sum_{q,p\neq 0}(a_{m_0+p,n_0+q} - \bar{x}_{m_0+p,n_0+q})\cos(\pi(\frac{p+q}{2}+\frac{2p(n_0N_f-\frac{D}{2})}{M})) \times LA_g[-qN_f,-pb]\}
\end{aligned}
$$

Equation (3.43) can be further simplified to:

$$
\tilde{y}_{m_0,n_0} = a_{m_0,n_0} + \sum_{q\neq 0} a_{m_0,n_0+q}h_q + v_{n_0}, \qquad (3.44)
$$

where v is global noise, and h_q the coefficients of the equivalent ISI channel with:

$$
h_q = L\cos(\frac{\pi}{2}q)A_g[-qN_f,0]. \qquad (3.45)
$$

Note that:

$$
h_q = \begin{cases} 1, & \text{for } q=0 \\ 0, & \text{for } q \text{ odd.} \end{cases} \qquad (3.46)
$$

This means that symbols at odd time instants n do not contribute to ISI. After *SIC* module, the signal $\tilde{y}$ is then processed by filters $\mathbf{p}$ and $\mathbf{q}$ in order to cancel ISI. The coefficients of filters $\mathbf{p}$ and $\mathbf{q}$ are computed according to the MMSE principle, presented in the previous chapter. The resulting signal $\mathbf{z}$ is then fed to the *SISO Demapping* block to compute the extrinsic LLRs of coded bits. These LLRs are considered as the *a priori* input of the *Decoder*, which is based on the Max-Log-MAP algorithm, discussed in the previous chapter.

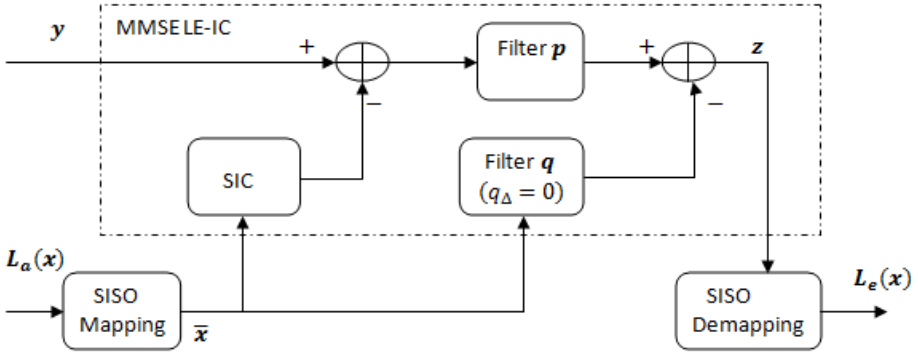

FIGURE 3.11: Structure of the SISO MMSE LE-IC.

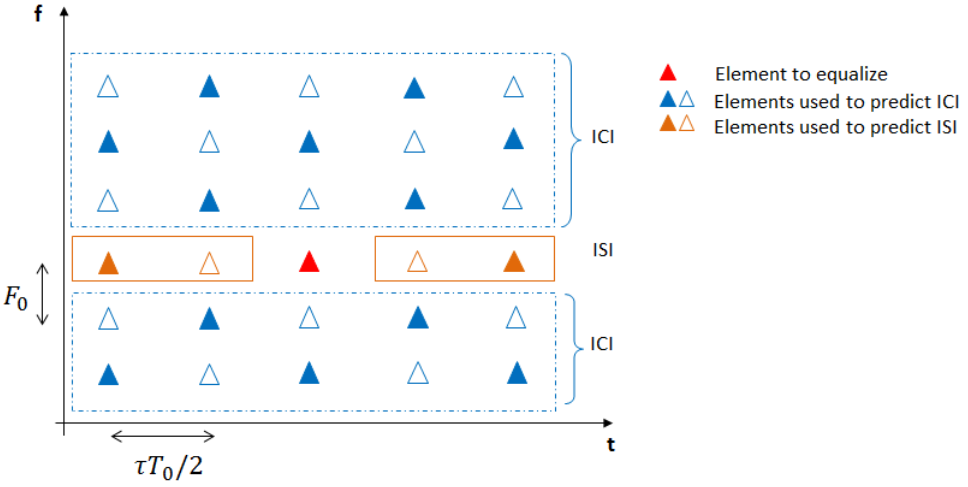

FIGURE 3.12: Time-domain ICI and ISI prediction and canceling.

3.4.2 Frequency-domain MMSE turbo-equalization

Unlike OFDM, OFDM/OQAM modulation offers the possibility of using different prototype filters having different time-frequency localization features. An FTN-OQAM transceiver using FTN signaling creates additional interferences to the useful signal. As shown in Fig. 3.8, pulse shapes well localized in frequency domain suffer less from ICI than those well localized in time. Furthermore, for the lowest τ values, their ISI is higher than their ICI. Hence, for these pulse shapes, it is worthwhile testing the MMSE equalizer along the frequency axis. This can be translated by virtually rotating the time and frequency axes in Fig. 3.12, as it is shown in Fig. 3.13, where the red triangle is the target element. ISI is caused by the orange triangles at the same time instant and side subcarriers, while ICI is caused by the blue triangles. Before equalizing the signal, the *SIC* module estimates first ICI based on the soft information delivered by the *Decoder*. Equation (3.39) can be reformulated as:

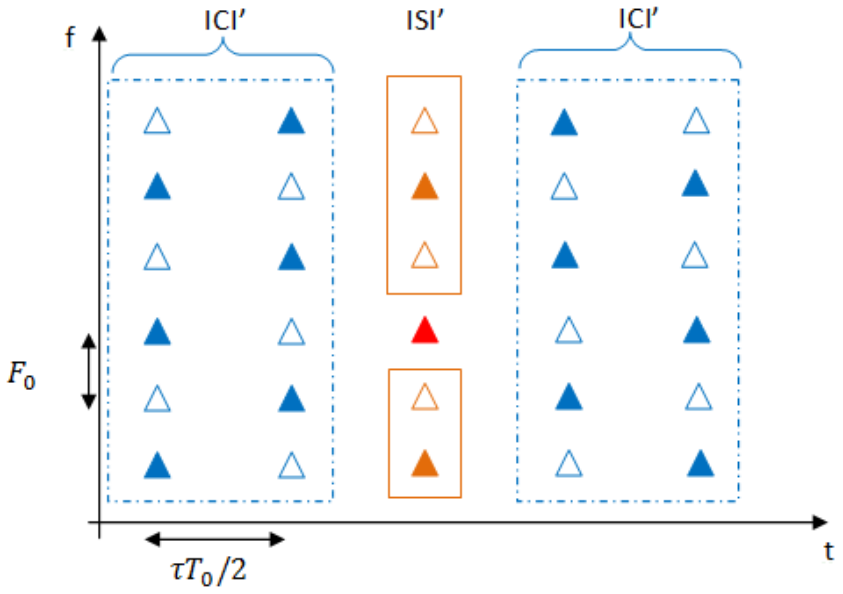

FIGURE 3.13: Frequency-domain ICI and ISI prediction and canceling.

$$
\begin{aligned}
y_{m_0,n_0} &= \underbrace{a_{m_0,n_0}}_{useful\ signal} \\
&+ \underbrace{\Re\{L\sum_{p\neq 0} a_{m_0+p,n_0} e^{j\pi(\frac{p}{2}+\frac{2p(n_0N_f-\frac{D}{2})}{M})} \times LA_g[0,-pb]\}}_{ISI} \\
&+ \underbrace{\Re\{\sum_{p,q\neq 0} a_{m_0+p,n_0+q} e^{j\pi(\frac{p+q}{2}+\frac{2p(n_0N_f-\frac{D}{2})}{M})} \times LA_g[-qN_f,-pb]\}}_{ICI}. \qquad (3.47)
\end{aligned}
$$

The *SIC* module estimates ICI based on the soft estimated symbols $\bar{x}_{m,n}$ delivered by the *SISO Mapping*. Let $\bar{y}_{m_0,n_0}$ be the output of *SIC* block, we have:

$$
\begin{aligned}
\tilde{y}_{m_0,n_0} &= y_{m_0,n_0} - \bar{y}_{m_0,n_0} \qquad (3.48) \\
&= a_{m_0,n_0} + \underbrace{\Re\{\sum_{p\neq 0} a_{m_0+p,n_0} e^{j\pi(\frac{p}{2}+\frac{2p(n_0N_f-\frac{D}{2})}{M})} \times LA_g[0,-pb]\}}_{ISI} \\
&+ \underbrace{\Re\{\sum_{p,q\neq 0} (a_{m_0+p,n_0+q} - \bar{x}_{m_0+p,n_0+q}) e^{j\pi(\frac{p+q}{2}+\frac{2p(n_0N_f-\frac{D}{2})}{M})} \times LA_g[-qN_f,-pb]\}}_{residual\ ICI}.
\end{aligned}
$$

Similarly to the time-domain MMSE equalization, when the estimated symbols are not equal to the transmitted ones, residual ICI is still present in the signal $\tilde{y}_{m,n}$. In case of

transmitting over an AWGN channel, (3.48) is reformulated as:

$$\tilde{y}_{m_0,n_0} = a_{m_0,n_0} + \sum_{p\neq 0} a_{m_0+p,n_0} \cos(\pi(\frac{p}{2} + \frac{2p(n_0 N_f - \frac{D}{2})}{M})) \times LA_g[0,-pb] + v_{n_0}, \quad (3.49)$$

which can be further simplified to:

$$\tilde{y}_{m_0,n_0} = a_{m_0,n_0} + \sum_{p\neq 0} a_{m_0+p,n_0} l_{p,n_0} + v_{n_0}, \quad (3.50)$$

where v_{n_0} is the overall noise composed of the Gaussian noise and of the residual ICI, and l_{p,n_0} are the coefficients of the equivalent ISI channel in case of frequency-domain equalization expressed as:

$$l_{p,n_0} = \cos(\pi(\frac{p}{2} + \frac{2p(n_0 N_f - \frac{D}{2})}{M})) \times LA_g[0,-pb]. \quad (3.51)$$

We can notice from this expression, that unlike the previous case, the equivalent channel depends also on time instant n_0. This means that the coefficients of filters $\mathbf{p}$ and $\mathbf{q}$ need to be computed for each time instant n_0. The equalized signal is then fed to the *SISO Demapping* block to compute the extrinsic LLRs of the coded bits.

3.5 Simulation results

In this section, we evaluate the performance of the proposed FTN-OQAM transceiver in terms of BER vs. SNR. First we present an algorithm to investigate the packing factor that our transceiver can reach while keeping its performance close to the one of Nyquist-based OFDM/OQAM systems. Then, we compare the performance of the FTN-OQAM transceiver using different pulse shapes.

3.5.1 Effective minimum lossless packing factor investigation

In this section, we examine the minimum value of the FTN packing factor achieved by the FTN-OQAM transceiver. In fact, the packing factor depends on the channel coding rate. We illustrate in Fig. 3.14 the BER curves of the FTN-OQAM transceiver, after having performed 9 iterations at the receiver side, using QPSK modulation, FS filtering, different FTN packing factors ($\tau = 0.7, 0.8$, and 0.9) and different coding rates. We used a rate-$\frac{1}{4}$ RSC code with generator polynomials in octal notation (1,15/13,15/13,17/13) for the *Channel coding* in Fig. 3.10 and a *Puncturing* module at its output to ensure different coding rates. As we can notice from Fig. 3.14, the BER performance of the FTN-OQAM transceiver depends on the coding rate: For coding rates as high as $\frac{8}{9}$, the FTN-OQAM transceiver can not support a packing factor $\tau = 0.7$, while for lower coding rates, the BER curve for $\tau = 0.7$ improves.

In what follows, we investigate the minimum value of the packing factor that the FTN-OQAM transceiver can achieve, while providing performance close to the Nyquist one under the same SNR condition. The numerical value of this packing factor is named the effective minimum lossless packing factor and is investigated for each pulse shape

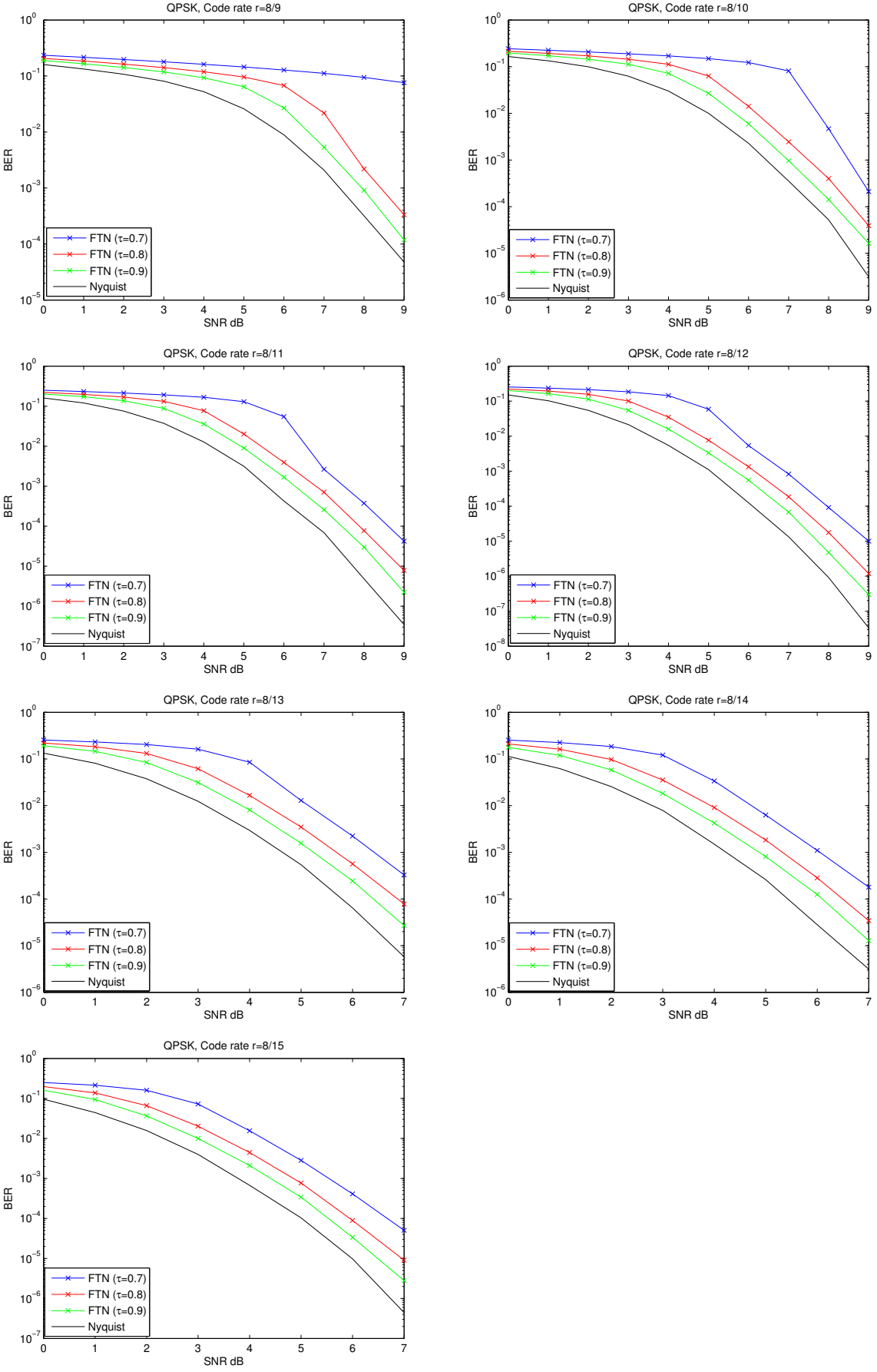

FIGURE 3.14: BER performance of the proposed FTN-OQAM transceiver using FS filtering, QPSK and different coding rates.

and modulation order, regardless of the number of iterations. The proposed algorithm is based on the EXIT chart analysis of the aforementioned MMSE LE-IC turbo equalizer [26]. Our objective is to find the smallest packing factor that the FTN-OQAM transceiver can achieve without performance loss, for a given coding rate, pulse shape, modulation order and SNR. The methodology of the effective minimum lossless packing factor search is summarized in Fig. 3.15. Indeed, we repeatedly implement this method for different pulse shapes and modulation orders.
The target convergence performance with Nyquist signaling is fixed at BER of 10^{-5}, which we call Nyquist Error-Free (NEF) performance in the sequel. The search process begins by generating the SNR value corresponding to the NEF point and initializing the FTN packing factor to 0.1. Using these values, the EXIT chart is generated. If the EXIT tunnel is closed or if the EXIT chart does not reach NEF performance, the packing factor is incremented by a fixed step and the previous operation is repeated. The iterative process continues until the EXIT tunnel opens and the EXIT chart reaches NEF performance. The FTN packing factor estimated using this method is a numerical value, the precision of which depends on the step value. Note that the proposed algorithm provides only a numerical value of the smallest achievable packing factor and not the number of iterations needed for convergence.

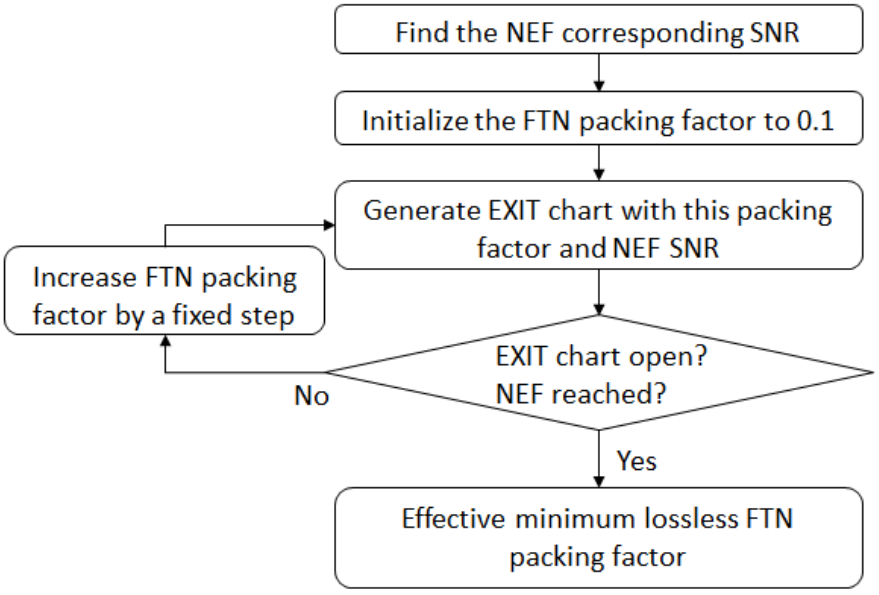

FIGURE 3.15: Search process for the effective minimum lossless FTN packing factor.

In what follows, we present the FTN packing factor investigation only for the IOTA pulse shape with filter length $L = 4M$ as an example. In our simulations, we assume the number of subcarriers is $M = 64$ and all the subcarriers are to be modulated. The outer code used is a rate-$\frac{1}{2}$ (1, 5/7) RSC code. The interleaver is assumed to be random and the NEF point is fixed at BER of 10^{-5}. At the receiver side, the MMSE filter has a length of 30 coefficients. The equalization is performed in the time domain and the outer decoder is based on Max-Log-MAP algorithm. According to our BER vs. SNR simulation with IOTA pulse shape, the SNR corresponding to NEF yields to 6.2 dB, 12.6 dB and 18.3 dB for QPSK, 16-QAM and 64-QAM, respectively. It is also worth noting that in the AWGN channel case, different pulse shapes with Nyquist signaling always

lead to identical BER performance.

In Fig. 3.16, we can see that the EXIT chart starts to open for a packing factor around 0.7, meaning that the iterative process begins to converge. At FTN packing factor of 0.9 and at the end of the iterative process, the mutual information of the FTN detector almost reaches the Nyquist one i.e., our FTN-OQAM receiver converges to the Nyquist performance. Thus, the FTN packing factor of 0.9 is identified as the numerical value of the effective minimum lossless packing factor for QPSK using IOTA filter. Figures 3.17 and 3.18 report the EXIT charts for 16-QAM and 64-QAM, respectively. The numerical value of the effective minimum lossless packing factor is between 0.8 and 0.9 for 16-QAM and 0.9 for 64-QAM. As mentioned earlier, we can use time or frequency domain equalization to process the received signal according to the time-frequency localization features of the considered pulse shape. In Fig. 3.19, we compare the EXIT chart of both schemes using IOTA filter with 64-QAM and $\tau = 0.9$. In this configuration, MMSE LE-IC with time-domain equalization permits converging to the Nyquist performance. This is in accordance with results of Fig. 3.8, where we clearly see that for IOTA pulse shape the ISI power is less than ICI.

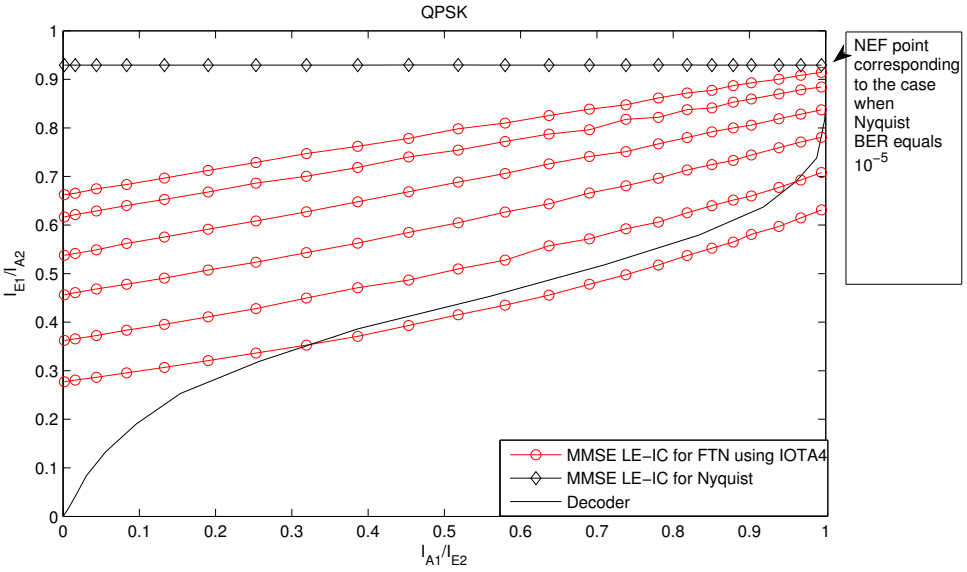

FIGURE 3.16: EXIT chart for MMSE LE-IC with QPSK using IOTA at SNR=6.2 dB. The FTN packing factor ranges from 0.4 (bottom) to 0.9 (top) in step of 0.1.

The same search process was carried out for other pulse shapes: SRRC filter ($L = 4M$) with different roll-off factors (ρ); PHYDYAS filter ($L = 4M$); TFL filter ($L = M$), FS filter ($L = 4M$); and EGF ($L = 4M, \lambda = 2$) filter. Table 3.2 summarizes the numerical values of the effective minimum lossless FTN packing factors for each pulse shape and modulation order as well as the recommended equalization domain. As shown in Fig. 3.14, the performance of the FTN-OQAM transceiver is related to the used code and coding rate. Meaning that the effective minimum lossless FTN packing factors will normally depend on the code and coding rate as well.

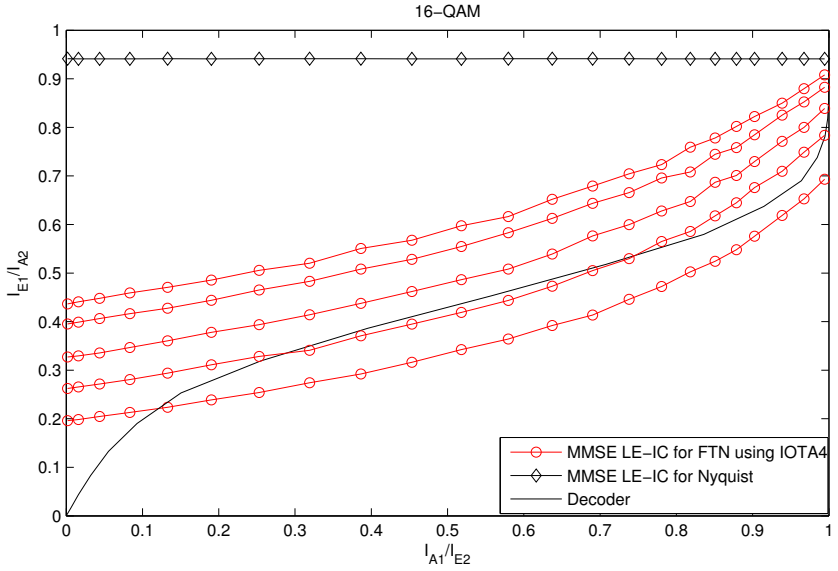

FIGURE 3.17: EXIT chart for MMSE LE-IC with 16-QAM using IOTA at SNR=12.6 dB. The FTN packing factor ranges from 0.5 (bottom) to 0.9 (top) in step of 0.1.

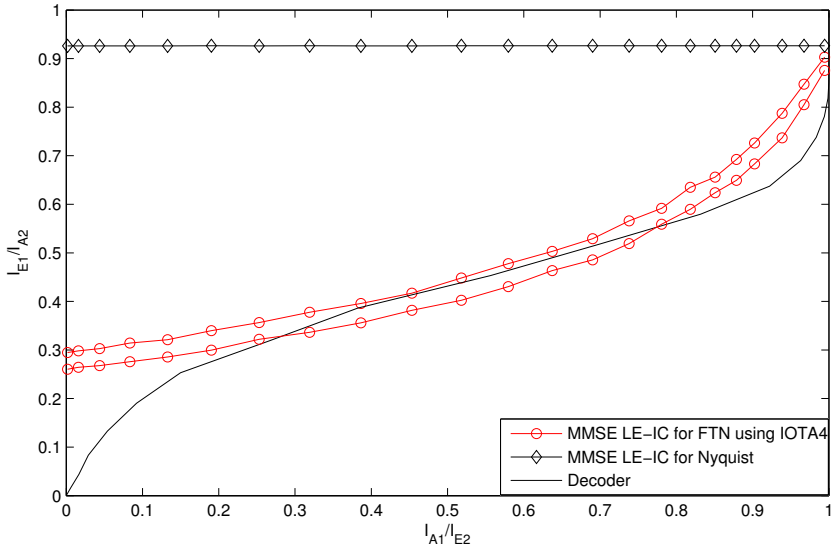

FIGURE 3.18: EXIT chart for MMSE LE-IC with 64-QAM using IOTA at SNR=18.2 dB. The FTN packing factor ranges from 0.8 (bottom) to 0.9 (top).

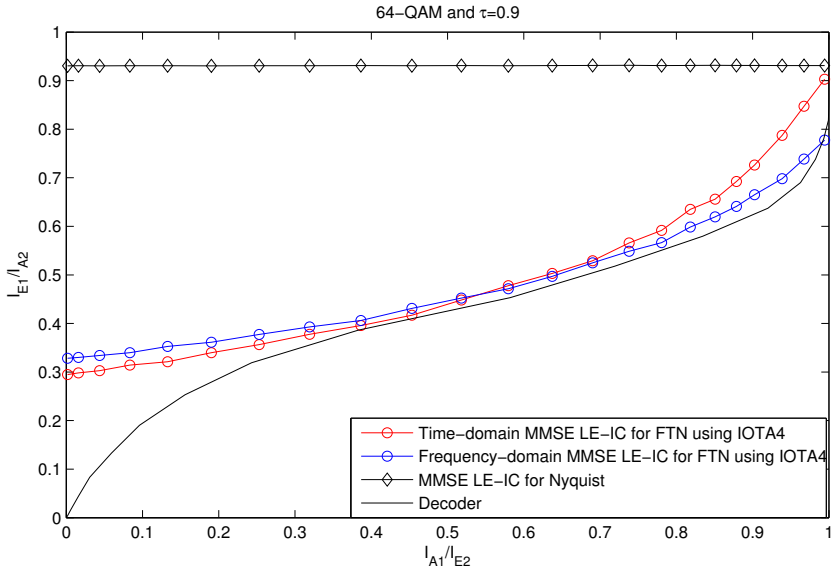

FIGURE 3.19: EXIT chart for MMSE LE-IC with 64-QAM and $\tau = 0.9$, using time-domain and frequency-domain equalization.

Pulse shapes	Equalization domain	QPSK	16-QAM-	64-QAM
SRRC ($\rho = 0.5$)	frequency-domain	0.9	0.9	0.9
SRRC ($\rho = 0.3$)	frequency-domain	0.9	0.9	0.9
PHYDYAS	frequency-domain	0.9	0.9	0.9
FS	frequency-domain	0.9	0.9	0.9
IOTA	time-domain	0.9	0.9	0.9
TFL	time-domain	0.9	0.9	> 0.9
EGF ($\lambda = 2$)	time-domain	0.9	0.9	> 0.9

TABLE 3.2: Numerical values of the effective minimum lossless FTN packing factors and recommended equalization domain for different pulse shapes and modulation orders.

3.5.2 Performance of the proposed FTN-OQAM transceiver

We keep the same configuration as in the previous section and compare the BER performance of the FTN-OQAM transceiver to a classical Nyquist-based OFDM/OQAM system. First, we compare the performance of the different pulse shapes, in terms of BER vs. SNR, for the retained values of the effective minimum lossless FTN packing factors. For each pulse shape, the equalization domain is chosen according to Table 3.2. The result is given in Fig. 3.20, where we can observe that the BER curve does not only depend on the modulation order and the packing factor τ, but also on the chosen pulse shape: for QPSK modulation and $\tau = 0.9$, SRRC ($\rho = 0.5, 0.3$), FS and PHYDYAS filters perform better than the other pulse shapes. We report, in Table 3.3, the recommended pulse shapes for each modulation order.

Next, we compare the BER performance of the FTN-OQAM transceiver to a classical Nyquist-based OFDM/OQAM system. Fig. 3.21 shows the BER curves of the proposed FTN-OQAM transceiver using SRRC ($\rho = 0.5$) filtering and a packing factor $\tau = 0.9$ in

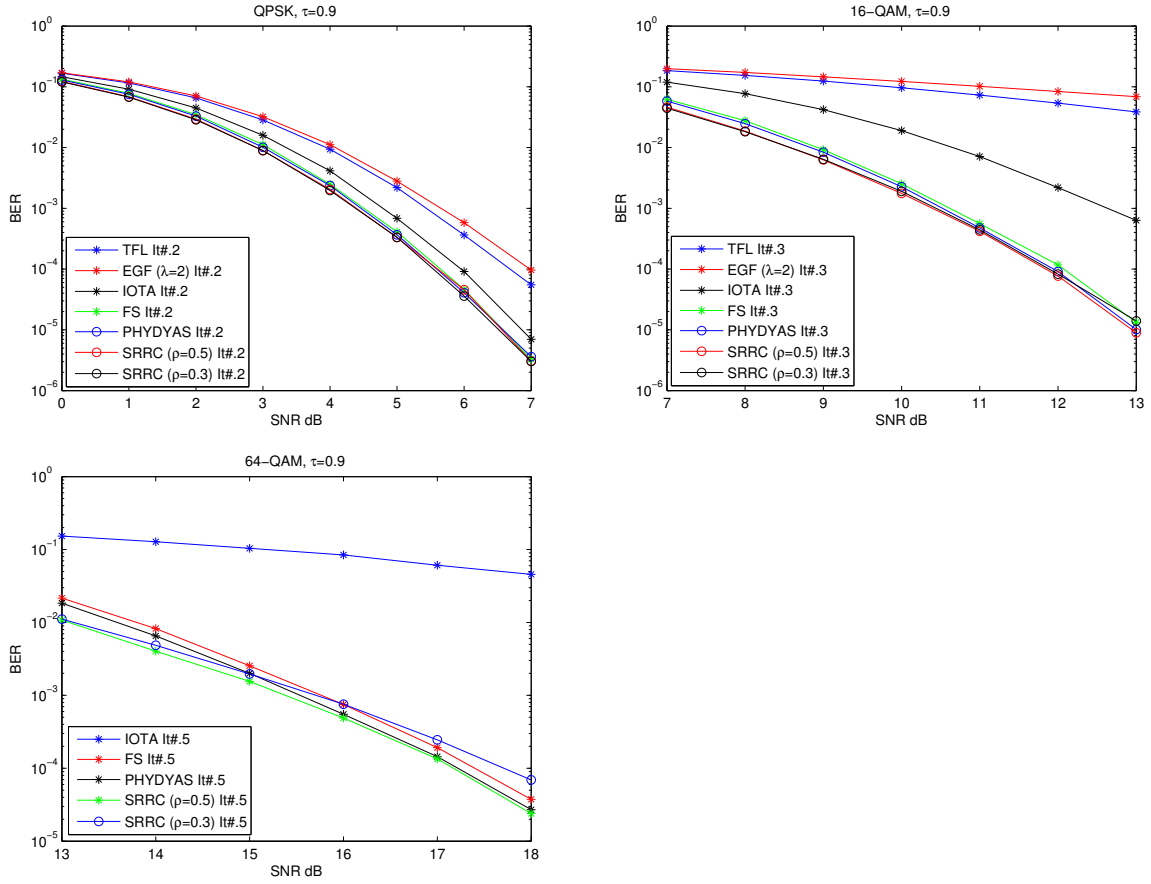

FIGURE 3.20: BER performance of the FTN-OQAM transceiver using different pulse shapes and modulation orders, and $\tau = 0.9$.

Modulation order	Recommended pulse
QPSK	SRRC ($\rho = 0.5, 0.3$), PHYDYAS and FS
16-QAM	SRRC ($\rho = 0.5, 0.3$), PHYDYAS and FS
64-QAM	SRRC ($\rho = 0.5$), PHYDYAS, FS

TABLE 3.3: Recommended pulse shapes for different modulation orders and τ=0.9.

case of QPSK, 16-QAM and 64-QAM. Results show that the BER performance is very close to the Nyquist-based OFDM/OQAM system: for QPSK modulation, the BER curve of the FTN-OQAM transceiver converges to the Nyquist one after performing only 2 iterations at the receiver side. We summarize in Table 3.4 the number of iterations needed at the receiver side, as well as the achieved rate growth.

In the following, we evaluate the FTN-OQAM transceiver for FTN packing factors below the achievable FTN packing factors. We provide in Fig. 3.22, the BER curves using QPSK modulation and PHYDYAS filtering while keeping the same simulation configuration. The packing factor varies from 0.7 to 0.8 and the equalizer operates along the frequency axis. When $\tau = 0.7$, the rate improvement is up to 42 % at a cost of BER performance loss compared to the Nyquist case (1.5 dB loss at a BER around 10^{-4}). The number of iterations needed for convergence is equal to 3. By setting $\tau = 0.8$, the

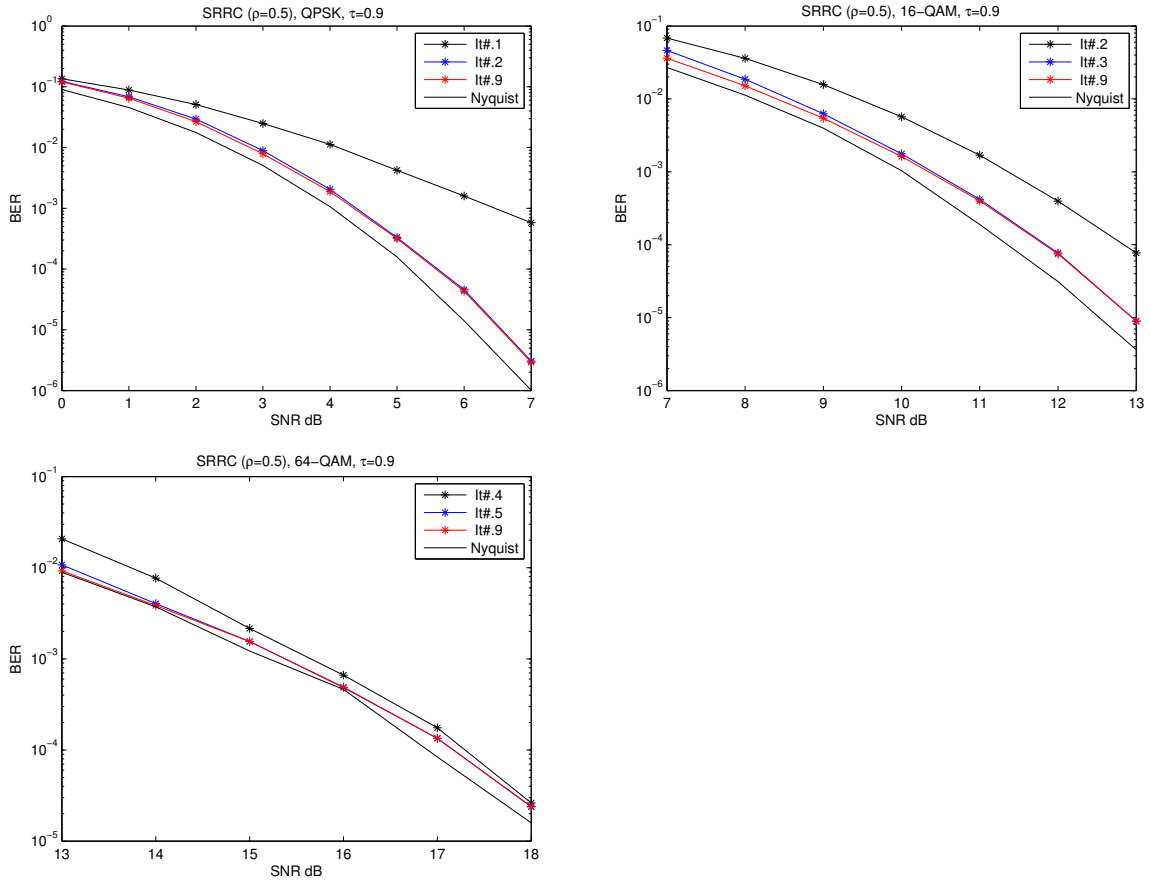

FIGURE 3.21: BER performance of the FTN-OQAM transceiver Vs. Nyquist system for different modulation orders

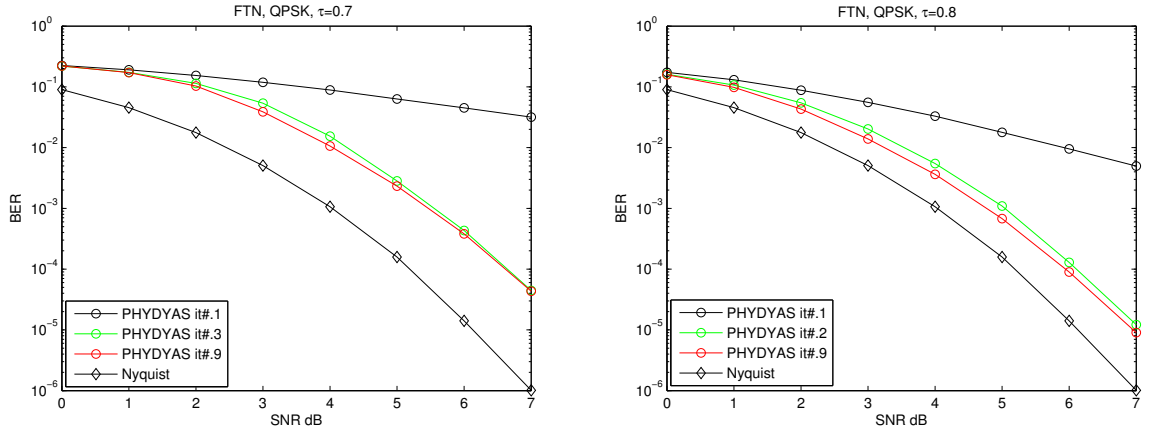

FIGURE 3.22: BER performance of the FTN-OQAM transceiver Vs. Nyquist system using QPSK modulation, PHYDYAS filtering and $\tau = 0.7$ and 0.8.

Modulation order	number of iterations	Rate growth
QPSK	2	1.11
16-QAM	3	1.11
64-QAM	5	1.11

TABLE 3.4: Number of iterations needed for each modulation order to reach an effective minimum lossless FTN packing factor equal to 0.9.

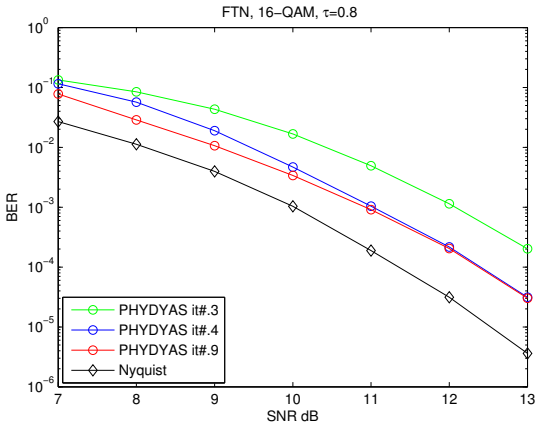

FIGURE 3.23: BER performance of the FTN-OQAM transceiver Vs. Nyquist system using 16-QAM modulation, PHYDYAS filtering and τ =0.8.

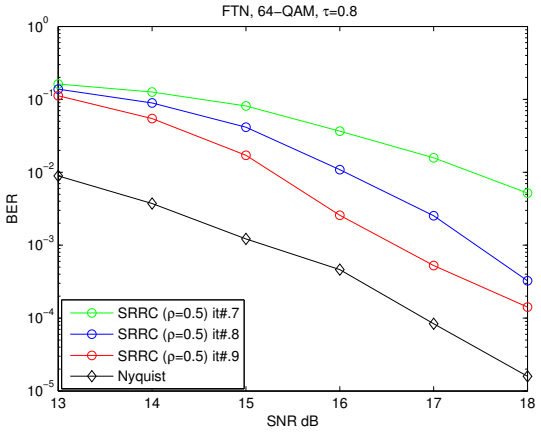

FIGURE 3.24: BER performance of the FTN-OQAM transceiver Vs. Nyquist system using 64-QAM modulation, SRRC (ρ=0.5) filtering and τ =0.8.

rate improvement is 25% with less than 1 dB loss at a BER of 10^{-5}, while the number of needed iterations is only 2.
In case of 16-QAM modulation, the BER results using PHYDYAS filtering and $\tau = 0.8$ are given in Fig. 3.23. The rate growth is now 25% with a loss of 1 dB at a BER around 10^{-4}. The number of needed iterations at the receiver side is equal to 4. Fig. 3.24 provides a comparison between the BER curves when considering 64-QAM modulation, SRRC (ρ=0.5) and $\tau = 0.8$. The receiver needs to perform 9 iterations and the gap between the Nyquist and the FTN curves is about 1.5 dB at a BER of 10^{-4}. We summarize in Table 3.5 the recommended pulse shapes, found through simulations, and

the number of needed iterations for each τ.

Modulation order	FTN packing factor (τ)	Recommended pulse shape	# of iterations
QPSK	0.7	PHYDYAS	3
	0.8	PHYDYAS, SRRC (ρ =0.3, 0.5)	2
16-QAM	0.8	FS, PHYDYAS, SRRC (ρ=0.5)	4
64-QAM	0.8	SRRC (ρ=0.5)	9

TABLE 3.5: Recommended pulse shapes and number of necessary iterations for each modulation order to reach different FTN packing factors.

3.5.3 A word about complexity

In this section, we evaluate the complexity of one iteration performed by the proposed turbo-based receiver. To this end, we compute the number of additions and multiplications (for real symbols) performed by each block at the receiver side, see Table 3.6.

	# of $\times$	# of $+$
MMSE (time)	$B + L_f(3 + 3L_f + L_q)$	$2B + L_f(2L_f + 2 + L_q) + M(h_t + \Delta)$
MMSE (frequency)	$B + \frac{BL_f}{M}(3L_f + 3 + L_q)$	$B(1 + \frac{L_f(2+L_q+2L_f)+M+h_t+\Delta}{M})$
SIC (time)	$2h_f\frac{B}{M}(2h_t + 1)(1 + 3M)$	$2Bh_f(2h_t + 1) + B$
SIC (frequency)	$2h_t\frac{B}{M}(2h_f + 1)(1 + 3M)$	$2Bh_t(2h_f + 1) + B$
SISO mapping	$(2 + 4\log_2(Q))BQ$	$(1 + 2\log_2(Q))BQ$
SISO demapping	$BQ\log_2(Q)(4 + \log_2(Q)) + \frac{B}{2}$	$B\log_2(Q)(2 + Q(3 + \log_2(Q))) + \frac{B}{2}$
Decoder	$N_i(2 + 4\nu) - 1$	$N_i(18 + 14\nu) - 12\nu - 6$

TABLE 3.6: Number of performed additions and multiplications performed by each block of the receiver.

M is the number of subcarriers. $L_q = L_f + 2h_t$, and L_f and Δ are the length and the delay of the MMSE equalizer, respectively. $[-h_t, h_t]$ is the interval of symbols considered for ISI and $[-h_f, h_f]$ the interval of subcarriers considered for ICI. N_i is the number of information bits fed to the channel encoder. $B = \frac{2N_i}{r\log_2(Q)}$ is the number of transmitted symbols with r the coding rate and Q the modulation order. ν is the number of the states of the code.
Let us consider: M=64 subcarriers, L_f=30, Δ=15, $h_t = h_f$ =4, $r = \frac{1}{2}$, ν=4 and N_i=71424 information bits. The overall complexity of the receiver considering different modulation orders is given in Table 3.7. As expected, the complexity increases with the modulation order. Moreover, we observe that the receiver performs slightly less operations when the MMSE equalizer operates along the time axis. This is due to the fact that in frequency-domain equalization, the filters parameters should be computed for each time instant.

Modulation order	Time-domain equalization		Frequency-domain equalization	
	# of $\times$	# of $+$	# of $\times$	# of $+$
QPSK	4.5×10^7	2.5×10^7	5.4×10^7	3.2×10^7
16-QAM	7.4×10^7	5.4×10^7	7.8×10^7	5.7×10^7
64-QAM	27.4×10^7	21.4×10^7	27.7×10^7	21.6×10^7

TABLE 3.7: Complexity of one performed iteration at the receiver side considering different modulation orders.

3.6 Conclusion

In this chapter, we have presented an efficient implementation of the FTN-OQAM transceiver which, differently from the SoTA solution [2], approaches very closely the FTN theoretical rate growth without increasing the complexity when switching from the Nyquist mode to the FTN mode. We provided an analysis of the FTN-induced interference and showed that the power of ISI and ICI varies according to the time-frequency localization features of the prototype filters. Moreover, a turbo-like receiver based on MMSE filtering in time and frequency domains was presented instead of a MAP-based equalizer. Further, we proposed an algorithm to investigate the numerical values of the effective minimum lossless FTN packing factors, supported by this transceiver, for each pulse shape and modulation order.

We reported, through EXIT charts analysis, the recommended equalization domain for each pulse shape and compared their performance in terms of BER vs. SNR. Indeed, we showed that the proposed equalizer should better operate along time axis for prototype filters well localized in time-domain and vice-versa. In [107], the proposed transceiver achieves a packing factor $\tau = 0.5$. However, results were only presented for QPSK modulation and the proposed receiver is based on MAP algorithm which leads to important complexity increase when high modulation orders are targeted. Through simulation results, we showed that our proposed FTN-OQAM transceiver can support high modulation orders while keeping the receiver complexity at a reasonable level since the equalizer complexity depends only linearly on the length of the equivalent ISI channel. In fact, a rate growth of 11% was achieved for 64-QAM after performing only 5 iterations at the receiver while still converging to the Nyquist performance. In the case of 16-QAM modulation, a rate improvement up to 25% can be achieved at the price of 1 dB loss around a BER of 10^{-4} after performing only 4 iterations at the receiver side.

Signaling faster than the Nyquist rate causes additional interferences even for transmissions over AWGN channel. In this chapter, we showed that FTN-self interference can be modeled as an equivalent channel of ISI and ICI. The coefficients of the equivalent interference channel can be deduced from the expression of the transmitted signal. Therefore, the interference coefficients are available at the transmitter side, which can be equivalent to transmissions over a multipath channel with perfect channel state information at the transmitter. In the next chapter, we propose to take advantage of this available information to reduce FTN-self interference and improve the FTN-OQAM transceiver performance.

Part of the results presented in this chapter were published in IEEE International Conference on Communications (ICC) in 2015 [108]:

H. Lin, N. Lahbabi, P. Siohan and X. Jiang, “An efficient FTN implementation of the OFDM/OQAM system", ICC’15, London, UK, June 2015.

Chapter 4

Precoded FTN-OQAM

4.1 Introduction

In this chapter, we aim at improving the FTN-OQAM transceiver presented in the previous chapter. Although the signals are only packed in time domain, with respect to the Nyquist rate, the useful signal is also impacted by ICI in addition to ISI. However, FTN-induced interferences are perfectly known by the transmitter which leads to the question of whether techniques aiming at cancelling interference at the transmitter side can be considered. Our objective in this chapter is to investigate a new precoding technique for the FTN-OQAM transceiver to reduce FTN-self interferences. To this end, we introduce three families of precoders to the transmission chain depicted in Fig. 3.10 in order to suppress ICI and/or ISI and detail the corresponding receiver for each precoder.

As presented in the previous chapter, assuming the physical channel is noiseless and distortion-free, the received signal at time instant n_0 and on subcarrier m_0 can be expressed as (3.6):

$$y_{m_0,n_0} = a_{m_0,n_0} + \underbrace{\sum_{\substack{q=-l \\ q\neq 0}}^{l} h_q a_{m_0,n_0+q}}_{ISI} + \underbrace{\sum_{\substack{p=-l' \\ p\neq 0}}^{l'} \sum_{q=-l}^{l} l_{p,q,n_0} a_{m_0+p,n_0+q}}_{ICI_{n_0}}, \tag{4.1}$$

where $a_{m,n}$ are the transmitted OQAM symbols and factors (l, l') represent the zone of symbols contributing to ISI and ICI, respectively.

$$h_q = L\cos(\frac{\pi}{2}q)A_g[-qN_f, 0], \tag{4.2}$$

and

$$l_{p,q,n_0} = L\cos(\pi(\frac{p+q}{2} + \frac{2p(n_0N_f - \frac{D}{2})}{M}))A_g[-qN_f, -pb] \tag{4.3}$$

are the coefficients of the equivalent channel of ISI and ICI, respectively. L is the length of the filter g and A_g is its discrete ambiguity function. M is the number of subcarriers, $D = L - 1$ and $N_f = \lfloor \tau.\frac{M}{2} \rfloor$ is the FTN expansion/decimation factor.
The received signal is the sum of the useful signal and of the interference terms that are

known at the transmitter side. Therefore, this additional term can be calculated and pre-canceled. A well known precoding method based on interference pre-cancellation is the Tomlinson-Harashima Precoding (THP) presented in chapter 2.
According to this technique, the transmitter has perfect channel state information and successively precodes each symbol $a_{m,n}$ by removing the interference caused by previous symbols $a_{m,n-q}$, with $1 \leq q \leq l$ and l the length of the channel impulse response. In case of FTN signaling, each symbol $a_{m,n}$ interferes with symbols $a_{m+p,n+q}$ with $(p,q) \in [-l',l'] \times [-l,l]$, i.e., FTN-induced interference is caused by past and future neighbors. For our FTN-OQAM transceiver, precoded symbols at time instant n and on subcarrier m can be expressed as:

$$c_{m,n} = a_{m,n} - \underbrace{\sum_{q=-l}^{-1} h_q c_{m,n+q} - \sum_{p=-l'}^{-1}\sum_{q=-l}^{l} l_{p,q,n} c_{m+p,n+q}}_{Past\ precoded\ symbols} - \underbrace{\sum_{q=1}^{l} h_q a_{m,n+q} - \sum_{p=1}^{l'}\sum_{q=-l}^{l} l_{p,q,n} a_{m+p,n+q}}_{Future\ symbols} \tag{4.4}$$

where, $c_{m+p,n+q}, (p,q) \in [-l',-1] \times [-l,-1]$ are the past precoded symbols according to THP method, and $a_{m+p,n+q}, (p,q) \in [1,l'] \times [1,l]$ are the future interfering symbols. When the latter are also precoded, they cause a new interference different from the one removed from $a_{m,n}$ in (4.4). Hence, the nature of FTN-self interference makes it difficult to jointly precode all the transmitted symbols.

In the following, we detail our proposed precoding solution for the FTN-OQAM transceiver called Sparse Interference Pre-Cancellation (SIPC). Firstly, we propose to precode only a sub-group of the transmitted symbols, meaning that symbols used in (4.4) to precode the symbol $a_{m,n}$ are not modified and remain normal OQAM symbols. Secondly, the modulo operation in the THP method is dropped. This operation was originally introduced to control the amplitude of the precoded symbols. Although this operation is removed, the transmitted signal power does not increase. Compared to the Nyquist case, the FTN signal power increases due to the additional interferences. Since the latter are reduced through precoding, the signal power decreases compared to the non-precoded transceiver. The structure of the proposed precoded FTN-OQAM transceiver is depicted in Fig. 4.1, where dashed blocks are related to the SIPC method. We considered three precoding families depending on whether ICI and/or ISI are pre-canceled. For each precoder, we detail the structure of the transmitter and its corresponding receiver. Then, we evaluate the BER performance considering the numerical values of the minimum FTN packing factors found in the previous chapter, i.e., $\tau = 0.9$ and different modulation orders. Based on BER results, we present the recommended pulses for each precoder as well as on the number of iterations needed at the receiver side. In the last section, we evaluate the precoded FTN-OQAM transceiver performance when τ is below 0.9 (τ=0.7, 0.8). For each modulation order and packing factor, the recommended precoders are presented and then compared to the FTN-OQAM transceiver detailed in chapter 3 to highlight the precoding benefits.

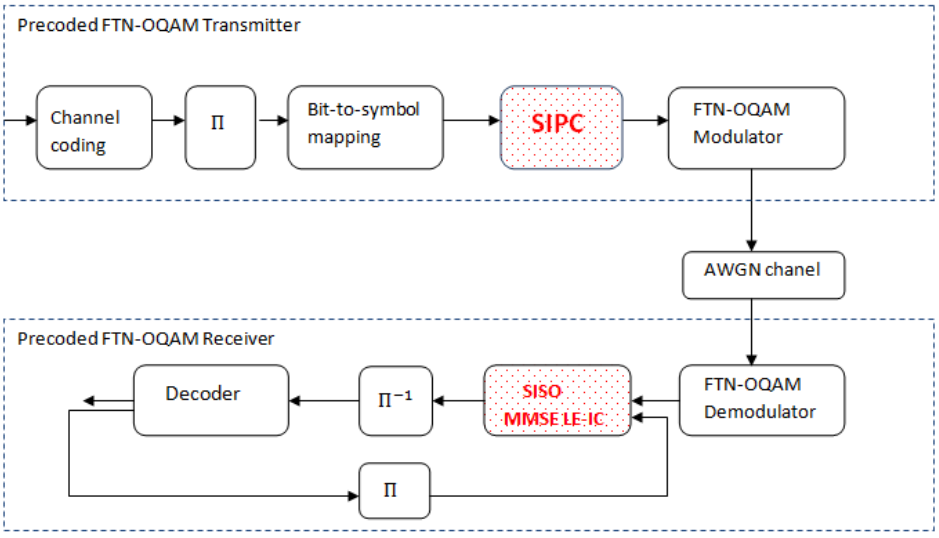

FIGURE 4.1: The proposed precoded FTN-OQAM transceiver. Dashed blocks are related to the SIPC method.

4.2 Precoded FTN-OQAM transceiver: ISI and ICI cancellation

4.2.1 SIPC along time and frequency axes

In this section, we present the SIPC precoder along time and frequency axes (SIPC-tf). Our objective is to cancel ICI and ISI from a sub-group of the transmitted symbols. The precoded symbols at time instant n and on subcarrier m are formulated as:

$$c_{m,n} = a_{m,n} - \alpha\{\sum_{\substack{q=-k \\ q\neq 0}}^{k} h_q a_{m,n+q}\} - \beta\{\sum_{\substack{p=-k' \\ p\neq 0}}^{k'}\sum_{q=-l}^{l} l_{p,q,n} a_{m+p,n+q}\}, \tag{4.5}$$

where $a_{m,n}$ are OQAM symbols. The pair $(k, k') \in \mathbb{Z}^2$ represents the zone of symbols considered for pre-canceling ISI and ICI, respectively. Moreover, we introduce two factors α and β to control the amount of removed interference. In a time-frequency lattice, the precoded symbols are positioned at subcarriers m and at time instants n such that :

$$\begin{cases} m = b \bmod(k'+1), \ (b \in \mathbb{N}, \ b \leq k') \\ n = a \bmod(k+2), \text{ and } n = (a+1) \bmod(k+2), \ (a \in \mathbb{N}, \ a \leq (k+1)) \end{cases} \tag{4.6}$$

Fig. 4.2 illustrates a precoding pattern example. The green triangles represent the precoded symbols, while the blue and red ones represent the non-precoded symbols. In this example, we consider that the nearest two symbols, represented here by the blue triangles, contribute mostly to ISI, i.e., we set $k = 2$. At a subcarrier m, we alternate between two precoded and non-precoded symbols. In fact, for each symbol at time instant n, it is shown that symbols at odd positions do not contribute to ISI (3.46). Similarly, we

consider that symbols at the closest subcarriers, represented here by the red triangles, contribute mostly to ICI, i.e., we set $k' = 1$. Therefore, our precoding solution is sparse: only a group of the transmitted symbols are precoded while the rest remain unmodified OQAM symbols.

The proposed precoded FTN-OQAM transceiver is reported in Fig. 4.1. First, informa-

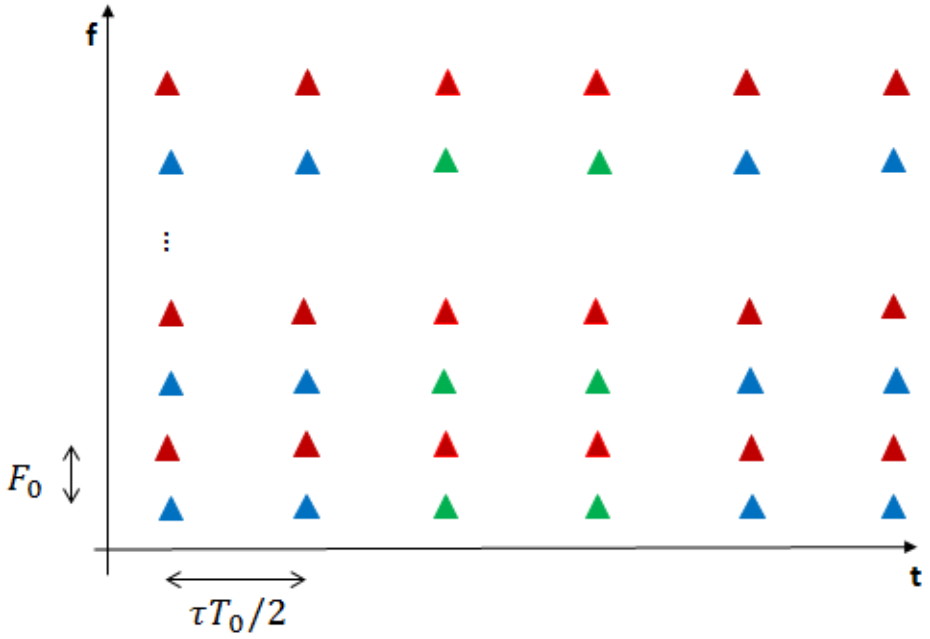

FIGURE 4.2: Time-frequency lattice of FTN-OQAM with SIPC-tf precoding. Green triangles represent precoded symbols while the red and blue triangles represent OQAM symbols.

tion bits are encoded. By setting the index pair (k, k'), we determine the number of the precoded and non-precoded symbols. Considering that B symbols are to be transmitted and setting $(k = 2,\ k' = 1)$, the number of precoded and non-precoded symbols is $B_1 = \frac{B}{4}$ and $B_2 = \frac{3B}{4}$, respectively. Then, encoded bits constituting the different groups of symbols are interleaved separately. Finally, the *SIPC* module precodes symbols at the chosen time and frequency positions according to (4.5).

4.2.2 The receiver structure

At the receiver side, the MMSE LE-IC equalizer detailed in the previous chapter is modified to take the introduced SIPC module into account. We propose a 3-stage MMSE LE-IC equalizer to process separately the precoded and non-precoded symbols. Keeping the same configuration as in the previous section $(k = 2,\ k' = 1)$, symbols at the green positions are decoded first, followed by the ones at the blue positions and finally by the ones represented by red triangles. The precoded symbols represented by the green triangles are detected first since they are less impacted by interference. Thus, their contribution to ISI with the non-precoded symbols at the same subcarriers, represented here by the blue triangles, can be removed. The latter are then decoded in the second stage. Finally, the contribution of symbols represented by the green and blue triangles

to ICI with the ones represented by the red triangles can be canceled and the latter are then detected. For example, we consider that :

$$\text{green triangles} = \{(m,n),(m \text{ even}, n = 3 \text{ and } 0 \bmod(4))\} \tag{4.7}$$

$$\text{blue triangles} = \{(m,n),(m \text{ even}, n = 1 \text{ and } 2 \bmod(4))\} \tag{4.8}$$

$$\text{red triangles} = \{(m,n), m \text{ odd }\} \tag{4.9}$$

We also consider that B symbols are transmitted and that each subcarrier is composed of N_s symbols. At a subcarrier m, a matrix formulation of the precoded symbols can be expressed as:

$$\mathbf{C}_m = \mathbf{W}\mathbf{A}_m - \beta\mathbf{L}_1\mathbf{A}_{m+1} - \beta\mathbf{L}_{-1}\mathbf{A}_{m-1}, \tag{4.10}$$

where $\mathbf{C}_m = [c_{m,1}, c_{m,2}, ..., c_{m,N_s}]^T$ and $\mathbf{A}_m = [a_{m,1}, a_{m,2}, ..., a_{m,N_s}]^T$ are the precoded and OQAM symbols, respectively. $\mathbf{W}$ and $\mathbf{L}_p$, $p \in [-l', l']$, are the $N_s \times N_s$ precoding matrices given by:

$$\mathbf{W} = \begin{pmatrix} 1 & 0 & & & & ... & & & 0 \\ 0 & 1 & 0 & & & ... & & & 0 \\ -\alpha h_{-2} & 0 & \frac{1}{h_0} & 0 & -\alpha h_2 & 0 & 0 & ... & 0 \\ 0 & -\alpha h_{-2} & 0 & \frac{1}{h_0} & 0 & -\alpha h_2 & 0 & ... & 0 \\ \vdots & & & \ddots & \ddots & \ddots & & & \vdots \\ 0 & & & & 0 & 1 & 0 & 0 & 0 \\ 0 & & & & & 0 & 1 & 0 & 0 \\ 0 & & ... & & 0 & -\alpha h_{-2} & 0 & \frac{1}{h_0} & 0 \\ 0 & & & & & 0 & -\alpha h_{-2} & 0 & \frac{1}{h_0} \end{pmatrix} \tag{4.11}$$

$$\mathbf{L}_p = \begin{pmatrix} l_{p,1,1} & l_{p,2,1} & ... & l_{p,l,1} & 0 & ... & 0 \\ l_{p,-1,2} & l_{p,1,2} & ... & l_{p,l,2} & 0 & ... & 0 \\ \vdots & & \ddots & & ... & \ddots & 0 \\ 0 & ... & 0 & l_{p,-l,N_s} & ... & l_{p,-1,N_s} & l_{p,1,N_s} \end{pmatrix} \tag{4.12}$$

Similarly, the $N_s \times N_s$ matrix of the ISI equivalent channel is expressed as:

$$\mathbf{H} = \begin{pmatrix} h_0 & ... & h_l & 0 & ... & 0 \\ h_{-1} & h_0 & ... & h_l & & \vdots \\ \vdots & & \ddots & & \ddots & 0 \\ 0 & ... & 0 & h_{-l} & ... & h_0 \end{pmatrix} \tag{4.13}$$

The 3-stage MMSE LE-IC equalizer is detailed in Fig. 4.3. The received precoded symbols are processed first. At even subcarrier indices m, the latter are expressed as:

$$\mathbf{Y}_m = \mathbf{H}\mathbf{C}_m + \sum_{\substack{p=-l', p \text{ even} \\ p \neq 0}}^{l'} \mathbf{L}_p\mathbf{C}_{m+p} + \sum_{\substack{p=-l' \\ p \text{ odd}}}^{l'} \mathbf{L}_p\mathbf{A}_{m+p}, \tag{4.14}$$

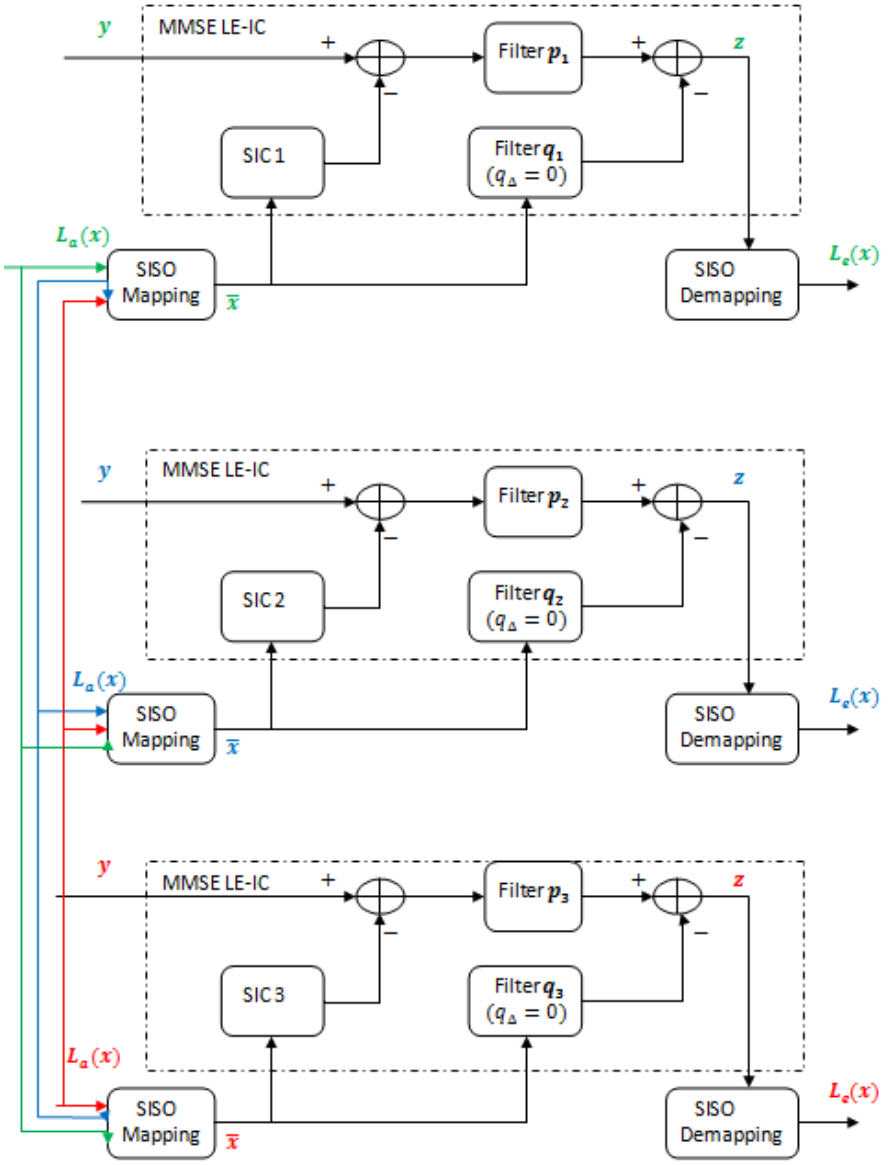

FIGURE 4.3: Structure of the SISO MMSE IC-LE used for SIPC-tf precoding.

with, $\mathbf{Y}_m = [y_{m,1}, y_{m,2}, ..., y_{m,N_s}]^T$. By inserting (4.10) into (4.14), we obtain:

$$\begin{aligned}\mathbf{Y}_m &= \mathbf{HWA}_m - \beta\mathbf{HL}_1\mathbf{A}_{m+1} - \beta\mathbf{HL}_{-1}\mathbf{A}_{m-1} + \sum_{\substack{p=-l' \\ p\ odd}}^{l'} \mathbf{L}_p\mathbf{A}_{m+p} \\ &+ \sum_{\substack{p=-l', p\ even \\ p\neq 0}}^{l'} \mathbf{L}_p[\mathbf{WA}_{m+p} - \beta\mathbf{L}_1\mathbf{A}_{m+p+1} - \beta\mathbf{L}_{-1}\mathbf{A}_{m+p-1}].\end{aligned} \tag{4.15}$$

This expression can be further simplified to:

$$\begin{aligned}\mathbf{Y}_m &= \mathbf{HWA}_m + (\mathbf{L}_1 - \beta\mathbf{HL}_1)\mathbf{A}_{m+1} + (\mathbf{L}_{-1} - \beta\mathbf{HL}_{-1})\mathbf{A}_{m-1} + \sum_{\substack{p=-l' \\ p\neq\pm1,\, p\ odd}}^{l'} \mathbf{L}_p\mathbf{A}_{m+p} \\ &+ \sum_{\substack{p=-l', p\ even \\ p\neq0}}^{l'} \mathbf{L}_p[\mathbf{WA}_{m+p} - \beta\mathbf{L}_1\mathbf{A}_{m+p+1} - \beta\mathbf{L}_{-1}\mathbf{A}_{m+p-1}]. \end{aligned} \tag{4.16}$$

In this expression, the first term counts for the useful signal and ISI, while the other terms represent ICI. To decode the received signal, block *SIC1* removes first ICI based on soft estimated symbols delivered by the decoder and the *SISO mapping*. Depending on whether time or frequency domain equalization is considered, the coefficients of filters $\mathbf{p}_1$ and $\mathbf{q}_1$ are computed, as indicated in chapter 2 (2.86), and the signal is then equalized. As in the previous chapter, *SISO Mapping* and *SISO Demapping* blocks are used to exchange bit-level and symbol-level information between the equalizer and the decoder.

In a second step, we decode the non-precoded symbols received at the same subcarriers m. First, using the LLRs delivered by the decoder in step 1, the *SISO Mapping* block calculates the corresponding soft estimated symbols. Hence, the *SIC2* module cancels ICI coming from side subcarriers as well as ISI caused by the precoded symbols. Then, the coefficients of filters $\mathbf{p}_2$ and $\mathbf{q}_2$ are calculated. Finally, the signal is equalized and decoded.

Parameter α

Recalling the expression of h_q:

$$h_q = L\cos(\frac{\pi}{2}q)A_g[-qN_f, 0], \tag{4.17}$$

and knowing that A_g is even, we have $h_q = h_{-q}$. Based on the product matrix $\mathbf{HW}$, we can deduce that the received non-precoded symbols are weighted by a factor $(1 - 2\alpha h_2^2)$. As we can notice, the introduced parameter α not only controls the amount of pre-canceled ISI but also the amplitude of the received non-precoded symbols.

At the third stage, we decode the non-precoded symbols received at odd subcarrier indices m:

$$\mathbf{Y}_m = \mathbf{HA}_m + \sum_{\substack{p=-l' \\ p\ odd}}^{l'} \mathbf{L}_p\mathbf{C}_{m+p} + \sum_{\substack{p=-l' \\ p\neq0,p\ even}}^{l'} \mathbf{L}_p\mathbf{A}_{m+p}. \tag{4.18}$$

Replacing $\mathbf{C}_{m+p}$ by its expression, we obtain:

$$\mathbf{Y}_m = \mathbf{HA}_m + \sum_{\substack{p=-l' \\ p\ odd}}^{l'} \mathbf{L}_p[\mathbf{WA}_{m+p} + \mathbf{L}_1\mathbf{A}_{m+p+1} + \mathbf{L}_{-1}\mathbf{A}_{m+p-1}] + \sum_{\substack{p=-l' \\ p\neq0,p\ even}}^{l'} \mathbf{L}_p\mathbf{A}_{m+p}$$

$$= (\mathbf{H} - \beta\mathbf{L}_1\mathbf{L}_{-1} - \beta\mathbf{L}_{-1}\mathbf{L}_1)\mathbf{A}_m + \sum_{\substack{p=-l' \\ p\neq 0, p\ even}}^{l'} \mathbf{L}_p\mathbf{A}_{m+p} \tag{4.19}$$

$$+ \sum_{\substack{p=-l' \\ p\neq \pm 1, p\ odd}}^{l'} \mathbf{L}_p[\mathbf{W}\mathbf{A}_{m+p} + \mathbf{L}_1\mathbf{A}_{m+p+1} + \mathbf{L}_{-1}\mathbf{A}_{m+p-1}]$$

$$+\mathbf{L}_1\mathbf{W}\mathbf{A}_{m+1} + \mathbf{L}_{-1}\mathbf{W}\mathbf{A}_{m-1} - \beta\mathbf{L}_1^2\mathbf{A}_{m+2} - \beta\mathbf{L}_{-1}^2\mathbf{A}_{m-2}.$$

As $\mathbf{L}_p$ depends on time instant n, the first term representing the useful signal and ISI depends on time as well. Thus, we propose to equalize the received signal using MMSE LE-IC in the frequency domain. As we can observe, parameter β controls not only the amount of pre-canceled ICI but also the amplitude of the received non-precoded symbols. First, the block *SIC3* suppresses ICI caused by side subcarriers using the soft symbols estimated by the *SISO Mapping* module. Then, the coefficients of filters $\mathbf{p}_3$ and $\mathbf{q}_3$ are computed for each time instant n. Finally, the signal is equalized and decoded.

4.2.3 BCJR decoder modification

In order to process separately the received symbols, encoded bits mapped to each group of symbols are interleaved separately. In Fig. 4.1, the *Decoder* is based on Max-Log-MAP algorithm. As explained in the second chapter in section 2.5.1, the decoder takes *a priori* $L_a(c_{k,i})$ information as input and calculates the *a posteriori* LLRs of the coded bits $L(c_{k,i})$ defined as:

$$L(c_{k,i}) = \ln \frac{Pr(c_{k,i} = 1|\{L_a(c_{k,i})\})}{Pr(c_{k,i} = 0|\{L_a(c_{k,i})\})}. \tag{4.20}$$

This metric is calculated using the BCJR algorithm and the Max-Log approximation:

$$L(c_{k,i}) = \max_{v\to v':c_{k,i}=1} \{\alpha_{k-1}(v) + \gamma_k(v \to v') + \beta_k(v')\} - \tag{4.21}$$

$$\max_{v\to v':c_{k,i}=0} \{\alpha_{k-1}(v) + \gamma_k(v \to v') + \beta_k(v')\}. \tag{4.22}$$

This operation is applied for all the transitions $v \to v'$ in the code trellis having 1 or 0 for the coded bit $c_{k,i}$ at time k. Forward and backward metrics $\alpha_0(v)$ and $\beta_N(v')$, with N_c the size of coded bits, are initialized to 0.

Considering the precoding pattern of Fig. 4.2 with $(k = 2, k' = 1)$, the N_c coded bits are decoded in 3 steps. The first $\frac{N_c}{4}$ bits are decoded at stage 1, the following $\frac{N_c}{4}$ bits are decoded at stage 2 and the last $\frac{N_c}{2}$ bits are decoded at stage 3. Unlike the forward metric $\alpha_0(v)$, the metrics $\alpha_{\frac{N_c}{4}}(v)$ and $\alpha_{\frac{N_c}{2}}(v)$ are not initialized to 0 and are computed by the decoder at stage 1 and 2, respectively. Similarly, the backward metrics $\beta_{\frac{N_c}{4}-1}(v')$ and $\beta_{\frac{N_c}{2}-1}(v')$ are not initialized at 0 but calculated by the decoder at stage 2 and 3, respectively. The BCJR modifications consist in changing the value of the initial forward metric and the final backward metric at each decoding stage. Indeed, these metrics are not initially set to 0. Instead, they are computed by the decoders and exchanged during the different decoding stages.

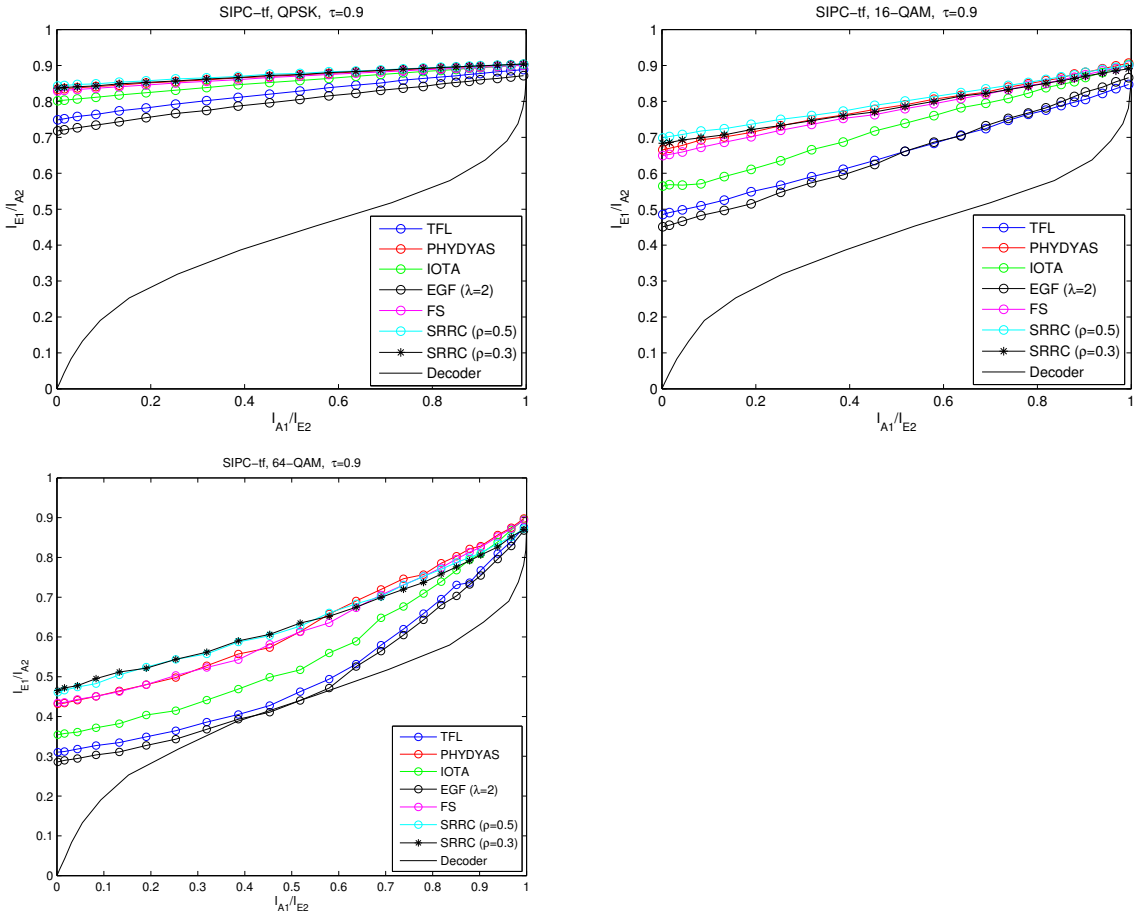

FIGURE 4.4: EXIT chart analysis of the FTN-OQAM transceiver combined with SIPC-tf precoding for QPSK, 16-QAM, 64-QAM and $\tau = 0.9$.

4.2.4 Simulation results

In this section, we evaluate the performance of SIPC-tf precoding method in terms of EXIT chart analysis and BER vs. SNR. We considered the effective minimum lossless packing factor found in the previous chapter, i.e., $\tau = 0.9$. We kept the same simulation parameters as in the previous chapter: $(1, 5/7)$ RSC code with rate $\frac{1}{2}$ and Gray mapping. We used a random interleaver for the encoded bits composing each group of symbols. The receiver is based on MMSE LE-IC equalization: the length of the MMSE filter is 30 and the delay is 15. The decoder is based on Max-Log-MAP algorithm. We also used different pulse shapes: TFL ($L = M$), EGF ($L = 4M$, λ=2), IOTA ($L = 4M$), FS ($L = 4M$), PHYDYAS ($L = 4M$), SRRC ($L = 4M$, ρ=0.5) and SRRC ($L = 4M$, ρ=0.3). The precoding factors are $k = 2$ and $k' = 1$.

Fig. 4.4 shows the EXIT chart analysis of the precoded FTN-OQAM transceiver for different pulse shapes and modulation orders: QPSK, 16-QAM and 64-QAM. As we can notice, the EXIT curve depends on the employed pulse shape. For all the modulation orders considered, the recommended pulse shapes are: SRRC (ρ=0.5), SRRC (ρ=0.3), FS and PHYDYAS filters as the tunnel between the decoder and the equalizer is wider. In case of 64-QAM modulation, the tunnel between the decoder and the equalizer using

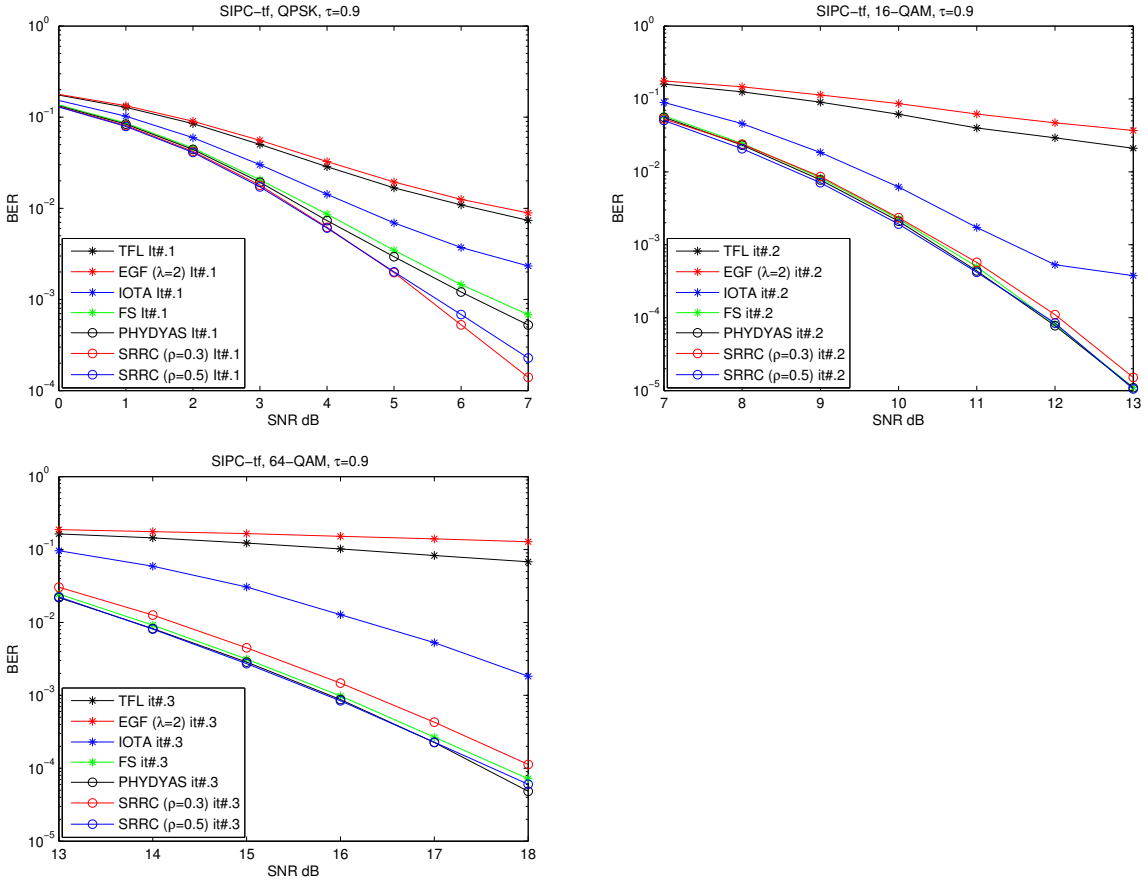

FIGURE 4.5: BER vs. SNR performance of the proposed FTN-OQAM transceiver combined with SIPC-tf precoding for QPSK, 16-QAM, 64-QAM and $\tau = 0.9$.

TFL and EGF (λ=2) is almost closed. Fig. 4.5 shows the BER curves of the different pulse shapes for different modulation orders. The BER performance is consistent with the EXIT chart analysis. In case of QPSK modulation, our results show that all the pulse shapes enable the receiver to converge to nearly similar BER after performing 2 iterations. However, when using the SRRC (ρ=0.5 and 0.3), PHYDYAS and FS filters, the receiver shows better BER performance at the first iteration. For 16-QAM modulation, our results show that the receiver converges to the same BER performance using different pulse shapes. However, the number of necessary iterations is equal to 2 when the SRRC (ρ=0.5 and 0.3), PHYDYAS and FS filters are used, instead of 3 iterations in case of IOTA filtering and 4 iterations for the TFL and EGF (λ=2) filters. Finally, results in case of 64-QAM modulation show that the PHYDYAS, FS and SRRC (ρ=0.5) filters provide better BER performance and permit the receiver to converge after performing 3 iterations. Moreover, the receiver needs to perform 4 iterations in case of SRRC (ρ=0.3) and IOTA filtering. In case of TFL and EGF (λ=2) filters, the number of necessary iterations is 6 and 7, respectively. We summarize the number of needed iterations for each pulse shape in Table 4.1.

Next, we compare the performance of the precoded and non-precoded FTN-OQAM transceiver using the recommended pulse shapes. The EXIT chart analysis is given in Fig. 4.6, where the black curve represents the decoder and the blue and green curves represent the equalizer of the precoded and non-precoded transceiver, respectively. In

Pulse shape	QPSK	16-QAM	64-QAM
TFL	2	4	6
EGF (λ=2)	2	4	7
IOTA	2	3	4
FS	2	2	3
PHYDYAS	2	2	3
SRRC (ρ=0.5)	2	2	3
SRRC (ρ=0.3)	2	2	4

TABLE 4.1: Number of necessary iterations for each pulse shape in case of SIPC-tf precoding and $\tau = 0.9$.

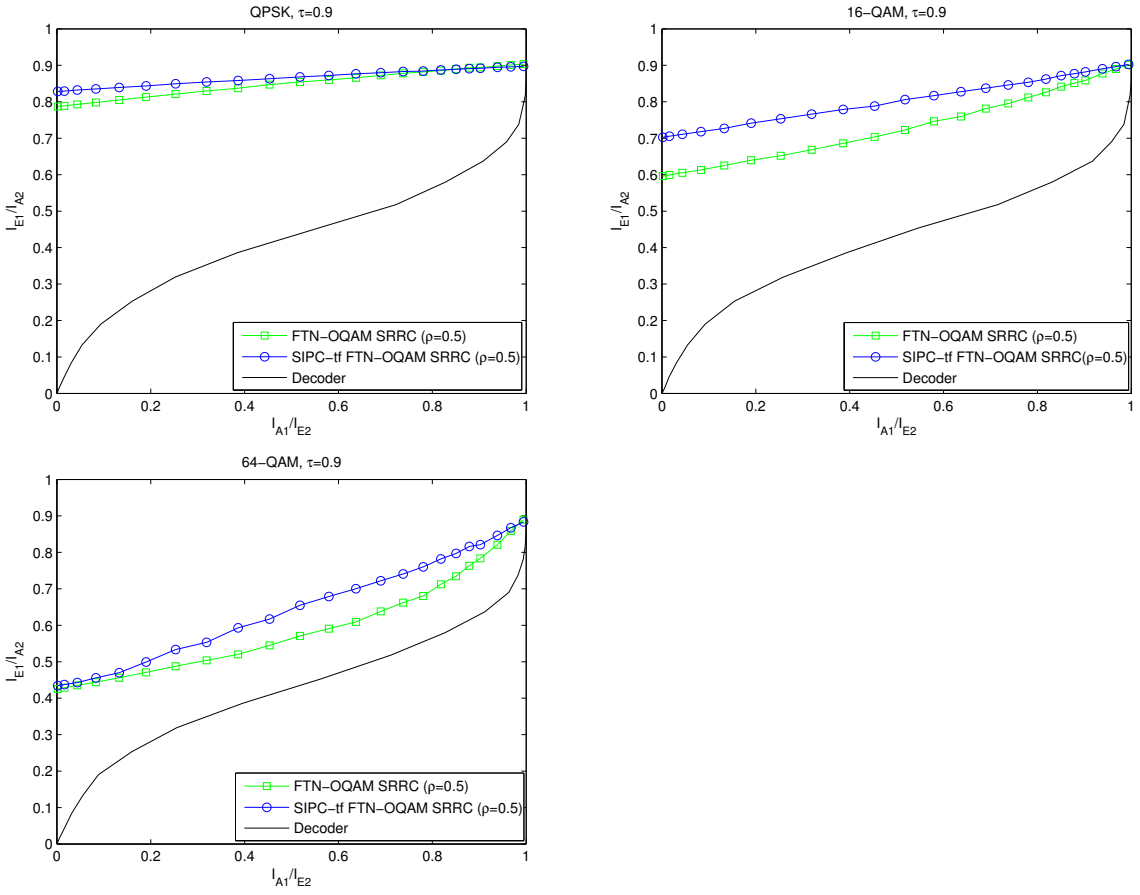

FIGURE 4.6: Comparison of the EXIT chart analysis between the precoded and non-precoded FTN-OQAM transceiver using SRRC (ρ=0.5) filtering, $\tau = 0.9$ and different modulation orders.

case of QPSK modulation, the blue curve is almost identical to the green one, although the mutual information at the equalizer output is slightly higher at the first iteration. In case of 16-QAM and 64-QAM, the tunnel between the decoder and the blue curve is wider meaning that less iterations are necessary for the receiver convergence. The BER results given in Fig. 4.7 are consistent with the EXIT chart analysis. Indeed, in case of QPSK modulation, the receiver of both systems needs 2 iterations to converge. However, the first iteration is improved by the SIPC-tf precoding. For 16-QAM modulation, we

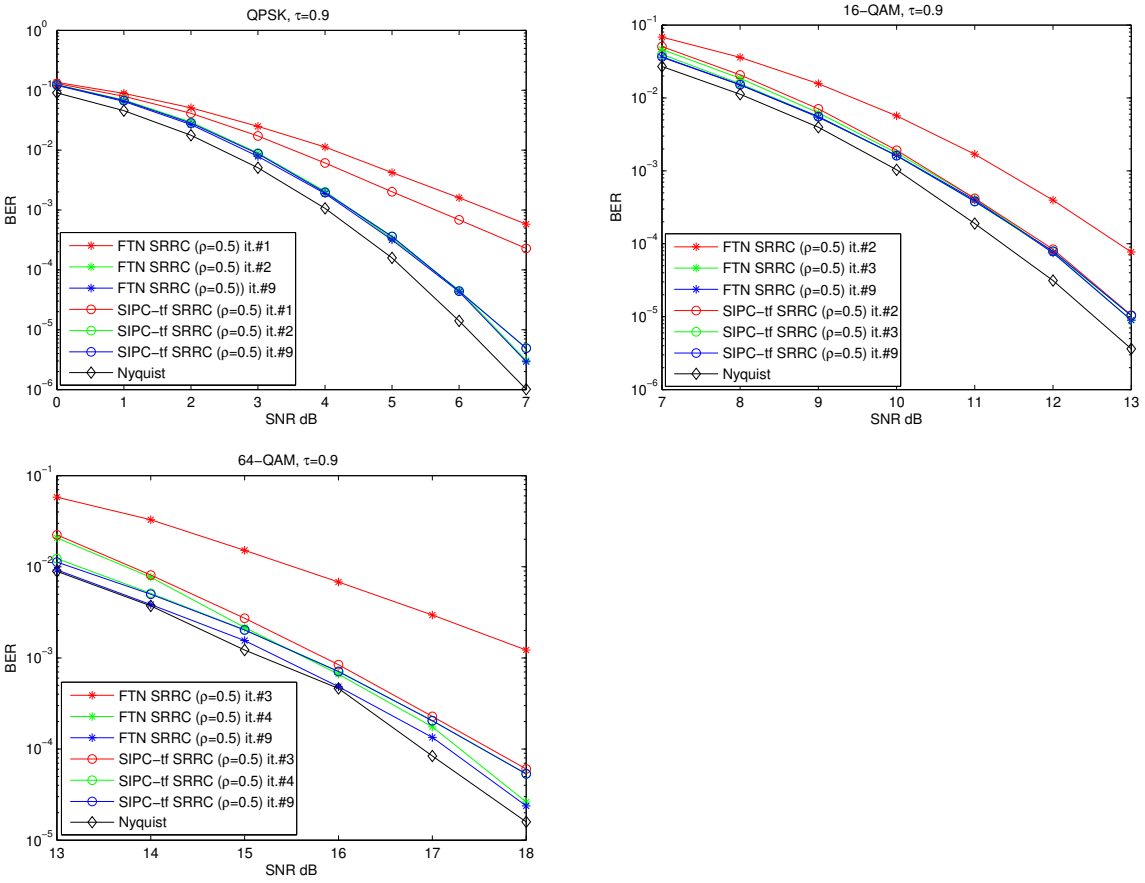

FIGURE 4.7: Comparison of the BER performance between the precoded and non-precoded FTN-OQAM transceiver using SRRC (ρ=0.5) filtering, $\tau = 0.9$ and different modulation orders.

can observe that the precoded FTN-OQAM transceiver needs to perform only 2 iterations at the receiver side instead of 3 in case of the non-precoded transceiver. Similarly, for 64-QAM modulation, the proposed precoding enables the receiver to converge after performing only 3 iterations instead of 4. Table 4.2 summarizes the recommended pulse shapes and the number of necessary iterations for each modulation order.

Modulation order	Recommended pulse	# of iterations
QPSK	SRRC ($\rho = 0.5, 0.3$), PHYDYAS and FS	2
16-QAM	SRRC ($\rho = 0.5, 0.3$), PHYDYAS and FS	2
64-QAM	SRRC (ρ=0.5), PHYDYAS, FS	3

TABLE 4.2: Recommended pulse shapes and number of necessary iterations for each modulation order in case of SIPC-tf precoding and τ=0.9.

4.2.5 A word about complexity

In this paragraph, we evaluate the Tx/Rx complexity increase due to SIPC-tf precoding. To this end, we compute the number of additions and multiplications performed only by the different blocks related to SIPC-tf for one iteration. On-line computations are

the operations performed at each iteration, while Off-line computations are independent of the iterations number, see (4.23)-(4.26). Note that the number of additions and multiplications are computed for real symbols.

$$\begin{aligned} N_{Off-line\ \times} &= 2Lh_f(1+L_h(6+4L))+2L_h(1+\frac{B}{M})(1+L_q)+k \\ &\quad +\frac{B}{M}(5+9\frac{B}{M}+\frac{M}{4}(k+2k'L_h)) \end{aligned} \tag{4.23}$$

$$N_{Off-line\ +} = 2Lh_f(1+L(1+L_h))+19\frac{B^2}{M^2}+2L_fL_q(1+\frac{B}{M})+\frac{B(k+2k'L_h)}{4} \tag{4.24}$$

$$N_{On-line\ \times} = L_f(1+\frac{B}{M})(3L_f+3+L_q)+3\frac{B}{4}(1+h_t) \tag{4.25}$$

$$N_{On-line\ +} = L_f(1+\frac{B}{M})(2L_f+2+L_q)+3\frac{B}{4}h_t \tag{4.26}$$

where M=64 is the number of subcarriers, $L=4M$ the pulse length, L_f=30 the length of the MMSE equalizer, $[-h_t,h_t]$ the interval of symbols considered for ISI while $[-h_f,h_f]$ is the interval of subcarriers considered for ICI, with h_t=h_f=4. $L_h=2h_t+1$ and $L_q=L_f+L_h-1$. $B=\frac{2N_i}{r\log_2(Q)}$ is the number of symbols with N_i=71424 the number of information bits, r the coding rate and Q the modulation order. $k=2$ and $k'=1$ are the precoding parameters. Results for different modulation orders are given in Table 4.3. We observe that complexity increase is essentially caused by off-line operations which are related to the precoding operation at the transmitter side and to the computation of the equivalent channel of interferences for the precoded and non-precoded symbols. Moreover, the on-line computations number decreases with the modulation order. This is due to the fact that for a fixed number of information bits N_i, the number of the transmitted symbols decreases. Meaning that less operations are performed by the equalizer and *SIC* blocks. For 64-QAM modulation, the overall complexity of the precoding (the total number of additions and multiplications) represents only 1.13% of the overall complexity of the turbo receiver (using time-domain equalization) represented in Table 3.7.

Modulation order	Off-line computations		On-line computations	
	# of $\times$	# of $+$	# of $\times$	# of $+$
QPSK	6.6×10^7	1.1×10^8	9.3×10^6	7.1×10^6
16-QAM	3.1×10^7	3.2×10^7	4.7×10^6	$3.6\times.10^6$
64-QAM	2.5×10^7	1.8×10^7	3.1×10^6	2.4×10^6

TABLE 4.3: Number of performed additions and multiplications by SIPC-tf precoder.

4.3 Precoded FTN-OQAM transceiver: ISI cancellation

4.3.1 SIPC along time axis

The second proposed precoder is SIPC along time axis (SIPC-t). The idea behind is to remove ISI from a sub-group of the transmitted symbols. To this end, these symbols are precoded by canceling ISI caused by their neighbors while the latter remain unmodified OQAM symbols. In this scenario, the factor $\beta = 0$ and the precoded symbols are expressed as:

$$c_{m,n} = a_{m,n} - \alpha\{\sum_{\substack{q=-k \\ q\neq 0}}^{k} h_q a_{m,n+q}\}, \tag{4.27}$$

where k defines the interval of symbols considered for ISI pre-cancellation. As the precoding solution is sparse, only symbols at a set of positions (m, n) are modified. In a time-frequency lattice, m and n are the subcarrier and time indices, respectively. At each subcarrier m, the precoded symbols are situated at time indices n such that :

$$\{n = a \bmod(k+2) \quad \text{and } n = a+1 \bmod(k+2),\ a \in \mathbb{N},\ a \leq k+1\}. \tag{4.28}$$

We illustrate a precoding pattern example in Fig. 4.8, where the green and red triangles represent the precoded and the non-precoded symbols, respectively. In this example, we consider that ISI is mainly caused by the nearest two symbols and set $k = 2$. Furthermore, equation (3.46) shows that:

$$h_q = 0, \qquad q \text{ odd} \tag{4.29}$$

Considering a symbol at time index n and at subcarrier m, its neighbors at odd time indices do not contribute to ISI. Therefore, we propose to alternate between two precoded and non-precoded symbols:

$$\text{green triangles} = \{(m,n), (m \text{ even}, n = 3 \text{ and } 0 \bmod(4))\} \tag{4.30}$$

$$\text{red triangles} = \{(m,n), (m \text{ odd}, n = 1 \text{ and } 2 \bmod(4))\} \tag{4.31}$$

The matrix formulation of the precoded symbols is:

$$\mathbf{C}_m = \mathbf{W}\mathbf{A}_m, \tag{4.32}$$

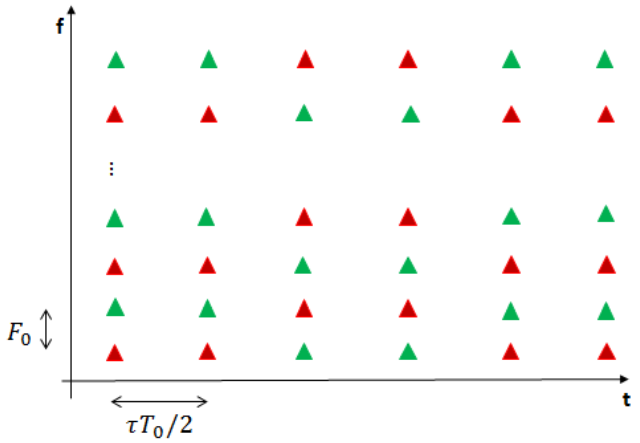

FIGURE 4.8: Time-frequency lattice of FTN-OQAM with SIPC-t precoding. The green and red triangles represent precoded and OQAM symbols, respectively.

where, $\mathbf{C}_m = [c_{m,1}, c_{m,2}, ..., c_{m,N_s}]^T$ and $\mathbf{A}_m = [a_{m,1}, a_{m,2}, ..., a_{m,N_s}]^T$. In this configuration, the precoding matrix $\mathbf{W}$ is expressed as:

$$\underset{m\ even}{\mathbf{W}} = \begin{pmatrix} 1 & 0 & & & & ... & & & 0 \\ 0 & 1 & 0 & & & ... & & & 0 \\ -\alpha h_{-2} & 0 & \frac{1}{h_0} & 0 & -\alpha h_2 & 0 & 0 & ... & 0 \\ 0 & -\alpha h_{-2} & 0 & \frac{1}{h_0} & 0 & -\alpha h_2 & 0 & ... & 0 \\ \vdots & & & \ddots & \ddots & \ddots & & & \vdots \\ 0 & & & & 0 & 1 & 0 & 0 & 0 \\ 0 & & & & & 0 & 1 & 0 & 0 \\ 0 & & ... & & 0 & -\alpha h_{-2} & 0 & \frac{1}{h_0} & 0 \\ 0 & & & & & 0 & -\alpha h_{-2} & 0 & \frac{1}{h_0} \end{pmatrix} \tag{4.33}$$

for even subcarrier indices, and:

$$\underset{m\ odd}{\mathbf{W}} = \begin{pmatrix} \frac{1}{h_0} & 0 & -\alpha h_2 & 0 & 0 & & & ... & 0 \\ 0 & \frac{1}{h_0} & 0 & -\alpha h_2 & 0 & & & ... & 0 \\ 0 & 0 & 1 & 0 & & ... & & & 0 \\ 0 & 0 & 0 & 1 & 0 & ... & & & 0 \\ \vdots & & & \ddots & \ddots & \ddots & & & \vdots \\ 0 & ... & 0 & -\alpha h_{-2} & 0 & \frac{1}{h_0} & 0 & 0 & 0 \\ 0 & & & 0 & -\alpha h_{-2} & 0 & \frac{1}{h_0} & 0 & 0 \\ 0 & & & ... & & & 0 & 1 & 0 \\ 0 & & & ... & & & & 0 & 1 \end{pmatrix} \tag{4.34}$$

for odd subcarrier indices.

We keep the same precoded FTN-OQAM transceiver presented in Fig. 4.1: information bits are encoded first. Then, the coded bits mapped to the precoded and non-precoded

symbols are interleaved separately. Finally, the *SIPC* module removes ISI from the selected sub-group of the transmitted symbols.

4.3.2 The receiver structure

At the receiver side, we propose a two-stage processing as depicted in Fig. 4.9. The first stage of the receiver decodes the precoded symbols while the non-precoded ones are detected at the second stage. The equivalent channel of FTN-self interference is independent of the subcarrier index. Without any restriction, we consider the received signal at even subcarrier indices m:

$$\mathbf{Y}_m = \mathbf{H}\mathbf{C}_m + \sum_{\substack{p=-l' \\ p\neq 0}}^{l'} \mathbf{L}_p \mathbf{C}_{m+p}, \tag{4.35}$$

where $\mathbf{Y}_m = [y_{m,1}, y_{m,2}..., y_{m,N_s}]^T$. By replacing $\mathbf{C}_m$ by its expression, we get:

$$\mathbf{Y}_m = \underset{m\ even}{\mathbf{H}}\ \underset{even}{\mathbf{W}}\ \mathbf{A}_m + \sum_{\substack{p=-l', p\ even \\ p\neq 0}}^{l'} \mathbf{L}_p \underset{m\ even}{\mathbf{W}}\ \mathbf{A}_{m+p} + \sum_{\substack{p=-l' \\ p\ odd}}^{l'} \mathbf{L}_p \underset{m\ odd}{\mathbf{W}}\ \mathbf{A}_{m+p}. \tag{4.36}$$

The first term of (4.36) represents the useful signal and ISI, while the remaining terms count for ICI.

First, we determine the coefficients of filters $\mathbf{p}_1$ and $\mathbf{q}_1$ based on the turbo equalization principle. The *SIC 1* block removes ICI caused by side subcarriers from the precoded symbols. The resulting signal is then equalized and fed to the *Decoder*. At the second stage, the coefficients of filters $\mathbf{p}_2$ and $\mathbf{q}_2$ are first deduced. The *SIC 2* block removes ICI from the non-precoded symbols as well as ISI caused by the precoded symbols. The resulting signal is then equalized and fed to the *Decoder*.

4.3.3 BCJR decoder modification

We consider the precoding pattern example given in Fig. 4.8 with $k = 2$. The first $\frac{N_c}{2}$ coded bits are decoded at the first stage, while the last $\frac{N_c}{2}$ bits are decoded at the second stage. The decoding sticks to the aforementioned BCJR algorithm with Max-Log-MAP approximation. The forward and backward metrics $\alpha_0(v)$ and $\beta_{N_c-1}(v')$ are initialized to 0. Furthermore, the metrics $\alpha_{\frac{N_c}{2}}(v)$ and $\beta_{\frac{N_c}{2}-1}(v')$ are not set to 0. Instead, they are calculated by the decoder at the first and the second step, respectively. These metrics are then exchanged between the decoders of the different processing stages.

4.3.4 Simulation results

In this section, we evaluate the performance of SIPC-t precoding method in terms of EXIT chart analysis and BER vs. SNR considering the effective minimum lossless packing factor found in the previous chapter, i.e., $\tau = 0.9$. We keep the same simulation

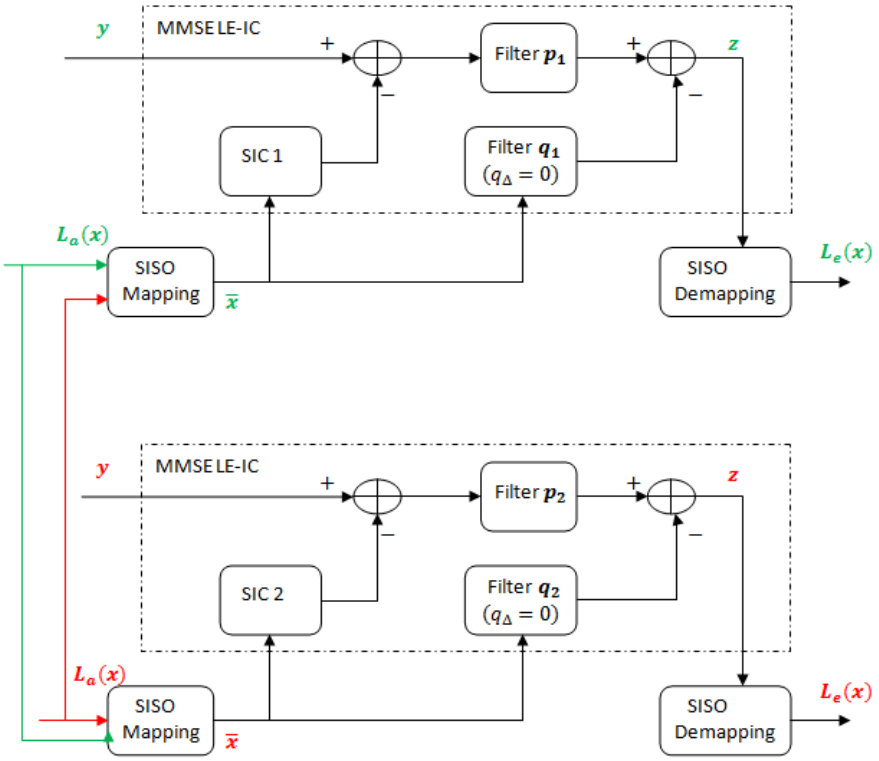

FIGURE 4.9: Structure of the SISO MMSE IC-LE used for FTN-OQAM with SIPC-t precoding.

parameters as in the previous section and consider that $k = 2$.

Fig. 4.10 shows the EXIT chart analysis of the precoded FTN-OQAM transceiver for different pulse shapes and modulation orders: QPSK, 16-QAM and 64-QAM. We can notice that the EXIT curve depends on the used pulse shape. Considering QPSK and 16-QAM modulation, SRRC (ρ=0.5) and SRRC (ρ=0.3) filters have the widest tunnel between the decoder and the equalizer. In case of 64-QAM modulation, the tunnel is closed when TFL and EGF (λ=2) filters are used, while it is quite wide when SRRC (ρ=0.5), SRRC (ρ=0.3), FS and PHYDYAS filters are considered.

Fig. 4.11 shows the BER curves using different pulse shapes. The BER results are consistent with the EXIT chart analysis. Indeed, for QPSK modulation, the receiver converges to similar BER results using all the considered pulses after performing 2 iterations. However, at the first iteration, better BER results are achieved using the SRRC (ρ=0.5) and SRRC (ρ=0.3) filters. When 16-QAM modulation is considered, our results show that all the filters lead to similar BER performance. However, better results are achieved using the SRRC (ρ=0.5 and 0.3) filter which enables the receiver to converge after performing 3 iterations. For the remaining pulse shapes, the number of necessary iterations is 3 in case of PHYDYAS and FS filtering, 4 in case of IOTA and 5 for the TFL and EGF (λ=2) filters. Considering 64-QAM modulation, simulation results show that the best BER performance is achieved using the SRRC (ρ=0.5), FS, PHYDYAS and IOTA filters. However, the number of necessary iterations is 4 when the SRRC (ρ=0.5),

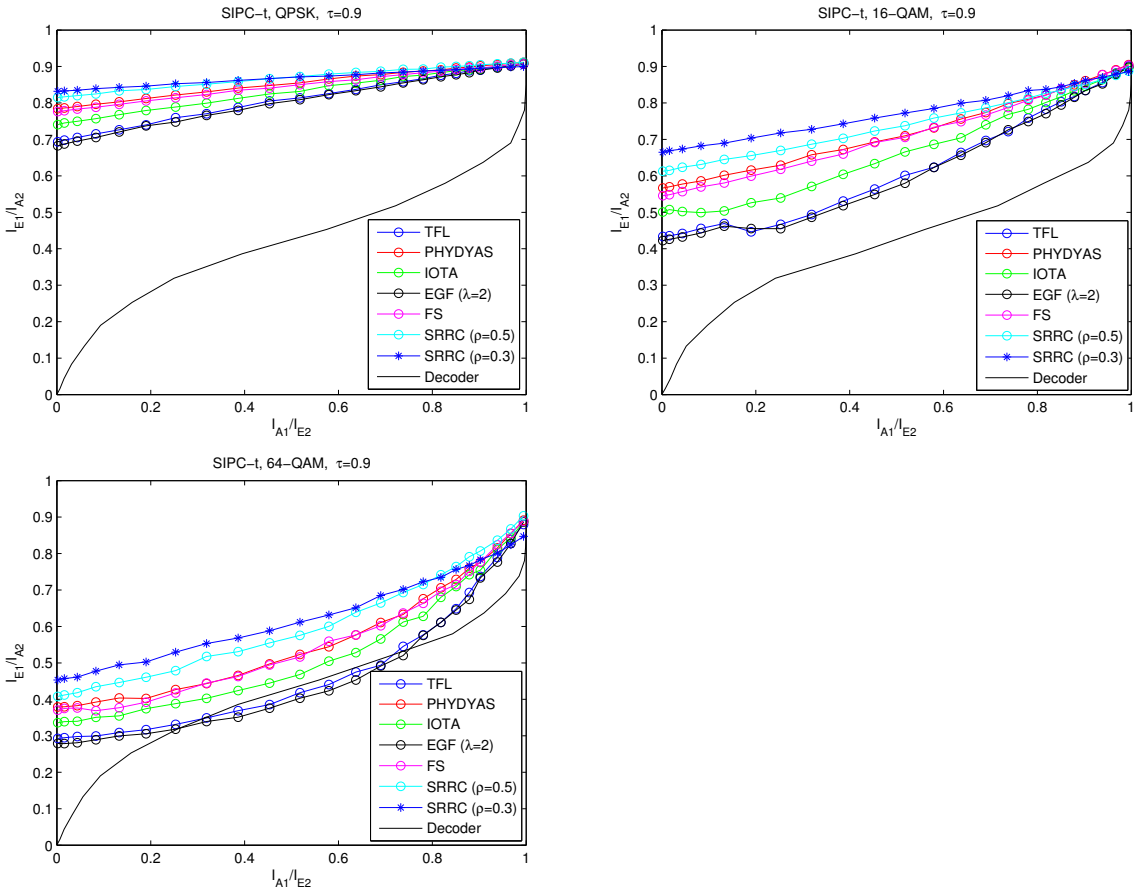

FIGURE 4.10: EXIT chart analysis of the proposed FTN-OQAM transceiver combined with SIPC-t precoding for QPSK, 16-QAM, 64-QAM and $\tau = 0.9$.

FS and PHYDYAS filters are employed instead of 6 iterations in case of the IOTA filter. Moreover, when using the TFL and EGF (λ=2) filters, the receiver does not converge. The number of necessary iterations for each pulse shape is given in Table 4.4.

Pulse shape	QPSK	16-QAM	64-QAM
TFL	2	5	-
EGF (λ=2)	2	5	-
IOTA	2	4	6
FS	2	3	4
PHYDYAS	2	3	4
SRRC (ρ=0.5)	2	3	4
SRRC (ρ=0.3)	2	3	4

TABLE 4.4: Number of necessary iterations for each pulse shape in case of SIPC-t precoding and $\tau = 0.9$.

In what follows, we compare the performance of the precoded and non-precoded FTN-OQAM transceiver using SRRC (ρ=0.5 and 0.3) filtering. The EXIT chart analysis is given in Fig. 4.12, where the decoder is represented by the black curve. The equalizer of the precoded and non-precoded transceiver is represented by the blue and green curves,

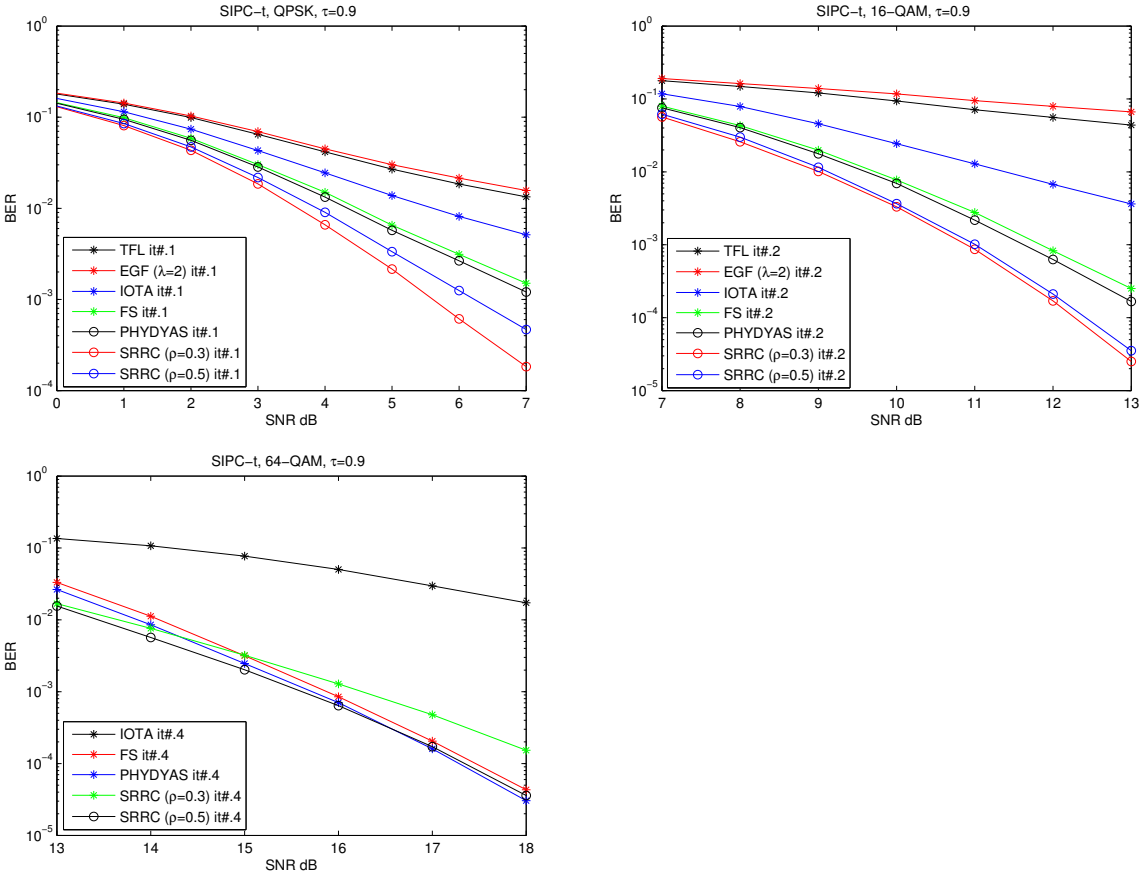

FIGURE 4.11: BER vs. SNR performance of the proposed FTN-OQAM transceiver combined with SIPC-t precoding for QPSK, 16-QAM, 64-QAM and $\tau = 0.9$.

respectively. In case of QPSK modulation, we notice that SIPC-t precoding provides a higher mutual information value at the equalizer output at the beginning of the iterative process. For 16-QAM and 64-QAM, the tunnel between the decoder and the equalizer of both transceivers is almost identical. The BER results given in Fig. 4.13 are consistent with the EXIT chart analysis. Indeed, the receiver of both systems needs to perform 2 iterations in case of QPSK modulation. However, the first iteration is improved by the SIPC-t precoding. This behavior can be interpreted by the fact that the iterative process starts with a higher mutual information value at the decoder input. For 16-QAM modulation, we can observe that 3 iterations are necessary for both transceivers. The BER curve at the second iteration is improved by SIPC-t precoding. Similarly, for 64-QAM modulation, both transceivers need to perform 4 iterations at the receiver side. At the third iteration, the precoded FTN-OQAM transceiver performs better than the non-precoded one. Table 4.5 summarizes the recommended pulse shapes and the number of necessary iterations for each modulation order.

4.3.5 A word about complexity

In this section, we evaluate the complexity increase due to SIPC-t precoding. To this end, we calculate the number of additions and multiplications (for real symbols) performed only by the different blocks of the SIPC-t precoder during one iteration. Equations

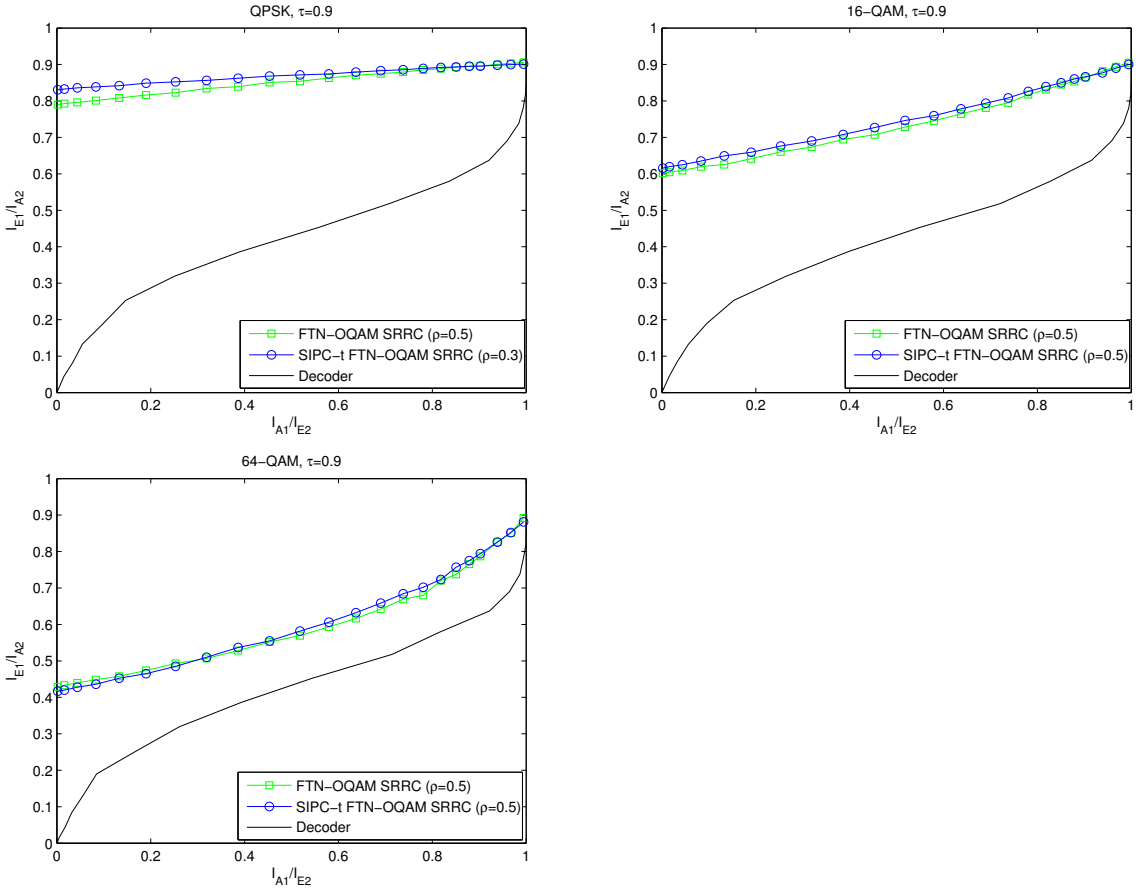

FIGURE 4.12: Comparison of the EXIT chart analysis between the precoded and non-precoded FTN-OQAM transceiver using SRRC (ρ=0.5, 0.3) filtering, $\tau = 0.9$ and different modulation orders.

Modulation order	Recommended pulses	# of iterations
QPSK	SRRC ($\rho = 0.5, 0.3$)	2
16-QAM	SRRC ($\rho = 0.5, 0.3$), PHYDYAS, FS	3
64-QAM	SRRC (ρ=0.5), PHYDYAS, FS	4

TABLE 4.5: Recommended pulse shapes and number of necessary iterations for each modulation order in case of SIPC-t precoding.

(4.37)-(4.40) detail the number of on-line and off-line operations. For the same parameters as for the SIPC-tf precoding, the corresponding numerical values are given in Table 4.6 for each modulation order. We observe that the precoding complexity is due essentially to off-line operations and that it decreases with the modulation order. Referring to Table 3.7, the SIPC-t precoding increases the overall transceiver complexity (i.e., the total number of additions and multiplications) only by 0.08%, due to on-line computations, in case of 64-QAM modulation.

$$N_{Off-line\ \times} = k(1 + \frac{B}{2}) + \frac{B^2}{M^2} + 2L_h(L_q + 1) \tag{4.37}$$

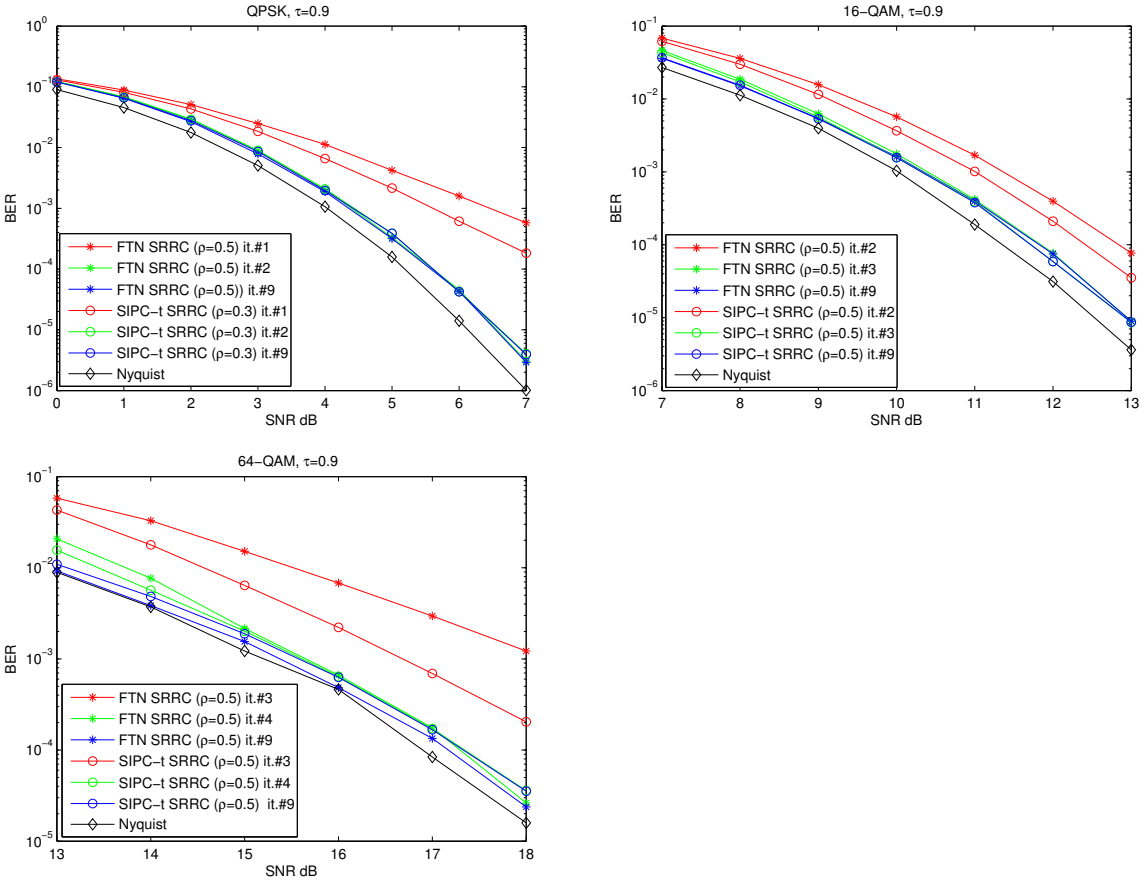

FIGURE 4.13: Comparison of the BER performance between the precoded and non-precoded FTN-OQAM transceiver using SRRC (ρ=0.5, 0.3) filtering, $\tau = 0.9$ and different modulation orders.

$$N_{Off-line\ +} = 2L_qL_h + \frac{B^2}{M^2} + \frac{Bk}{2} \tag{4.38}$$

$$N_{On-line\ \times} = B(k + \frac{h_t + 1}{2}) + L_f(3 + 3L_f + L_q) \tag{4.39}$$

$$N_{On-line\ +} = B(k + \frac{h_t}{2}) + L_f(2 + 2L_f + L_q) \tag{4.40}$$

Modulation order	Off-line computations		On-line computations	
	# of $\times$	# of $+$	# of $\times$	# of $+$
QPSK	5.1×10^6	5.1×10^6	6.5×10^5	$5.7 \times .10^5$
16-QAM	1.3×10^6	1.3×10^6	3.3×10^5	2.9×10^5
64-QAM	6.0×10^5	6.0×10^5	2.2×10^5	1.9×10^5

TABLE 4.6: Number of performed additions and multiplications by SIPC-t precoder.

4.4 Precoded FTN-OQAM transceiver: ICI cancellation

4.4.1 SIPC along frequency axis

The third proposed precoder, aiming at ICI pre-cancellation, is SIPC along frequency axis (SIPC-f). In this scenario, $\alpha = 0$ and a sub-group of the transmitted symbols are precoded:

$$c_{m,n} = a_{m,n} - \beta\{ \sum_{\substack{p=-k' \\ p\neq 0}}^{k'} \sum_{q=-l}^{l} l_{p,q,n} a_{m+p,n+q}\} \tag{4.41}$$

where k' defines the interval of symbols considered for ICI cancellation. Since the proposed precoding method is sparse, only symbols at subcarrier indices m such that:

$$\{m = b \bmod(k'+1),\ b \in \mathbb{N},\ b \leq k'\} \tag{4.42}$$

are precoded, while the remaining subcarriers contain unchanged OQAM symbols. A matrix formulation of the precoded symbols is expressed as:

$$\mathbf{C}_m = \mathbf{A}_m - \beta \sum_{\substack{p=-k' \\ p\neq 0}}^{k'} \mathbf{L}_p \mathbf{A}_{m+p}, \tag{4.43}$$

where, $\mathbf{C}_m = [c_{m,1}, c_{m,2}, ..., c_{m,N_s}]^T$ and $\mathbf{A}_m = [a_{m,1}, a_{m,2}, ..., a_{m,N_s}]^T$. A precoding pattern example is illustrated in Fig. 4.14, where the green and red triangles represent precoded and non-precoded subcarriers, respectively. In this configuration, we considered that ICI is mainly caused by the nearest subcarriers, i.e., we set $k' = 1$.

As in the previous section, the precoded transceiver is reported in Fig. 4.1. After channel coding, coded bits mapped to the precoded and non-precoded symbols are interleaved separately. This enables the receiver to decode separately the different groups of symbols.

4.4.2 The receiver structure

The proposed receiver employs a two-stage processing to decode separately the different groups of symbols. Considering that symbols at even subcarrier indices are precoded, the received signal is:

$$\mathbf{Y}_m = \mathbf{H}\mathbf{C}_m + \sum_{\substack{p=-l' \\ p\neq 0}}^{l'} \mathbf{L}_p \mathbf{C}_{m+p}. \tag{4.44}$$

By setting $k' = 1$, we get:

$$\mathbf{Y}_m = \mathbf{H}[\mathbf{A}_m - \beta \sum_{\substack{p=-1 \\ p\neq 0}}^{1} \mathbf{L}_p \mathbf{A}_{m+p}] + \sum_{\substack{p=-l', p\ even \\ p\neq 0}}^{l'} \mathbf{L}_p \mathbf{C}_{m+p} + \sum_{\substack{p=-l' \\ p\ odd}}^{l'} \mathbf{L}_p \mathbf{A}_{m+p}. \tag{4.45}$$

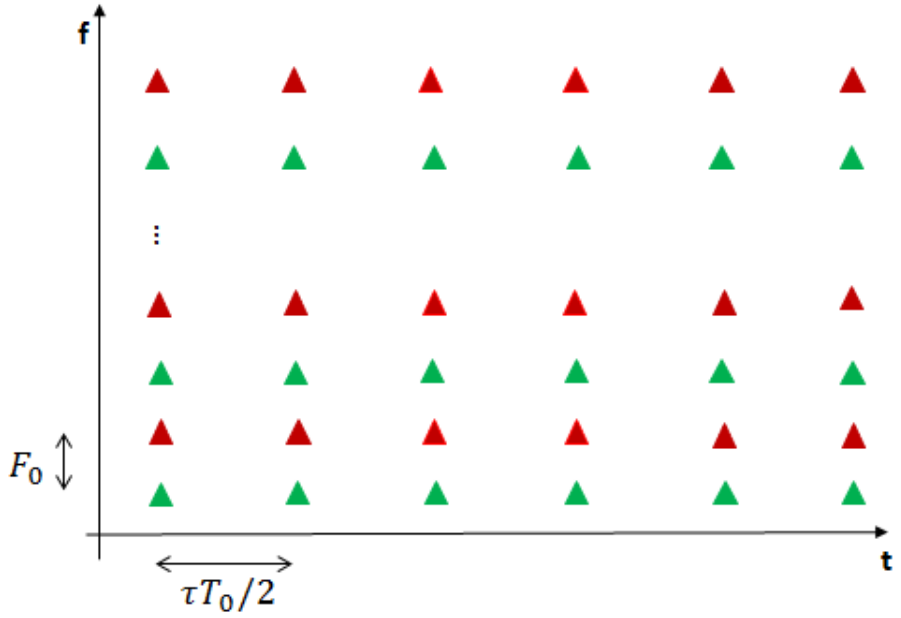

FIGURE 4.14: Time-frequency lattice of FTN-OQAM with SIPC-f precoding. Green and red triangles contain precoded and OQAM symbols, respectively.

The receiver structure is similar to the one presented in Fig. 4.9. The coefficients of filters $\mathbf{p}_1$ and $\mathbf{q}_1$ are computed according to the turbo equalization principle. The equivalent channel characteristics are deduced from (4.45). Using the soft estimated symbols delivered by the *SISO Mapping* module, the *SIC 1* block removes ICI from the received signal. The resulting signal is then equalized and fed to the *Decoder*.

At the second stage, the non-precoded symbols are processed. Firstly, the characteristics of the equivalent channel are deduced from the expression of the received non-precoded signal at odd subcarrier indices:

$$\mathbf{Y}_m = \mathbf{H}\mathbf{A}_m + \sum_{\substack{p=-l' \\ p \ odd}}^{l'} \mathbf{L}_p \mathbf{C}_{m+p} + \sum_{\substack{p=-l', p \ even \\ p\neq 0}}^{l'} \mathbf{L}_p \mathbf{A}_{m+p}. \tag{4.46}$$

By replacing $\mathbf{C}_{m+p}$ by its expression, we get:

$$\begin{aligned} \mathbf{Y}_m \;=\; & (\mathbf{H} - \beta\mathbf{L}_1\mathbf{L}_{-1} - \beta\mathbf{L}_{-1}\mathbf{L}_1)\mathbf{A}_m + \sum_{\substack{p=-l' \\ p \ even}}^{l'} \mathbf{L}_p \mathbf{A}_{m+p} \\ & + \sum_{\substack{p \ odd, \ p=-l' \\ p\neq\pm 1}}^{l'} \mathbf{L}_p[\mathbf{W}\mathbf{A}_{m+p} - \beta\mathbf{L}_1\mathbf{A}_{m+p+1} - \beta\mathbf{L}_{-1}\mathbf{A}_{m+p-1}] \\ & + \mathbf{L}_1\mathbf{W}\mathbf{A}_{m+1} + \mathbf{L}_{-1}\mathbf{W}\mathbf{A}_{m-1} - \beta\mathbf{L}_1^2\mathbf{A}_{m+2} - \beta\mathbf{L}_{-1}^2\mathbf{A}_{m-2} \end{aligned} \tag{4.47}$$

As for the SIPC-tf precoder, the equivalent channel depends on time instant n. Hence,

the coefficients of filters $\mathbf{p}_1$ and $\mathbf{q}_1$ should be computed for each time instant and the received signal is equalized in the frequency-domain. Based on the soft estimated symbols delivered by the *SISO Mapping*, the *SIC 2* module removes ICI introduced by the precoded and the non-precoded subcarriers as well. The resulting signal is then equalized and fed to the *Decoder*.

4.4.3 BCJR decoder modification

The BCJR decoder is modified as explained for the SIPC-t precoder. We consider that the length of coded bits is N_c and set $k' = 1$. Hence, the precoded and non-precoded symbols are both composed of $\frac{N_c}{2}$ bits. The first $\frac{N_c}{2}$ coded bits are decoded at the first stage, while the last $\frac{N_c}{2}$ bits are decoded at the second stage. As for SIPC-t precoding, the forward and backward metrics $\alpha_0(v)$ and $\beta_{N_c-1}(v')$ are initialized to 0. Furthermore, the metrics $\alpha_{\frac{N_c}{2}}(v)$ and $\beta_{\frac{N_c}{2}-1}(v')$ are not set to 0 but calculated by the decoder at step 1 and 2, respectively. These metrics are then exchanged between the decoders of the different processing stages.

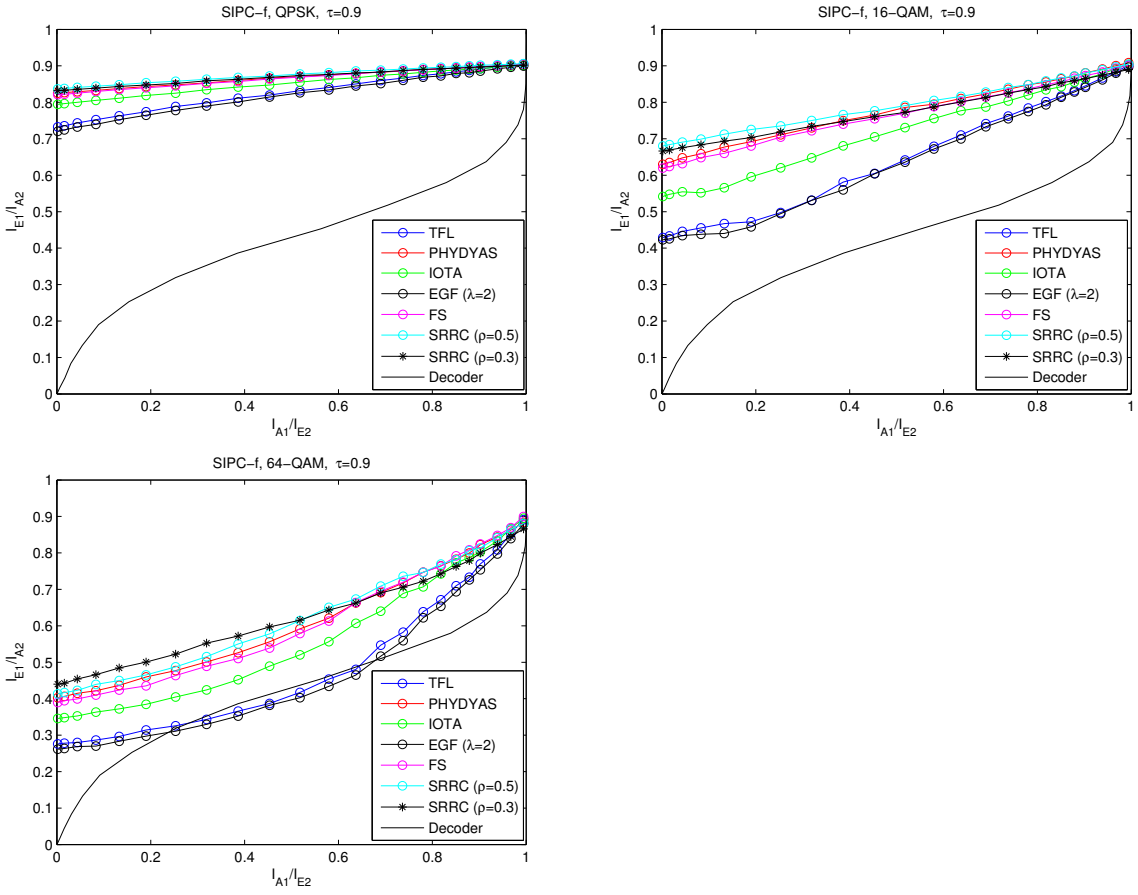

FIGURE 4.15: EXIT chart analysis of the proposed FTN-OQAM transceiver with SIPC-f precoding for QPSK, 16-QAM, 64-QAM and $\tau = 0.9$.

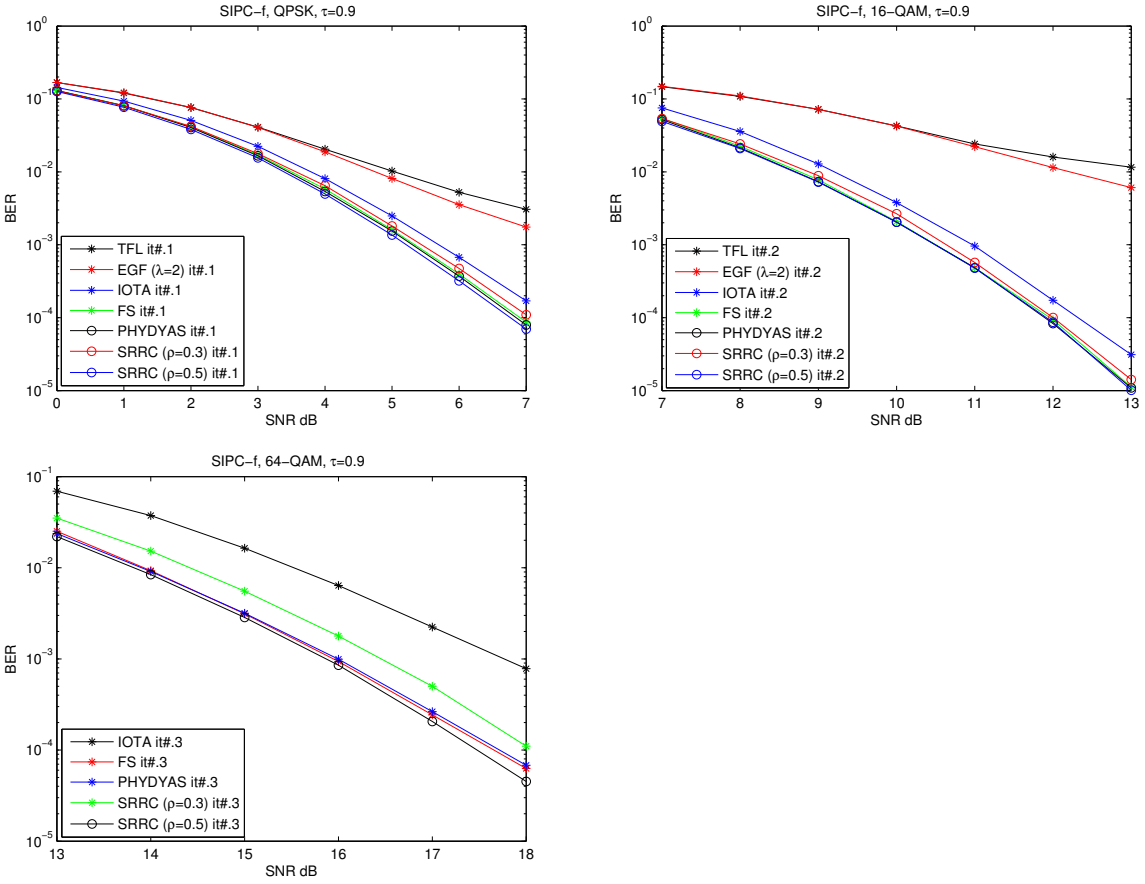

FIGURE 4.16: BER vs. SNR performance of the proposed FTN-OQAM transceiver with SIPC-f precoding for QPSK, 16-QAM, 64-QAM and $\tau = 0.9$.

4.4.4 Simulation results

In this section, we evaluate the performance of the FTN-OQAM transceiver combined with SIPC-f precoding in terms of EXIT chart analysis and BER vs. SNR. We keep the same simulation parameters as in the previous section and set $k' = 1$.

The EXIT chart analysis of the precoded FTN-OQAM transceiver is shown in Fig. 4.15. Results for QPSK and 16-QAM modulation show that, at the beginning of the iterative process, the mutual information value at the decoder input is higher when SRRC (ρ=0.5 and 0.3), FS and PHYDYAS filters are employed. Indeed, Fig. 4.16 shows that these pulse shapes perform better than the other pulses in terms of BER. In case of QPSK, the receiver converges after performing 2 iterations. When 16-QAM is considered, the receiver achieves better BER results using the SRRC (ρ=0.5 and 0.3), FS and PHYDYAS filters, and converges after performing 2 iterations. In case of the remaining pulse shapes, the receiver needs to perform 3 iterations to converge using the IOTA filter, and 4 iterations while using the TFL and EGF (λ=2) filters. In case of 64-QAM modulation, SRRC (ρ=0.5), FS and PHYDYAS filters have the most open tunnel between the decoder and the equalizer. Moreover, our simulation results show that they outperform the other pulse shapes in terms of BER performance and enable the receiver to converge after performing 3 iterations. The number of necessary iterations is 4 when

the IOTA and SRRC (ρ=0.3) filters are employed. When using the TFL and EGF (λ=2) filters, the receiver does not converge. Table 4.7 summarizes the number of necessary iterations for each pulse shape.

Pulse shape	QPSK	16-QAM	64-QAM
TFL	2	4	-
EGF (λ=2)	2	4	-
IOTA	2	3	4
FS	2	2	3
PHYDYAS	2	2	3
SRRC (ρ=0.5)	2	2	3
SRRC (ρ=0.3)	2	2	4

TABLE 4.7: Number of necessary iterations for each pulse shape in case of SIPC-f precoding and $\tau = 0.9$.

Next, we compare the performance of the precoded and non-precoded FTN-OQAM transceiver using the recommended pulse shapes. The EXIT chart analysis is given

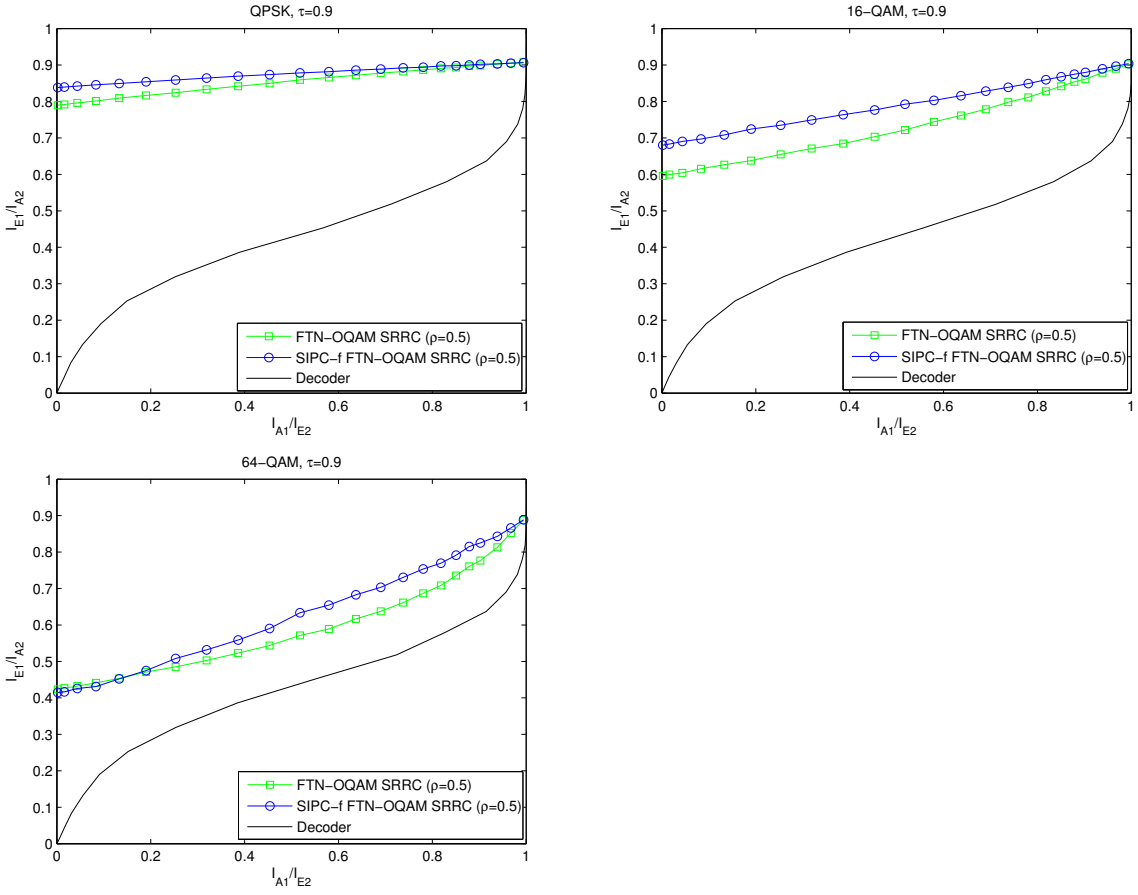

FIGURE 4.17: Comparison of the EXIT chart analysis between the precoded and non-precoded FTN-OQAM transceiver using SRRC (ρ=0.5) filtering, $\tau = 0.9$ and different modulation orders.

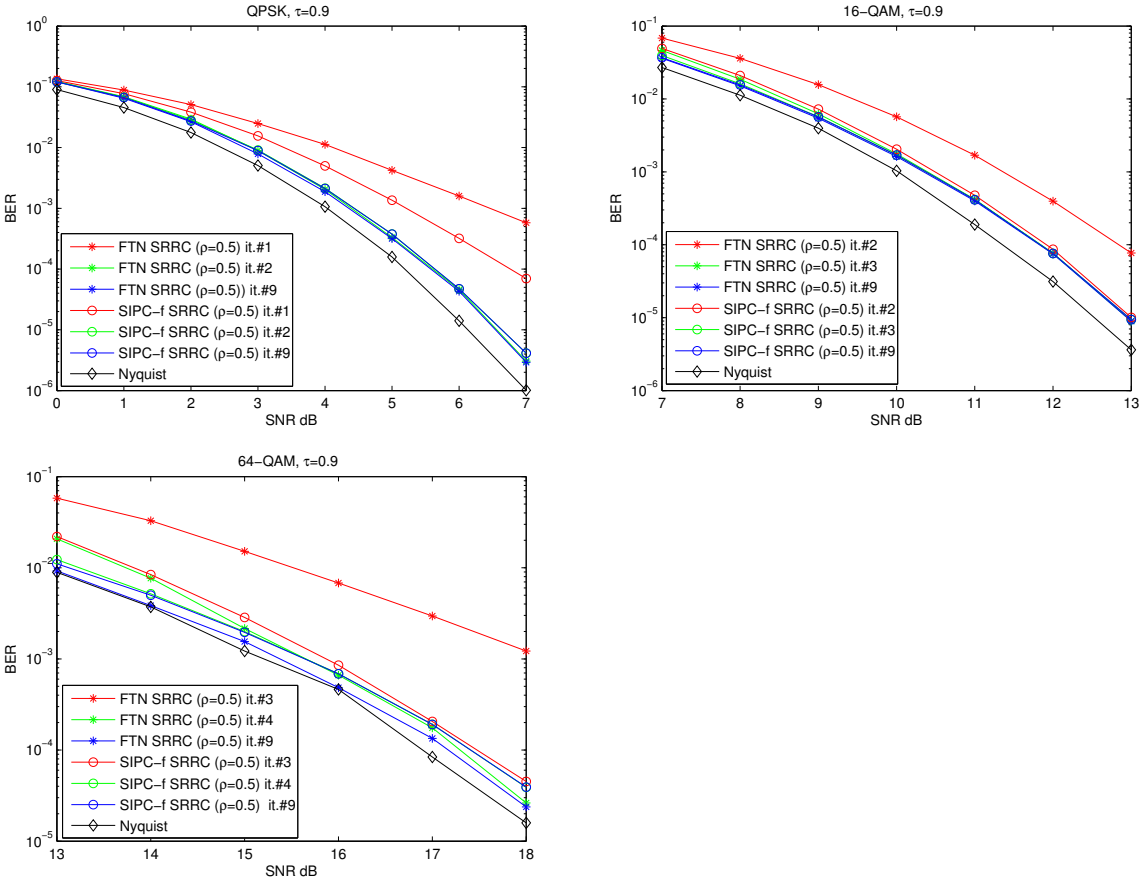

FIGURE 4.18: Comparison of the BER performance between the precoded and non-precoded FTN-OQAM transceiver using SRRC (ρ=0.5) filtering, $\tau = 0.9$ and different modulation orders.

in Fig. 4.17, where the black curve represents the decoder and the blue and green curves represent the equalizer of the precoded and non-precoded transceiver, respectively. In case of QPSK modulation, the blue curve is identical to the green one, although the initial mutual information is slightly higher with the precoder. In case of 16-QAM and 64-QAM, the tunnel between the decoder and the blue curve is wider meaning that less iterations are necessary for the precoded FTN-OQAM receiver. The BER results given in Fig. 4.18 are consistent with the EXIT chart analysis. Indeed, in case of QPSK modulation, the receiver of both systems needs to perform 2 iterations to converge. However, the first iteration is improved by the SIPC-f precoding. For 16-QAM, we can observe that the precoded FTN-OQAM receiver needs to perform only 2 iterations instead of 3 in case of the non-precoded transceiver. Similarly, using SIPC-f precoding allows the receiver to converge after performing only 3 iterations instead of 4 in case of 64-QAM modulation. Table 4.8 summarizes the recommended pulse shapes and the number of necessary iterations for the FTN-OQAM transceiver combined with SIPC-f precoding.

Modulation order	Recommended pulses	# of iterations
QPSK	SRRC ($\rho = 0.5, 0.3$), PHYDYAS and FS	2
16-QAM	SRRC ($\rho = 0.5, 0.3$), PHYDYAS and FS	2
64-QAM	SRRC (ρ=0.5), PHYDYAS, FS	3

TABLE 4.8: Recommended pulse shapes and number of necessary iterations for different modulation orders in case of SIPC-f precoding and for $\tau = 0.9$.

4.4.5 A word about complexity

In order to evaluate the additional complexity of SIPC-f precoding, we calculate the number of additions and multiplications (for real symbols) performed only by the related blocks during one iteration, see equations (4.48)-(4.51). For the same parameter values as in the previous section, the corresponding numerical values for different modulation orders are given in Table 4.9. As we can observe, complexity increase is mainly caused by off-line computations and decreases as a function of the modulation order. In case of 64-QAM, the overall receiver complexity (i.e., the total number of additions and multiplications) represented in Table 3.7 increases merely by 1.1% due to on-line computations.

$$N_{Off-line\ \times} = \frac{B}{M}(L_h(Mk' + 2) + 2L_fL_q + 5 + 8\frac{B}{M}) + 2Lh_f(1 + L_h(6 + 4L)) \quad (4.48)$$

$$N_{Off-line\ +} = 2Lh_f(1 + L(1 + L_h)) + \frac{B}{M}(16\frac{B}{M} + L_hMk' + 2L_fL_q) \quad (4.49)$$

$$N_{On-line\ \times} = \frac{B}{M}(\frac{M}{2}(h_t + 1) + L_f(3 + 3L_f + L_q)) \quad (4.50)$$

$$N_{On-line\ +} = \frac{B}{M}(\frac{M}{2}h_t + L_f(2 + 2L_f + L_q)) \quad (4.51)$$

Modulation order	Off-line computations		On-line computations	
	# of $\times$	# of +	# of $\times$	# of +
QPSK	6.5×10^7	9.1×10^7	$9.1 \times .10^6$	7.0×10^6
16-QAM	3.2×10^7	2.8×10^7	4.6×10^6	3.5×10^6
64-QAM	2.6×10^7	1.6×10^7	3.0×10^6	2.3×10^6

TABLE 4.9: Number of performed additions and multiplications by SIPC-f precoding.

4.5 Performance comparison between the proposed precoders

The objective of this section is to compare the BER performance of the three precoders. Based on our simulation results, we present the recommended pulse shapes for each precoder depending on the modulation order and on the packing factor. Then, we give the recommended precoder for each modulation order and τ value. Finally, we compare the

precoded and non-precoded FTN-OQAM transceiver to underline the advantages of the proposed precoding.

Based on the BER results of the precoded FTN-OQAM transceiver, we reported in Tables 4.10, 4.11 and 4.12 the recommended pulse shapes together with the number of necessary iterations for each precoder. Then, we compared the performance of the FTN-OQAM transceiver employing the different precoders and the recommended pulses. The results are illustrated in Figs. 4.19, 4.20, 4.21. Note that in case of QPSK modulation, the three precoders provide almost identical results. The recommended precoders for each modulation order and packing factor are summarized in Table 4.13. Finally, the performance of the FTN-OQAM transceiver employing these precoders is evaluated and compared to the non-precoded transceiver in Figs. 4.22, 4.23 and 4.24. For each modulation order and packing factor, simulations were conducted using one of the recommended pulses from Tables 3.5, 4.10, 4.11 and 4.12.

Modulation order	τ	Recommended pulse	# of iterations
QPSK	0.7	IOTA	3
	0.8	FS, SRRC (ρ=0.5, 0.3), PHYDYAS	2
16-QAM	0.7	FS, IOTA	6
	0.8	FS, PHYDYAS	3
64-QAM	0.8	PHYDYAS, FS	6

TABLE 4.10: Recommended pulse shapes and number of necessary iterations for different modulation orders in case of SIPC-tf precoding.

Modulation order	τ	Recommended pulse	# of iterations
QPSK	0.7	IOTA TFL, EGF (λ=2)	3
	0.8	FS, PHYDYAS	2
16-QAM	0.7	FS, PHYDYAS	7
	0.8	FS, PHYDYAS, IOTA	4
64-QAM	0.8	PHYDYAS, FS	8

TABLE 4.11: Recommended pulse shapes and number of necessary iterations for different modulation orders in case of SIPC-t precoding.

Modulation order	τ	Recommended pulse	# of iterations
QPSK	0.7	IOTA, TFL, FS, PHYDYAS	3
	0.8	PHYDYAS, SRRC (ρ=0.5, 0.3), IOTA	2
16-QAM	0.7	FS, PHYDYAS, IOTA, TFL	8
	0.8	FS, PHYDYAS	3
64-QAM	0.8	PHYDYAS, FS	7

TABLE 4.12: Recommended pulse shapes and number of necessary iterations for different modulation orders in case of SIPC-f precoding.

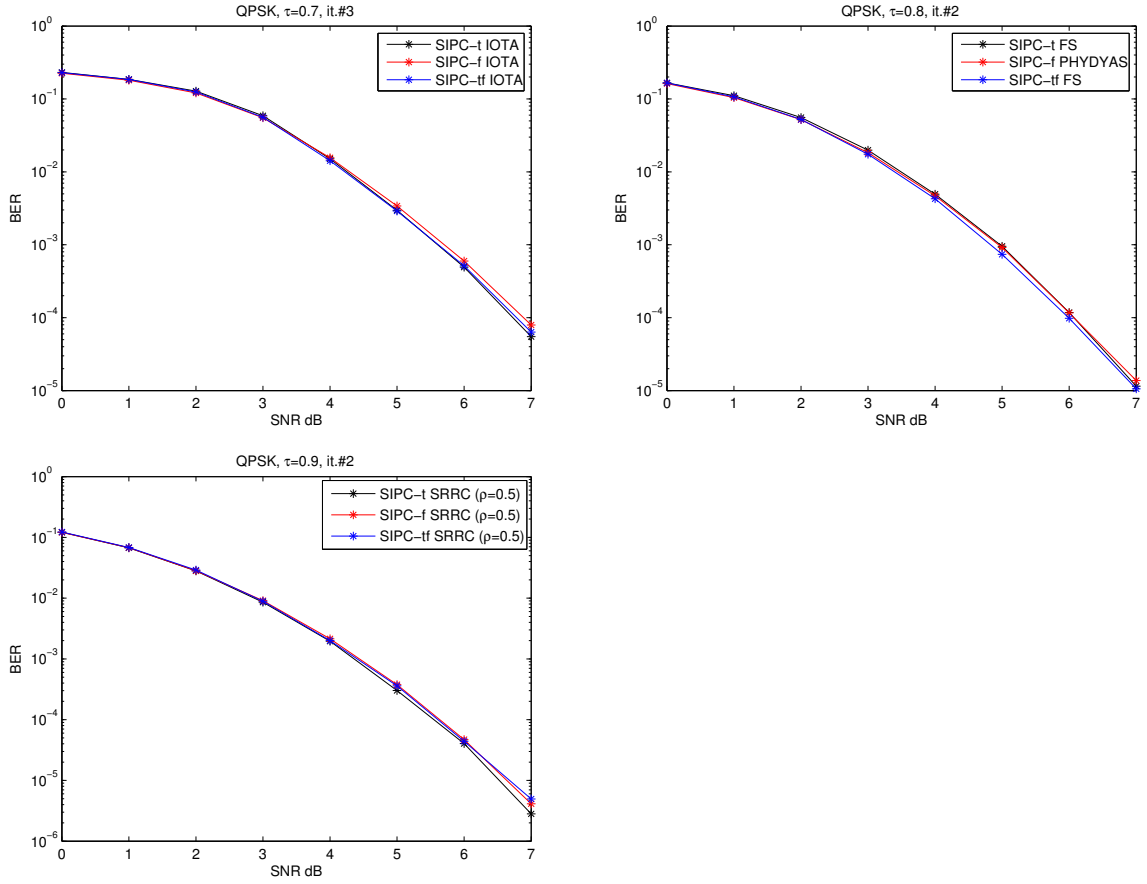

FIGURE 4.19: BER comparison of the three precoders using QPSK modulation.

Modulation order	Packing factor (τ)	Recommended precoders
QPSK	0.7	SIPC-f, SIPC-tf, SIPC-t
	0.8	SIPC-f, SIPC-tf, SIPC-t
	0.9	SIPC-f, SIPC-t, SIPC-tf
16-QAM	0.7	SIPC-tf, SIPC-t
	0.8	SIPC-tf
	0.9	SIPC-f, SIPC-tf
64-QAM	0.8	SIPC-tf, SIPC-t
	0.9	SIPC-tf, SIPC-t

TABLE 4.13: Recommended precoders for different modulation orders and packing factors.

Fig. 4.22 shows the BER results for QPSK modulation. In case of $\tau = 0.7$, the proposed precoding technique SIPC-f allows the FTN-OQAM transceiver to perform only 2 iterations instead of 3 at the receiver side. At a BER around 10^{-4}, the precoded FTN-OQAM transceiver has less than 2 dB loss compared to Nyquist-based systems. However, at this packing factor, a rate growth of 42% is achieved. For a packing factor $\tau = 0.8$, both systems converge after performing 2 iterations at the receiver side. However, the first iteration is improved by the SIPC-f precoding technique. A rate growth of 25% is achieved for a loss of 1 dB at a BER around 10^{-5}.

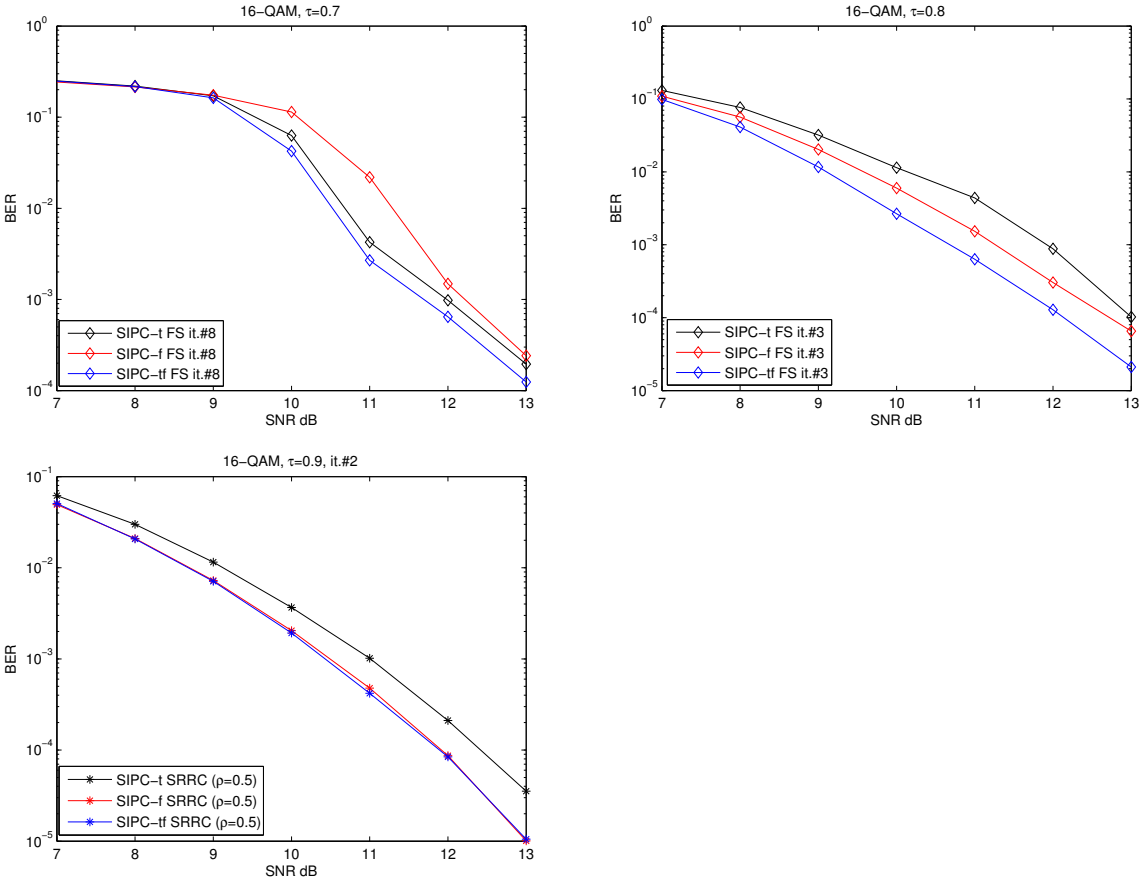

FIGURE 4.20: BER comparison of the three precoders using 16-QAM modulation.

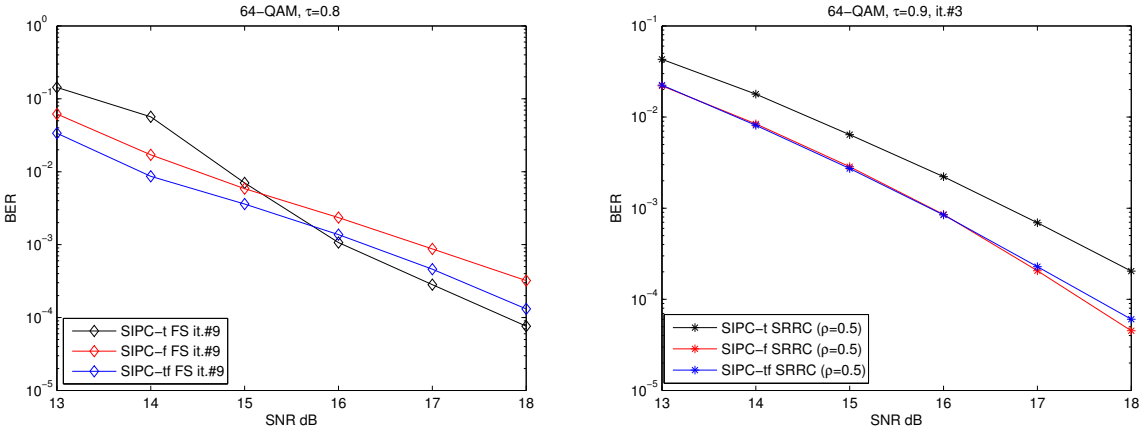

FIGURE 4.21: BER comparison of the three precoders using 64-QAM modulation.

Results for 16-QAM modulation are illustrated in Fig. 4.23. In case of $\tau = 0.7$, the SIPC-tf precoding enables the FTN-OQAM receiver to converge after having performed 6 iterations instead of 9. The FTN rate growth in this case is of 42% to the detriment of 2 dB loss at a BER around 10^{-4}. In case of a packing factor $\tau = 0.8$, the SIPC-tf precoding enables the receiver to perform only 3 iterations instead of 4. A rate gain of 25% is achieved for less than 1 dB loss at a BER around 10^{-5}.

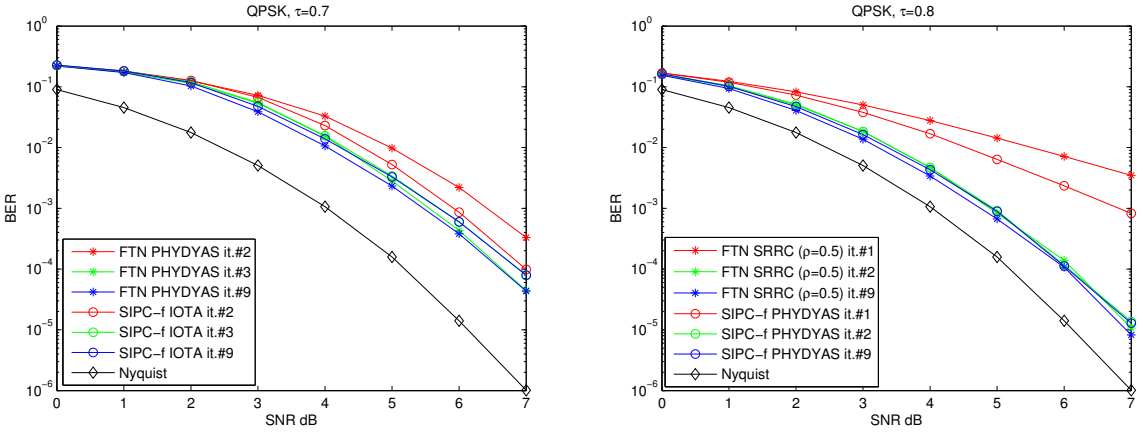

FIGURE 4.22: BER evaluation of the FTN-OQAM transceiver combined with SIPC-f precoding for QPSK modulation and FTN packing factors $\tau = 0.7$ and $\tau = 0.8$.

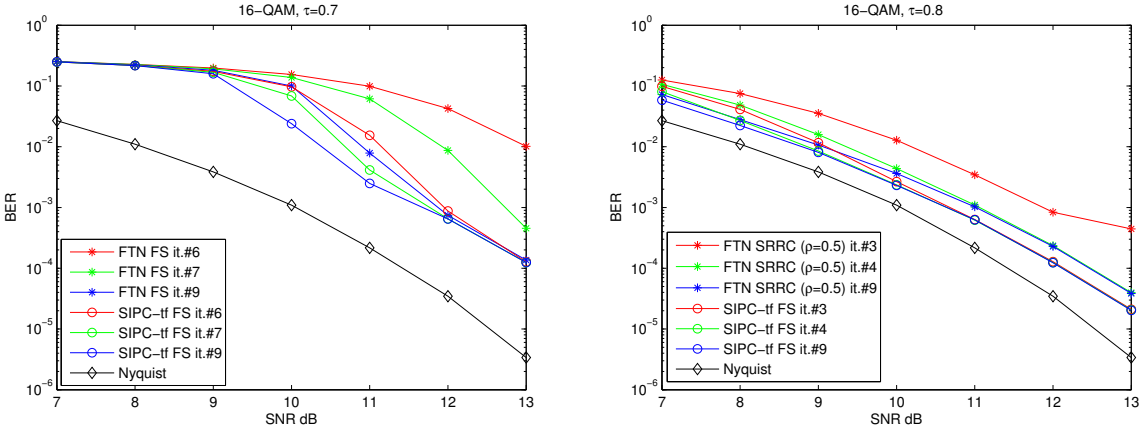

FIGURE 4.23: BER evaluation of the FTN-OQAM transceiver combined with SIPC-tf precoding for 16-QAM modulation and FTN packing factors $\tau = 0.7$ and $\tau = 0.8$.

Fig. 4.24 presents the BER performance of both systems in case of 64-QAM modulation and $\tau = 0.8$. The proposed SIPC-t precoding allows the receiver to converge after having performed 8 iterations instead of 9. As we can notice, the BER curves of the different iterations are improved by the precoding solution. In this scenario, a rate gain of 25% is achieved for a loss of 1 dB at a BER around 10^{-4}.

Additionally, the proposed precoding technique enhances the FTN-OQAM transceiver performance regardless of the employed pulse shape. We consider 16-QAM modulation and a packing factor $\tau = 0.9$ as an example. Results in terms of BER are given in Fig. 4.25 for various pulse shapes. As we stated earlier, our solution reduces the number of necessary iterations for the precoded FTN-OQAM receiver: when the recommended precoders and pulse shapes (PHYDYAS, FS, and SRRC (ρ=0.3 and 0.5) filters) are considered, the receiver needs to perform only 2 iterations instead of 3. Moreover, combining the FTN-OQAM transceiver with the proposed precoders allows to use other pulse shapes as well. In fact, the BER curves of the precoded FTN-OQAM transceiver using TFL, EGF (λ=2) and IOTA filters converge to the Nyquist-based systems performance,

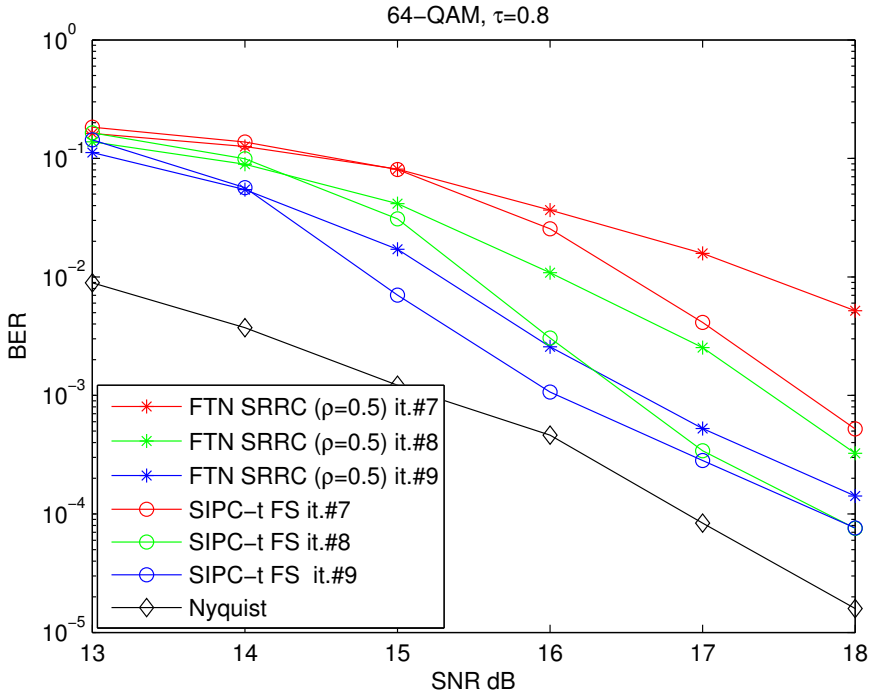

FIGURE 4.24: BER evaluation of the FTN-OQAM transceiver combined with SIPC-t precoding for 64-QAM modulation and FTN packing factor $\tau = 0.8$.

which is not the case without precoding. We observe similar behavior for the different modulation orders and packing factors.

4.6 Conclusion

In this chapter, we reviewed the FTN-OQAM transceiver discussed in the previous chapter to take advantage of the available information about FTN-induced interference at the transmitter. Since this interference is perfectly known by the transmitter, we proposed a new precoding technique named Sparse Interference Pre-Cancellation (SIPC) to reduce it. As it is difficult to jointly precode all the transmitted symbols, we suggested to remove interference from only a sub-group of the transmitted symbols. The remaining symbols are unmodified OQAM symbols. Depending on whether ICI and/or ISI is pre-canceled, three families of precoders were presented as well as the corresponding receiver architectures.

Based on simulation results, we reported the recommended precoders and pulse shapes for each modulation order and packing factor τ varying from 0.7 to 0.9. Additionally, we compared the BER performance of both the precoded and non-precoded FTN-OQAM transceivers. Through simulations, we showed that both transceivers reach similar BER results in case of QPSK modulation, although the BER at the first iteration is improved by the proposed precoding. In terms of EXIT chart analysis, this behavior is interpreted by the fact that the tunnel between the equalizer and the decoder curves is wider when the precoding is considered because the mutual information value at the equalizer output (or equivalently at the decoder input) is higher. When high modulation orders are

considered, the gain achieved by the proposed precoding is more important. Considering low τ values and high modulation orders (τ=0.7 for 16-QAM and τ=0.8 for 64-QAM), i.e., in the case of severe interferences, we showed that our precoding enables to reduce the number of necessary iterations at the receiver side, and to improve the transceiver performance in terms of BER vs SNR. In this scenario, the EXIT charts showed that the tunnel between the equalizer and the decoder is tight in case of the non-precoded transceiver. The proposed precoding reduces the interference caused by FTN signaling, which allows to widen the EXIT tunnel between the equalizer and the decoder and permits better BER results. As τ increases, the proposed precoding reduces the number of necessary iterations at the receiver side. Although both transceivers converge to close performance, the BER results at the first iterations are improved thanks to the precoding. Moreover, we showed in the previous chapter that the receiver complexity, in terms of number of performed additions and multiplications operations, increases with the modulation order. Therefore, the proposed precoding reduces the receiver complexity since less iterations are now needed at the receiver side. On the other hand, when the used pulse shape is fixed, we showed that the FTN-OQAM transceiver performs better when combined with SIPC precoding. For instance, the FTN-OQAM transceiver employing TFL filtering does not converge in case of τ=0.9 and 16-QAM modulation, while it performs close to the Nyquist performance thanks to SIPC precoding.

Obviously, the obtained results depend on the used channel code as well as on the coding rate. The introduced SIPC precoders aim at reducing FTN-self interference and the corresponding receivers process first the precoded symbols and then the non-precoded ones. When the achievable effective minimum lossless packing factor is considered, the EXIT tunnel of the precoded transceiver is wider since symbols are less impacted by interference. Consequently, we can conjecture that SIPC precoding will enable the FTN-OQAM transceiver to reduce the number of necessary iterations and to improve the BER results, especially at the first iterations. Additionally, the proposed precoding is also expected to enhance the transceiver performance for τ values below the minimum FTN packing factor, i.e., when the equalizer curve is close to the decoder one in the EXIT analysis.

Part of the results presented in this chapter were published in IEEE European Wireless Conference in 2016 [109]. We also filed a patent on the proposed SIPC precoding:

N. Lahbabi, H. Lin, C. Abdel Nour, C. Douillard and P. Siohan, “Sparse Interference Pre-Cancellation for FTN-OQAM systems", EW’16, Oulu, Finland, May 2016.

N. Lahbabi, H. Lin and P. Siohan, “ Pré-annulation dispersée des interférences pour les transmissions FTN. " 2015. Reference N° R27445FR.

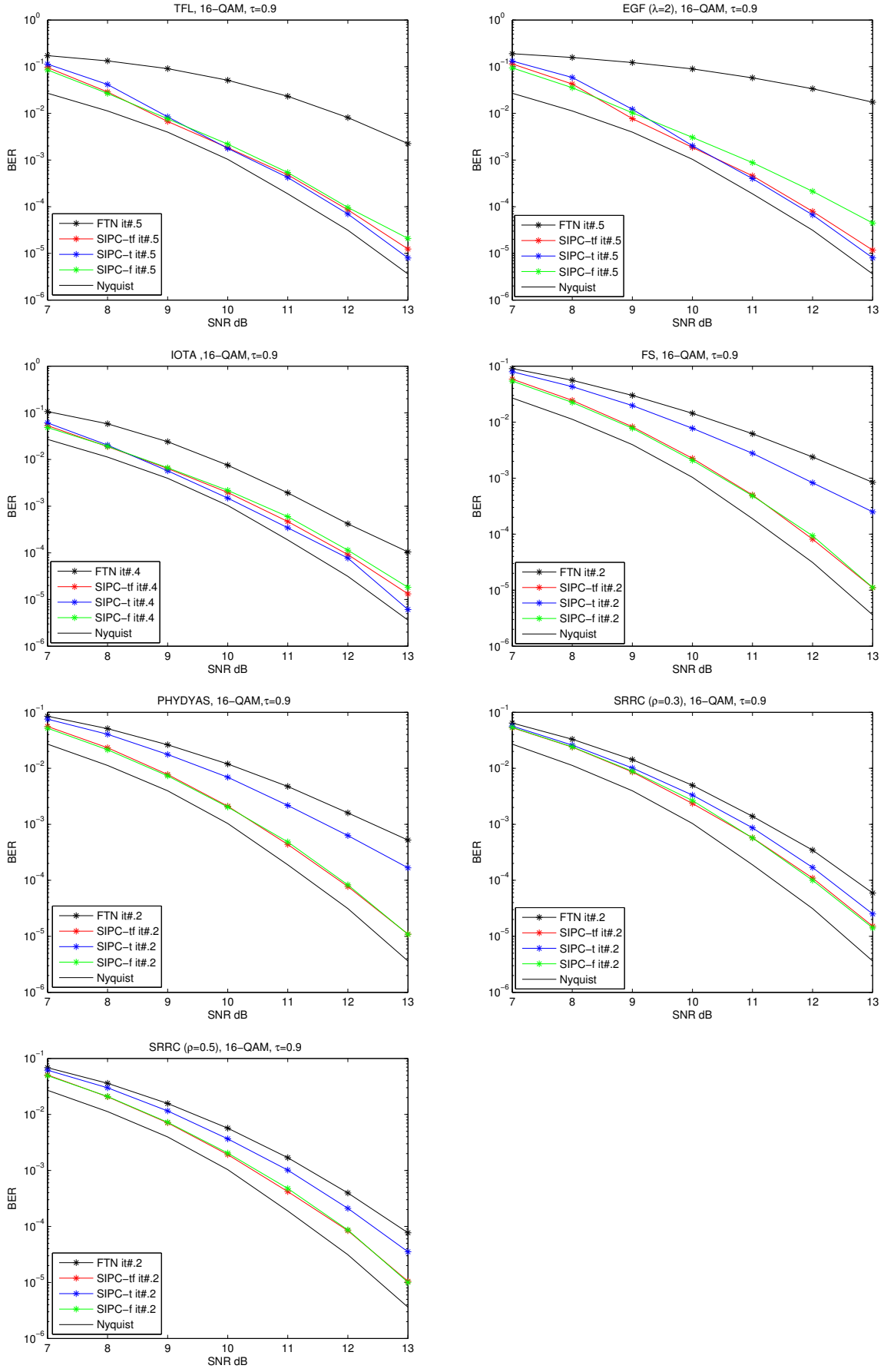

FIGURE 4.25: BER comparison between the precoded and non-precoded FTN-OQAM transceiver using different pulse shapes, 16-QAM-modulation and $\tau = 0.9$.

Chapter 5

An enhanced design for FTN-OQAM transceiver

5.1 Introduction

In the previous chapter, we detailed a new precoding technique for FTN signaling and OFDM/OQAM modulation. We proposed to remove FTN-self interference from a sub-group of the transmitted symbols while keeping the remaining symbols as normal constellation. Hence, the precoded and non-precoded symbols are impacted differently by the interference induced by FTN signaling. In this chapter, we aim at further improving the FTN-OQAM transceiver to approach the performance of Nyquist-based systems with better spectral efficiency. First, we propose to modify the channel encoder by using different coding rates for bits composing the precoded and non-precoded symbols. Then, we modify the bit-to-symbol mapping to take into account the different bit-level protection of the Gray mapping. Finally, we also propose a new symbol to time-frequency positions mapping different from the one conventionally used by OFDM/OQAM modulation.

5.2 Channel coding rate adaptation

When signaling faster than the Nyquist rate, self-interference is introduced to the transmitted data since the orthogonality condition does not hold. In the previous chapter, we detailed a new precoding technique to reduce this interference at the transmitter side. In fact, we proposed to divide the transmitted symbols into two sub-groups: the first one contains precoded symbols while the second one contains normal OQAM symbols. The precoding operation consists in canceling, from the first sub-group of symbols, interference caused by the second one. Due to this interference pre-cancellation, these two sub-groups of symbols are impacted differently by interference and exhibit different BER.

Fig. 5.1 illustrates this behavior for a transmission over AWGN channel. The BER of the precoded (using SIPC-t precoding) and non-precoded symbols are plotted on the same diagram for comparison purpose. The simulation results are reported for 16-QAM modulation and PHYDYAS filtering. We kept the same simulation parameters as in the previous chapter: $(1, \frac{5}{7})$ RSC code with coding rate $r = \frac{1}{2}$, random interleaving and Gray

mapping. The receiver is based on MMSE LE-IC equalization: the length of the MMSE filter is 30 and the delay is 15. The decoder is based on the Max-Log-MAP algorithm. The precoding parameter is $k = 2$, and all the $M = 64$ subcarriers are supposed to be modulated. As in the previous chapter, a factor α is introduced to control the amount of the removed interferences. As we now focus on channel coding and mapping strategies, most often our simulations will be carried out with the PHYDYAS prototype filter (with $L = 4M$) which was one the mostly recommended pulse shape in the two previous chapters. The BER curves are plotted after performing different number of iterations at the receiver side depending on the packing factor τ.

For a low packing factor $\tau = 0.7$, our simulation results show that the receiver converges after performing 7 iterations. Since the introduced interferences are stronger, the BER performance at all the performed iterations show that the precoded symbols present better BER results. We plotted the BER after 7 iterations in Fig. 5.1. By increasing the packing factor, the non-precoded symbols show better BER at the first iterations. In fact, by setting $\tau = 0.8$ the BER performance of both the precoded and non-precoded symbols converge to similar results. However, the non-precoded symbols present better BER results at the first performed iterations as shown in Fig. 5.1. Similar behavior is observed in case of $\tau = 0.9$: both group of symbols converge to identical BER performance after performing 3 iterations by the receiver, and the non-precoded symbols show better BER results at the first iterations. This is due to the fact that less interference is caused with high τ values, and that the two-stage receiver decodes first the precoded symbols and then cancels their induced interference from the non-precoded ones before the decoding step.

We observe the same BER behavior in case of 64-QAM modulation, as shown in Fig. 5.2. Firstly, the number of performed iterations depends also on τ. Secondly, with $\tau = 0.8$ the non-precoded symbols show better BER results at the first 7 iterations and then both groups of symbols show identical BER results. Similar conclusions are drawn when $\tau = 0.9$.

Our objective in this section is to further enhance the precoded FTN-OQAM transceiver by modifying the channel coding rate used for each sub-group of the transmitted symbols. We consider the precoded FTN-OQAM transceiver depicted in Fig. 4.1, where the *Channel coding* block encodes N_i information bits and delivers N_c encoded bits. We also consider that the N_c encoded bits are converted to B OQAM symbols. We have:

$$\begin{aligned} B &= B_1 + B_2 \\ N_c &= N_{c1} + N_{c2} \\ N_i &= N_{i1} + N_{i2} \end{aligned} \tag{5.1}$$

where the index 1 in N_{i1} and N_{c1} refers to the precoded symbols, while the index 2 in N_{i2} and N_{c2} refers to the non-precoded ones. The N_{c1} encoded bits, corresponding to the N_{i1} information bits, are interleaved and then converted to B_1 OQAM symbols. Similarly, the N_{c2} encoded bits corresponding to the N_{i2} information bits, are interleaved and converted to B_2 OQAM symbols. The number of the precoded and non-precoded symbols is determined by the precoding parameters k and k'. Then, the *SIPC* module cancels, from the B_1 symbols, the interference caused by the B_2 symbols. Contrary to

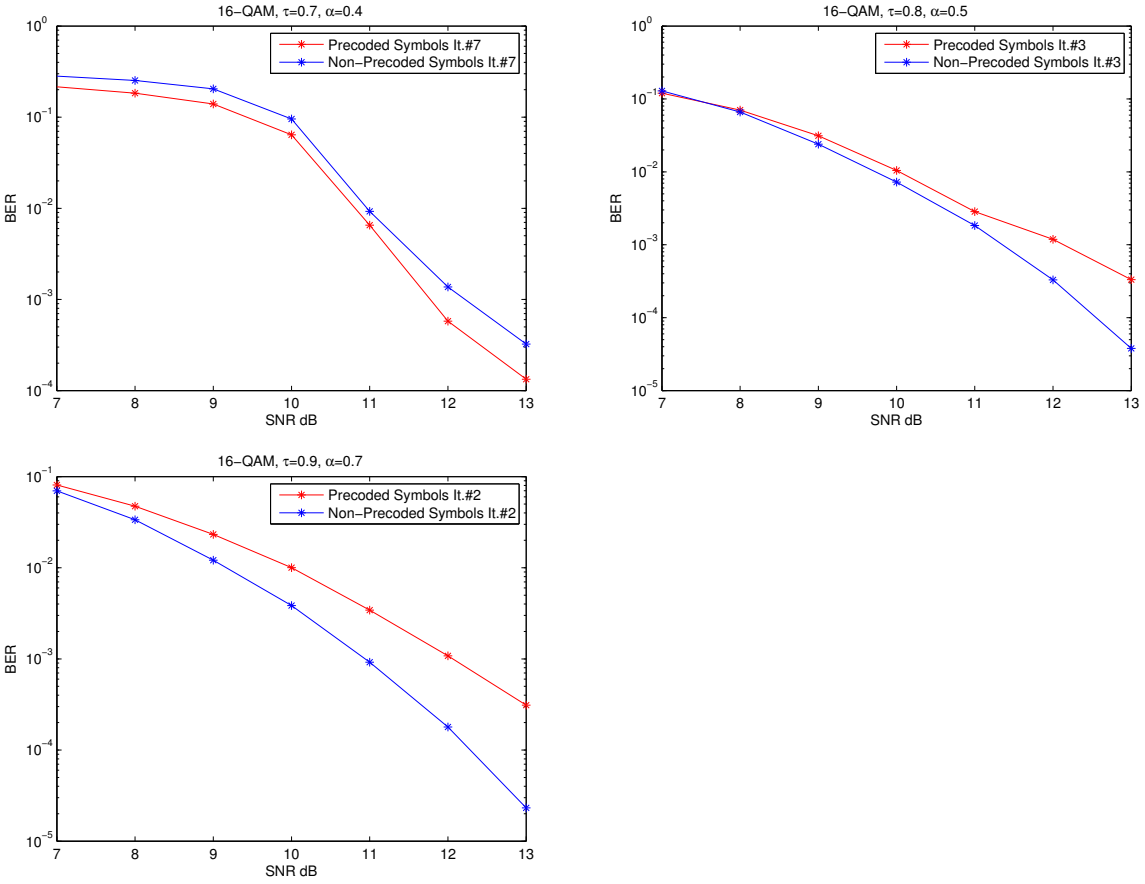

FIGURE 5.1: BER evaluation of the FTN-OQAM transceiver using SIPC-t precoding, 16-QAM modulation and PHYDYAS filtering.

the coding scheme in Fig. 4.1, where the N_{i1} and N_{i2} bits are encoded with the same coding rate, we propose to use different local coding rates r_1 and r_2 to encode the N_{i1} and N_{i2} information bits, respectively. The number of encoded bits N_c is kept unchanged and N_{i1} and N_{i2} are chosen as multiples of r_1 and r_2, respectively. Thus, different protection levels in terms of channel coding are ensured for the precoded and non-precoded symbols. Depending on whether $r_1 \leq r_2$ or $r_2 \leq r_1$, the precoded symbols are more protected than the non-precoded ones, and vice-versa.

We suppose that $r_1 \leq r_2$ and replace the *channel coding* and Π blocks by the scheme depicted in Fig. 5.3. The first group of N_{i1} bits is encoded and then punctured by the block $Punct_1$, resulting in a group of $N_{c1} = \frac{N_{i1}}{r_1}$ bits. These bits are then interleaved. Similarly, the second group of N_{i2} bits is encoded and punctured, resulting in a group of $N_{c2} = \frac{N_{i2}}{r_2}$ bits, which are then interleaved. These two groups of bits are concatenated to obtain the N_c coded bits and are then converted to OQAM symbols. Depending on which precoder is chosen, the B_1 symbols are then precoded. Although several local coding rates are used, the overall initial coding rate remains unchanged. Similar modifications are introduced when the local coding rates are chosen such that $r_2 \leq r_1$.

Simulation results

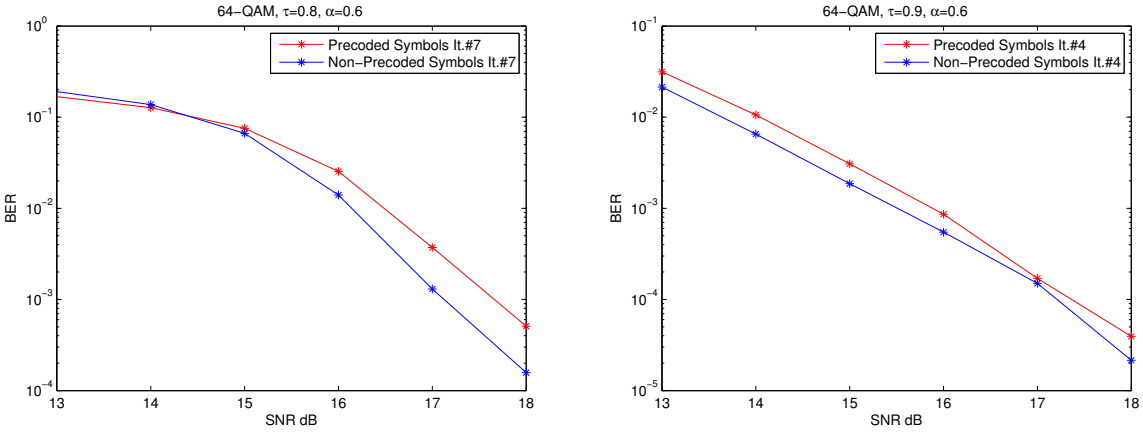

FIGURE 5.2: BER evaluation of the FTN-OQAM transceiver using SIPC-t precoding, 64-QAM modulation and PHYDYAS filtering.

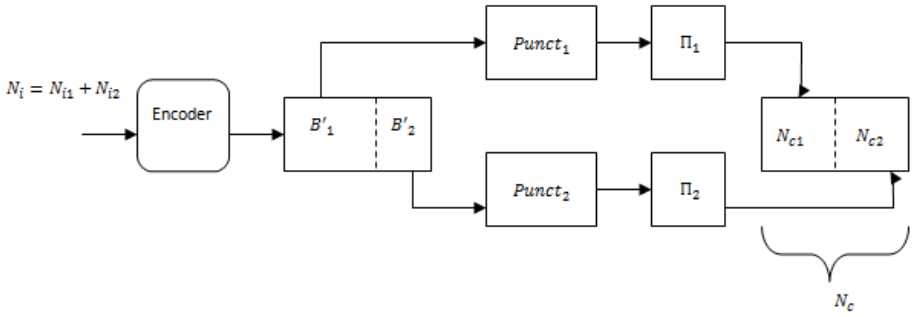

FIGURE 5.3: The proposed channel encoder and interleaver.

In this section, we evaluate the impact of the code rate adaptation on the BER performance of the transmission scheme, depending on the modulation order and the packing factor. Simulation results are provided in terms of BER vs. SNR. We use different local rates to encode the N_{i1} and N_{i2} information bits, while keeping the same effective coding rate, i.e., $r = \frac{1}{2}$. We consider an RSC encoder of rate $\frac{1}{4}$ and generator polynomials in octal notation (1,15/13,15/13,17/13):

$$\begin{aligned} g_1(x) &= 1 \\ g_2(x) &= \frac{1+x^2+x^3}{1+x+x^3} \\ g_3(x) &= \frac{1+x^2+x^3}{1+x+x^3} \\ g_4(x) &= \frac{1+x+x^2+x^3}{1+x+x^3} \end{aligned} \tag{5.2}$$

(5.3)

We also consider Gray mapping and random interleaving. The precoding method is SIPC-t, aiming at ISI cancellation, with $k = 2$. We keep the same receiver configuration as in the previous section: the receiver is based on MMSE LE-IC equalization, the

MMSE filter is of length 30 and delay 15, and the decoder is based on Max-Log-MAP algorithm. First, we plot the EXIT chart analysis representing the mutual information exchange between the equalizer and the decoder considering several coding rates:

$$\{\frac{8}{13}, \frac{5}{13}, \frac{8}{14}, \frac{6}{14}, \frac{8}{15}, \frac{7}{15}, \frac{8}{16}, \frac{8}{17}, \frac{9}{17}, \frac{8}{18}, \frac{10}{18}, \frac{8}{19}, \frac{11}{19}\}$$

Then we select the pairs of coding rates (r_1, r_2) that ensure an open tunnel between the equalizer and the decoder. Finally, we evaluate the BER performance of the FTN-OQAM transceiver using the selected coding rates r_1 and r_2 in case of 16-QAM and 64-QAM modulation.

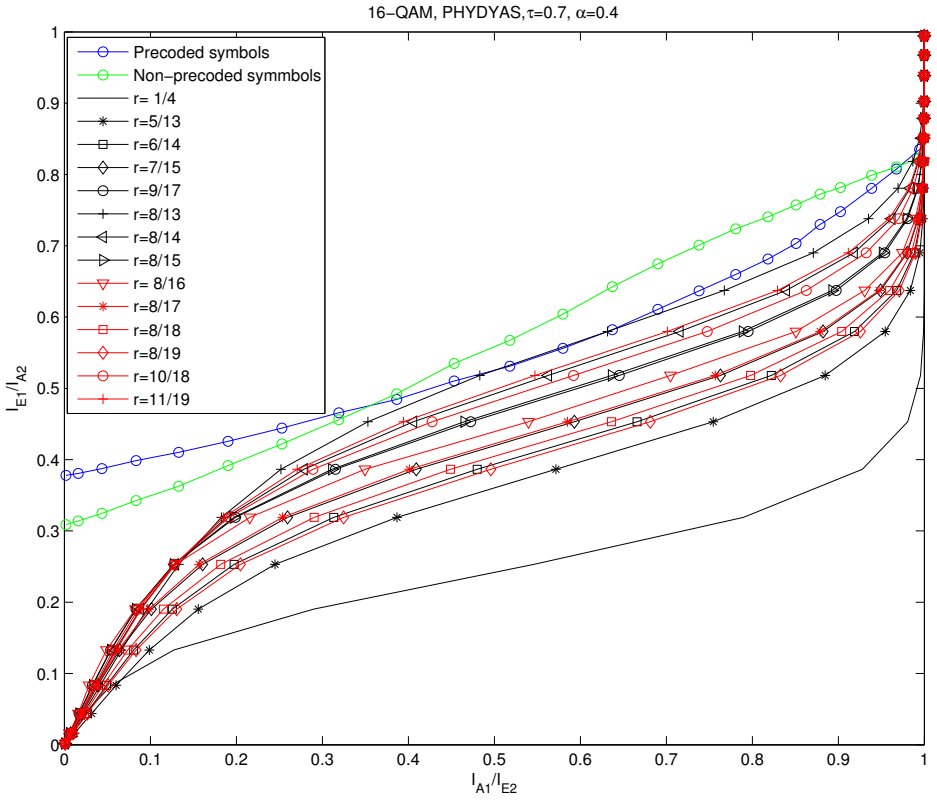

FIGURE 5.4: EXIT chart analysis of the FTN-OQAM transceiver combined with SIPC-t precoding using PHYDYAS filtering, 16-QAM modulation and $\tau = 0.7$.

16-QAM modulation

In the previous chapter, we showed that the recommended pulse shapes for the SIPC-t precoding are: FS ($L = 4M$), PHYDYAS ($L = 4M$) and SRRC ($L = 4M$, ρ=0.5) filters, see Table 4.11. As an example, we give in Fig. 5.4 the EXIT chart analysis of the receiver using PHYDYAS filtering and $\tau = 0.7$. The precoding parameters are $k = 2$ and $\alpha = 0.4$. At the beginning of the EXIT analysis, the performance reached with the precoded symbols, represented by the blue curve, outperforms the one obtained with the non-precoded ones. However, the tunnel between the green curve, representing the non-precoded symbols, and the different decoders gets wider as the EXIT analysis continues.

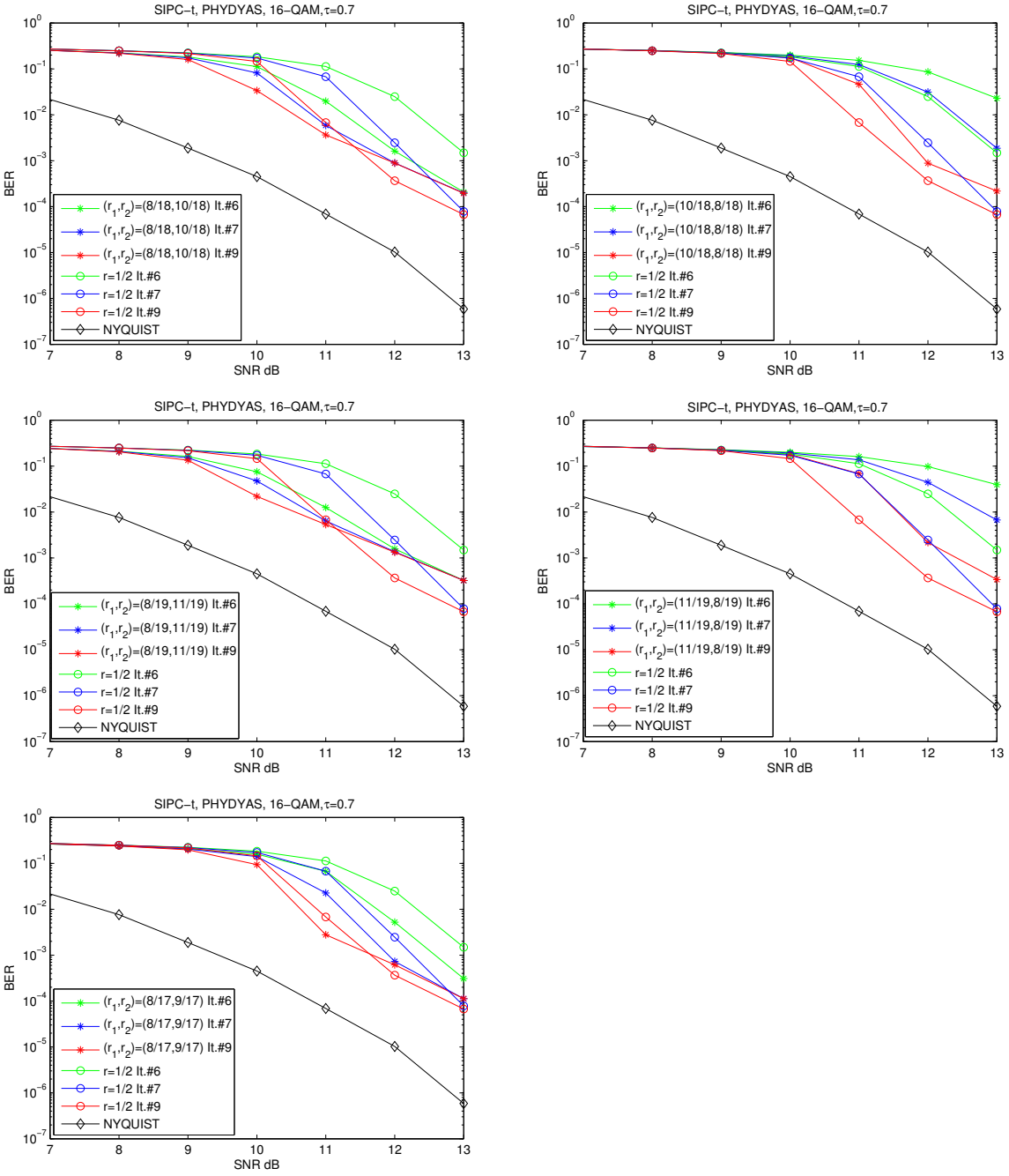

FIGURE 5.5: BER evaluation of the enhanced channel coding in case of PHYDYAS filtering, 16-QAM modulation and $\tau = 0.7$.

In addition, we observe that the opening of the EXIT tunnel is related to the coding rate. We selected various coding rates r_1 and r_2 to encode the N_{i1} and N_{i2} information bits. In Fig. 5.5, we compare the BER performance of the considered transceiver in two scenarios: using either the same coding rate for all the transmitted bits or different local coding rates while keeping the effective rate unchanged, i.e., $r = \frac{1}{2}$. Curves with circles and asterisks correspond to the first and second scenario, respectively. The black curve with diamonds corresponds to the Nyquist-based OFDM/OQAM transceiver with the same effective rate, i.e., $r = \frac{1}{2}$. Note that we used the same RSC encoder for all scenarios but performed different puncturing to obtain the desired coding rates. From

Fig. 5.4, we can see that the tunnel between the blue curve and the decoder is closed when the coding rate equals $\frac{8}{13}$. Moreover, the decoder curves are almost identical when employing the pairs $(\frac{8}{17}, \frac{7}{15})$, $(\frac{9}{17}, \frac{8}{15})$, $(\frac{6}{14}, \frac{8}{19})$ and $(\frac{11}{19}, \frac{8}{14})$ of coding rates. Therefore we selected the following coding rates for the BER evaluation:

$$(r_1, r_2) \in \{(\frac{8}{18}, \frac{10}{18}), (\frac{10}{18}, \frac{8}{18}), (\frac{8}{19}, \frac{11}{19}), (\frac{11}{19}, \frac{8}{19}), (\frac{8}{17}, \frac{9}{17})\}$$

Firstly, the results show that it is recommended to use a stronger coding rate to encode the N_{i1} information bits, i.e., $r_1 \leq r_2$. This is confirmed by the EXIT charts in Fig. 5.4 which show that the blue curve, representing the precoded symbols, is closer to the decoder curves than the green one representing the non-precoded symbols. Secondly, we notice that the BER performance of the receiver after performing 6 and 7 iterations are improved when using the proposed channel encoder with $(r_1, r_2) \in \{(\frac{8}{19}, \frac{11}{19}), (\frac{8}{18}, \frac{10}{18}), (\frac{8}{17}, \frac{9}{17})\}$. Moreover, the results show that by setting $(r_1, r_2) = (\frac{8}{17}, \frac{9}{17})$, the receiver converges to better results for low SNRs after performing 9 iterations. Thus, for the 16-QAM modulation and $\tau = 0.7$, the recommended coding rate (r_1, r_2) is $(\frac{8}{17}, \frac{9}{17})$. We obtain similar results when FS filtering is employed: the BER curves at the first iterations are improved when $r_1 \leq r_2$. At the final iteration, the proposed channel coding provides better results for low SNRs but both coding strategies converge to similar results for high SNRs.

The EXIT chart analysis in case of 16-QAM modulation, PHYDYAS filtering and τ=0.8 is illustrated in Fig. 5.6. Obviously, the tunnel between the decoder and both the blue and the green curves widens as the packing factor increases. We can also observe that the tunnel between the decoder and the green curve, representing the non-precoded symbols, is still wider than the tunnel between the decoder and the blue curve representing the precoded symbols. In this scenario, we selected the pair of coding rates $(r_1, r_2) = (\frac{8}{17}, \frac{9}{17})$ and evaluated the BER performance in Fig. 5.7. Results show that the proposed channel coding does not improve the BER performance. On the contrary, using the same coding rate for both N_{i1} and N_{i2} information bits outperforms the results obtained using different coding rates. We observe similar behavior using SRRC (ρ=0.5) filtering and $\tau = 0.9$. Figs. 5.8 and 5.9 represent the EXIT chart analysis and the BER results, respectively. The FTN-OQAM transceiver achieves better results by employing the same coding rate for all the transmitted information bits.

This behavior can be explained based on the EXIT charts in Figs. 5.4, 5.6 and 5.8. For all τ values, the tunnel between the decoder and the curve of the non-precoded symbols is wider than the tunnel between the decoder and the one representing the precoded symbols. This results implies intuitively that a stronger code should be used to encode information bits composing the precoded symbols, i.e., $r_1 \leq r_2$. However, the tunnel between the decoder and both the blue and the green curve is wider as τ increases, which is obvious since less FTN-self interferences are introduced. By considering $r_1 \leq r_2$ for τ= 0.7, the decoding of the precoded symbols is improved. This impacts directly the detection of the non-precoded symbols since the two-stage receiver decodes first the precoded and then the non-precoded symbols. Consequently, the EXIT tunnel becomes wider which explains the BER improvement, especially at the first iterations. However, as τ increases the EXIT tunnel is originally wider and the intersection between the decoder curve and both the blue and the green curve is close to the NEF point (represented by

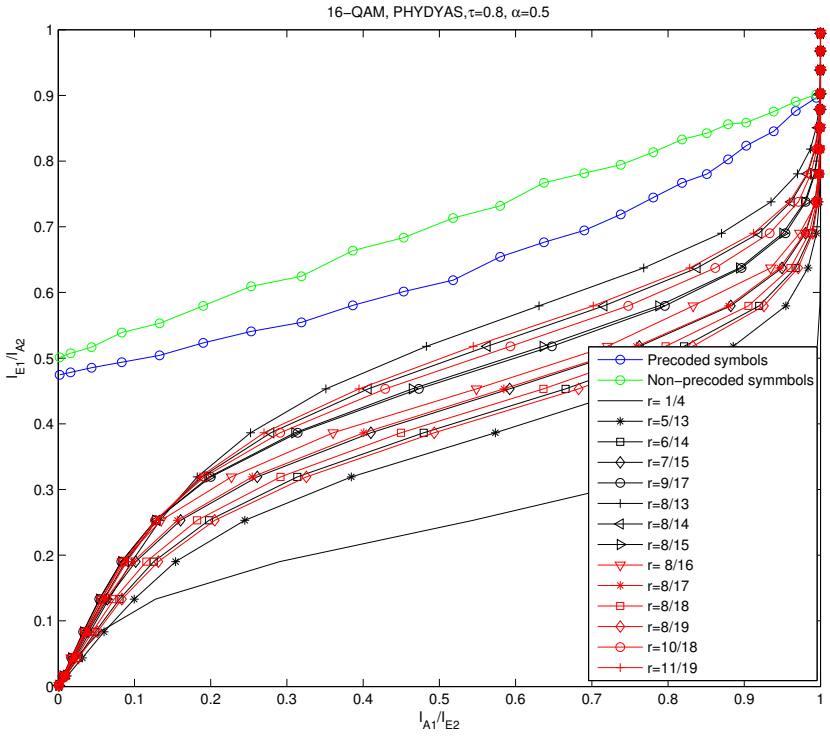

FIGURE 5.6: EXIT chart analysis of the FTN-OQAM transceiver combined with SIPC-t precoding using PHYDYAS filtering, 16-QAM modulation and $\tau = 0.8$.

the point (1, 0.92), see Fig. 3.17 in Chapter 3). The proposed channel coding widens the EXIT tunnel but does not improve the intersection point between the decoder and the equalizer curves. Consequently, the proposed channel coding does not improve the

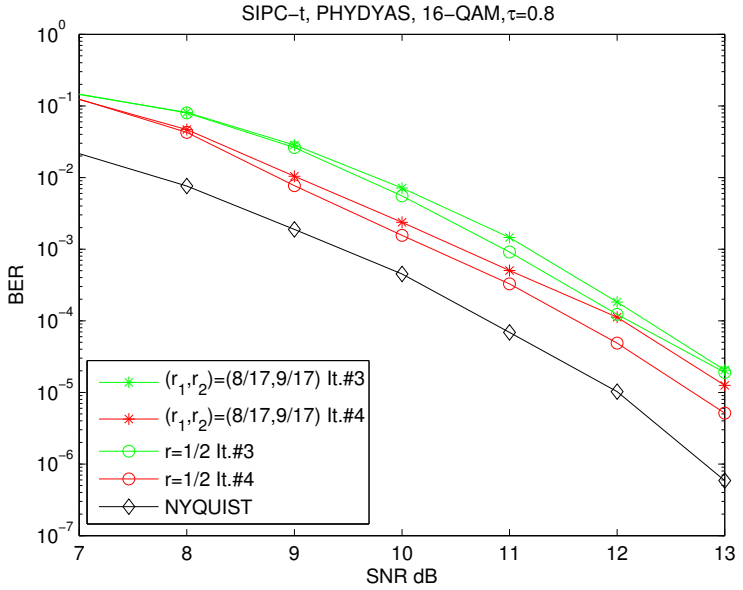

FIGURE 5.7: BER evaluation of the enhanced channel coding in case of PHYDYAS filtering, 16-QAM modulation and $\tau = 0.8$.

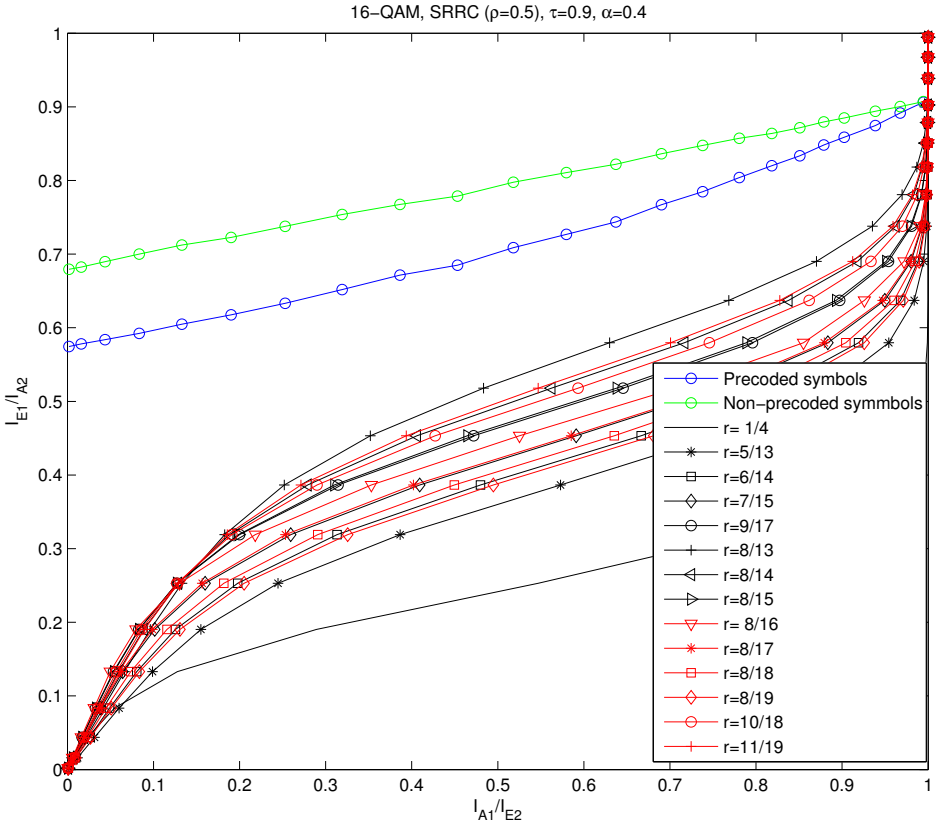

FIGURE 5.8: EXIT chart analysis of the FTN-OQAM transceiver combined with SIPC-t precoding using SRRC (ρ=0.5) filtering, 16-QAM modulation and $\tau = 0.9$.

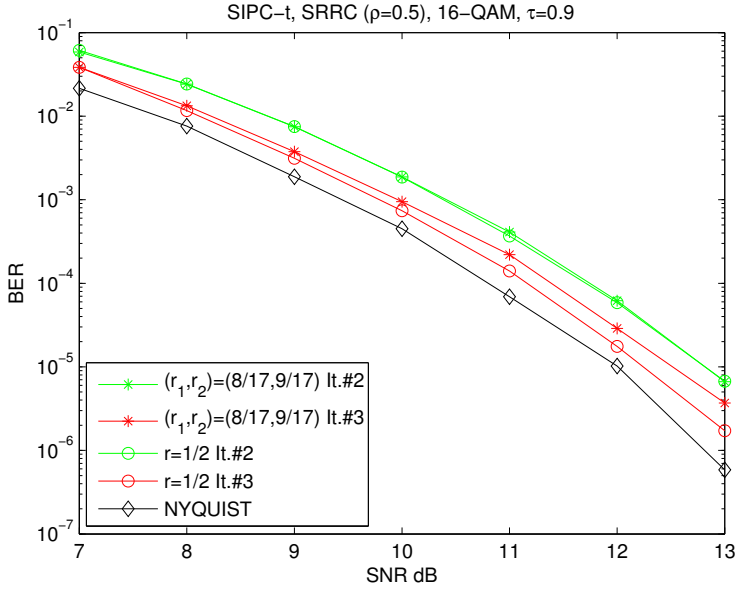

FIGURE 5.9: BER evaluation of the enhanced channel coding in case of SRRC (ρ=0.5) filtering, 16-QAM modulation and $\tau = 0.9$.

BER results.

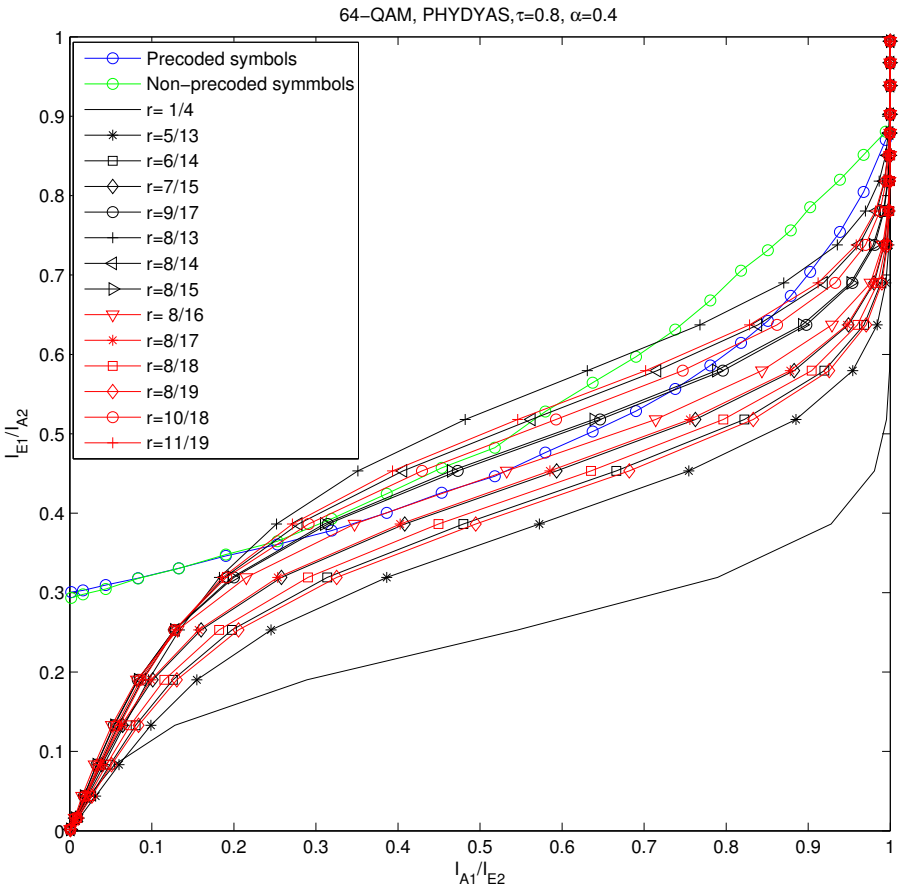

FIGURE 5.10: EXIT chart analysis of the FTN-OQAM transceiver combined with SIPC-t precoding using PHYDYAS filtering, 64-QAM modulation and $\tau = 0.8$.

64-QAM modulation

In what follows, we evaluate the BER performance of the proposed channel coding when 64-QAM modulation is envisaged. When τ is equal to 0.8 and 0.9, the recommended pulse shapes for the SIPC-t precoder are: FS, PHYDYAS and SRRC (ρ=0.5) filters, see Table 4.11.

Fig. 5.10 illustrates the EXIT chart analysis considering PHYDYAS filtering and τ=0.8. We observe that the tunnel between the decoder and the green curve representing the non-precoded symbols is wider than the tunnel between the decoder and the blue curve representing the precoded symbols. However, both curves are close to the decoder curves with the different coding rates. This leads to the question of whether improving the decoding of the precoding symbols, i.e., by setting $r_1 \leq r_2$, will widen the EXIT tunnel between the equalizer and the decoder to achieve better BER results. From the EXIT chart, we observe that the tunnel between the blue curve and the decoder is open for the

coding rates $\frac{6}{14}$, $\frac{7}{15}$, $\frac{8}{17}$, $\frac{8}{18}$ and $\frac{8}{19}$. The BER evaluation of the precoded FTN-OQAM transceiver using PHYDYAS filtering and τ=0.8 is evaluated in Fig. 5.11. We considered the following pairs of coding rates:

$$(r_1, r_2) \in \{(\frac{6}{14}, \frac{8}{14}), (\frac{7}{15}, \frac{8}{15}), (\frac{8}{17}, \frac{9}{17}), (\frac{8}{18}, \frac{10}{18}), (\frac{8}{19}, \frac{11}{19})\}$$

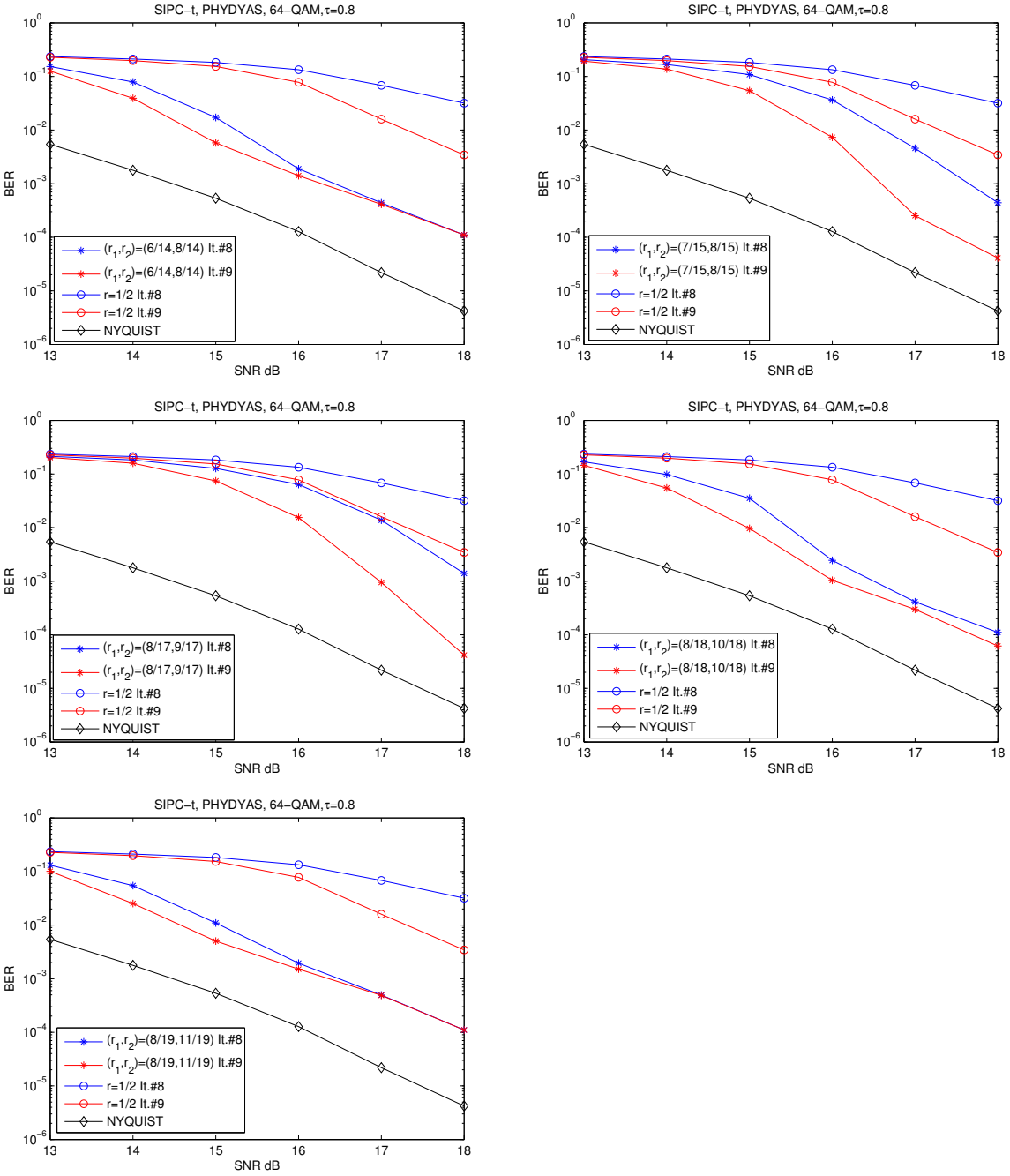

FIGURE 5.11: BER evaluation of the enhanced channel coding in case of PHYDYAS filtering, 64-QAM modulation and $\tau = 0.8$.

Results show that employing different local coding rates gives better BER results. Moreover, we observe that the receiver performance is even more enhanced when the N_{i1} bits, composing the precoded symbols, are encoded with a strong code. In particular,

when $r_1 \in \{\frac{6}{14}, \frac{8}{18}, \frac{8}{19}\}$. We obtain the same results using FS and SRRC (ρ=0.5) filtering.

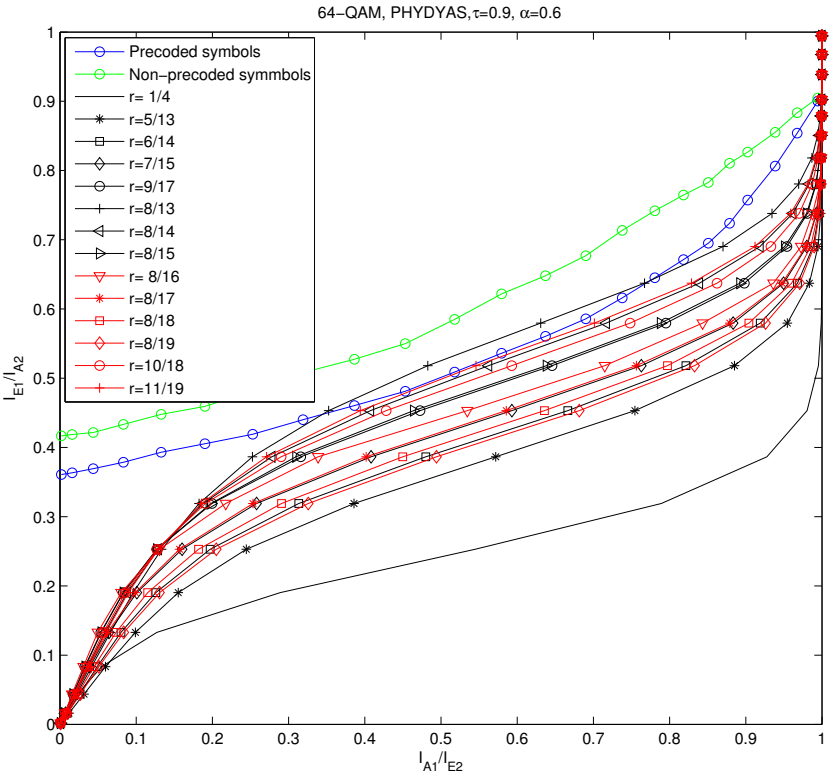

FIGURE 5.12: EXIT chart analysis of the FTN-OQAM transceiver combined with SIPC-t precoding using PHYDYAS filtering, 64-QAM modulation and $\tau = 0.9$.

As for the 16-QAM case, results show that low r_1 values do not enhance the BER performance for higher τ values. Figs. 5.12 and 5.13 represent the EXIT chart and the BER results when τ=0.9, respectively. We considered $(r_1, r_2) = (\frac{8}{17}, \frac{9}{17})$ for the BER evaluation. In this case, we notice that the receiver converges to better BER while using the same coding rate for all the transmitted symbols. We obtain the same results for the FS and SRRC (ρ=0.5) pulse shapes with $\tau = 0.9$: although the BER results at first iterations are improved by the proposed channel coding, the receiver converges to better performance using the same coding rate for all information bits as shown in Fig. 5.14. This behavior can be explained in the same way as in the 16-QAM modulation scenario. For $\tau = 0.8$, the EXIT charts show that the tunnel between the blue curve and the decoder, using a coding rate $\frac{8}{16}$, is closed and that the NEF (see Fig. 3.18 in Chapter 3) point is not reached. This leads to the question of whether the transceiver performance can be improved by enhancing the decoding of the precoding symbols. Indeed, considering a stronger coding rate r_1 improves the decoding of the precoded symbols, which impacts the decoding of the non-precoded ones at the second step of the two-stage receiver. As τ increases, the EXIT tunnel between the decoder and both the blue and the green curves is wider and the intersection point is close to the NEF one. The proposed channel decoding permits only to widen the tunnel opening, which can explain the BER results at the first iterations in Fig. 5.14, and does not improve the intersection point with the decoder curve.

We can conjecture that the proposed channel coding is recommended when the EXIT chart shows that the equalizer curve is very close to the decoder one, meaning that it improves the soft information exchange between the soft equalizer and the decoder. Considering the precoded FTN-OQAM transceiver, we showed that the introduced channel coding is recommended for low FTN packing factors: $\tau = 0.7$ for 16-QAM modulation and $\tau = 0.8$ for 64-QAM modulation. In these scenarios, the precoded FTN-OQAM transceiver exhibits better BER results when using different local coding rate r_1 and r_2 to encode the N_{i1} and N_{i2} information bits, respectively with $r_1 \leq r_2$. We should mention that the transceiver complexity, in terms of number of addition and multiplication operations, does not increase when the proposed encoding is employed.

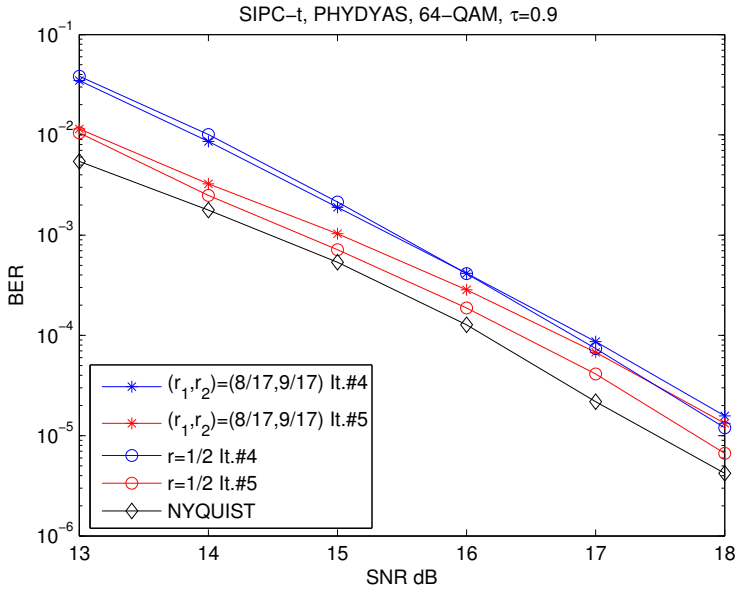

FIGURE 5.13: BER evaluation of the enhanced channel coding in case of PHYDYAS filtering, 64-QAM modulation and $\tau = 0.9$.

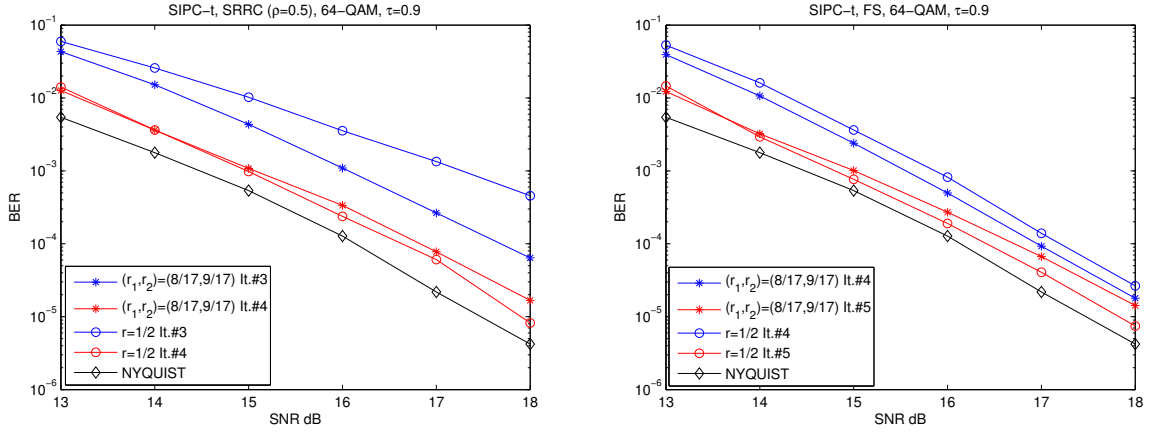

FIGURE 5.14: BER evaluation of the enhanced channel coding in case of FS and SRRC (ρ=0.5) filtering, 64-QAM modulation and $\tau = 0.9$.

5.3 Gray mapping enhancement

Considering a high-order modulation such as 16-QAM and 64-QAM, it is known that the error protection level of each bit depends on its position in the Gray mapping. We consider the 16 and 64-QAM Gray mapping depicted in Figs. 5.15 and 5.16. In case of 16-QAM modulation, two protection levels are available for each 4-bit symbol. The first level is represented by bits b_0 and b_2, while the second level is represented by bits b_1 and b_3. On the other hand, the 64-QAM modulation presents three protection levels for each 6-bit symbol. Bits b_0 and b_3 constitute the first level, while bits b_1 and b_4 constitute the second level and bits b_2 and b_5 the third level. In Fig. 4.1, the RSC channel encoder has an effective rate $r = \frac{1}{2}$ and delivers encoded bits that are first interleaved and then mapped to complex symbols. In this section, we propose a bit reordering to place the systematic bits at the highly protected positions of the Gray mapping. In fact, the RSC encoder delivers systematic bits representing information bits at its input and redundancy, i.e., parity bits. The proposed bits mapping aims at improving the decoding of the transmitted information bits. To this end, the systematic and parity bits delivered by the channel encoder are interleaved individually and then reordered before being converted to complex symbols. In the following, we detail the bit-to-symbol mapping modifications for the non-precoded and precoded FTN-OQAM transceivers.

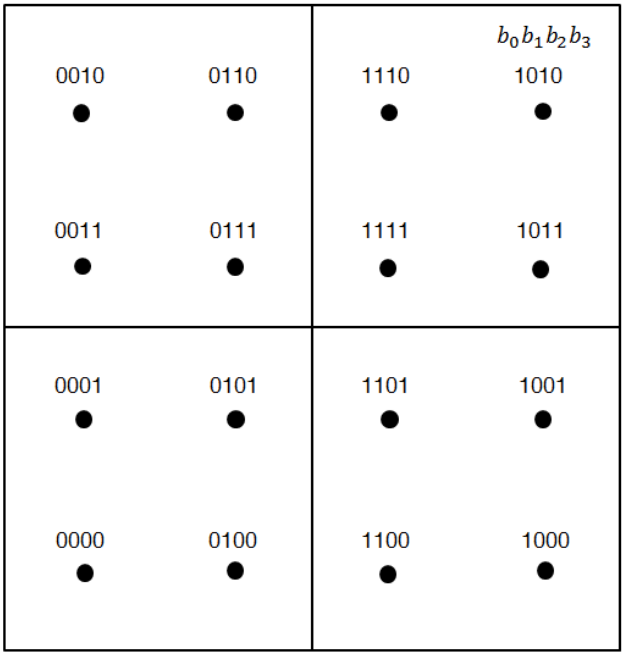

FIGURE 5.15: 16-QAM Gray Mapping.

5.3.1 Non-precoded FTN-OQAM transceiver

We consider the FTN-OQAM transceiver detailed in Fig. 3.10. The RSC channel encoder delivers systematic bits, i.e., information bits, and parity bits, i.e., redundancy. The systematic and parity bits are then interleaved separately. When 16-QAM modulation is envisaged, the interleaved systematic bits are placed at positions b_0 and b_2. The

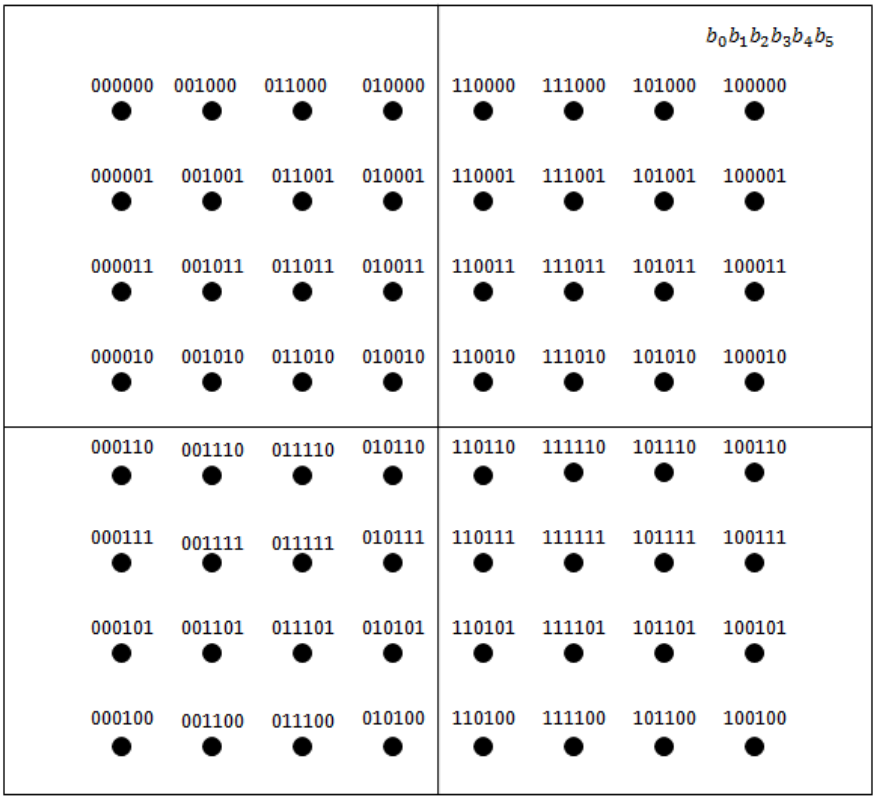

FIGURE 5.16: 64-QAM Gray Mapping.

remaining positions b_1 and b_3 are occupied by the corresponding interleaved parity bits. Then, each 4 bits are converted to complex symbols and fed to the FTN modulator block. Thus, the bit reordering ensures that the useful bits, i.e., the transmitted information bits, occupy the highly protected positions of the Gray mapping. The same idea applies in case of 64-QAM modulation where each complex symbol is composed of 6 bits. Similarly, the systematic and parity bits are interleaved separately. In this scenario, three protection levels are available. The interleaved systematic bits are placed at positions b_0, b_3 and b_1, while their corresponding interleaved parity bits are placed at positions b_4, b_2 and b_5, respectively. Note that the parity bits corresponding to the systematic bits placed at positions b_1 are mapped to positions b_4, since they constitute the second level of error protection. The reordered bits are then converted to complex symbols and fed to the FTN-OQAM modulator.

At the receiver side, we keep the same turbo-like processing presented in Chapter 3. However, the soft LLRs calculated by the SISO mapping module should be reordered before the decoding step. Depending on the modulation order and the bit ordering used, we recover the LLRs of the systematic and parity bits. Then, they are de-interleaved separately and fed to the channel decoder. After the decoding step, the new computed LLRs are interleaved individually, reordered and fed to the SISO MMSE for the next iteration.

In what follows, we report the simulation results comparing the performance of the FTN-OQAM transceiver using the Gray mapping and the enhanced Gray mapping. The simulation configurations are: $(1, \frac{5}{7})$ RSC code with coding rate $r = \frac{1}{2}$ and random interleaving. The number of subcarriers is $M = 64$. The receiver configuration is kept unchanged: MMSE LE-IC based equalization with an MMSE filter of length 30 and delay 15. The decoder is based on Max-Log-MAP algorithm.

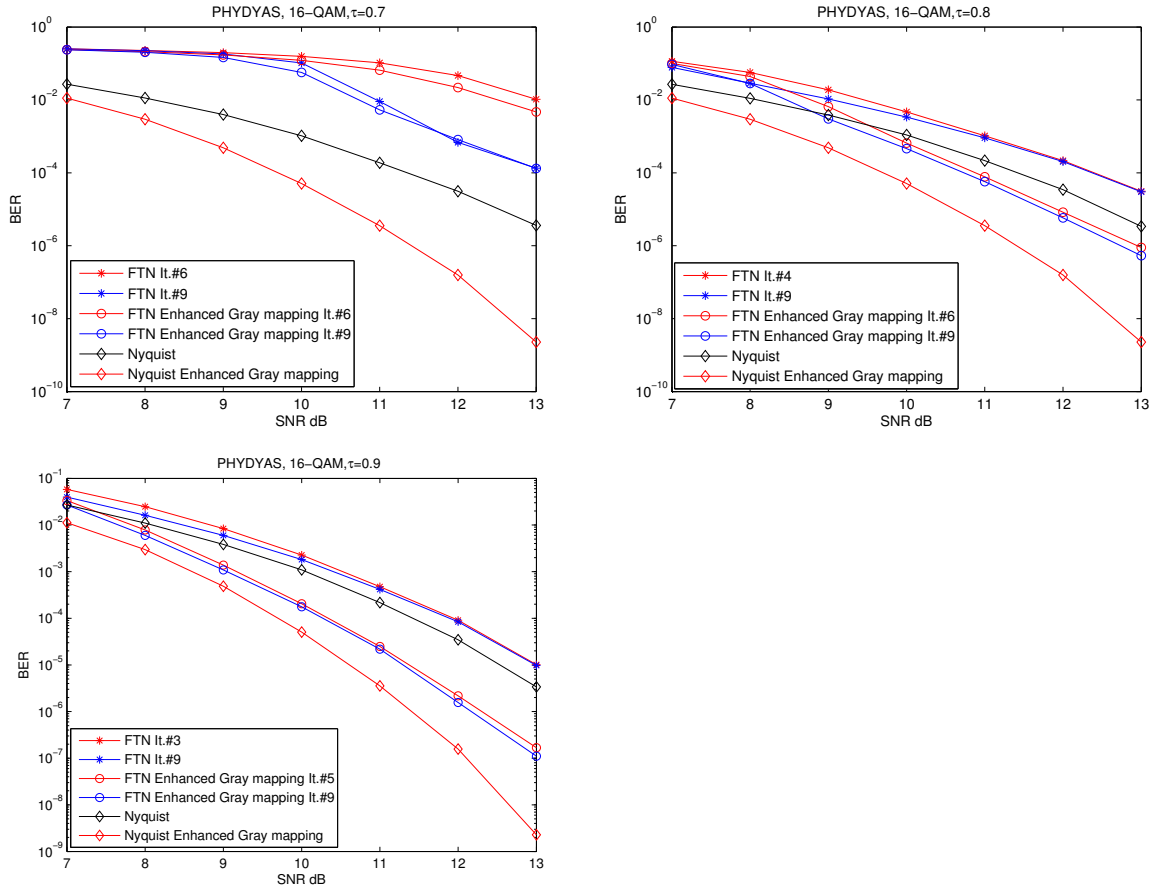

FIGURE 5.17: BER evaluation of the FTN-OQAM transceiver using the proposed bit-to-symbol mapping in case of PHYDYAS filtering and 16-QAM modulation.

In Fig. 5.17, we compare both bit-to-symbols mapping methods considering 16-QAM modulation and PHYDYAS filtering. The FTN packing factor τ varies from 0.7 to 0.9. The black curve with diamonds represents the BER using the Gray mapping and Nyquist signaling, while the BER using the enhanced bits mapping is represented by the red curve with diamonds. The results show that the proposed bits mapping presents better BER results than the classical Gray mapping. The performance improvement is even larger for high τ values. In fact, both bits mapping methods provide almost similar results when $\tau = 0.7$. For higher packing factors, considerable results improvement are obtained using the enhanced bits mapping and the receiver converges always to Nyquist performance. Note that the number of necessary iterations at the receiver side changes. The number of necessary iterations is defined as the minimum number of iterations from which no further performance improvements are obtained. For $\tau = 0.8$, the number of necessary iterations at the receiver side is 6 when employing the proposed bits mapping

instead of 4 in case of classical Gray mapping. When $\tau = 0.9$, the number of necessary iterations is 5 instead of 3 in case of Gray mapping. We obtain similar results for the other recommended pulse shapes.

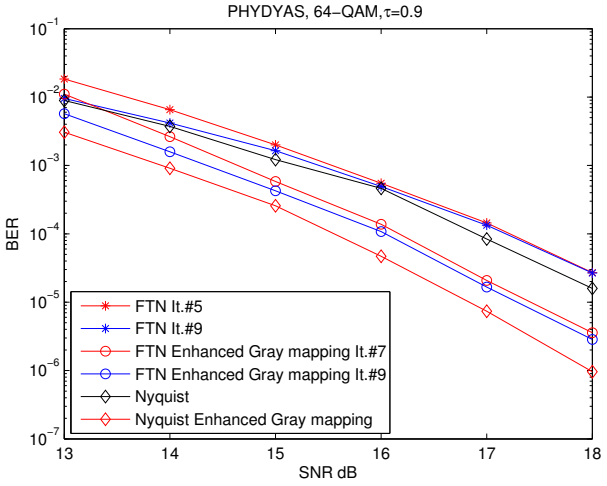

FIGURE 5.18: BER evaluation of the FTN-OQAM transceiver using the proposed bit-to-symbol mapping in case of PHYDYAS filtering, 64-QAM modulation and τ=0.9.

We increase the constellation order and evaluate the BER performance of the proposed bits mapping considering 64-QAM modulation. Our simulation results showed that the enhanced Gray mapping is recommended for high FTN packing factors, i.e., $\tau = 0.9$ and that it is outperformed by the classical Gray mapping for $\tau = 0.8$. Fig. 5.18 presents a BER comparison in case of PHYDYAS filtering and $\tau = 0.9$. As we can observe, the receiver has better BER performance and performs very close to the Nyquist red curve with diamonds. At the receiver side, the number of necessary iterations is now 7 instead of 5 in case of the classical Gray mapping. Similar behavior is observed for the other pulse shapes.
From these results, we conjecture that the enhanced bits mapping ensures considerable improvements, in terms of BER performance, when high modulation orders and packing factors are envisaged. Considering 16-QAM and 64-modulation, the gain in performance is obtained when $\tau > 0.7$ and $\tau > 0.8$, respectively. Although the BER results outperform the ones obtained using the classical Gray mapping, the number of necessary iterations increases.

5.3.2 Precoded FTN-OQAM transceiver

Considering the precoded FTN-OQAM transceiver, two sub-groups of symbols are transmitted. We denote by S_1 and P_1 the set of systematic and parity bits composing the precoded symbols. We employ the bit ordering detailed in the previous paragraph. Depending on the envisaged modulation order, the S_1 interleaved bits are mapped to the highly protected positions of the Gray mapping. The remaining positions are occupied by the corresponding interleaved P_1 bits. Similarly, sets S_2 and P_2 represent the systematic and parity bits composing the non-precoded symbols. Depending on the modulation order used, 16 or 64-QAM modulation, the S_2 interleaved bits are mapped to the positions

with the best protection level, while the remaining positions contain the interleaved P_2 bits. Finally, the interleaved bits are converted to complex symbols and the precoding operation is performed by the SIPC module.

At the receiver side, the reordering of soft LLRs at the input and the output of the channel decoder should be taken into account. As in the previous section, the soft LLRs of the systematic and parity bits should be de-interleaved individually. After the decoding step, the new computed LLRs of the systematic and parity bits are interleaved separately, reordered and then fed to the SISO mapping module.

In the following, we evaluate the BER performance of the precoded FTN-OQAM transceiver. We consider the SIPC-t precoding method with $k = 2$. We keep the same configurations as in the previous section. The simulation results in case of 16-QAM modulation, PHYDYAS and SRRC (ρ=0.5) filtering are given in Figs. 5.19 and 5.20. As in the previous section, both bit-to-symbol mapping methods lead to identical results in case of $\tau = 0.7$. The BER improvement provided by the enhanced Gray mapping gets higher as the FTN packing factor increases: with $\tau = 0.9$, we notice that the enhanced Gray mapping enables the receiver to outperform the Nyquist performance using the classical Gray mapping. Moreover, the receiver approaches very closely the red curve with diamonds representing the Nyquist performance using the enhanced Gray mapping. In terms of necessary number of iterations, the receiver needs to perform 6 iterations with $\tau = 0.8$ when employing the enhanced Gray mapping instead of 4 iterations in case of the classical bits mapping. When $\tau = 0.9$, the receiver needs to perform 3 iterations for both bits mapping strategies.

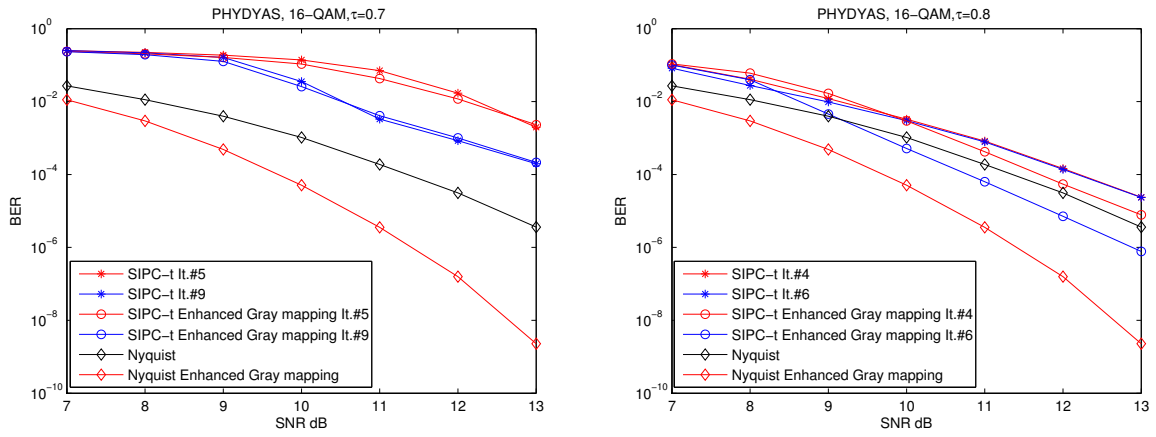

FIGURE 5.19: BER evaluation of the FTN-OQAM transceiver combined with SIPC-t precoding and the proposed bit-to-symbol mapping in case of PHYDYAS filtering and 16-QAM modulation.

The same BER behavior is observed when the modulation order is increased to 64. Results in case of $\tau = 0.8$ and PHYDYAS filtering are presented in Fig. 5.21. Although the BER at first iterations is improved by the proposed bit-to-symbol mapping, the classical Gray mapping provides the best results. However, a considerable improvement is achieved by the enhanced Gray mapping when $\tau = 0.9$ as shown in Fig. 5.22: after performing 5 iterations at the receiver side, the BER results outperform the Nyquist

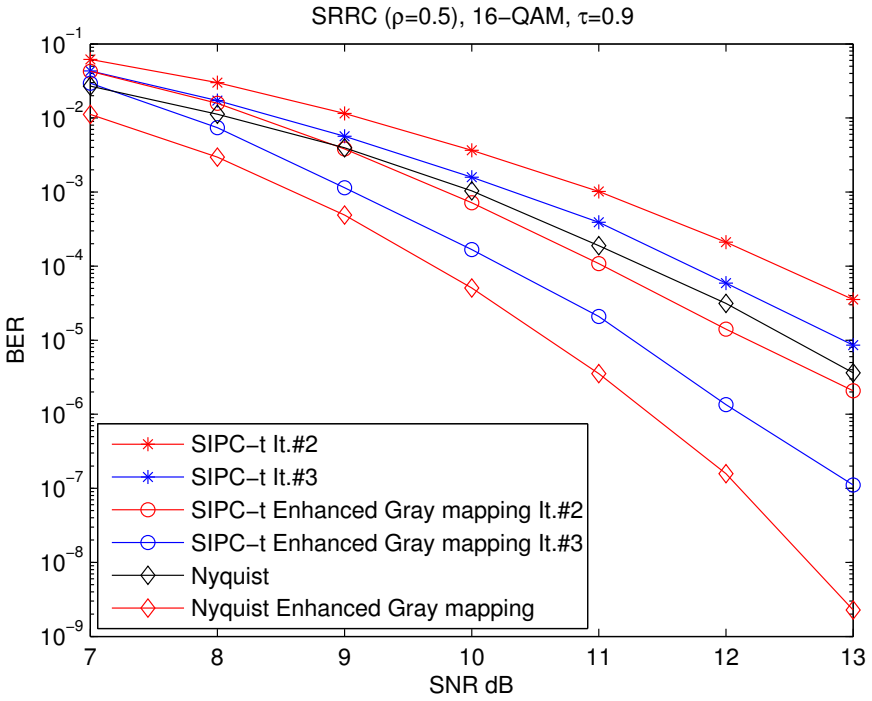

FIGURE 5.20: BER evaluation of the FTN-OQAM transceiver combined with SIPC-t precoding and the proposed bit-to-symbol mapping in case of SRRC (ρ=0.5) filtering and 16-QAM modulation.

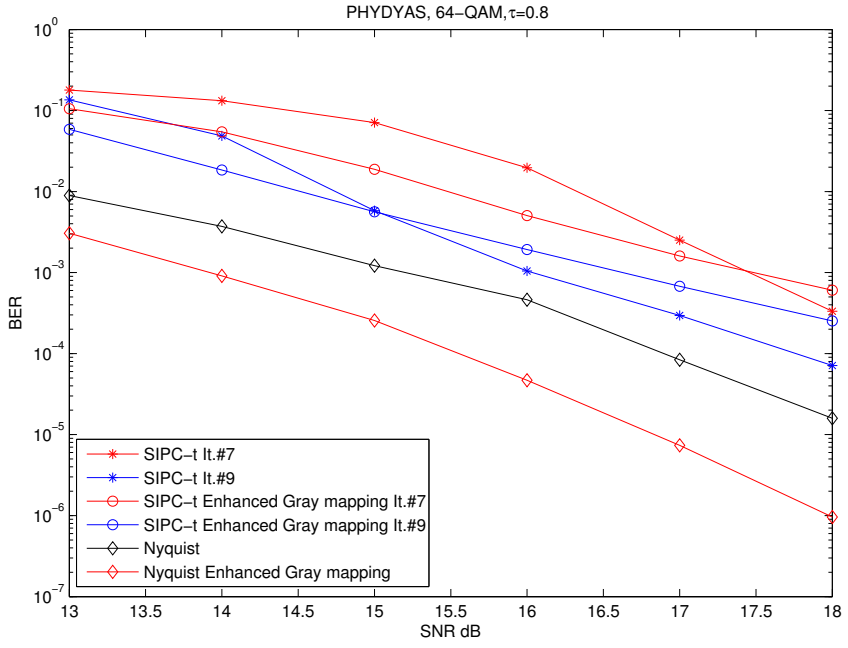

FIGURE 5.21: BER evaluation of the FTN-OQAM transceiver combined with SIPC-t precoding and the proposed bit-to-symbol mapping in case of PHYDYAS filtering, 64-QAM modulation and $\tau = 0.8$.

ones using classical Gray mapping and performs very close to the Nyquist red curve with

diamonds.

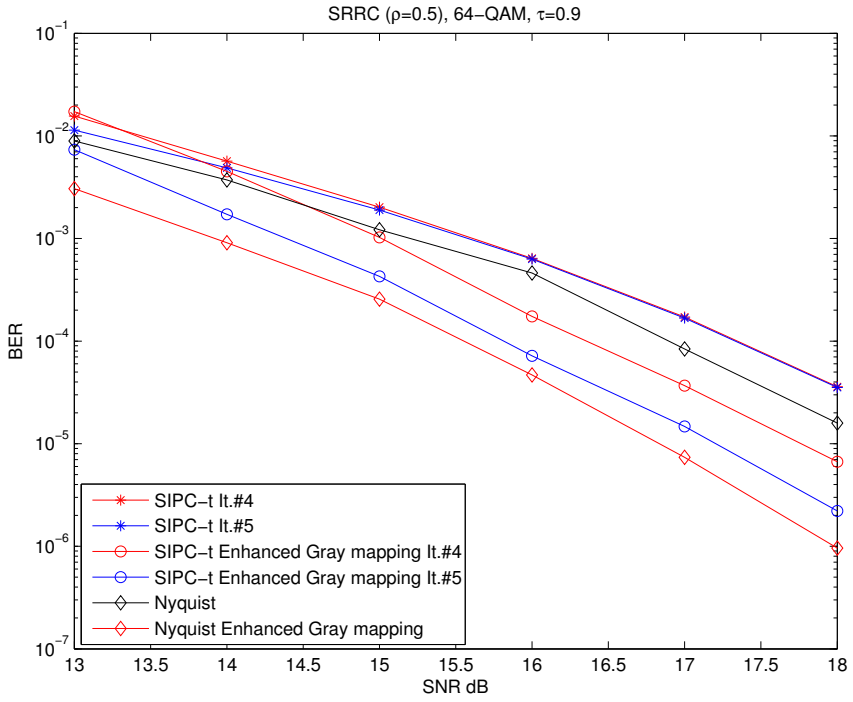

FIGURE 5.22: BER evaluation of the FTN-OQAM transceiver combined with SIPC-t precoding and the proposed bit-to-symbol mapping in case of SRRC (ρ=0.5) filtering, 64-QAM modulation and $\tau = 0.9$.

The precoded FTN-OQAM transceiver presents a similar behavior when combined with other precoding methods. For instance, Fig. 5.23 reports the simulation results in case of SIPC-f precoding with $k' = 1$ and PHYDYAS filtering. As we can observe, our method leads to considerable improvement in terms of BER for the 16 and 64-QAM modulation. The number of necessary iterations at the receiver side increases when modifying the bits mapping: for 16-QAM modulation, the receiver needs to perform 5 iterations instead of 3 in case of $\tau = 0.8$, and 3 iterations instead of 2 in case of $\tau = 0.9$. For 64-QAM modulation and $\tau = 0.9$, 5 iterations are now needed at the receiver side instead of 3.

From these results, we conclude that the proposed bit-to-symbol mapping is recommended when high τ values are targeted for both the precoded and non-precoded transceivers. Results showed a considerable BER improvement to the detriment of an increase of the iterations number. In the previous chapter, we showed that the SIPC precoding allows to decrease the number of necessary iterations. Considering the enhanced bits mapping, the proposed precoding still allows to perform less iterations at the receiver side than the non-precoded transceiver. Note that the enhanced Gray mapping does not increase the complexity, in terms of number of addition and multiplication operations, of the different blocks of the transmission chain. In fact, the proposed modifications involve only bit scheduling and does not cause any additional complexity. The complexity increase is only due to the increased number of necessary iterations.

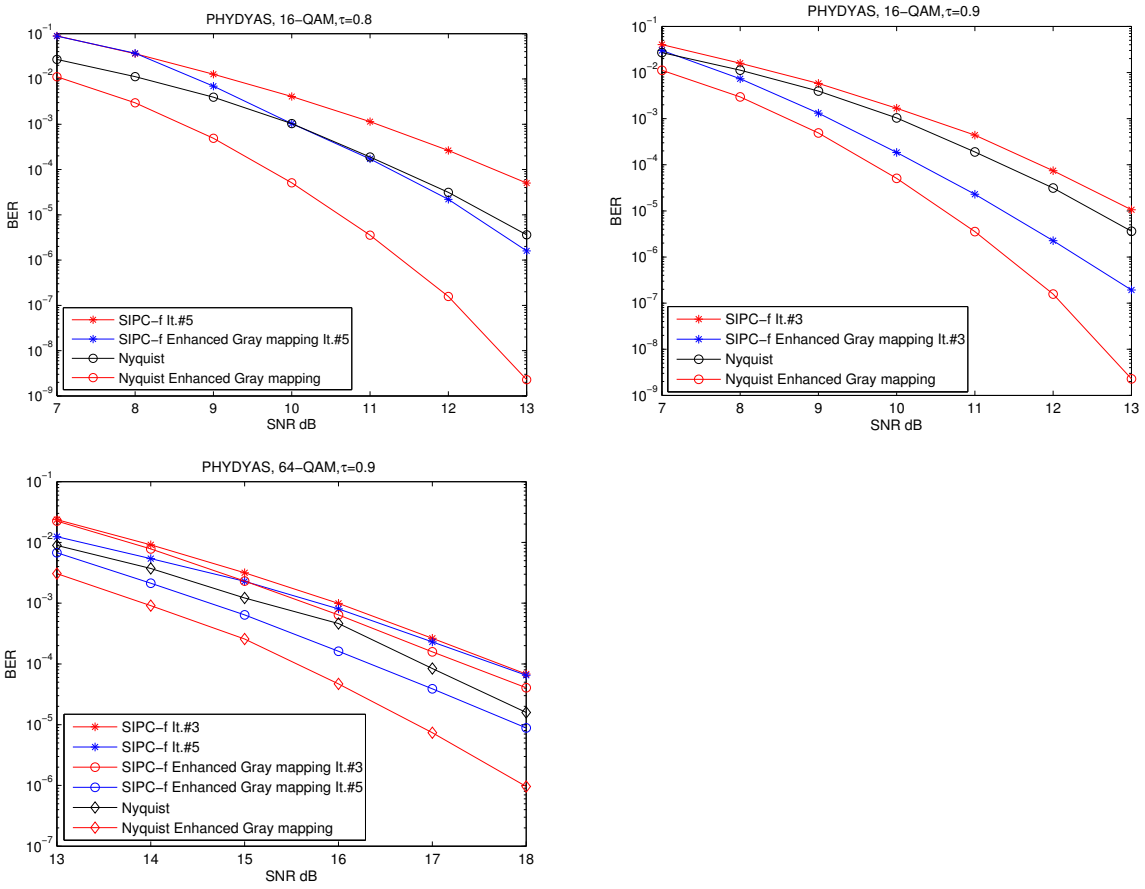

FIGURE 5.23: BER evaluation of the FTN-OQAM transceiver combined with SIPC-f precoding and the proposed bit-to-symbol mapping using PHYDYAS filtering, 16 and 64-QAM modulation and $\tau = 0.8$ and 0.9.

5.4 Symbols mapping enhancement

Our objective in this section is to take into account FTN-self interference when mapping OQAM symbols to time and frequency positions. Classically, in OFDM/OQAM modulation the real and imaginary parts of a complex symbol $c_{m,n}$ are transmitted separately with a time offset equal to $\frac{T_0}{2}$, while requiring that two adjacent symbols in time and frequency have a phase difference equal to $\frac{\pi}{2}$. Table 5.1 details the transmission structure.

	$nT_0 - \frac{T_0}{2}$	nT_0	$nT_0 + \frac{T_0}{2}$
$(2m+1)F_0$	$c^{\Re}_{2m+1,n-1}$	$jc^{\Im}_{2m+1,n}$	$c^{\Re}_{2m+1,n+1}$
$2mF_0$	$jc^{\Im}_{2m,n-1}$	$c^{\Re}_{2m,n}$	$jc^{\Im}_{2m,n+1}$
$(2m-1)F_0$	$c^{\Re}_{2m-1,n-1}$	$jc^{\Im}_{2m-1,n}$	$c^{\Re}_{2m-1,n+1}$

TABLE 5.1: Symbols transmission scheme of OFDM/OQAM modulation.

When OFDM/OQAM modulation is combined with FTN signaling, additional interferences are introduced to the transmitted signal. In the previous chapters, we showed that FTN-self interference depends on the time index of the transmitted symbols. Considering the FTN-OQAM transceiver depicted in Fig. 4.1, the received symbol at time index

n_0 and subcarrier index m_0 as derived in (4.1) is:

$$y_{m_0,n_0} = a_{m_0,n_0} + \underbrace{\sum_{\substack{q=-l \\ q\neq 0}}^{l} h_q a_{m_0,n_0+q}}_{ISI} + \underbrace{\sum_{\substack{p=-l' \\ p\neq 0}}^{l'} \sum_{q=-l}^{l} l_{p,q,n_0} a_{m_0+p,n_0+q}}_{ICI_{n_0}}, \tag{5.4}$$

where: $a_{m,n}$ are the transmitted OQAM symbols, the pair (l, l') defines the interval of symbols contributing to ISI and ICI, respectively, and

$$h_q = L\cos(\frac{\pi}{2}q)A_g[-qN_f, 0], \tag{5.5}$$

and

$$l_{p,q,n_0} = L\cos(\pi(\frac{p+q}{2} + \frac{2p(n_0N_f - \frac{D}{2})}{M}))A_g[-qN_f, -pb] \tag{5.6}$$

are the equivalent channels of ISI and ICI, respectively (4.2), (4.3). L is the length of the pulse shape g and A_g is its discrete ambiguity function. $D = L - 1$, M the number of subcarriers and N_f is the FTN decimation/expansion factor. In chapter 3, we formulated the interference power and showed that it is time dependent and periodic. Its period N_0 is expressed as (3.33):

$$N_0(p, N_f) = \begin{cases} 1, & \text{if} \quad p = 0 \\ \frac{M}{2pN_f}, & \text{if} \quad p \neq 0 \quad \text{and} \quad \text{mod}(M, 2pN_f) = 0 \\ \frac{M}{\text{gcd}(M,2pN_f)} & \text{if} \quad p \neq 0 \quad \text{and} \quad \text{mod}(M, 2pN_f) \neq 0, \end{cases} \tag{5.7}$$

where p is the subcarrier index. Independently of p, we define the global period as:

$$N_0^G = N_0(1, N_f) \tag{5.8}$$

In Fig. 4.1, the transmitter employs a RSC channel encoder and randomly interleaves the encoded bits. These bits are then converted to OQAM symbols and then mapped to time-frequency positions, see Table 5.1. Hence, the systematic and parity bits of the same codeword could be both converted to symbols mapped to positions that are highly impacted by interference. To overcome this issue, we propose to first interleave separately the systematic and parity bits. The interleaved bits are then converted to OQAM symbols. Finally, we map symbols made up of systematic bits to positions that are least affected by interference, and symbols made up of parity bits to the remaining positions. In the following, we present a new symbol to time-frequency positions mapping for the precoded and non-precoded FTN-OQAM transceiver.

5.4.1 Precoded FTN-OQAM transceiver

We consider the precoded FTN-OQAM transceiver, depicted in Fig. 4.1, and modify the blocks Π and *bit-to-symbol mapping* as illustrated in Fig. 5.24. We keep the same $(1, \frac{5}{7})$ RSC encoder with coding rate $r = \frac{1}{2}$. The *Channel coding* block delivers $N_c = N_{c1} + N_{c2}$

coded bits, with N_{c1} and N_{c2} the number of bits composing the precoded and non-precoded symbols, respectively. We denote by S_1 and S_2 the sets of systematic bits of the N_{c1} and N_{c2} coded bits, respectively. Similarly, sets P_1 and P_2 contain the parity bits of the N_{c1} and N_{c2} bits, respectively. First, as interference is known at the transmitter side, we compute its power at the precoded symbols positions. These positions are then sorted in ascending order of their interference power and divided into two sets I_1 and I_2 of equal length. The set I_1 contains the first half of these positions, while the set I_2 contains the other half. Note that positions in I_1 are less impacted by interference than positions in I_2. Finally, the S_1 bits are interleaved and converted to OQAM symbols and then successively mapped to positions of I_1. Similarly, symbols obtained from the interleaved bits in P_1 are mapped to positions in I_2. On the other hand, we compute the interference power of the non-precoded symbols positions. These positions are sorted in an ascending order and divided into two sets J_1 and J_2 of equal length. Similarly, the symbols obtained from interleaved systematic bits in S_2 are mapped to positions in J_1, while the symbols obtained from interleaved bits in P_2 are mapped to positions in J_2. Finally, the SIPC module cancels interference from symbols localized at positions in I_1 and I_2.

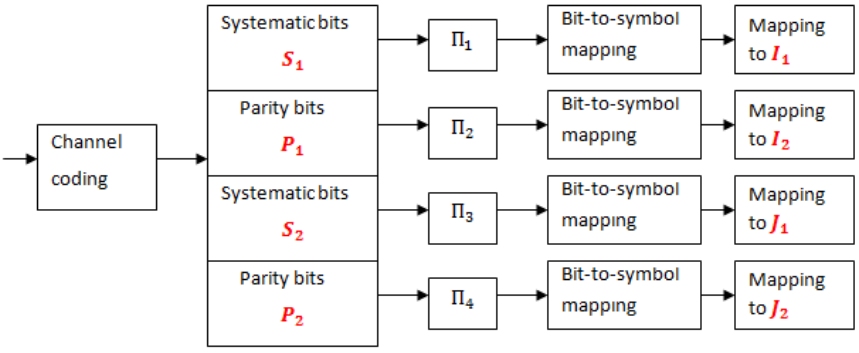

FIGURE 5.24: The proposed symbols to time-frequency positions mapping in case of the precoded FTN-OQAM transceiver.

5.4.1.1 SIPC-t precoding

In this paragraph, we detail the enhanced symbols mapping in case of the FTN-OQAM transceiver combined with the SIPC-t precoding method. The precoded symbols are expressed as (4.27):

$$c_{m,n} = a_{m,n} - \alpha\{\sum_{\substack{q=-k \\ q\neq 0}}^{k} h_q a_{m,n+q}\}. \tag{5.9}$$

Each subcarrier is composed of N_s symbols, with N_s being a multiple of the period N_0^G:

$$N_s = dN_0^G,\ d \in \mathbb{N}. \tag{5.10}$$

We consider a subcarrier of index m and calculate the interference power at the first N_0^G time instants. These N_0^G positions are then sorted in ascending order of their interference power. Let I be the set of (m,n) frequency and time indices of the precoded symbols,

we have:

$$I = \{(m,n) :\ n = a \bmod(k+2) \quad and \quad n = a+1 \bmod(k+2),\ \ a \in \mathbb{N},\ a \leq k+1\}, \tag{5.11}$$

with $0 \leq n \leq N_0^G - 1$,$0 \leq m \leq M-1$, and:

$$I^G = \{(m,n) :\ n = n' + bN_0^G\ (m,n') \in I,\ b \in \mathbb{N},\ 1 \leq b \leq d-1\} \tag{5.12}$$

the set of sorted indices of all the precoded symbols. As the considered coding rate is $r = \frac{1}{2}$, the systematic and parity block of bits are of equal lengths. First, the S_1 interleaved systematic bits are converted to OQAM symbols. These symbols are then mapped to time-frequency positions in the set I_1 defined by:

$$I_1 = \{(m,n) \in I^G,\ 0 \leq n \leq \frac{N_0^G}{2} - 1\}. \tag{5.13}$$

Similarly, the P_1 interleaved parity bits are first converted to OQAM symbols and then mapped to time-frequency positions in the set I_2 defined by:

$$I_2 = \{(m,n) \in I^G,\ \frac{N_0^G}{2} \leq n \leq N_0^G - 1\}. \tag{5.14}$$

We proceed similarly for the non-precoded symbols. let J be the set of sorted indices (m,n) of the non-precoded symbols with:

$$0 \leq m \leq M-1, \quad \text{and} \quad 0 \leq n \leq N_0^G - 1,$$

and

$$J^G = \{(m,n) :\ n = n' + bN_0^G\ (m,n') \in J,\ b \in \mathbb{N},\ 1 \leq b \leq d-1\} \tag{5.15}$$

the sorted indices of all the non-precoded symbols. The S_2 interleaved systematic bits are first converted to OQAM symbols and then mapped (m,n) positions in the set J_1 defined as:

$$J_1 = \{(m,n) \in J^G,\ 0 \leq n \leq \frac{N_0^G}{2} - 1\}. \tag{5.16}$$

The P_2 interleaved parity bits are converted to OQAM symbols and then mapped to time-frequency positions in the set J_2 defined by:

$$J_2 = \{(m,n) \in J^G,\ \frac{N_0^G}{2} \leq n \leq N_0^G - 1\}. \tag{5.17}$$

Finally, the SIPC module removes ISI from the precoded symbols according to (5.9).

5.4.1.2 SIPC-f precoding

In this paragraph, we consider the FTN-OQAM transceiver combined with SIPC-f precoding, where precoded symbols are obtained as (4.41):

$$c_{m,n} = a_{m,n} - \beta\{\sum_{\substack{p=-k' \\ p\neq 0}}^{k'} \sum_{q=-l}^{l} l_{p,q,n} a_{m+p,n+q}\}. \tag{5.18}$$

As mentioned earlier, FTN-self interference is independent of the subcarrier index. At a subcarrier m, the first N_0^G time indices are sorted in ascending order of their interference power. Let I^G be the set of sorted time-frequency indices of all the precoded symbols defined as:

$$I^G = \{(m,n) :\ n = n' + bN_0^G,\ (m,n') \in I,\ b \in \mathbb{N},\ 1 \leq b \leq d-1\}, \tag{5.19}$$

with I being:

$$I = \{(m,n) : (m = a \bmod (k'+1), 0 \leq m \leq M-1, 0 \leq n \leq N_0^G - 1),\ a \in \mathbb{N},\ a \leq k'\}. \tag{5.20}$$

We define sets I_1 and I_2 as in (5.13) and (5.14), respectively. First, the S_1 interleaved systematic bits are converted to OQAM symbols. These symbols are then mapped to time-frequency positions in I_1. Similarly, the P_1 interleaved parity bits are first converted to OQAM symbols and then mapped to positions in I_2.

We denote by J the set of non-precoded symbols frequency and time indices (m,n) such as: $0 \leq n \leq N_0^G - 1$ and $0 \leq m \leq M-1$. The time-frequency positions of all the non-precoded symbols are in J^G defined as:

$$J^G = \{(m,n) :\ n = n' + bN_0^G,\ (m,n') \in J,\ b \in \mathbb{N},\ 1 \leq b \leq d-1\}. \tag{5.21}$$

Firstly, the S_2 interleaved systematic bits are converted to OQAM symbols and then mapped to positions in J_1. Secondly, the P_2 interleaved parity bits are converted to OQAM symbols and then mapped to positions in J_2. Finally, the precoding operation is carried out by the SIPC module according to (5.18).

5.4.2 Non-precoded FTN-OQAM transceiver

The proposed symbols mapping in case of the FTN-OQAM transceiver is depicted in Fig. 5.25. In this scenario, the interference power at time indices $0 \leq n \leq N_0^G - 1$ of a subcarrier m are computed. These positions are then sorted in ascending order of interference power. We define J as:

$$J = \{(m,n) :\ 0 \leq m \leq M-1,\ 0 \leq n \leq N_0^G - 1\} \tag{5.22}$$

and

$$J^G = \{(m,n) :\ n = n' + bN_0^G,\ (m,n') \in J,\ b \in \mathbb{N},\ 1 \leq b \leq d-1\}. \tag{5.23}$$

The channel encoder delivers S systematic bits and P parity bits which are interleaved separately. Then, the S interleaved bits are converted to OQAM symbols and mapped to time-frequency positions in the set J_1 defined by:

$$J_1 = \{(m,n) \in J^G,\ 0 \leq n \leq \frac{N_0^G}{2} - 1\}. \tag{5.24}$$

Similarly, the P interleaved parity bits are first converted to OQAM symbols and then mapped to time-frequency positions in the set J_2 defined by:

$$J_2 = \{(m,n) \in J^G,\ \frac{N_0^G}{2} \leq n \leq N_0^G - 1\}. \tag{5.25}$$

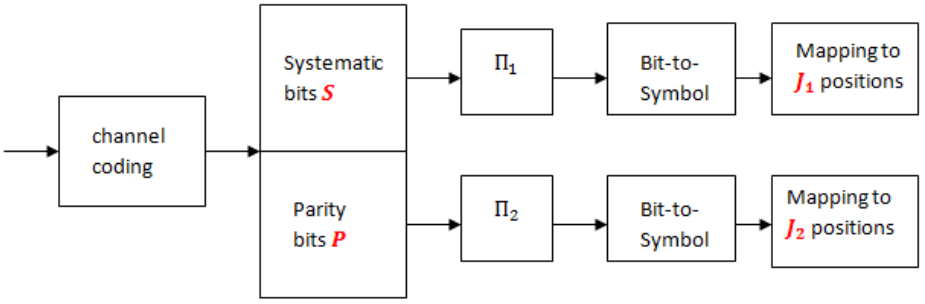

FIGURE 5.25: The proposed symbols to time-frequency positions mapping for the FTN-OQAM transceiver.

For both the precoded and non-precoded FTN-OQAM transceivers, some modifications should be taken into account at the receiver side. We keep the same turbo-based receiver, where soft LLRs are exchanged between the equalizer and the decoder. After SISO demapping, the soft LLRs corresponding to systematic and parity bits are de-interleaved individually. After the decoding step, the new LLRs of the systematic and parity bits are interleaved separately and then converted to soft symbols by the *SISO mapping* module. These symbols are then mapped to the defined positions before the equalization step.

5.4.3 Simulation results

Fig. 5.26 shows the interference power $P_I(n_0)$ of positions $n_0 \in [1 : N_0^G]$ using IOTA ($L = 4M$) filtering and FTN packing factors τ ranging from 0.6 to 0.9. As expected, the interference power depends on n_0. These positions are sorted in ascending order of their interference power as given in Table 5.2. Results in case of the precoded and non-precoded FTN-OQAM transceiver are provided in the next section. We keep the same transceiver configuration: $M = 64$, $(1, \frac{5}{7})$ RSC encoder with coding rate $r = \frac{1}{2}$, the MMSE filter length is 30 and the delay is 15. The decoder is based on the Max-Log-MAP algorithm.

5.4.3.1 SIPC-t precoding

In this section, we provide simulation results of the enhanced symbols mapping in case of the FTN-OQAM transceiver combined with SIPC-t precoding. The precoding factor k is kept unchanged, i.e., $k = 2$.

Our simulation results showed that both symbols mapping strategies, meaning the conventional OFDM/OQAM mapping and our symbols mapping, provide similar results in

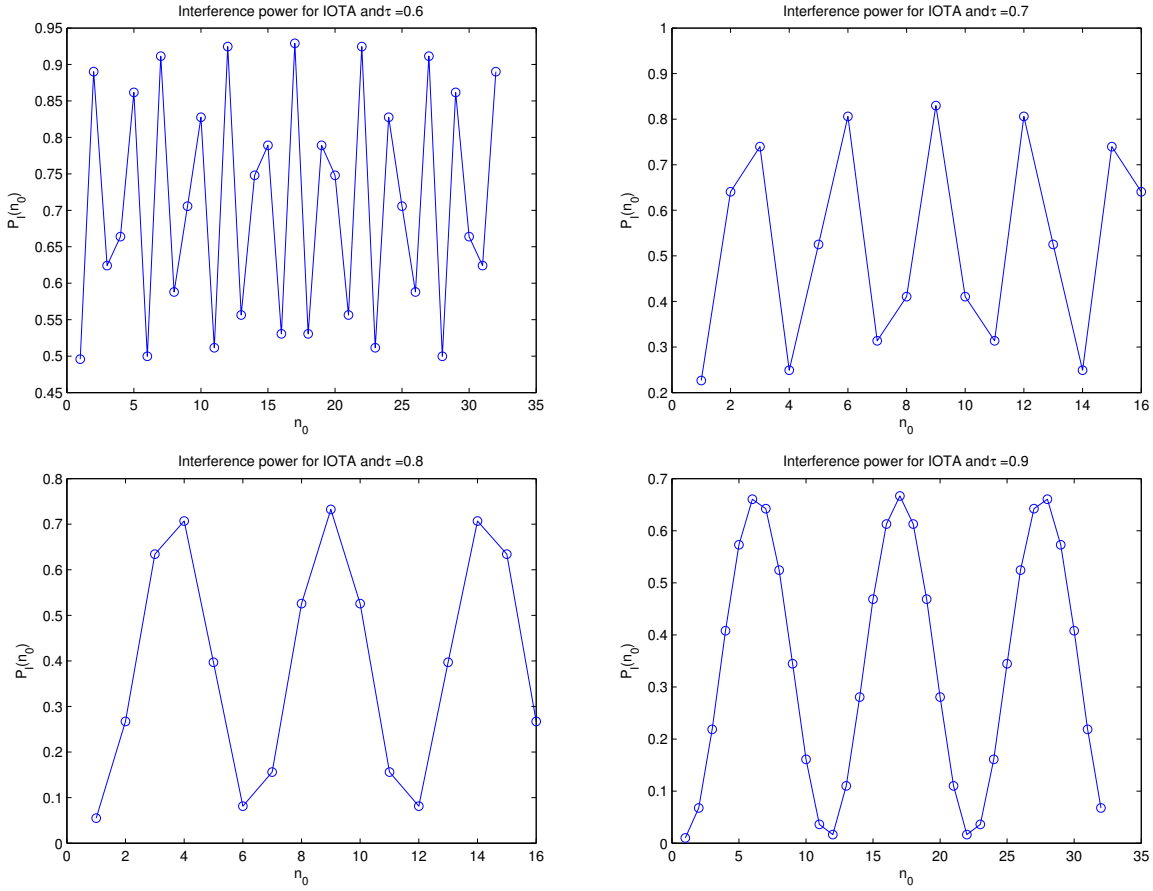

FIGURE 5.26: Interference power as a function of the time index position n_0.

τ	sorted positions n_0
0.6	$\{n_1,n_6,n_{28},n_{23},n_{11},n_{18},n_{16},n_{13},n_{21},n_{26},n_8,n_3,n_{31},n_4,n_{30},n_{25}$ $,n_9,n_{20},n_{14},n_{19},n_{15},n_{10},n_{24},n_5,n_{29},n_2,n_{32},n_7,n_{27},n_{22},n_{11},n_{17}\}$
0.7	$\{n_1,n_4,n_{14},n_7,n_{11},n_{10},n_8,n_{13},n_5,n_{16},n_2,n_3,n_{15},n_6,n_{12},n_9\}$
0.8	$\{n_1,n_6,n_{12},n_{11},n_7,n_{16},n_2,n_5,n_{13},n_{10},n_8,n_{15},n_3,n_4,n_{14},n_9\}$
0.9	$\{n_1,n_{22},n_{12},n_{11},n_{23},n_{32},n_2,n_{21},n_{13},n_{10},n_{24},n_{31},n_3,n_{20},n_{14},n_9$ $,n_{25},n_{30},n_4,n_{19},n_{15},n_8,n_{26},n_{29},n_5,n_{18},n_{16},n_7,n_{27},n_{28},n_6,n_{17}\}$

TABLE 5.2: Sorted time indices n_0 in ascending order of their interference power.

case of QPSK modulation and FTN packing factors τ ranging from 0.6 to 0.9. In what follows, we evaluate the simulation results only in case of 16 and 64-QAM modulations.

Fig. 5.27 shows the BER results in case of 16-QAM modulation, IOTA filtering and τ varying from 0.7 to 0.9. When $\tau = 0.7$, we notice that our proposed symbols mapping improves the BER results, especially at low SNRs. In fact, the BER of the receiver after performing 7 iterations, presented by the red curve with asterisks, is improved and approaches the BER curve of the 9^{th} iteration at SNR=13 dB. As for iteration 9, we observe that the BER curve is better for low SNRs. For $\tau = 0.8$, results show that the new symbols mapping provides better BER results at iteration 3. However, both systems converge to the same BER curve at iteration 5. The same behavior is observed

for $\tau = 0.9$: both symbols mapping techniques provide identical BER results at iteration 4, although the BER at the second iteration is better when the new symbols mapping is employed.

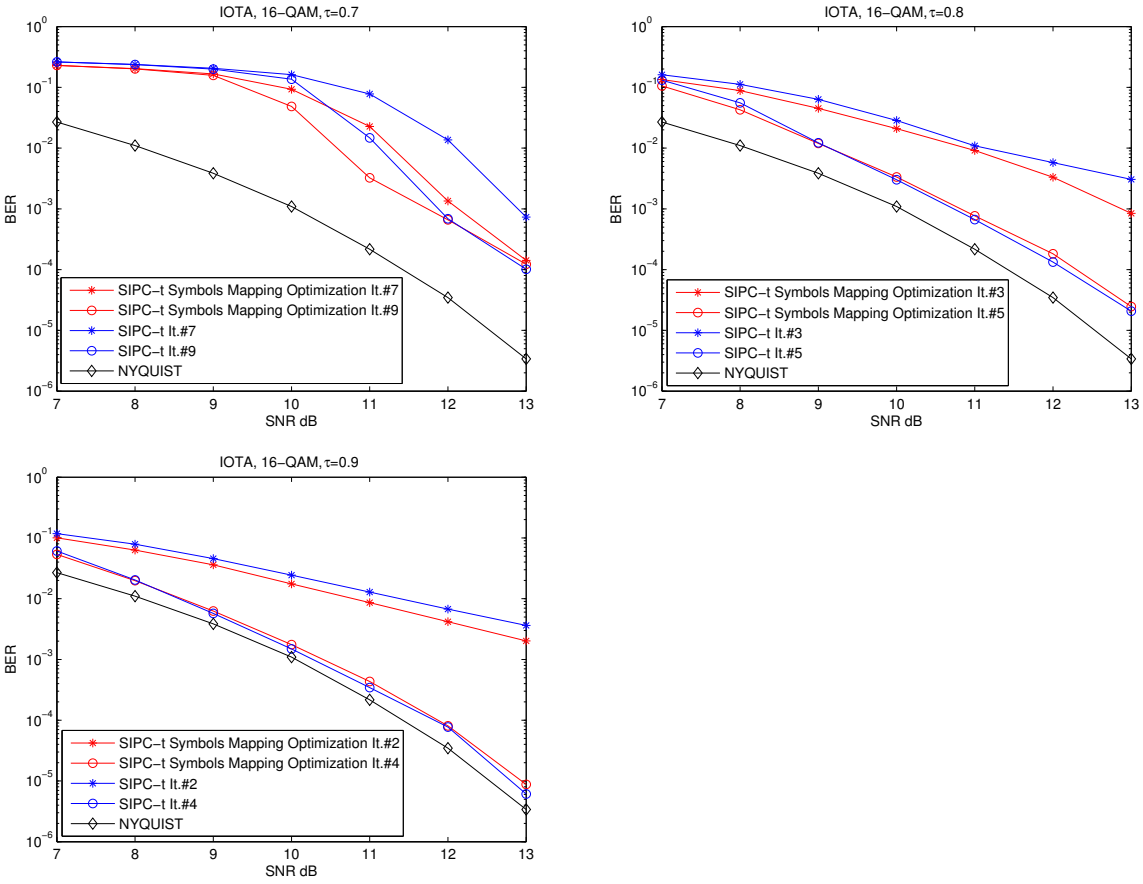

FIGURE 5.27: BER evaluation of the FTN-OQAM transceiver using the proposed symbols mapping and SIPC-t precoding in case of 16-QAM modulation and IOTA filtering.

Similarly, we compare in Fig. 5.28 the BER results of both symbols mapping methods when 64-QAM is envisaged. For $\tau = 0.8$, our proposed method provides significant improvement compared to the classical OFDM/OQAM mapping. Indeed, the BER of the different iterations is enhanced and the receiver converges after performing 9 iterations. With $\tau = 0.9$, we observe the same behavior as in the 16-QAM case: both symbols mapping enable the receiver to converge to nearly identical BER results after performing 7 iterations. Moreover, thanks to the proposed symbols mapping, the BER curves at the previous iterations are improved: we obtain 1 dB gain at a BER around 10^{-3} after performing 5 iterations at the receiver side. We obtained similar results for the FS and PHYDYAS filters, recommended for SIPC-t precoding with $\tau = 0.7$, as shown in Fig. 5.29.

In the light of these results, we conclude that the proposed symbols mapping is recommended in case of high modulation orders and low FTN packing factors which correspond

to the scenario where FTN-induced interferences are more severe. In fact, the new symbols mapping gives better results for 16-QAM and with $\tau = 0.7$ and 64-QAM with $\tau = 0.8$.

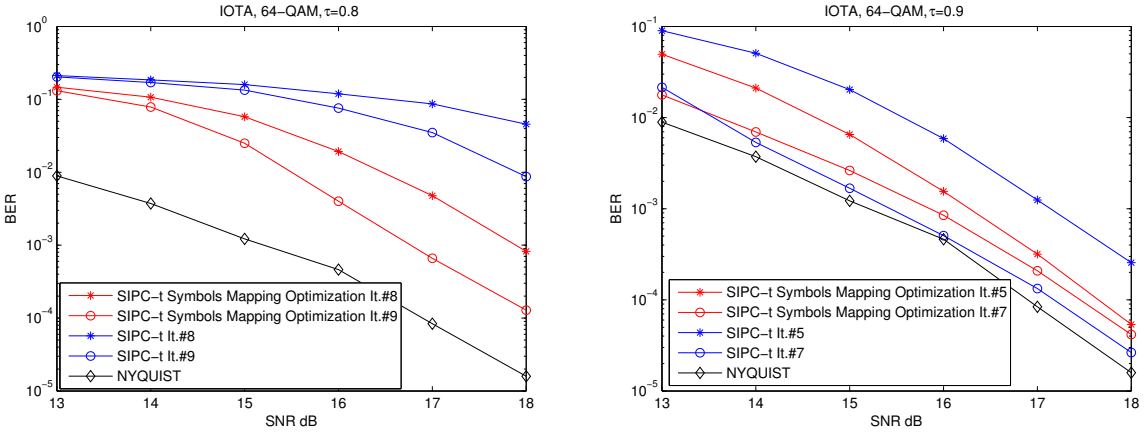

FIGURE 5.28: BER evaluation of the FTN-OQAM transceiver using the proposed symbols mapping and SIPC-t precoding in case of 64-QAM modulation and IOTA filtering.

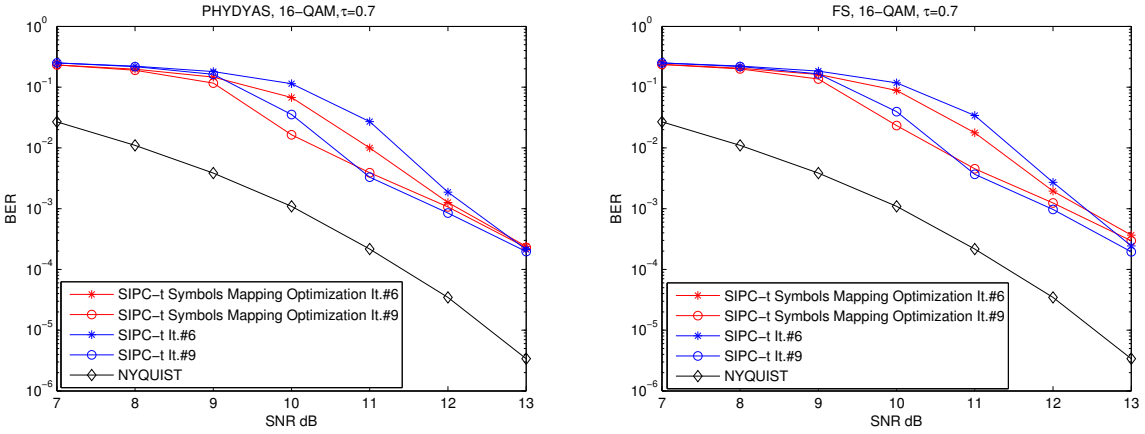

FIGURE 5.29: BER evaluation of the FTN-OQAM transceiver using the proposed symbols mapping and SIPC-t precoding in case of 16-QAM modulation for $\tau = 0.7$ and the PHYDYAS and FS pulse shapes.

5.4.3.2 SIPC-f precoding

In what follows, we evaluate the proposed symbols mapping in case of the FTN-OQAM transceiver combined with SIPC-f precoding. We keep the same simulation configurations and set $k' = 1$. Considering 16-QAM modulation with $\tau = 0.7$, the recommended pulse shapes are: IOTA, TFL, PHYDYAS and FS filters, see Table 4.12. Fig. 5.30 shows a BER comparison of both symbols mapping techniques. We observe that the proposed symbols mapping provides slightly better results when TFL filtering is used. For the remaining pulse shapes, both symbols mapping strategies lead to similar results. Moreover, we obtain similar BER results using both symbols mapping when the packing

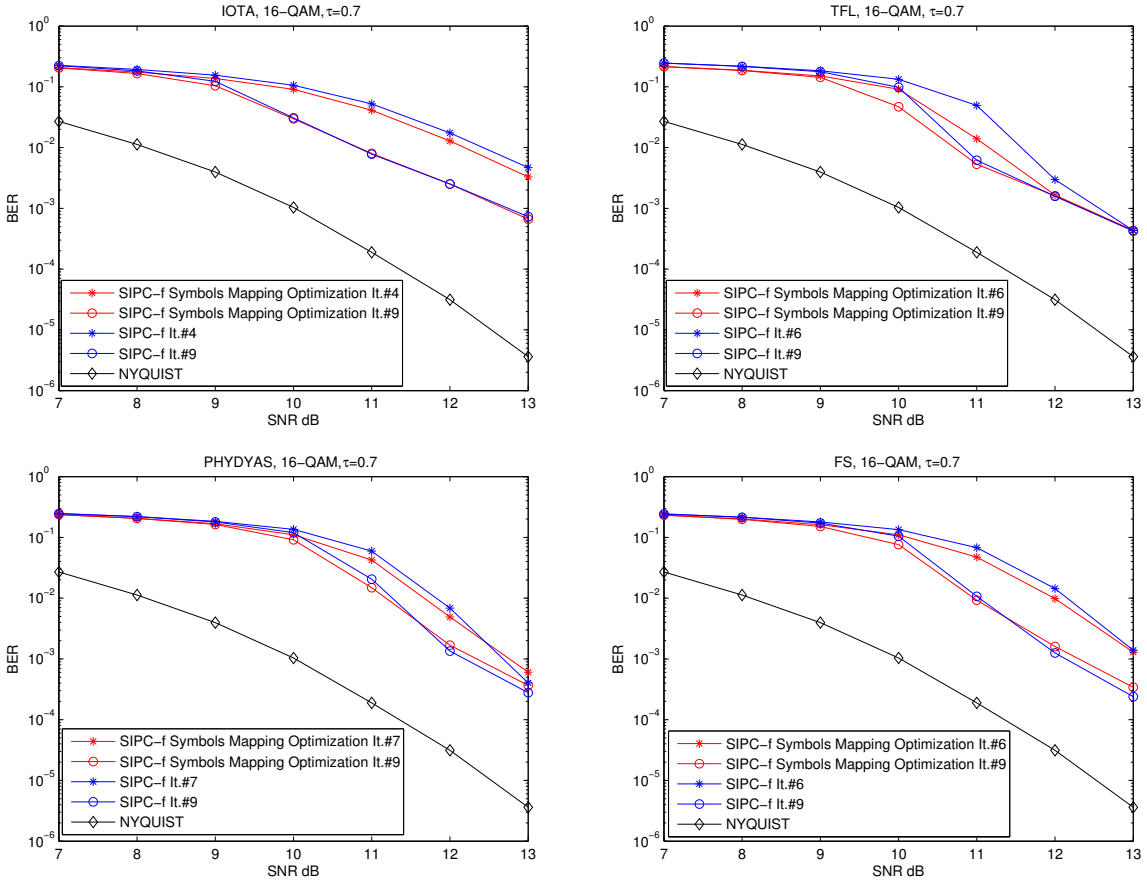

FIGURE 5.30: BER evaluation of the FTN-OQAM transceiver using the proposed symbols mapping and SIPC-f precoding in case of 16-QAM modulation for $\tau = 0.7$ and the IOTA, TFL, PHYDYAS and FS pulse shapes.

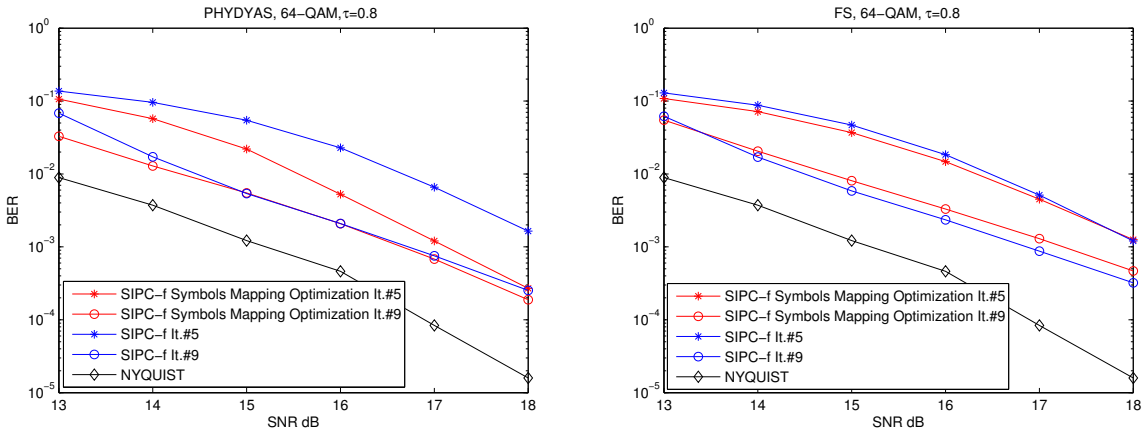

FIGURE 5.31: BER evaluation of the FTN-OQAM transceiver using the proposed symbols mapping and SIPC-f precoding in case of 64-QAM modulation for $\tau = 0.8$ and the PHYDYAS and FS pulse shapes.

factor τ is equal to 0.8 or 0.9.

Considering 64-QAM modulation and $\tau = 0.8$, the recommended pulse shapes are FS and PHYDYAS filters. Fig. 5.31 shows that the proposed symbols mapping lead to better results when the PHYDYAS filtering is considered. In fact, it enhances the receiver BER results at all the performed iterations. At high SNR of 18 dB, the receiver converges after performing only 5 iterations.

We conclude that the BER improvement is more important in case of SIPC-t than SIPC-f precoding. The proposed symbols mapping improves the BER performance for the SIPC-f precoding when high modulation orders and low FTN packing factors are considered: τ=0.7 and τ=0.8 for 16 and 64-QAM modulation, respectively. However the BER gain is only observed for certain pulse shapes: the TFL and PHYDYAS filters for 16 and 64-QAM modulation, respectively.

5.4.3.3 Non-precoded FTN-OQAM transceiver

In this section, we compare the BER results of the non-precoded FTN-OQAM transceiver using the classical OFDM/OQAM symbols mapping and our proposed method. As for the precoded FTN-OQAM transceiver scenario, BER results in case of QPSK modulation are identical. Hence, we focus on high order modulation orders and give in Fig. 5.32 the BER comparison in case of 16-QAM modulation, IOTA filtering and τ varying from 0.7 to 0.9. As we can see, the proposed symbols mapping improves the BER results for all the considered packing factors. In fact, for $\tau = 0.7$ the BER results after performing 9 iterations at the receiver side is enhanced, although both systems do not converge to the classical Nyquist based systems. When $\tau = 0.8$, the receiver performance using the symbols mapping is improved at all the performed iterations. The receiver converges after performing 5 iterations and a 1 dB gain is obtained at BER around 10^{-3}. In a similar way, our proposed symbols mapping improves the receiver performance in case of $\tau = 0.9$. Indeed, the receiver converges after performing 4 iterations instead of 5. Moreover, 1 dB gain is obtained at a BER around 10^{-4}. We obtain similar results for the FS, PHYDYAS and SRRC (ρ=0.5) filters which are recommended for 16-QAM modulation. The proposed symbols mapping improves the receiver BER results at all the performed iterations when $\tau = 0.7$. As τ increases, the receiver converges to identical results using both symbols mapping. However, the BER results at the first performed iterations are better when using the proposed symbols mapping.

Fig. 5.33 evaluates the BER performance considering 64-QAM modulation and τ varying from 0.8 to 0.9. We used FS filtering since the receiver does not converge using the IOTA filter. We observe that the proposed symbols mapping enables significant improvement when $\tau = 0.8$: the FTN-OQAM transceiver using the classical OFDM/OQAM symbols mapping does not converge even after performing 9 iterations at the receiver side. Using the new symbols mapping, the receiver converges after performing 8 iterations. Moreover, the gap between the FTN and the Nyquist curves is reduced to 1.5 dB at a BER around 10^{-3}. Finally, we can observe that both systems have nearly similar BER results when $\tau = 0.9$. The proposed symbols mapping leads to similar results in case of PHYDYAS and SRRC (ρ=0.5) filters. The FTN-OQAM transceiver performance is considerably

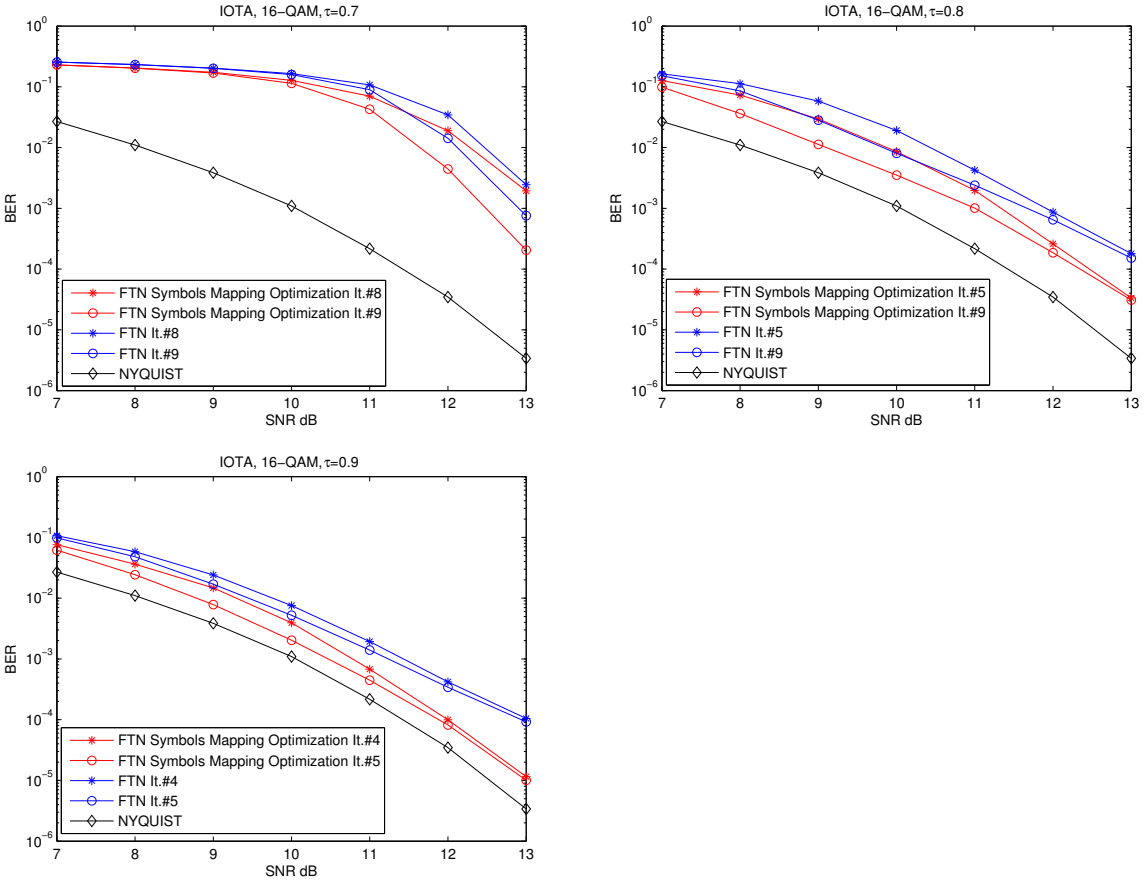

FIGURE 5.32: BER evaluation of the FTN-OQAM transceiver using the proposed symbols mapping, 16-QAM modulation and IOTA filtering.

improved when $\tau = 0.8$: the receiver converges after performing 8 iterations instead of 9.

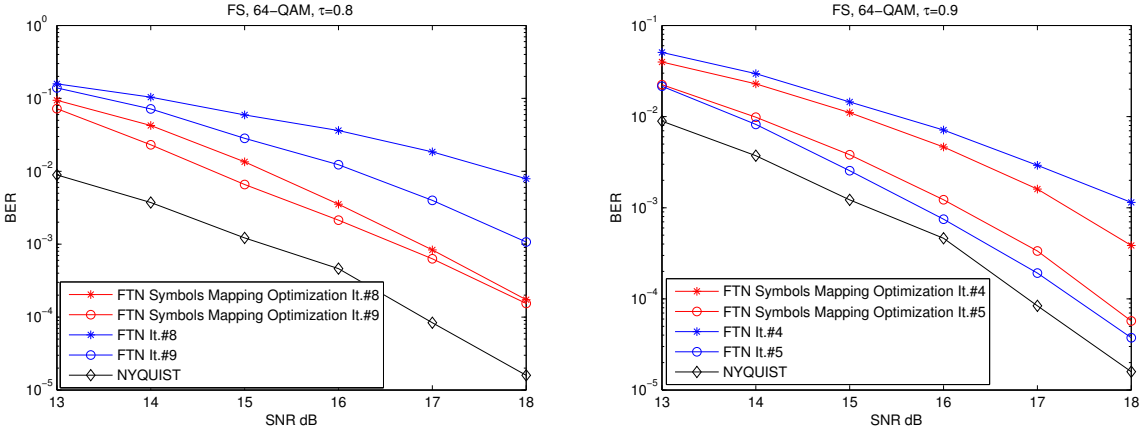

FIGURE 5.33: BER evaluation of the FTN-OQAM transceiver using SIPC-t precoding and PHYDYAS filtering.

The simulation results show that is recommended to employ the enhanced symbols mapping in case of 16-QAM modulation with $\tau = 0.7$, as well as in case of 64-QAM modulation with $\tau = 0.8$.

5.5 Bits mapping Vs. Symbols mapping

The BER evaluation of the proposed bits mapping and symbols mapping shows that the results depend on the FTN packing factor τ. In this paragraph, we report the recommended technique for each FTN-OQAM transceiver. Table 5.3 summarizes the recommended modifications for the FTN-OQAM transceiver, as well as the number of necessary iterations for the receiver convergence. As mentioned earlier, the proposed symbols mapping enhances the transceiver performance for low τ values, while the proposed bits mapping leads to better results in case of high τ values.

Modulation order	τ	Pulse shapes	Recommended mapping	# of iterations
16-QAM	0.7	FS	Symbols mapping	9
		PHYDYAS	Symbols mapping	9
		SRRC (ρ=0.5)	Symbols mapping	9
	0.8	FS	Bits mapping	6
		PHYDYAS	Bits mapping	6
		SRRC (ρ=0.5)	Bits mapping	6
	0.9	FS	Bits mapping	5
		PHYDYAS	Bits mapping	5
		SRRC (ρ=0.5)	Bits mapping	4
64-QAM	0.8	FS	Symbols mapping	9
		PHYDYAS	Symbols mapping	9
		SRRC (ρ=0.5)	Symbols mapping	9
	0.9	FS	Bits mapping	8
		PHYDYAS	Bits mapping	8
		SRRC (ρ=0.5)	Bits mapping	7

TABLE 5.3: Recommended mapping strategy for the FTN-OQAM transceiver.

We reach the same conclusions in case of the combination of SIPC-t precoding with the FTN-OQAM transceiver, see Table 5.4. The proposed symbols mapping is recommended for low τ values, while the enhanced bits mapping is recommended in case of high τ values. Finally, simulation results showed that the proposed symbols mapping and bits mapping provide identical BER performance in case of 16-QAM modulation with $\tau = 0.7$ and the SIPC-f precoder. For this precoder, the enhanced bits mapping is recommended, see Table 5.5. By comparing the three tables, we notice that the number of iterations at the receiver side is decreased when the precoding is employed, which is in accordance with the previous chapter.

Modulation order	τ	Pulse shapes	Recommended mapping	# of iterations
16-QAM	0.7	PHYDYAS	Symbols mapping	8
	0.8	PHYDYAS	Bits mapping	6
	0.9	SRRC (ρ=0.5)	Bits mapping	3
64-QAM	0.8	PHYDYAS	Symbols mapping	8
	0.9	PHYDYAS	Bits mapping	7
		SRRC (ρ=0.5)	Bits mapping	5

TABLE 5.4: Recommended mapping strategy for the FTN-OQAM transceiver combined with SIPC-t precoding.

Modulation order	τ	Pulse shapes	Recommended mapping	# of iterations
16-QAM	0.7	PHYDYAS	Symbols or Bits mapping	9
	0.8	PHYDYAS	Bits mapping	5
	0.9	PHYDYAS	Bits mapping	3
64-QAM	0.8	PHYDYAS	Bits mapping	9
	0.9	PHYDYAS	Bits mapping	5

TABLE 5.5: Recommended mapping strategy for the FTN-OQAM transceiver combined with SIPC-f precoding.

5.6 Joint enhancement of channel coding and Gray mapping

In this section, we propose to combine the channel encoder presented in Section 5.2 with the enhanced Gray mapping method. The channel encoding is performed as illustrated by Fig. 5.3. However, the encoded bits at both puncturing blocks outputs are separated into systematic and parity bits. These bits are then interleaved individually and reordered such as the systematic bits occupy the highly protected positions of the Gray mapping as detailed in Section 5.3. The puncturing blocks ensure different local coding rates r_1 and r_2 while keeping the same overall coding rate unchanged. When $r_1 \leq r_2$, more parity bits are removed from the B'_2 coded bits than from the B'_1 bits, and vice-versa. Thus, the information bits at the $Punct_2$ block output are not equally protected by the channel encoder. As the 64-QAM modulation provides three bits protection levels, we propose to place the systematic bits that are less protected, by the coding, at positions b_0 and b_3 having the highest protection level. After the bit scheduling and conversion to OQAM symbols, the B_1 symbols are precoded according to the selected SIPC precoder. At the receiver side, this bit scheduling should be taken into account when exchanging soft LLRs between the equalizer and the decoder. In addition, the LLRs of the systematic and parity bits are interleaved and de-interleaved individually.

5.7 Joint enhancement of channel coding and symbol mapping

In this section, we propose to jointly modify the channel coding and the symbols mapping as depicted in Fig. 5.34. As in Section 5.2, we use different local coding rates r_1 and r_2 to encode the N_{i1} and N_{i2} information bits. To this end, the B'_1 coded bits composing

the precoded symbols are punctured by the $Punct_1$ module, while the B'_2 coded bits composing the non-precoded symbols are punctured by the $Punct_2$. We consider an RSC encoder with coding rate r'. The effective coding rate is kept equal to $\frac{1}{2}$, meaning that the blocks of systematic and parity bits have equal lengths. Without any restriction, we suppose that $r_1 \leq \frac{1}{2} \leq r_2$. Both puncturing patterns performed by $Punct_1$ and $Punct_2$ modules remove parity bits to provide the desired coding rates. Hence, the encoded bits at the $Punct_1$ output have more parity than systematic bits. We separate these encoded bits into three sets: S_1 contains the systematic bits and P_1 the corresponding parity bits while P'_1 contains the additional parity bits (since $r_1 \leq \frac{1}{2}$). On the other hand, the coded bits at the $Punct_2$ output contain more systematic than parity bits, since $\frac{1}{2} \leq r_2$. These coded bits are separated into three sets: S_2 and P_2 contain the systematic bits and their corresponding parity bits. The set S'_2 contains the systematic bits whose all parity bits have been removed. Each of these six sets is then interleaved individually and then converted to OQAM symbols. These symbols are then mapped to time-frequency positions as presented in Section 5.4.

Let us consider the FTN-OQAM transceiver combined with SIPC-t precoding. The precoding parameter is kept $k = 2$, i.e, the precoded and non-precoded symbols have equal lengths. Therefore, sets S_1, P_1, S_2 and P_2 have equal lengths. Moreover, sets P'_1 and S'_2 have also equal lengths. The S_1 and P_1 bits are interleaved and converted to OQAM symbols of length l_1 and then mapped to positions in I_1 and I_2, respectively. Similarly, the P'_1 bits are interleaved and converted to OQAM symbols of length l_2 and then mapped to positions in I'_1. As mentioned in Section 4.4, the mapping positions are determined according to the interference power as follows:

$$I_1 = \{(m,n) \in I^G,\ 0 \leq n \leq l_1 - 1\}, \tag{5.26}$$

$$I_2 = \{(m,n) \in I^G,\ l_1 \leq n \leq 2l_1 - 1\}, \tag{5.27}$$

and

$$I'_1 = \{(m,n) \in I^G,\ 2l_1 \leq n \leq N_0^G - 1\}, \tag{5.28}$$

where I^G is given by (5.12).

Similarly, the S'_2 bits are interleaved and converted to OQAM symbols and then mapped to time-frequency positions in J'_1. The OQAM symbols made of the interleaved S_2 and P_2 bits are mapped to positions in J_1 and J_2, respectively. These sets represent sorted time-frequency indices according to their interference power and are defined as:

$$J'_1 = \{(m,n) \in J^G,\ 0 \leq n \leq l_2 - 1\}, \tag{5.29}$$

$$J_1 = \{(m,n) \in J^G,\ l_2 \leq n \leq l_2 + l_1 - 1\}, \tag{5.30}$$

and

$$J_2 = \{(m,n) \in J^G,\ l_1 + l_2 \leq n \leq N_0^G - 1\}, \tag{5.31}$$

where J^G is given by (5.15).

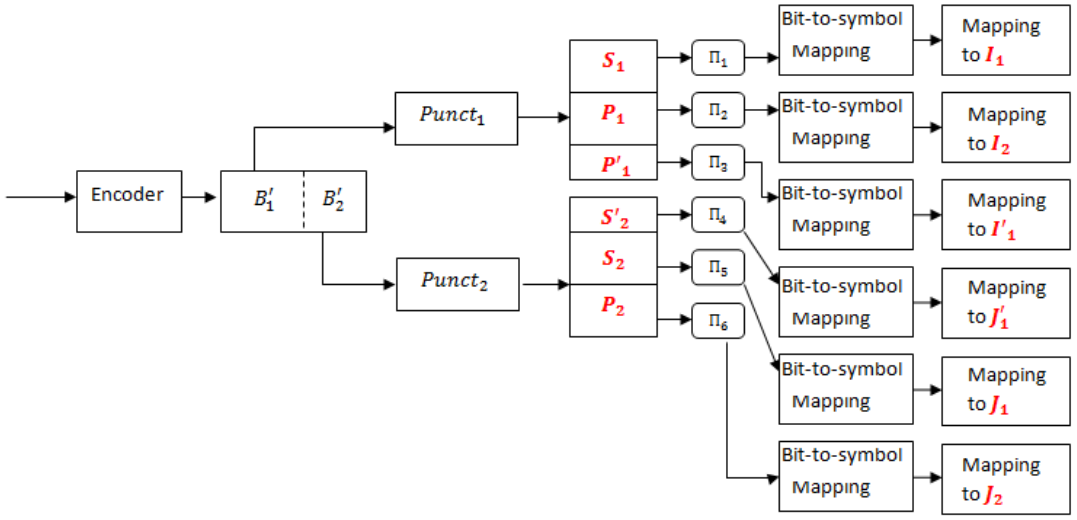

FIGURE 5.34: Joint enhancement of channel encoding and symbols mapping of the precoded FTN-OQAM transceiver.

In case of SIPC-f precoding, the sets of time-frequency indices are defined similarly by replacing I^G and J^G as in (5.19) and (5.21).

At the receiver side, the soft LLRs of systematic and parity bits computed by the *SISO Mapping* block should be de-interleaved individually before being fed to the decoder. On the other hand, the new computed LLRs of systematic and parity bits should also be interleaved separately. In addition, the *SISO Mapping* maps the soft estimated symbols to the determined time-frequency positions before the equalization step.

Simulation results

In this paragraph, we evaluate the BER performance of the FTN-OQAM transceiver combined with SIPC-t precoding and the proposed channel coding, bits mapping and symbols mapping modifications. To this end, we use the same RSC encoder of Section 4.2, with rate $\frac{1}{4}$, and random interleaving. The effective coding rate is $r = \frac{1}{2}$ and the receiver configuration is kept unchanged. We performed two puncturing patterns to have $r_1 = \frac{8}{17}$ and $r_2 = \frac{9}{17}$. The obtained BER curves when considering 16-QAM modulation and PHYDYAS filtering are given in Fig. 5.35. We used the same encoder to plot the Nyquist BER represented with the black curve with diamonds. The puncturing keeps the effective rate $r = \frac{1}{2}$ unchanged. When τ=0.7, we observe that the proposed symbols mapping provides better results at the first 7 iterations. As the number of performed iterations increases, the BER curve is slightly improved at low SNRs by the modified symbols mapping, and at high SNRs by the proposed bits mapping. As τ increases, the proposed methods provide similar results, although the BER curve is slightly better when using the modified bits mapping. In case of 64-QAM modulation, results are given in Fig. 5.36 for $\tau = 0.8$ and PHYDYAS filtering. As we can observe, both bits and symbols mapping enable a very important improvement of the BER. In fact, our results showed that the proposed symbols mapping provides better BER results at the

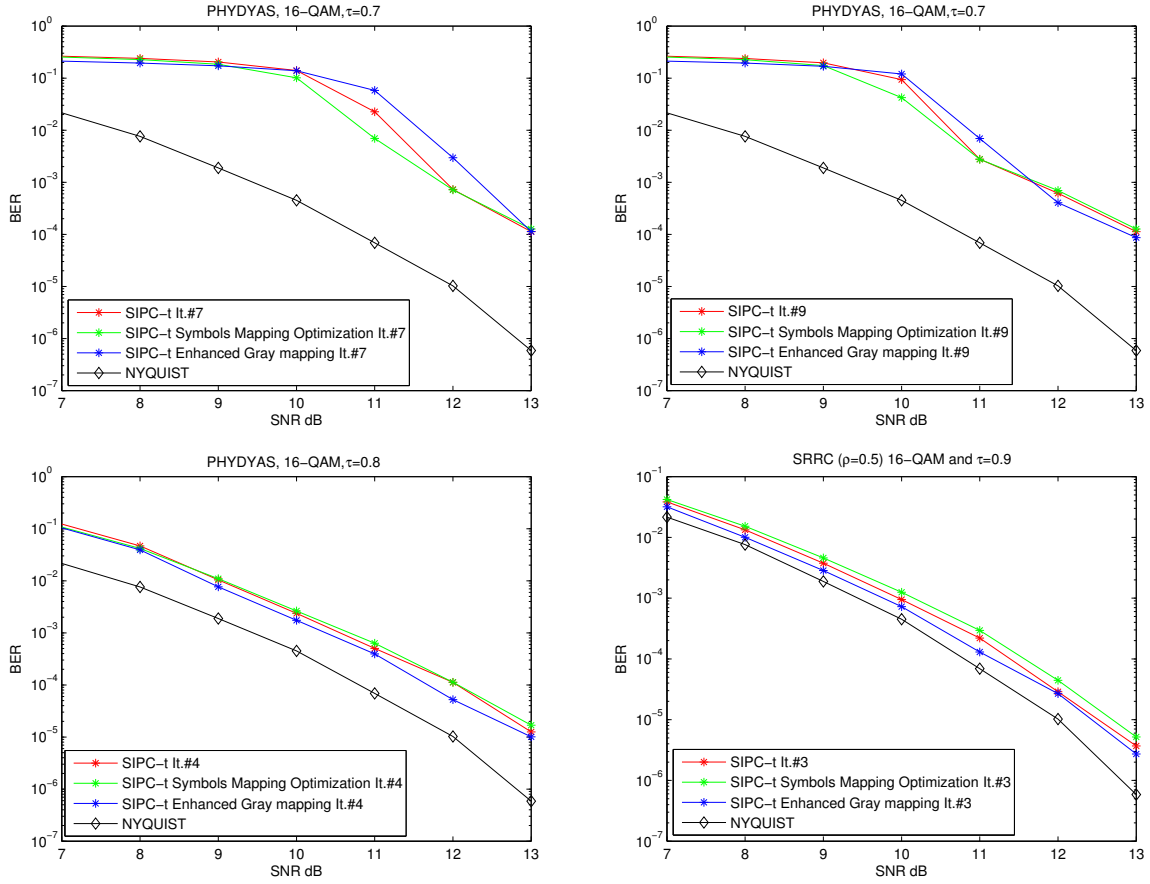

FIGURE 5.35: BER evaluation of the FTN-OQAM transceiver using SIPC-t precoding, PHYDYAS filtering and 16-QAM modulation.

first performed iterations. However, as the iterative process continues, the enhanced bits mapping enables the receiver to approach the Nyquist curve after performing 8 iterations at the receiver side with a gap of 1 dB at an error rate around 10^{-4}.

Fig. 5.37 illustrates the BER results for 64-QAM modulation when τ is set to 0.9 and the SRRC (ρ=0.5) pulse shape is used. We keep the same coding rates r_1 and r_2. In this scenario, the results show that it is recommended to combine the modified channel coding with the proposed bits mapping. Moreover, the achieved BER approaches very closely the Nyquist curve after performing only 4 iterations at the receiver side.

Based on these results, we can conjecture that the performance of the precoded FTN-OQAM transceiver is further improved when the proposed channel coding is combined with the modified bits mapping and symbols mapping. Considering low FTN packing factors, τ= 0.7 for 16-QAM and τ=0.8 for 64-QAM modulation, the proposed symbols mapping provides better BER results at the first performed iterations. As the iterative process goes on, more gain can be obtained using the enhanced bits mapping, especially for 64-QAM modulation. Moreover, the proposed bits mapping enables significant BER improvement as τ and the modulation order increase.

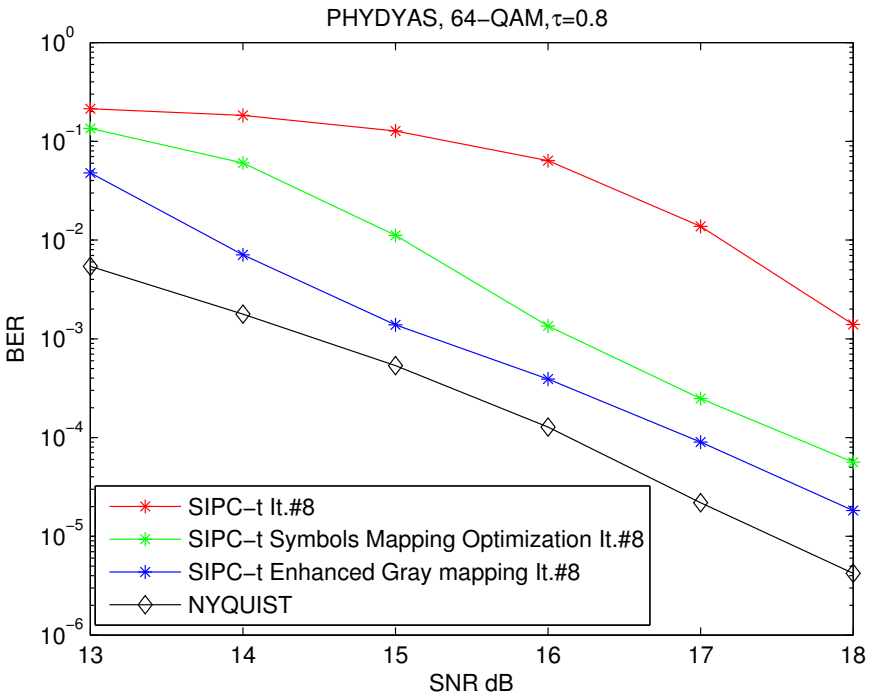

FIGURE 5.36: BER evaluation of the FTN-OQAM transceiver using SIPC-t precoding, PHYDYAS filtering, 64-QAM modulation and $\tau = 0.8$.

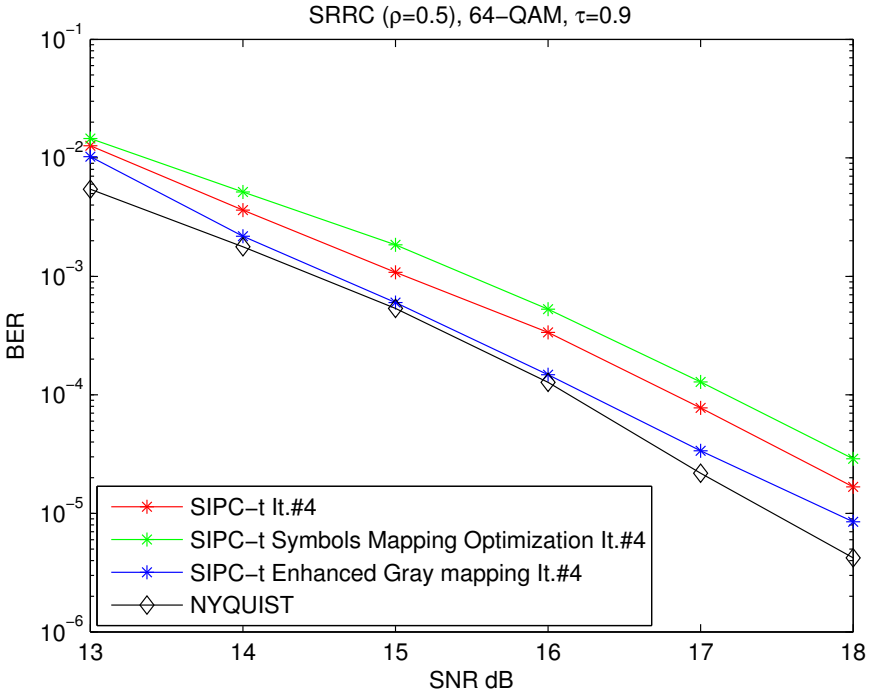

FIGURE 5.37: BER evaluation of the FTN-OQAM transceiver using SIPC-t precoding, SRRC (ρ=0.5) filtering, 64-QAM modulation and $\tau = 0.9$.

5.8 Conclusion

In this chapter, we aimed at enhancing the performance of the precoded and non-precoded FTN-OQAM transceiver. To this end, we introduced several modifications at the transmitter end. In case of the precoded FTN-OQAM transceiver, we proposed to further improve the precoding performance by modifying the channel encoder. Since the precoded and non-precoded symbols exhibit different BER, we proposed to employ two local coding rates to encode the precoded and non-precoded symbols while keeping the effective coding rate unchanged. Hence, different coding protection for the two groups of the transmitted symbols can be obtained. Our simulation results, in case of a transmission over AWGN channel, show that it is recommended to use a strong code to encode the precoded symbols. Moreover, the proposed channel coding enhances the transceiver performance when low FTN packing factors are considered: $\tau = 0.7$ in case of 16-QAM and $\tau = 0.8$ for 64-QAM modulation.
Considering high modulation orders, the Gray mapping presents different bit protection levels depending on the bit position. We proposed a bit reordering to take into account the different bit protection levels. Therefore, the useful information bits are placed at the highest protected positions. We presented the enhanced bits mapping for the precoded and non-precoded transceiver. Via simulation results, we showed that our bits reordering scheme enables significant BER improvement when high τ values are considered.
Moreover, as the FTN-self interference depends on the time instance of the transmitted symbols, we introduced a new symbol to time-frequency positions mapping different from the classical OFDM/OQAM mapping. Our objective is to map the useful information bits to positions which are less impacted by interference. The new symbols mapping structure was detailed in case of the non-precoded FTN-OQAM transceiver as well as for the FTN-OQAM transceiver combined with the SIPC-t and SIPC-f precoding. Through simulations, we showed that it is recommended to employ the enhanced symbols mapping in case of low FTN packing factors. Indeed, better BER results were achieved with 16-QAM and $\tau = 0.7$, as well as with 64-QAM modulation and $\tau = 0.8$.
Finally, we detailed a joint enhancement of the channel coding, the bits mapping and the symbols mapping. In this scenario, when different local coding rates are used, results showed that the receiver achieves better BER performance when the proposed bits mapping and symbols mapping are employed. However, we should also note that it is difficult to draw exact conclusions concerning the obtained results, since the gain using the different proposed techniques depends on various parameters such as the modulation order, the packing factor and the pulse shape.

Part of results presented in this chapter have been published in IEEE International Conference on Communications [110]. We also filed a patent on the enhanced design of SIPC precoding:

N. Lahbabi, H. Lin, C. Abdel Nour, C. Douillard and P. Siohan, “An enhanced coding strategy for FTN-OFDM/OQAM transceiver design", ICC’17, Paris, France, May 2017.

N. Lahbabi, H. Lin, C. Abdel Nour, C. Douillard and P. Siohan, “ Optimisation de la pré-annulation dispersée des interférences pour les transmissions FTN" 2016. Reference N° R28751FR.

Chapter 6

Conclusion

Our work has been motivated by the continuously increasing mobile data volume which constrains the future radio systems to include advanced modulations/waveforms offering higher data rates with more efficient bandwidth usage. One possibility is to improve the classical Nyquist-based digital transmission systems by signaling faster than the Nyquist rate. FTN transmissions were originally introduced by Mazo as a means to improve the spectral efficiency. He stated that the transmission rate is not necessarily limited by the Nyquist rate, meaning that faster transmission rate can be envisaged provided that interference is accepted. The main goal in my thesis was to define and evaluate a new transmission mode involving FTN signaling with OFDM/OQAM modulation to boost the transmission throughput.

6.1 Research contribution

In this dissertation, we mainly focused on OFDM/OQAM systems signaling faster than the Nyquist rate. We considered only packing the signals closer in time domain compared to the Nyquist rate. The major contributions of our work involved an efficient implementation of an FTN transceiver using OFDM/OQAM modulation (chapter 3), a new precoding technique aiming at reducing FTN-self interference at the transmitter side (chapter 4), and the proposal of an enhanced design of FTN-OQAM transceiver (chapter 5).

The first work concerning FTN-OQAM transceivers was presented in [2]. However, the complexity of their solution increases compared to traditional OFDM/OQAM systems due to the introduced FTN related blocks. Moreover, their receiver relies on MAP algorithm meaning that its complexity increases with the modulation order. In chapter 3, we investigated the concept of FTN signaling combined with OFDM/OQAM modulation over AWGN channel. Our objective is to propose a new implementation of FTN signaling approaching very closely the FTN theoretical rate improvement without complexity increase when switching from Nyquist to FTN mode. Differently from the SoTA solution, we proposed a turbo-like receiver based on linear MMSE equalization. As known, the complexity of such equalizers depends only on the channel impulse response and is independent of the modulation order which makes them good candidates if high modulation orders are envisaged. Since OFDM/OQAM modulation employs various pulse

shapes having different time-frequency localization properties, we showed that the MMSE equalizer should better operate along time axis when the prototype filter is well localized in time domain and vice-versa. Furthermore, we proposed an algorithm based on EXIT chart analysis to investigate the smallest packing factor the FTN-OQAM transceiver can achieve while providing a BER performance close to the Nyquist one. Differently from the SoTA solution, we targeted high modulation orders and showed that a rate improvement of 11% is achievable, in case of 64-QAM modulation, with a performance very close to the Nyquist one and after performing only 5 iterations at the receiver side. We also showed that the rate improvement can be up to 25% with 16-QAM modulation at the cost of 1 dB loss around a BER of 10^{-4} compared to the Nyquist performance while only 4 iterations are needed at the receiver side.

When signaling faster than the Nyquist rate, the pulses orthogonality is no longer valid and interferences are intentionally added to the transmitted signal even when transmitting over AWGN channel. In chapter 3, we provided an analytical expression of this interference and showed that it can be modeled by an equivalent interference channel. However, this interference is perfectly known by both the transmitter and the receiver which is similar to transmissions over multipath channels with perfect CSI at the transmitter. In chapter 4, we investigated a new precoding scheme we called Sparse Interference Pre-Cancellation to remove FTN-induced interference at the transmitter side. Given the nature of this interference, it is difficult to jointly precode all the transmitted symbols. Therefore, we proposed to remove interference from only a sub-group of the transmitted symbols, hence the sparse nature of our method. To this end, we introduced three precoder families depending on whether ISI and/or ICI cancellation is envisaged. The corresponding receivers deal first with the precoded symbols and then with the non-precoded ones. Our main objective was to improve the decoding of the precoded symbols and to remove their contribution to interference with the non-precoded ones before decoding the latter. A significant gain can be achieved thanks to the proposed precoding especially in case of high modulation orders and low packing factors, which means when FTN-self interference is severe. Since less interference is introduced to the transmitted symbols, EXIT chart analysis showed that the tunnel between the equalizer and the decoder is now wider, compared to the non-precoded FTN-OQAM scenario, meaning that the exchange of soft information between the soft equalizer and the decoder is improved. This is confirmed by the fact that less iterations are needed at the receiver side. Moreover, an important gain in terms of BER is obtained when considering high modulation orders and low packing factors (results were given for 16-QAM with τ=0.7 and 64-QAM with τ=0.8).

Our goal in chapter 5 was to enhance the different blocks of the FTN-OQAM transceiver to take into account the interference introduced by FTN signaling. The proposed modifications concerned the channel encoder, the bit-to symbols mapping and the symbols to time and frequency positions mapping. In the precoded FTN-OQAM transceiver, the precoded and non-precoded symbols exhibit different BER since they are affected differently by interference. Thus, we proposed to adapt the channel encoder by using different local coding rates, to encode the precoded and non-precoded symbols, while keeping the original coding rate unchanged. We showed that an important gain is obtained in case of high modulation orders and low packing factors (16-QAM with τ=0.7 and 64-QAM with τ=0.8) when using a stronger code to encode the precoded symbols. Secondly, we proposed to take advantage of the different bit level protections provided

by the Gray mapping in case of high modulation orders. As the channel coding is based on convolutional codes, we proposed to order the encoded bits to place information bits at highly protected positions of the Gray mapping and redundancy bits at the less protected positions. The new bits ordering enabled significant BER improvement for high packing factors: $0.8 \leq \tau$ for 16-QAM modulation and τ=0.9 for 64-QAM modulation. Finally, we proposed a new mapping of symbols to time-frequency positions different from the classical mapping used by OFDM/OQAM modulation. This is motivated by the fact that in a time and frequency lattice, the transmitted symbols at different time instants are impacted differently by interference. Considering convolution channel codes, we proposed to map symbols made up with information bits to time-frequency positions which are less affected by interference and to place symbols made up with redundancy bits at the remaining positions. Our method enabled BER improvement when high modulation orders (16 and 64-QAM modulation) and low packing factors (τ=0.7 and 0.8, respectively) are considered.

6.2 Directions for future work

This dissertation revealed the promising potential of FTN signaling as an interesting means to boost the transmitted throughput. As FTN transmissions are still an ongoing research field, we list below some future directions to further evaluate FTN signaling in multi carrier systems.

6.2.1 Channel coding

Throughout this thesis, the channel coding was mainly based on convolution codes with a coding rate of $\frac{1}{2}$. It is known that the correction capability of convolution codes increases with the length of the register memory. Turbo codes consist in associating several small RSC codes to imitate a convolution code with large memory. Fig. 3.18 in chapter 2 represents a turbo encoder architecture involving two RSC codes separated by an interleaver. In a turbo encoded FTN-OQAM transceiver, this turbo encoder can replace the channel coding block in Fig. 4.10. The corresponding receiver is then composed of the linear MMSE equalizer and the turbo decoder. Meaning that the receiver should involve two iteration loops: an outer loop between the equalizer and the turbo decoder, and an inner loop between the two RSC decoders. Hence, the iteration scheduling at each loop should be investigated.

When combining the FTN-OQAM transceiver with SIPC precoding, several modifications should be taken into account. Let us consider N_i information bits at the encoder input, with N_{i1} bits composing the precoded symbols and N_{i2} bits composing the non-precoded ones. We denote by N_c the number of encoded bits at the first RSC encoders and by N_{c1} and N_{c2} the number of encoded bits related to the N_{i1} and N_{i2} information bits, respectively. The N_{i1} and N_{i2} information bits should be interleaved individually. We denote by N_d the number of encoded bits at the second RSC encoder and by N_{d1} and N_{d2} the number of encoded bits related to the interleaved N_{i1} and N_{i2} information bits, respectively. Then, the N_{i1}, N_{c1} and N_{d1} bits are concatenated and mapped to OQAM symbols. Similarly, the N_{i2}, N_{c2} and N_{d2} bits are concatenated and mapped to OQAM symbols. Finally the SIPC module precodes the first group of symbols. At

the receiver side, the precoded symbols are decoded first followed by the non-precoded ones. This is enabled by individually interleaving the bits composing the precoded and non-precoded symbols. Moreover, the default values of the beginning and ending states should be modified as shown in section 4.2.3 of chapter 4.

Without puncturing, the coding rate ensured by the turbo encoder in Fig. 3.18 is $\frac{1}{3}$. In the precoded FTN-OQAM transceiver, both groups of symbols are encoded using the same coding rate. The coding rate of the precoded and non-precoded symbols can be adapted following the proposed channel coding in chapter 5. To this end, two different puncturing blocks should be introduced to ensure the chosen coding rates.

The proposed bits mapping and symbols mapping presented in chapter 5 can also be employed. Indeed for the bits mapping, the N_{i1} information bits are mapped to highly protected positions of the Gray mapping, while the N_c and N_d bits are mapped to the remaining positions. For the symbols mapping, the N_i, N_c and N_d bits are first mapped individually to OQAM symbols. Then symbols made up of information bits are mapped to time-frequency positions which are less affected by interference. Then symbols made up of redundancy bits are mapped to the remaining positions.

6.2.2 PAPR

The high PAPR represents one of the most disadvantages of OFDM systems. Generally, the PAPR of single carrier systems is affected by the employed pulse shape and the constellation order. For multi carrier systems, it was shown that the PAPR is mainly affected by the number of subcarriers [111]. In FTN systems, the transmitted symbols are packed closer, with respect to the Nyquist rate, in time and/or in frequency domains. By decreasing FTN packing factors, the symbols are more overlapped and consequently the PAPR increases, meaning that FTN systems present high PAPR when compared to Nyquist-based systems using the same modulation order and pulse shape. However, it is more interesting to compare the PAPR of FTN and Nyquist systems under the condition of equivalent spectral efficiency. In this scenario, FTN signaling can enable promising PAPR gain as it was shown in [81] in case of single carrier systems and in [85] for satellite communications.

6.2.3 Other equalization schemes

In this dissertation, we mainly focused on linear equalization to keep the receiver complexity under a reasonable level. Although, linear MMSE equalization is sub-optimal compared to MAP equalization, its complexity is independent of the constellation order which makes it suitable for FTN systems targeting high constellation orders. Other equalization schemes could be investigated for FTN signaling, such as Expectation Propagation (EP) algorithm which is a technique used to approximate a probability distribution with exponential family distributions. This technique has been proposed in [112] in case of MIMO systems with high constellation orders and number of antennas. The authors proposed an iterative algorithm to approximate the symbol posteriori distribution $P(\mathbf{u}/\mathbf{y})$ with a Gaussian distribution that is optimized using the EP framework. With $\mathbf{u} = [u_1, ..., u_n]^T$ the transmitted vector of i.i.d symbols of a set A and n the number of

transmitters. The received signal is denoted by $\mathbf{y} = \mathbf{H}\mathbf{u} + \mathbf{w}$, with $\mathbf{H}$ the $m \times n$ complex MIMO channel matrix, m the number of receiving antennas and $\mathbf{w}$ the additive white circular-symmetric complex Gaussian noise. The algorithm complexity is $O(n^3 L + n|A|L)$ with L the number of iterations.

Bibliography

[1] C. Siclet. *Application de la théorie des bancs de filtres à l'analyse et à la conception de modulations multiporteuses orthogonales et biorthogonales.* PhD thesis, University of Rennes 1, 2002.

[2] D. Dasalukunte, F. Rusek, J. B. Anderson, and V. Owall. Transmitter architecture for faster-than-Nyquist signaling. In *IEEE International Symposium on Circuits and Systems*, pages 1028–1031, May 2009.

[3] D. Dasalukunte, F. Rusek, and V. Owall. An iterative decoder for multicarrier faster-than-Nyquist signaling systems. In *IEEE International Conference on Communication*, pages 1–5, May 2010.

[4] M. Plumb. Fantastic 4G. In *IEEE Spectrum, volume 49*, pages 51–53, Jan. 2012.

[5] Cisco. Global Mobile Data Traffic Forecast Update, 2016-2021 White paper. 2017.

[6] J. Andrews, S. Buzzi, W. Choi, S. Hanly, A. Lozano, A. Soong, and J. Zhang. What will 5G be? In *IEEE J. Sel Areas Commun., volume 32, no. 6*, pages 1065–1082, Jun. 2014.

[7] In *FP7 European Project 317669 METIS (Mobile and Wireless Communications Enablers for the Twenty-Twenty Information society) 2012. https://www.metis2010.com/.*

[8] In *FP7 European Project 318555 5G NOW (5th Generation Non-Orthogonal Waveforms for Asynchronous Signaling) 2012. http://www.5gnow.eu/.*

[9] E. Hossain and M. Hasan. 5G cellular: key enabling technologies and research challenges. In *IEEE Instrum. Meas. Mag., vol. 18, no. 3*, pages 11–21, Jun. 2015.

[10] H. Nyquist. Certain factors affecting telegraph speed. In *The Bell System Technical Journal*, volume 3, pages 324–346, April 1924.

[11] H. Nyquist. Certain topics in telegraph transmission theory. In *Transactions of the American Institute of Electrical Engineers*, volume 47, pages 617–644, Feb. 1928.

[12] N. C. Beaulieu. Introduction to "certain topics in telegraph transmission theory". In *Proceedings of the IEEE*, volume 90, pages 276–279, Feb. 2002.

[13] J. M. Wozencraft and I. M. Jacobs. *Principles of Communication Engineering.* 1965.

[14] H. J. Landau. Sampling, data transmission, and Nyquist rate. In *Proceedings of the IEEE*, volume 55, pages 1701–1706, Oct. 1967.

[15] B. R. Saltzberg. Intersymbol interference error bounds with application to ideal bandlimited signaling. In *IEEE Transactions on Information Theory*, volume 14, pages 563–568, July 1968.

[16] J. Saltz. Optimum mean-square decision feedback equalization. In *The Bell System Technical Journal*, volume 52, pages 1341–1373, Oct. 1973.

[17] J.B. Anderson and F. Rusek. Improving OFDM: Multistream Faster-than-Nyquist Signaling. In *6th Int. ITG Conf. Source and Channel Coding.*, Apr. 2006.

[18] P. Siohan, C. Siclet, and N. Lacaille. Analysis and design of OFDM/OQAM systems based on filterbank theory. In *IEEE Transactions on Signal Processing*, volume 50(5), pages 1170–1183, 2002.

[19] J. Mazo. Faster-than-Nyquist signaling. In *Bell System Technical Journal*, volume 54, pages 1451–1462, 1975.

[20] F. Rusek and J. B. Anderson. The two dimensional Mazo limit. In *IEEE International Symposium on Information Theory*, pages 970–974, Sept. 2005.

[21] A. Prlja, J. B. Anderson, and F. Rusek. Receivers for faster-than-Nyquist signaling with and without turbo equalization. In *IEEE International Symposium on Information Theory*, pages 464–468, July 2008.

[22] A. Peled and A. Ruiz. Frequency domain data transmission using reduced computational complexity algorithms. In *ICASSP'80, volume 3, number 7*, pages 964–967, April 1980.

[23] R. W. Chang. Synthesis of band-limited orthogonal signals for multi-channel data transmission. In *Bell. Syst. Tech. Journal, volume 45*, pages 1775–1796, December 1966.

[24] B. R. Saltzberg. Performance of an efficient parallel data transmission system. In *IEEE Transactions on Communications Technology, Vol. 15, no. 6*, pages 805–811, 1967.

[25] B. Le Floch, M. Alard, and C. Berrou. Coded orthogonal frequency division multiplex. In *Proceedings of the IEEE*, volume 83, 1995.

[26] S. ten Brink. Convergence of iterative decoding. In *Electron. Lett., vol. 35, no. 13*, pages 1117–1119, Jun. 1999.

[27] G-E. Moore. Cramming more components onto integrated circuits. In *Electronics Magazine, vol. 38*, Apr. 1965.

[28] C. Walter. Kryder's law. In *Scientific American, vol. 293*, pages 32–33, Aug. 2005.

[29] J.G Proakis and S. Masoud. *Digital Communications*. McGraw-Hill, 2008.

[30] L. J. Cimini. Analysis and simulations of a digital mobile channel using Orthogonal Frequency Division Multiplexing. In *IEEE Transactions on Communications, volume COM-33, number 7*, pages 665–675, July 1985.

[31] P. A. Preenu and J. Renu. Comparison of PAPR reduction techniques in OFDM systems. In *IEEE International Conference on Communication and Electronics Systems (ICCES).*, Oct. 2016.

[32] N. J. Fliege. Orthogonal multiple carrier data transmission. In *European Transactions on Telecommunications*, volume 3 (3), pages 255–264, May-June 1992.

[33] P. Siohan and N. Lacaille. Analysis of OFDM/OQAM systems based on the filterbank theory. In *Globecom Rio de Janeiro (Brazil)*, pages 2279–2284, December 5-9 1999.

[34] H. Bölcskei. *Advances in Gabor Analysis.* Birkhäuser, 2003, Chapter Orthogonal frequency division multiplexing based on offset QAM, pages 321-352. 71.

[35] C. Roche and P. Siohan. A family of extended Gaussian functions with a nearly optimal localization property. In *Proc. Int. Workshop Multi-Carrier Spread-Spectrum, Germany,*, pages 179–186, Apr. 1997.

[36] D. Pinchon, P. Siohan, and C. Siclet. A fast design method for orthogonal modulated filter banks. In *ICASSP'02*, May 2002.

[37] D. Pinchon, P. Siohan, and C. Siclet. Design techniques for orthogonal modulated filterbanks based on a compact representation. In *IEEE Transctions on signal processing*, volume 52(6), pages 1682–1692, June 2004.

[38] G. Forney. Lower bounds on error probability in the presence of large intersymbol interference. In *IEEE Transactions on Communications*, volume 20, pages 76–77, Feb. 1972.

[39] G. J. Foschini. Contrasting performance of faster binary signaling with QAM. In *AT&T Bell Labs Technical Journal*, volume 63, pages 1419–1445, Oct. 1984.

[40] D. Hajela. On computing the minimum distance for faster than Nyquist signaling. In *IEEE Transactions on Information Theory*, volume 36, pages 289–295, Mar. 1999.

[41] H. Landau and J. Mazo. On the minimum distance problem for faster than Nquist signaling. In *IEEE Trans. Information Theory, IT-34*, pages 1420–1427, 1988.

[42] A. D. Liveris and C. N. Georghiades. Exploiting faster-than-Nyquist signaling. In *IEEE Transactions on Communications*, volume 51, pages 1502–1511, Sept. 2003.

[43] C.-K. Wang and L.-S. Lee. Practically realizable digital transmission significantly below the Nyquist bandwidth. In *IEEE Transactions on Communications*, volume 43, pages 166–169, Feb. 1995.

[44] F. Rusek. *Partial response and faster-than-Nyquist signaling.* PhD thesis, Lund University, Lund, Sweden, Sept. 2007.

[45] L. Bahl, J. Cocke, F. Jelinek, and J. Raviv. Optimal decoding of linear codes for minimizing symbol error rate. In *IEEE Transactions on Information Theory, vol. 20.*, pages 284–287, Mar. 1974.

[46] F. Rusek and J. B. Anderson. Successive interference cancellation in multistream faster-than-Nyquist signaling. In *Proc. The International Conference on Wireless Communications and Mobile Computing*, pages 1021–1026, July 2006.

[47] F. Rusek and J. B. Anderson. Serial and parallel concatenations based on faster than Nyquist signaling. In *Proc. IEEE International Symposium on Information Theory*, pages 1993–1997, July 2006.

[48] S. Ten Brink. Convergence behavior of iteratively decoded parallel concatenated codes. In *IEEE Transactions on Communications*, volume 49, pages 1727–1737, Oct. 2001.

[49] F. Rusek and J. B. Anderson. Non binary and pre-coded faster than Nyquist signaling. In *IEEE Transactions on Communications*, volume 56, pages 808–817, May 2008.

[50] F. Rusek and J. B. Anderson. Constrained capacities for faster than Nyquist signaling. In *IEEE Transactions on Information Theory*, volume 55, pages 764–775, Feb. 2009.

[51] F. Rusek and J. B. Anderson. Multistream faster than Nyquist signaling. In *IEEE Transactions on Communications*, volume 57, pages 1329–1340, May 2009.

[52] A. Prlja. *Reduced receivers for faster-than-Nyquist signaling and general linear channels*. PhD thesis, Lund University, Sweden, Lund, 2013.

[53] A. Prlja and J. B. Anderson. Reduced-complexity receivers for strongly narrowband intersymbol interference introduced by faster-than-Nyquist signaling. In *IEEE Transactions on Communications*, volume 60, No. 9, pages 2591–2601, Sept. 2012.

[54] D. Dasalukunte. *Multicarrier Faster-than-Nyquist signaling transceivers. From theory to practice*. PhD thesis, Lund University, Sweden, Lund, 2012.

[55] D. Dasalukunte, F. Rusek, J. B. Anderson, and V. Owall. A $0.8mm^2$ 9.6 mw implementation of a multicarrier faster-than-Nyquist signaling iterative decoder in 65 nm CMOS. In *Proc. European Solid State Circuits Conference, Bordeaux, France*, pages 173–176, Sept. 2012.

[56] D. Dasalukunte, F. Rusek, V. Owall, K. Ananthanarayanan, and M. Kandasamy. Hardware implementation of mapper for faster-than-Nyquist signaling transmitter. In *Proc. IEEE NORCHIP, Trondheim, Norway*, pages 1–5, Nov. 2009.

[57] Y. J. D. Kim. *Faster than Nyquist transmission over continuous-time channels: Capacity analysis and coding*. PhD thesis, McGill University, Montréal, Canada, Aug. 2013.

[58] Y. J. D. Kim and J. Bajcsy. On spectrum broadening of pre-coded faster-than-Nyquist signaling. In *Proc. IEEE Vehicular Technology Conference Fall, Ottawa ON*, pages 1–5, Sept. 2010.

[59] Y. J. D. Kim and J. Bajcsy. Information rates of cyclostationary faster-than-Nyquist signaling. In *Proc. Canadian Workshop on Information Theory, Kelowna, BC*, pages 1–4, May 2011.

[60] Y. J. D. Kim and J. Bajcsy. Faster-than-Nyquist broadcast signaling. In *Proc. Queen's Bennial Symposium on Communications, Kingston, Ontario*, pages 186–189, May 2012.

[61] Y. J. D. Kim and J. Bajcsy. An architecture for faster than Nyquist turbo broadcasting. In *Proc. International Symposium on Turbo Codes & Iterative Information Processing, Gothenburg, Sweden*, pages 170–175, Aug. 2012.

[62] Y. J. D. Kim and J. Bajcsy. Binary faster-than-Nyquist optical transmission via non-uniform power allocation. In *Proc. Canadian Workshop on Information Theory, Toronto, ON*, pages 191–196, June 2013.

[63] B. P. Smith and F. R. Kschischang. Future prospects for FEC in fiber-optic communications. In *IEEE Journal of Selected Topics in Quantum Electronics, vol. 16*, pages 1245–1257, Sept./Oct 2010.

[64] G. Colavolpe, T. Foggi, A. Modenini, and A. Piemontese. Faster-than-Nyquist and beyond: How to improve spectral efficiency by accepting interference. In *Optics Express, vol. 19*, pages 26600–26609, Dec. 2011.

[65] J.-X. Cai, C. R. Davidson, A. Lucero, H. Zhang, D. G. Foursa, O. V. Sinkin, W. W. Patterson, A. N. Pilipetskii, G. Mohs, and N. S. Bergano. 20tbits/s transmission over 6860 km with sub-Nyquist channel spacing. In *IEEE/OSA Journal of Lightwave Technology, vol. 30*, pages 651–657, Feb. 2012.

[66] J. Li, E. Tipsuwannakul, M. Karlson, and P. A. Andrekson. Exploiting the faster-than-Nyquist concept in wavelength-division multiplexing systems using duobinary shaping. In *ZTE Communications, vol. 10*, pages 23–29, Mar. 2012.

[67] A. Barbieri, D. Fertonani, and G. Colavolpe. Time-frequency packing for linear modulations: spectral efficiency and practical detection schemes. In *IEEE Transactions on Communications*, pages 2951–2959, Oct. 2009.

[68] A. Modenini, G. Colavolpe, and N. Alagha. How to significantly improve the spectral efficiency of linear modulations through time-frequency packing and advanced processing. In *IEEE International Conference on Communications*, pages 23–29, June 2012.

[69] A. Modenini, F. Rusek, and G. Colavolpe. Faster-than-Nyquist signaling for next generation communication architectures. In *European Signal Processing Conference (EUSIPCO)*, pages 1856–1860, Sept. 2014.

[70] I. Kanaras, A. Chorti, M. Rodrigues, and I. Darwazeh. Spectrally efficient FDM signals: bandwidth gain at the expense of receiver complexity. In *Proc. IEEE International Conference on Communications, Dresden, Germany*, pages 3701–3706, June 2009.

[71] S. Isam and I. Darwazeh. Precoded spectrally efficient FDM system. In *IEEE International Symposium on Personal, Indoor and Mobile Radio Communications, Istanbul, Turkey*, pages 99–104, Sept. 2010.

[72] I. Darwazeh, T. Xu, T. Gui, Y. Bao, and Z. Li. Optical SEFDM system: bandwidth saving using non-orthogonal sub-carriers. In *IEEE Photonics Technology Letters, vol. 26, No. 4*, pages 352–355, Dec. 2013.

[73] M. Hamamura and S. Tachikawa. Bandwidth efficiency improvement for multicarrier systems. In *IEEE International Symposium on Personal, Indoor and Mobile Radio Communications, Barcelona, Spain*, pages 48–52, Sept. 2004.

[74] W. Jiang, Y. Xun, Z. Xi-Lin, and D. Li. The prefix design and performance analysis of DFT-based overlapped frequency division multiplexing (OvFDM-DFT) system. In *International Workshop on Signal Design and Its Applications in Communications*, pages 361–364, Sept. 2007.

[75] F.-M. Han and X.-D. Zhang. Wireless multicarrier digital transmission via Weyl-Heisenberg frames over time-frequency dispersive channels. In *IEEE Transactions on Communications, vol. 57*, pages 1721–1733, June 2009.

[76] C. Siclet, D. Roque, H. Shu, and P. Siohan. On the study of faster-than-Nyquist multicarrier signaling based on frame theory. In *International Symposium on Wireless Communications Systems*, pages 251–255, Aug. 2014.

[77] Y. G. Yoo and J. H. Cho. Asymptotic optimality of binary faster-than-Nyquist signaling. In *IEEE Communications Letters, vol. 14*, pages 788–790, Sept. 2010.

[78] M. McGuire and M. Sima. Discrete time faster-than-Nyquist signaling. In *IEEE Global Telecommunications Conference, Miami, Florida*, pages 1–5, Dec. 2010.

[79] J. Yo, J. Park, F. Rusek, B. Kudryashov, and I. Bocharova. High order modulation in faster-than-Nyquist signaling communication systems. In *IEEE 80th Vehicular Technology Conference (VTC2014-Fall)*, pages 1–5, Sept. 2014.

[80] B. F. Beidas, R. I. Seshadri, M. Eroz, and L-N. Lee. Faster-than-Nyquist signaling and optimized signal constellation for high spectral efficiency communications in nonlinear satellite systems. In *IEEE Military Communications Conference.*, pages 818–823, Oct. 2014.

[81] C. Le, M. Schellmann, M. Fuhrwerk, and J. Peissig. On the practical benefits of faster-than-Nyquist signaling. In *International Conference on Advanced Technologies for Communications (ATC2014)*, pages 208–213, Oct. 2014.

[82] Physical layer for dynamic spectrum access and cognitive radio (FP7-ICT Project 211887 PHYDYAS). [Online]. Available: tp://www.ict-phydyas.org/.

[83] R. Tajan, B. Benammar, C. Poulliat, and M-L. Boucheret. On coding for Faster-Than-Nyquist Signaling. In *IEEE International Black Sea Conference on Communications and Networking (BlackSeaCom).*, May. 2015.

[84] R. Tajan, C. Poulliat, and M-L. Boucheret. Circular Faster Than Nyquist: Transmitter and Iterative Receiver Design. In *IEEE International Symposium on Turbo Codes & Iterative Information Processing (ISTC).*, Sept. 2016.

[85] J-A. Lucciardi, N. Thomas, M-L. Boucheret, C. Poulliat, and G. Mesnager. Trade-off between spectral efficiency increase and PAPR reduction when using FTN signaling: impact of non linearities. In *IEEE International Conference on Communications (ICC).*, May. 2016.

[86] C. Berrou, A. Glavieux, and P. Thitmajshima. Near Shannon limit error-correcting coding and decoding: Turbo-codes. In *Proc. IEEE International Conference on Communications, Geneva, Switzerland*, pages 1064–1070, May 1993.

[87] Third Generation Partnership Project. Technical specification group radio access network; multiplexing and channel coding (FDD). In *Technical Specification, 3GPP TS 25.212, ver. 7.0.0*, Mar. 2006.

[88] C. Douillard, M. Jézéquel, C. Berrou, N. Bengarth, J. Tousch, and N. Pham. The turbo code standard for DVB-RCS. In *Proc. International Symposium on Turco codes & Related Topics, Brest, France*, pages 535–538, Sept. 2000.

[89] Digital video broadcasting (DVB): Interaction channel for satellite distribution systems, ETSI EN 301 790, V1.5.1, European Standard (Telecommunication Series). May 2009.

[90] C. Berrou. *Codes and Turbo Codes.* Springer-Verlag, 2010.

[91] R. Le Bidan. Turbo-equalization for bandwidth-efficient digital communications over frequency-selective channels. In *Ph. D dissertation, l'ENST Bretagne, France*, 2006.

[92] A. Glavieux, C. Laot, and J. Labat. Turbo equalization over a frequency selective channel. In *Proc. International Symposium on Turco codes & Related Topics, Brest, France*, pages 96–102, Sept. 1997.

[93] C. Laot. Égalisation autodidacte et turbo-égalization applications aux canaux sélectifs en fréquence. In *Ph. D dissertation, Univ. de Rennes I, Rennes, France*, Jul. 1997.

[94] C. Laot, A. Glavieux, and J. Labat. Turbo-equalization: Adaptive equalization and channel decoding jointly optimized. In *IEEE J. Selected Areas Commun., vol. 19, no. 9*, pages 1744–1752, Sept. 2001.

[95] X. Wang and H. V. Poor. Iterative (turbo) soft interference cancellation and decoding for coded CDMA. In *IEEE Transactions on Comunications, vol. 47, no. 7*, pages 1046–1061, Jul. 1999.

[96] D. Reynolds and X. Wang. Low-complexity turbo equalization for diversity channels. In *Signal Processing, vol. 81, no. 5*, pages 989–995, May 2001.

[97] M. Tüchler, A. C. Singer, and R. Kötter. Minimum mean-squared error equalization using *a priori* information. In *IEEE Transactions on Signal Processing, vol. 50, no. 3*, pages 673–683, March 2002.

[98] M. Tüchler, R. Kötter, and A. C. Singer. Turbo equalization: Principles and new results. In *IEEE Transactions on Communications, vol. 50, no. 5*, pages 754–767, May 2002.

[99] C. Laot, R. Le Bidan, and D. Leroux. Low-complexity linear turbo equalization: A possible solution for EDGE. In *IEEE Transactions on Wireless Communications, vol. 4, no. 3*, pages 965–974, May 2005.

[100] N. Shengyu, G. Mingxi, and S. Yuehong. Precoding based on matrix decomposition for faster-than Nyquist signaling. In *International Conference on Electronics Information and Emergency Communication (ICEIEC)*, pages 194–197, May 2015.

[101] M. Tomlinson. New automatic equalizer employing modulo arithmetic. In *Electronics Letters, vol. 7*, pages 138–139, March 1971.

[102] H. Harashima and H. Miyakawa. A method for code conversion for digital communication channels with intersymbol interference. In *Transactions of the Insitute of Electronics and Communications Engineers of Japan., 52-A*, pages 272–273, June 1969.

[103] H. Harashima and H. Miyakawa. Matched-transmission technique for channels with intersymbol interference. In *IEEE Transactions on Communications, COM-20, 52-A*, pages 774–780, Aug. 1972.

[104] D. Chang, O. Omomukuyo, O. Dobre, R. Venkatesan, and P. Gillard. A faster-than-Nyquist PDM-16QAM scheme enabled by Tomlinson-Harashima precoding. In *International Conference on Transparent Optical Networks (ICTON)*, pages 1–4, Jul. 2015.

[105] D. Chang, O. Omomukuyo, O. Dobre, R. Venkatesan, P. Gillard, and C. Rumbolt. Tomlinson-Harashima precoding with soft detection for faster-than-Nyquist DP-16QAM coherent optical systems. In *Optical Fiber Communications Conference and Exhibition (OFC)*, pages 1–3, March 2015.

[106] Y. Dandach and P. Siohan. FBMC/OQAM modulators with half complexity. In *In Proceedings Globecom'11 (Houston, USA)*, pages 1–5, Dec. 2011.

[107] D. Dasalukunte, F. Rusek, and V. Owall. Multicarrier faster-than-Nyquist transceivers: Hardware architecture and performance analysis. In *IEEE Transactions on Circuits and Systems-I: Regular papers*, volume 58, pages 827–838, April 2011.

[108] H. Lin, N. Lahbabi, P. Siohan, and X. Jiang. An efficient FTN implementation of the OFDM/OQAM system. In *IEEE International Conference on Communications (ICC'15), London, UK*, pages 4787–4792, Jun. 2015.

[109] N. Lahbabi, H. Lin, A. N. Charbel, C. Douillard, and P. Siohan. Sparse interference pre-cancellation for FTN-OQAM systems. In *IEEE 22th European Wireless conference, Oulu, Finland*, pages 1–6, May 2016.

[110] N. Lahbabi, H. Lin, A. N. Charbel, C. Douillard, and P. Siohan. An enhanced coding strategy for FTN-OFDM/OQAM transceiver design. In *IEEE International Conference on Communications (ICC'17), Paris, France*, May 2017.

[111] A. Skrzypczak, P. Siohan, and J-P. Javaudin. Analysis of the Peak-To-Average Power Ratio for OFDM/OQAM. In *IEEE 7th workshop on Signal Processing Advances in Wireless Communications, SPAWC'06*, pages 1–5, Jul. 2006.

[112] J. Céspedes, P. B. Olmos, M. Sánchez-Fernández, and F. Perez-Cruz. Expectation propagation detection for high-order high-dimensional MIMO systems. In *IEEE Transactions on Communications, volume 62*, pages 2840–2849, Aug. 2014.

Résumé

La croissance exponentielle du trafic de données sans fils, causée par l'Internet mobile et les smartphones, contraint les futurs systèmes radio à inclure des modulations/formes d'ondes plus avancées offrant un débit plus élevé et une utilisation efficace des ressources spectrales. Les transmissions dites Faster-Than-Nyquist (FTN), introduites en 1975, sont parmi les meilleurs candidates pour répondre à ces besoins. En transmettant les symboles à une cadence plus rapide que celle définie par le critère de Nyquist, FTN peut théoriquement augmenter le débit mais en introduisant des interférences en contrepartie. Dans cette thèse, nous explorons le concept des transmissions FTN à travers un canal AWGN (Additive White Gaussian Noise) dans le contexte des modulations OFDM/OQAM (Orthogonal Frequency Division Multiplexing with Offset Quadrature Amplitude Modulation).

L'objectif principal de cette thèse est de présenter un système OFDM/OQAM qui permet de transmettre l'information au-delà de la cadence de Nyquist tout en tenant en compte la complexité globale du système. Tout d'abord, nous proposons une nouvelle implémentation efficace des systèmes OFDM/OQAM appliquant le concept FTN, désignée ici par FTN-OQAM, qui garde la même complexité que les systèmes OFDM/OQAM et qui permet un gain en débit très proche du gain théorique. Vu que la condition de Nyquist n'est plus respectée, le signal transmis est maintenant perturbé par des interférences. Pour remédier à ce problème, nous proposons un récepteur basé sur le principe de l'égalisation linéaire sous le critère minimum erreur quadratique moyenne avec annulation d'interférences appelé MMSE LE-IC. Le but de notre système est d'augmenter le débit de transmission, ce qui signifie que des constellations d'ordres élevés seront ciblées. Dans ce contexte, le MMSE LE-IC, dont la complexité est indépendante de la constellation, représente un bon compromis entre efficacité et complexité. Puisque la modulation OFDM/OQAM utilise différents types de formes d'ondes, nous proposons pour plusieurs d'entre elles un algorithme pour déterminer la valeur minimale du facteur d'accélération, en fonction de l'ordre de constellation, qui apporte un gain en efficacité spectrale tout en gardant les mêmes performances que les systèmes respectant le critère de Nyquist à un SNR fixé. Ensuite, nous étudions l'amélioration du traitement itératif de l'émetteur-récepteur. La méthode proposée consiste à combiner un précodeur avec le système FTN-OQAM afin de réduire les interférences causées par du FTN à l'émission. Nous proposons un modèle de précodage dispersé, car il est difficile de précoder conjointement tous les symboles transmis. Nous présentons trois familles de précodeurs avec les récepteurs correspondants. En outre, nous modifions différents blocs de l'émetteur FTN-OQAM tels que le codage canal, le mappage des bits et le mappage des symboles afin d'améliorer davantage le transmetteur FTN-OQAM. Les résultats présentés révèlent le potentiel important des systèmes proposés.

Mot clés: Faster-Than-Nyquist, OFDM/OQAM, Codage canal, précodage, Turbo égalisation, Annulation d'interférence.

Abstract

The exponential growth of wireless data traffic driven by mobile Internet and smart devices constrains the future radio systems to include advanced modulations/waveforms offering higher data rates with more efficient bandwidth usage. One possibility is to violate the well known Nyquist criterion by transmitting faster than the Nyquist rate, i.e., using a technique also known as Faster-Than-Nyquist (FTN) signaling. Nyquist-based systems have the advantage of simple transmitter and receiver architectures at the detriment of bandwidth efficiency. The idea of signaling beyond the Nyquist rate to trade the interference-free transmission for more throughput goes back to 1975. In this dissertation, we investigate the concept of FTN signaling over Additive White Gaussian Noise (AWGN) channel in the context of Orthogonal Frequency Division Multiplexing with Offset Quadrature Amplitude Modulation OFDM/OQAM modulation.

The main objective of our work is to present an OFDM/OQAM system signaling faster than the Nyquist one and explore its potential rate improvement while keeping under consideration the overall system complexity. First, we propose a new efficient FTN implementation of OFDM/OQAM systems, denoted by FTN-OQAM, that has the same complexity as OFDM/OQAM systems, while approaching very closely the FTN theoretical rate improvement. As the Nyquist condition is no longer respected, severe interference impacts the transmitted signals. To deal with the introduced interferences, we propose a turbo-like receiver based on Minimum Mean Square Error Linear Equalization and Interference Cancellation, named MMSE LE-IC. The aim of our system is to boost the transmission rate, which means that high constellation orders will be targeted. In this respect, the MMSE LE-IC, whose complexity is independent of the constellation, turns out to be a good candidate. Since OFDM/OQAM modulation can be equipped with different types of pulse shapes, we propose an algorithm to find, for different constellation orders, the minimum achieved FTN packing factor for various pulse shapes. Then, we aim at improving the iterative processing of the introduced transceiver. The proposed method involves combining a precoder with the FTN-OQAM system in order to remove FTN-induced interference at the transmitter. We also present a sparse precoding pattern as it is difficult to jointly precode all the transmitted symbols. We introduce three families of precoders along with the corresponding receivers. Furthermore, we propose several modifications of the FTN-OQAM transmitter concerning different blocks such as channel coding, bits mapping and symbols mapping to further enhance the FTN-OQAM transceiver design. Presented results reveal the significant potential of the proposed methods.

Keywords: Faster-Than-Nyquist, OFDM/OQAM, Channel coding, precoding, Turbo equalization, Interference cancellation.

IMT Atlantique
Bretagne-Pays de la Loire
École Mines-Télécom

N° d'ordre : 2017IMTA0017

IMT Atlantique Bretagne-Pays de la Loire - www.imt-atlantique.fr

Campus de Brest
Technopôle Brest-Iroise
CS 83818
29238 Brest Cedex 03
T +33 (0)2 29 00 11 11
F +33 (0)2 29 00 10 00

Campus de Nantes
4, rue Alfred Kastler - La Chantrerie
CS 20722
44307 Nantes Cedex 3
T +33 (0)2 51 85 81 00
F +33 (0)2 51 85 81 99

Campus de Rennes
2, rue de la Châtaigneraie
CS 17607
35576 Cesson Sévigné Cedex
T +33 (0)2 99 12 70 00
F +33 (0)2 99 12 70 08